University of Alberta

Spatiotemporal magnetization dynamics of patterned $Ni_{80}Fe_{20}$

by

Miroslav Belov 

A thesis submitted to the Faculty of Graduate Studies and Research in partial fulfillment of the

requirements for the degree of Doctor of Philosophy

Department of Physics

Edmonton, Alberta
Fall 2004

Your file Votre référence
ISBN: 0-612-95906-6
Our file Notre référence
ISBN: 0-612-95906-6

Acknowledgements

I would like to thank a number of people who have contributed to the development of this thesis and who have made my stay at University of Alberta enjoyable and rewarding.

First I would like to thank my supervisor Dr. Mark Freeman for the opportunity to study the field of micromagnets and scanning ultrafast microscopy. His support and patience have given me the freedom to explore a large field of physics and the chance of being involved in an exciting research in a group of highly educated and experienced physicists and engineers.

I am indebted to my colleagues Greg Ballentine, Kristen Buchanan, B.C. Choi, David Fortin, Wayne Hiebert, Sasha Krichevsky, Zhigang Liu, Marek Malac, Yan Pennec, Mark Roseman, Geoff Steeves and Xiaobin Zhu, for their helpful discussions and assistance.

I would like to acknowledge discussions and learning opportunities with academic staff in condensed matter physics (particularly Ray Egerton, Frank Marsiglio, Al Meldrum, Massimo Boninsegni and John Beamish).

I am thankful to Lynn Chandler for her advice during my study and for the proofreading of this thesis.

Special thanks to Don Mullin, Greg Popowich, Tony Walford, Jay Haverstock, Jim MacKinnon, Yolande Peske, Steve Rogers and Gilbert Lachat for their help and prompt technical assistance.

I would like to thank people from University of Alberta NanoFab, Ken Westra, Mirwais Aktary, Stephanie Bozic, Keith Franklin, Nicole Morin, Aruna Kroetch and from the Department of Electrical and Computer Engineering, Michael Brett and his GLAD group for their excellent support and advice during my experimental work on microfabrication of thin film magnetic structures.

I would like to especially thank my beloved wife Luba for her continuous support, understanding and encouragement.

Table of Contents

Appendices.

List of Figures

List of Symbols

α	Gilbert's damping constant
Δ_d	domain wall thickness
χ	magnetic susceptibility
γ	gyromagnetic ratio, $e/2m_e$
ε	dielectric constant
ε_0	permitivity of vacuum
φ	angular coordinate
Φ	scalar potential
λ	wavelength
μ	permeability, spin magnetic moment
μ_o	permeability of free space
μ_B	Bohr magneton
μm	micrometer, 10^{-6}
π	ratio of a circle's area to squared radius
σ	conductivity
ω	frequency
ϕ	angular coordinate
θ	angular coordinate
Ψ	wave function
a	lattice constant
A	ampere, exchange constant, vector potential
B	magnetic induction
c	speed of light in a vacuum
d	thickness, distance
D	electric induction
DC	direct current
e	charge of an electron, number with a natural logarithm of one
E	electric field, energy
EBL	electron-beam lithography
exp	experiment
f	frequency
F()	Fourier transform
Fe	iron
FFT	fast Fourier transform
FMR	ferromagnetic resonance
g	spectroscopic splitting factor
GHz	gigahertz
$\hbar$	Planck constant over 2π
h	time varying portion of magnetic field
H	magnetic field
H_{DC}	biasing magnetic field
H_d	demagnetizing magnetic field
H_{eff}	effective magnetic field
H_i	induced magnetic field
H_o	static component of magnetic field
H_ϕ,H_θ	magnetic field along ϕ or θ direction
Hz	hertz
i	imaginary number
I_p, I_s	incident light intensities
J	current density,
J, J_{mn}	exchange integral

k	wavevector
k_B	Boltzmann's constant
K_{ij}	demagnetizing coefficient
keV	kiloelectron volts
kHz	kilohertz
k_{neigh}	number of nearest neighbours
k_u	uniaxial anisotropy constant
L	angular momentum
l_{ex}	exchange length due to anisotropy
LLG	Landau-Lifshitz-Gilbert
m_e	mass of an electron
m	magnetization, magnetic moment, time varying portion of magnetization
M	magnetization
MHz	megahertz
M_o	static component of magnetization
M_s	saturation magnetization
n	surface normal, quantum number, index of refraction
N	number of cells
Ni	nickel
nm	nanometer
ns	nanosecond
N_x, N_y, N_z	demagnetizing factors
Oe	Oersted
p	polarization state of light
ps	picoseconds
r	position vector, reflected light coeficients
r_{ij}	distance vector
RKKY	Ruderman-Kittel-Kasuya-Yosida
S	spins
SEM	scanning electron microscope
MOKE	magneto-optical Kerr effect
Si	silicon
sim	simulation
t	time, thickness
T	temperature
T_1, T_2	Bloch-Bloembergen relaxation times
TEM	transmission electron microscope
Ti	titanium
TR-SKEM	time resolved scanning Kerr effect microscopy
v	velocity
V	voltage, volume
W	energy
w	volume energy density, width
x	Cartesian coordinate
y	Cartesian coordinate
z	Cartesian coordinate

1. Introduction.

The recent interest in high-speed information technology and spintronic applications has stimulated studies of micrometer and submicrometer magnetic structures within sub-nanosecond temporal range [1]. The effort to reveal smaller spatial details of the magnetic microstructures on very short time scales is driven by two interconnected, motivating aspects, first, the fundamental understanding of forces and laws of magnetism, and second, the opportunities for their application in new sensors, memory and information processing devices [2-3]. The progress in thin film deposition techniques and lithographic patterning processes provide capabilities for the production of magnetic structures at micrometer and nanometer scales. Engineered material properties such as anisotropy, saturation magnetization, complex geometrical patterning of single elements (or arrays) and new ways of excitation of magnetization oscillations create a large potential for industrial applications. The development of new materials and structures parallels the evolution of experimental scanning techniques based on the latest results in nanotechnology, condensed matter physics and optics. This new knowledge and the accompanying experimental techniques open new ways to acquire and process information about very small and complex systems and ultrafast processes.

The latest experiments in the field of microwave and optical microstructures prove that a rich world of waves and oscillations in dielectric and metallic films can be affected by complex 2-D and 3-D geometrical patterns. Extending this knowledge into the area of micromagnets suggests that "magnonic" structures could control magnetization oscillations at similar levels, and significantly expand opportunities in the

fields of computation and sensors. These opportunities were the major motivation for starting the work on this thesis. The ultrafast microscopy group at the Department of Physics with its history in the investigations of magnetic materials, and the NanoFab, the microfabrication facility on campus, with its background in thin film deposition and patterning, offered the necessary basis for complex experiments with thin film micromagnetic materials.

As suggested at the beginning of this work, new technological procedures (required for the fabrication of thin film micromagnetic structures with arbitrary shapes and sizes, in a range from a few tens of nanometers to tens of microns) had to be developed. To probe fabricated micromagnets at spatial and temporal scales of a few hundreds of nanometers and femtoseconds respectively, a scanning ultrafast Kerr microscope had to be built. To accomplish this, a focused experimental effort was required, that included knowledge and skills from the areas of optics and ultrafast lasers, precise spatial measurements, and electronic equipment for gathering the data from the experiment. A theoretical understanding of the interactions in complex magnetic systems sufficient to acquire insights into the micromagnetic dynamics of the magnetic structures, and numerical simulations of dynamics of patterned thin film magnetic films were also undertaken. The latest developments in software and hardware technology provided fast computational techniques for a comprehensive numerical study.

Chapter 2 of the thesis gives an overview of the fundamentals of magnetization oscillations, focusing on the dynamic behavior of magnetization oscillations in thin magnetic films. In addition, it provides the results of recent theoretical studies and experimental investigations of spin wave responses and magnon-magnon interactions in

thin film micromagnets. Chapter 3 introduces technological procedures for growing and patterning thin magnetic films developed during the work on this thesis. The focus is on thin film deposition by magnetron sputtering, electron beam lithography and the lift-off process. Planar structures (with micron and sub-micron features) fabricated using these techniques and analyzed by scanning electron, atomic force and optical microscopes are shown.

In Chapter 4, the interactions of light with magnetic thin films are briefly introduced and the experimental setup of the ultrafast time-resolved scanning microscope is described in detail.

Scanning results are analyzed in Chapter 5. Micron-sized squares and elliptical elements with and without internal lithographic pinholes are investigated and the resulting ferromagnetic curves, spatial and temporal renderings, and 2-D spatial images of magnetization oscillations (excited by a broadband transient magnetic pulse) are shown. The experimental data is compared with numerical simulations calculated by using the Landau-Lifshitz-Gilbert equation of motion. This chapter concludes with a discussion of the damping and magnon-magnon interactions in magnetic platelets with domain structures.

Bibliography.

[1] Special Issue on "**Magnetoelectronics**," Phys. Today 48, 24, 1995

[2] Prinz G.A., "**Magnetoelectronics**", Science 282, 1660, 1998

[3] Wolf S.A. et al., "**Spintronics: A Spin-Based Electronics Vision for the Future**", Science, 294, 1488, 2001

2. Micromagnets and their magnetization dynamics

2.1 Introduction

The concept of magnetic domains proposes that ferromagnetic materials with spontaneous magnetization exist in a demagnetized state. However, large numbers of atomic moments may be aligned over a macroscopic volume. If the directions of the domain orientation across a large volume of material are more or less random, the magnetization of a specimen can be zero. The behavior of such a complicated physical system is described by its (free) energy. The local or absolute minimum of this energy defines the state of the system. Even without an external applied field, the magnetization within a domain will be saturated, and it will lie in a direction determined by various constraints.

This chapter gives a brief explanation and a description for each typical interaction. The interactions in the magnetic system include the exchange (based on a quantum mechanical description), demagnetizing (the interaction based on a magnetostatic field approximation), anisotropic (crystal symmetry combined with spin-orbital interaction) and Zeeman (the interaction between the magnetization and the external field) interactions[†]. The fundamentals of the broadband ferromagnetic resonance effect, and the magnetization dynamics (via classical equations of torque and Maxwell equations) are also explained below. The spin wave relaxation and the magnon-magnon

[†] A detailed description of the software implementation of each above energies in the numerical simulation code is given in reference [110].

interactions in various infinite and finite ferromagnetic bodies and magnetic thin films are briefly discussed. Finally, a description of the interactions between the magnetization and electromagnetic fields in magnetic thin film structures is presented.

2.1.1 Exchange energy.

The fundamental explanation of exchange energy lies in the Coulomb interaction and the Pauli exclusion principle. The exchange interaction aligns or anti-aligns the spins in a magnetic material. Orbital moments are neglected, as they are assumed to be quenched by averaging the angular momentum to zero in a non-central crystal field. This assumption is mostly true for *3d* metals and less true for rare earth ions with *4f* orbitals. Using the Heisenberg-Dirac approximation [6] the exchange energy has a form

$$H_{exch} = -2 \Sigma_{ij} J_{ij} \boldsymbol{S}_i \boldsymbol{S}_j \qquad (2.1)$$

where J_{ij} is positive for ferromagnets and the spins are completely localized. The spin-orbit interactions are assumed in terms of the magnetocrystalline anisotropy. When the spin magnetic moments of the adjacent atoms i and j are oriented at relative angle φ_{ij}, the exchange energy between the two moments is

$$\Sigma_{ij} E_{ij} = -2\Sigma_{ij} JS^2 \cos \varphi_{ij} \approx JS^2 \Sigma_{ij} \varphi_{ij}^2 \qquad (2.2)$$

where $\varphi_{ij} << 1$, J is the exchange integral and S is the total spin quantum number of each atom. For example, for iron (with a b.c.c lattice) and with the spin $S = 1)$ the exchange integral [2] is

$$J = 0.15 k_B T_C \approx 2.16 \times 10^{-21} J \qquad (2.3)$$

Further approximations, such as $\varphi_{ij}^2 \approx |\boldsymbol{M}_i - \boldsymbol{M}_j|^2/\boldsymbol{M}_s^2 \approx |\boldsymbol{r}_i . \nabla \boldsymbol{M}_j|^2/\boldsymbol{M}_s^2 \approx a^2.(\nabla M_x^2 + \nabla M_x^2 + \nabla M_x^2)$, where a is the lattice constant, give exchange energy density

$$E_{exch} = A(\nabla M_x^2 + \nabla M_x^2 + \nabla M_x^2) \tag{2.4}$$

with $A = JS^2 k_{nn}/a$, is the exchange constant and k_{nn} is the number of nearest neighbors for each atom.

2.1.2 Magnetostatic energy

This is based on the interactions of localized classical magnetic moments. The magnetic field at point $\boldsymbol{r}_j$ produced by magnetic dipole $\boldsymbol{M}_i$, placed at coordinates $\boldsymbol{r}_i$, is

$$\boldsymbol{H}_j = 3(\boldsymbol{M}_i . \boldsymbol{r}_{ij}) . \boldsymbol{r}_{ij} / |\boldsymbol{r}|_{ij}^5 - \boldsymbol{M}_i / |\boldsymbol{r}|_{ij}^3 \tag{2.5}$$

where $\boldsymbol{r}_{ij} = \boldsymbol{r}_i - \boldsymbol{r}_j$. If the torque $\boldsymbol{T}_j$ acting on another dipole with a moment $\boldsymbol{M}_j(\boldsymbol{r}_j)$ is $\boldsymbol{M}_j \times \boldsymbol{H}_j$, then the potential energy from integrating the torque ij $U = -\boldsymbol{M}_j . \boldsymbol{H}_j$,·interaction energy E_{dipol} of all magnetic moments is the sum [18, 20]

$$E_{dipol} = \Sigma_{ij(i \neq j)} E_{ij} = -\Sigma_{ij(i \neq j)} \boldsymbol{M}_j . \boldsymbol{H}_j = \tag{2.6}$$

$$\Sigma_{ij(i \neq j)} 3(\boldsymbol{M}_i . \boldsymbol{r}_{ij})(\boldsymbol{M}_j . \boldsymbol{r}_{ij}) / |\boldsymbol{r}|_{ij}^5 + \boldsymbol{M}_i . \boldsymbol{M}_j / |\boldsymbol{r}|_{ij}^3 .$$

For specific structures (homogeneous ellipsoidal bodies) the internal magnetic fields $\boldsymbol{H}$ and magnetizations $\boldsymbol{M}$ are uniform. Placed in a homogeneous, external, magnetic field $\boldsymbol{H}_0$, equation (2.7) defines the internal magnetic field as

$$\boldsymbol{H} = \boldsymbol{H}_0 - N\boldsymbol{M} \tag{2.7}$$

where N is the demagnetizing factor tensor.

Relevant to the present work, in an infinite disk oriented in the plane (x,z), magnetized in-plane, $N_x=N_z=0$, $N_y=1$, and for an infinite disk oriented in the plane (x,y), magnetized perpendicularly, $N_x=N_y=0$, $N_z=1$.

Consider a sample of lateral dimensions L_x, L_y, thickness $h<<L_x,L_y$ and with periodic boundary conditions applied in the XY plane. In the demagnetizing field of a thin film finite structure [Mansuripur, 12, 19], the Fourier coefficients of a periodic function $M(x,y)$ are given by equations in Appendix 1.

2.1.3 Anisotropy energy

In a crystalline magnetic material, the magnetic properties vary depending on the crystallographic direction in which the magnetic dipoles are aligned [16]. The energy of the ferromagnetic crystal depends on the magnetization direction relative to the crystal axes. A measure of the magnetocrystalline anisotropy in the 'easy' magnetization direction (a direction of the highest symmetry of the crystal lattice) is the anisotropy field, which is the field required to rotate all the moments by 90° as one unit in a saturated, single crystal. For example, the easy magnetization direction of a permanent magnet based on ferrite or the rare earth alloys is uniaxial. It is also possible to have materials with multiple easy axes or where the easy direction can lie anywhere on a certain plane or on the surface of a cone. It is difficult to demagnetize a permanent magnet that has uniaxial anisotropy because it is resistant to the directional rotation of the magnetization. A coupling of the electronic orbitals to the lattice causes the anisotropy. In the easy direction of magnetization, this coupling creates orbitals in the lowest energy state. The magnetocrystalline anisotropy originates in the dipole-dipole

interaction between the relative orientation of magnetic moments and the crystal lattice axes. Other sources are the spin-spin and spin-orbital interactions (anisotropic exchange interaction due to the change in shape of atomic orbitals leading to the alteration of Coulomb energy).

In uniaxial crystals (with trigonal, tetragonal, and hexagonal symmetry, but neglecting anisotropy in the basal plane) the anisotropy energy per unit volume is

$$E_{an} = K_{1u} \sin^2\theta + K_{2u} \sin^4\theta + K_{3u} \sin^6\theta + \ldots \qquad (2.8)$$

where K_{1u} is the first-order uniaxial anisotropy constant and θ is the angle between the magnetization and the principal axis of the crystal. For a cubic crystal the anisotropy energy per unit volume is

$$E_{an} = K_{1c}(\alpha_1^2\alpha_2^2 + \alpha_1^2\alpha_3^2 + \alpha_2^2\alpha_3^2) + K_{2c}\,\alpha_1^2\alpha_2^2\alpha_3^2 + \ldots \qquad (2.9)$$

where K_{1c} is a first-order cubic anisotropy constant and α_1, α_2, α_3 are the directional cosines of the magnetization, relative to the crystal symmetry axes. K_2 and higher terms are usually neglected. Generally, the anisotropy will affect the distribution of the internal magnetic fields in the ferromagnetic material, depending on the orientation of the magnetic fields, the crystal axes and the shape axes of the specimen. The distribution of the crystal axes in a polycrystalline material leads to a distribution of internal fields.

The anisotropy can be expressed in terms of demagnetizing factors N^{an} starting from

$$\boldsymbol{H}_{an} = -\,\partial E_{an}/\partial \boldsymbol{M} \qquad (2.10)$$

as an anisotropy field,

$$\boldsymbol{H}_{an} = -\,N^{an}\boldsymbol{M}. \qquad (2.11)$$

(Equivalently, the demagnetizing effect discussed above may be thought of as a "shape anisotropy".) For uniaxial anisotropy the only nonzero demagnetizing factor value is

$$N^{an} = -2 K_{1u} / M_0 \qquad (2.12)$$

This is $N_{33}{}^{u}$ for a perpendicularly magnetized thin film and $N_{11}{}^{u}$ for a tangentially magnetized thin film. The demagnetizing factor N^{an} can be added to the demagnetizing factor of the magnetostatic field.

2.1.4 Zeeman energy

The energy of a magnetized structure (with magnetization $\boldsymbol{M}$) in an external applied magnetic field $\boldsymbol{H}_{ext}$ is given by the expression

$$E_Z = -\int_v \boldsymbol{M}(\boldsymbol{r}) \cdot \boldsymbol{H}_{ext}(\boldsymbol{r})\, d\boldsymbol{r} . \qquad (2.13)$$

2.1.5 Total energy and effective fields of the magnetic system

A magnetic system in an external magnetic field has its total energy given as the sum of contributions from exchange, demagnetizing, anisotropy and external fields [18]

$$E_{tot} = \Sigma_{ij} [W_{exch} + W_{anis} + W_{demag} + W_{ext}]\, d\, a^2 \qquad (2.14)$$

where i, j are lattice sites indices, a is the lattice distance and d is the film thickness. The effective field components in spherical coordinates can be derived using

$$\partial W / \partial \theta = -|\boldsymbol{M}|\, H_\theta \qquad (2.15)$$

and

$$\partial W / \partial \varphi = -|\boldsymbol{M}|\, \sin\theta\, H_\varphi .$$

With the exchange constant A, and the spherical coordinates r, φ, θ, the exchange energy between two moments $\boldsymbol{M}$, $\boldsymbol{M}_1$ is

$$W_{exch} = (1/2)\Sigma_{nn}\,(2A/a^2)(1 - \boldsymbol{M}/|\boldsymbol{M}|\,.\,\boldsymbol{M}_1/|\boldsymbol{M}_1|) = \tag{2.16}$$

$$(1/2)\Sigma_{nn}\,(2A/a^2)[\cos\theta\,\cos\theta_1 - \sin\theta\,\sin\theta_1\cos(\varphi-\varphi_1)]\,.$$

The sum in (2.16) is over nearest neighbors only. The effective exchange field using (2.23) is given by

$$H_{\theta exch} = -[2A/(|\boldsymbol{M}|a^2)][\sin\theta\,\cos\theta_1 - \cos\theta\,\sin\theta_1\cos(\varphi-\varphi_1)] \tag{2.17}$$

$$H_{\varphi exch} = -[2A/(|\boldsymbol{M}|a^2)][\sin\theta_1\sin(\varphi-\varphi_1)]\,. \tag{2.18}$$

For the anisotropy energy (with the uniaxial anisotropy and the easy axis given by θ_0,φ_0)

$$W_{anis} = K_u\,\{1 - [\cos\theta\,\cos\theta_0 + \sin\theta\,\sin\theta_0\cos(\varphi-\varphi_0)]^2\}\,. \tag{2.19}$$

The demagnetizing energy is summed over all pairs providing the expression

$$W_{demag} = (1/2)\,\Sigma_{sn}\,\boldsymbol{H}_{demag}\,.\,\boldsymbol{M}_{ij} = |M_{ij}||M_{i1j1}|(a^2h/2l^3)\,\{\cos\theta\,\cos\theta_1 + \tag{2.20}$$

$$\sin\theta\,\sin\theta_1[\cos(\varphi-\varphi_1) - 3\cos(\varphi-\psi)\,\cos(\varphi_1-\psi)]\}\,,$$

Where the prefactor *1/2* avoids double counting, and ψ is the angle of the line joining two dipoles (see the description in [18]). The energy of the magnetic system in the external field $\boldsymbol{H}$ is

$$W_{est} = -\boldsymbol{H}\,.\,\boldsymbol{M} = |M_{ij}|\,(H_x\sin\theta\,\cos\varphi + H_y\sin\theta\,\sin\varphi + H_z\cos\theta)\,. \tag{2.21}$$

2.2 Magnetic domains

Magnetic domains exist in order to reduce the energy of the system. The uniformly magnetized specimen shown in Fig. 2.1a has a large magnetostatic energy associated with it [21]. This is the result of the presence of magnetic poles at the surface of the specimen generating a demagnetizing field H_d.

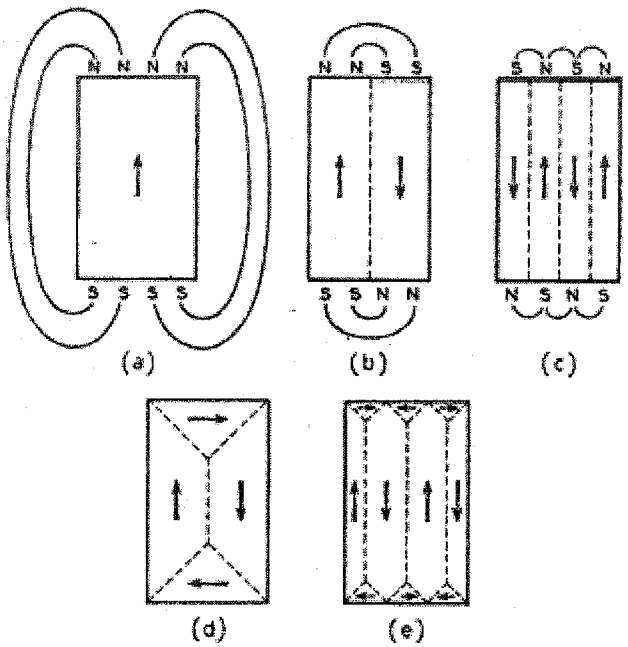

Fig. 2.1 A schematic illustration of the break up of magnetization into domains, (a) single domain, (b) 2 domains, (c) 4 domains and (d) closure domains.

The magnitude of H_d is dependent on the geometry and in general, is opposite to the direction of magnetization of the specimen. In general, if the sample has a high length-to-diameter ratio (and is magnetized in the long axis), then the demagnetizing field H_d and the magnetostatic energy will be low. The break up of the magnetization into two domains as illustrated in Fig. 2.1b reduces the magnetostatic energy by half. If the magnet breaks down into N domains, the magnetostatic energy is reduced (to a first approximation) by a factor of 1/N, hence Fig. 2.1c has a quarter of the magnetostatic energy of Fig. 2.1a. Figs. 2.1d, and 2.1e show a closure domain structure where the

magnetostatic energy is nearby zero. The introduction of a domain raises the overall energy of the system, therefore the division into domains only continues while the reduction in magnetostatic energy is greater than the energy required to form the domain wall. The energy associated with a domain wall is proportional to its area. The dipole moments of the atoms within the wall that are not pointing in the easy direction of magnetization are in a higher energy state. In addition, the neighboring atomic dipoles within the wall are not parallel each other and so the exchange energy is raised within the wall. The domain wall energy is an intrinsic property of a material depending on the degree of a magnetocrystalline anisotropy, saturation magnetization, and the strength of the exchange interaction between neighboring atoms. The thickness of the wall will vary in relation to these energies. A strong magnetocrystalline anisotropy will favor a narrow wall, whereas a strong exchange interaction will favor a wider wall.

When applying an external magnetic field, spins inside a wall are under a torque resulting in domain wall motion and displacement. Domains with magnetization direction aligned with the direction of the external field prevail and finally at a high external field the whole specimen reaches a uniformly saturated magnetization level. In given field, a minimum energy is achieved with a specific number of domains within a specimen. The number of domains will depend on the size and shape of the sample (which will affect the magnetostatic energy) and the intrinsic magnetic properties of the material, which will affect the magnetostatic energy and the domain wall energy. If the crystal, grain or polycrystal have large magnetocrystalline anisotropy, the inner magnetization is forced to align in the direction of the easy axis (parallel or antiparallel).

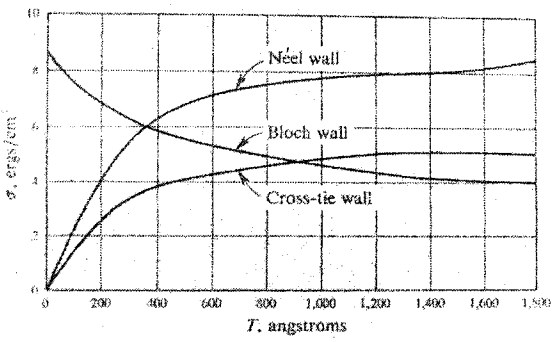

Fig. 2.2 Domain wall energy density as a function of film thickness [11]

The typical domain wall in a thin film is the symmetric Néel wall. Let us assume uniaxial anisotropy and an in-plane field H perpendicular to the axis of the Néel wall. The analytical solution E_N for the energy of the Néel domain wall [11] with the demagnetizing field dominating the anisotropy, is given by

$$E_N = [(2A)(\mu_0 M_s^2)]^{1/2} . \tag{2.22}$$

Fig. 2.2 graphs the domain wall energies as a function of film thickness. For the domain wall width the expression for D_N is given by

$$D_N = [(2A)/(\mu_0 M_s^2)]^{1/2} . \tag{2.23}$$

For Bloch walls the core profile w_{core} of a domain wall is [13]

$$w_{core} = 2\{A(1-h^2)/[(K_u - K_d)(1-c_0)^2]\}^{1/2} \tag{2.24}$$

where $h=HM_0/(2K_u)$ and the tail boundary value c_0 usually lies in the middle between h and 1. Usually K_d is much greater than K_u for soft magnetic materials such as Permalloy thin films with a thickness $d<50$nm. The thickness of a Bloch domain wall in thin films scales with the exchange length of the stray field K_d is

$$\Delta_d = \sqrt{(A/K_d)} \tag{2.25}$$

while in a bulk material with the uniaxial anisotropy constant K_u as

$$\Delta_u = \sqrt{(A/K_u)} . \tag{2.26}$$

The formula for tail width w_{tail} yields

$$w_{tail} = e^{-0.577} dK_d / K_u \qquad (2.27)$$

K_u usually has always some residual nonzero value. The influence of internal stresses and non-homogeneities can change at important level the exchange and anisotropic interactions [2, 11]. The presence of surfaces affects the lattice symmetry. The spin-orbital interactions and pinning of spins at surface centers (such as artificial or natural defects) can significantly change a local energy distribution.

Hysteresis and coercivity are two consequences of the various metastable energy states in the domain structure distribution. The coercivity mechanism has roots in domain wall pinning via defects, inhomogeneities and nonuniform distribution of magnetic properties. The strong dependence on temperature, volume, anisotropy and shape determines the relaxation rate (and hence the time-scale during which no change of magnetization occurs and ferromagnetic remains stable) exists. Metastability holds at local energetic minima. Small particles at finite temperature approach the superparamagnetic state and macroscopic ferromagnetic properties are lost [9].

The domains, the domain wall structure and the non-uniform internal field distribution play a fundamental role in spin wave generation, propagation and magnon-magnon interactions, as will be discuss below. Magnetoelectronic devices can be subdivided into single domain devices and domain wall devices. Domain wall structure can be controlled, moved, or created, see e.g. Cowburn in [22], offering important technological applications.

2.3 Ferromagnetic resonance.

The magnetization and angular momentum are related by

$$\boldsymbol{M} = \gamma \boldsymbol{L} = \mu_B (\boldsymbol{L} / h) \tag{2.28}$$

where γ is the gyromagnetic ratio

$$\gamma = -eg/2m_e \tag{2.29}$$

with the numerical value approx.0.88 x 10^{11} Hz/Tesla, e is the charge of the electron and g is the gyromagnetic factor (g~2 for an electron with spin 1/2). The Bohr magneton μ_B is defined as

$$\mu_B = g(eh/2m_e) . \tag{2.30}$$

Let us assume the Lorentz law of force for a point charge e with velocity $\boldsymbol{v}$ in the electric field $\boldsymbol{E(r)}$ and the magnetic field $\boldsymbol{B(r)}$

$$\boldsymbol{F(r)} = e\,[\boldsymbol{E(r)} + \boldsymbol{v} \times \boldsymbol{B(r)}] . \tag{2.31}$$

The net torque on the magnetic moment in the external magnetic field is

$$\boldsymbol{\tau} = \boldsymbol{M} \times \boldsymbol{B_0} \tag{2.32}$$

where $\boldsymbol{M}$ is the magnetic moment of a small current loop over the magnetic field $\boldsymbol{B(r)}$. The magnetic field has the uniform value $\boldsymbol{B_0} = \mu_0 \boldsymbol{H_0}$ over the area of the loop. Accordingly Newton's law

$$\boldsymbol{\tau} = d\boldsymbol{L}/dt \tag{2.33}$$

for the change with time of the magnetic moment in the field is

$$d\boldsymbol{M}/dt = \gamma \boldsymbol{M} \times \boldsymbol{B_0} . \tag{2.34}$$

Let us assume that the magnitude of $|M|$ remains constant. The torque is always orthogonal to M and in the absence of damping magnetic moment vector gyrates around the magnetic field vector B_0 with a Larmor frequency ω_L (see Fig. 2.3a),

$$\omega_L = \gamma |B_0| . \tag{2.35}$$

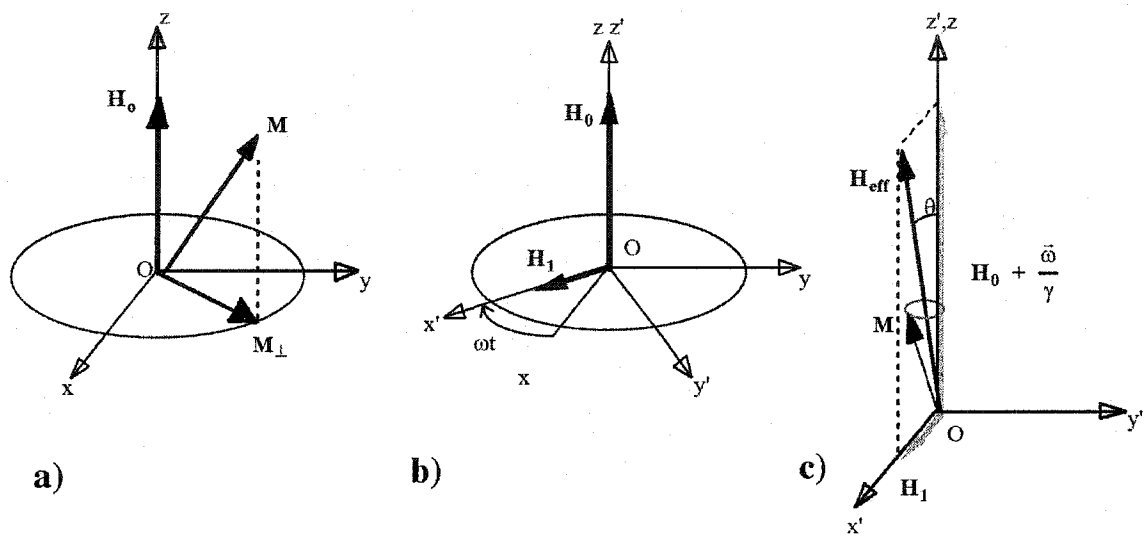

Fig. 2.3 The representation of magnetic field and magnetization vectors in reference frame (Oxyz) (a); and rotating (Ox' y' z') coordinate frames, (b) and (c).

Suppose there is an additional oscillating field such that the total field is

$$H=H_0 + H_1(t) \tag{2.36}$$

where $H_1(t)$ rotates in the (x, y) plane with frequency ω, Fig. 2.3b. From the point of view of the rotating frame, the precession occurs (around the effective field H_{eff}) as if the system of rotating axes constituted a fixed reference frame, Fig. 2.3c.

The effective field H_{eff} is given by the equation

$$H_{eff} = (H_0 + \omega / \gamma) + H_1(t) . \tag{2.37}$$

When the frequency of the oscillating external field matches the Larmor frequency, there is a resonance. In the rotating frame the magnetization vector gyrates around the apparent magnetic field, $\boldsymbol{H}_{eff} = \boldsymbol{H}_1(t)$.

Alternatively, from the known free energy F of the magnetic system with the energy of the magnetization $\boldsymbol{M}$ in an effective magnetic field $\boldsymbol{H}_{eff}$, the oscillation frequency ω_0 of the natural (uniform) mode is given (in spherical coordinates) as (see Suhl [57]),

$$\omega_0 = \gamma/(|\boldsymbol{M}| \sin\theta)\,[(\partial^2 F/\partial\theta^2)(\partial^2 F/\partial\varphi^2) - (\partial^2 F/\partial\theta\partial\varphi)^2]^{1/2}. \qquad (2.38)$$

2.4 Magnetization excitations and dynamics in ferromagnetics

For an investigation of magnetization oscillations, the ferromagnetic material and its properties will be described in a simple model. In this model, a large number of spins is present and each of these spins has magnetic moment [8]

$$\boldsymbol{m}_s = g\mu_B \mathbf{S}\,. \qquad (2.39)$$

All individual moments are aligned parallel to one another, creating one large magnetic moment.

The solution of Maxwell's equations (see Appendix 1) properly describes electromagnetic fields and magnetization inside and outside of any material including the ferromagnetic material. In the latter case the material condition

$$M = \chi_m H \qquad (2.40)$$

is required and, as will be shown later, is found by solving the dynamical Landau-Lifshitz-Gilbert equation of motion for magnetization.

At relatively large temperature, the thermal fluctuations of the crystal lattice start to play an important role and the interactions with phonons can change at a significant level the evolution of the local magnetization $\boldsymbol{M}$ [10, 11]. Applying the external field, the magnetic moment will precess around the direction of the effective local magnetic field $\boldsymbol{H}_{eff}$ because of torque $\boldsymbol{M} \times \boldsymbol{H}_{eff}$. The effective magnetic field is a vector sum of all static and transient spatially dependent fields. The total energy of the magnetic system, E_{tot}, is the sum of exchange, demagnetizing, anisotropy and external energies (as described in part 2.1.1-2.1.5) and, in a general case, the effective field is

$$\boldsymbol{H}_{eff}(\boldsymbol{r}) = - \partial E_{tot} / \partial \boldsymbol{M}(\boldsymbol{r}) . \qquad (2.41)$$

The classical equations of motion of the magnetic moment are the Landau-Lifshitz (LL) [15a] and, with the conventional incorporation of damping, more general Landau-Lifshitz-Gilbert equations (LLG) [15b] given by

$$d\boldsymbol{M}/dt = - \gamma \boldsymbol{M} \times \boldsymbol{H}_{eff} - (\gamma \alpha_{damp} / |\boldsymbol{M}|) \boldsymbol{M} \times d\boldsymbol{M}/dt \qquad (2.42)$$

where α_{damp} is a phenomenological damping constant. This equation is consistent with the condition for the constant magnitude of $\boldsymbol{M}$, $|\boldsymbol{M}| = const.$ or $\partial \boldsymbol{M}^2 / \partial t = 0$. This condition is a result of the averaging of $\boldsymbol{M}$ over many individual spins. This averaging requires that the spin does not vary too rapidly from site to site; spin-wave wavelengths must be many lattice spacings long [23]. The LL equation is identical with the LLG equation in the case of small damping [27]. Other equations are the Bloch-Bloembergen equations of the ferromagnetic relaxation [15c]

$$dM_z/dt = -\gamma(\boldsymbol{M} \times \boldsymbol{H}_{eff})_z - (M_z - M_0) / 2T_1 \qquad (2.43)$$

$$dM_{XY}/dt = -\gamma(\boldsymbol{M} \times \boldsymbol{H}_{eff})_{xy} - M_{xy} / 2T_2 \qquad (2.44)$$

where M_0 is the saturation magnetization and $1/T_1$ and $1/T_2$ are the longitudinal and transverse relaxation frequencies. These equations allow the change of the vector $\boldsymbol{M}$'s length [14,24]. The Bloch-Bloembergen equations are reduced to LLG in the case where both the damping and excursions of $\boldsymbol{M}$ are small. It was found (in thin film switching experiments, see [11]), that $|\boldsymbol{M}|$ is not conserved in the case of large surface roughness and other imperfections. For large excursions of $\boldsymbol{M}$ the magnitude $|\boldsymbol{M}|$ is not conserved as show for example the experimental results and discussion about precessional switching and coherent control of the precession, [28, 29].

If the external conditions change slowly enough, the Fokker-Planck equation leads to the Landau-Lifshitz-Bloch equation for a classical model where stochastic Langevin fields describe the spin-bath interactions. The spin-spin interactions are treated within the mean-field approximation. Callen in [24] showed a description of another kind of dynamical equation allowing a change of the number of magnons. In the study, the Landau-Lifshitz equation was augmented by another term proportional to $\boldsymbol{M}$ and a quantum mechanical treatment was applied.

At elevated temperatures, an alternative prescription is given by the Landau-Lifshitz-Bloch equations, containing both the transverse and longitudinal relaxation and interpolating between the Landau-Lifshitz equation at low temperatures and the Bloch equation at high temperatures (see, for example, Garanin [72, 70]).

The LLG equation is complemented by the Rado-Weertman boundary conditions [45]. The Rado-Weertman boundary conditions can be derived from the LLG equation leaving out the dipolar, anisotropy and external terms in a similar way as boundary conditions for electric and magnetic fields are derived from Maxwell equations.

In the numerical analysis of this thesis, the LLG equation is used for the simulation of the magnetization oscillations of finite magnetic elements. This introduction continues with a simplified description of basic properties of spin waves and their normal modes. Later, the linear microscopic and phenomenological theories of the excitation of a magnetic system will be described.

2.4.1 Spin waves.

Consider the Heisenberg Hamiltonian containing the Zeeman energy. The ground state is the static equilibrium configuration in which all spins in the sample are aligned parallel to the sufficiently strong applied *DC* field. The first excited single particle state has one spin flipped with very high exchange energy. In a collective excitation with each spin tipped at an angle β with respect to the direction of the effective magnetic field, we have the situation illustrated in Fig. 2.4. The angle β is small for small Zeeman energy and the angle α between successive spins is small for small exchange energy. The shortest distance between parallel spins in the direction of propagation given by wave vector $\boldsymbol{k}$ is the wavelength λ, $\boldsymbol{k}=(2\pi/\lambda)\boldsymbol{u}$, where $\mathbf{u}$ is an unit vector. The amplitude of the spin wave is quantized in the sense that total z component of magnetic moment is reduced by value $g\mu_B$.

A magnon (a quantized spin wave) with a wave vector $\boldsymbol{k}$ carries an energy $\hbar\omega_k$ and the magnon density corresponds to the amplitude of the spin wave. The total number of magnons is proportional to the magnetic energy of the system. If a $\boldsymbol{k}=0$ magnon is scattered to a $\boldsymbol{k}\neq 0$ magnon the total magnetization is changed,

$$M_{total} = M_0 V - g u_B \sum_{k \neq 0} n_k \tag{2.45}$$

where n_k is the number of magnons having wave vector $\boldsymbol{k}$, but the magnetic energy remains unchanged [11, 14, 30, 32].

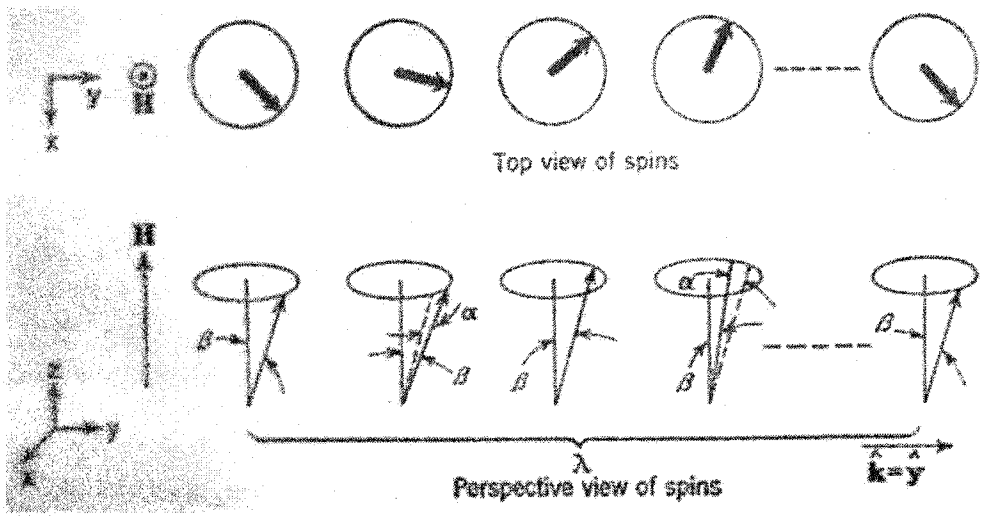

Fig. 2.4 The representation of a traveling spin wave in perspective and top views [14]

Equation (2.45) was derived using Holstein-Primakoff treatment [25] and is valid for small dipolar forces. Based on the neighboring spin dependence of the exchange energy $\boldsymbol{S}_i \cdot \boldsymbol{S}_j \sim cos(\alpha) \sim \alpha^2 \sim 1/\lambda^2$, the exchange energy of a magnon can be written as

$$E_{exch} = Dk^2 = \hbar\omega_{exch} \tag{2.46}$$

where D is the exchange constant defined later in equation (2.51).

The Zeeman energy of the magnetic system is

$$E_{Zeeman} = - M_z H = - g u_B \sum S_{iz} H = \hbar\omega_{Zeeman}. \tag{2.47}$$

In a typical experiment with a high-frequency pump field, this field is uniform over entire area of a sample and all spins experience the same initial torque if the sample is uniformly magnetized. The uniform-precession magnons have infinite wavelengths, or

$k=0$. The pumping field couples to the uniform mode spin wave, transferring energy to it and exciting this magnetization oscillation to higher quantum numbers. The quantum mechanical analysis of the resonance is based on the method of creation and destruction of magnons at the frequency of the spin wave of infinite wavelength [34]. In a more realistic case the dipole-dipole interactions must be included. The subsequent process is relaxation back to the ground state through annihilation or a de-excitation of uniform magnons.

The total number of normal modes of the magnetization oscillations is equal to the total number of spins contributing to the magnetization. These modes have wavelengths spanning the range from the sample dimensions to the lattice (interatomic) spacing. The long-wavelength spectrum depends on magnetostatic forces (including the external *AC* and *DC* fields and the demagnetizing fields). The short wavelength spin waves can be excited directly in special cases only, e.g. via a skin effect [44-46] or creating a strongly non-uniform field. In addition, the short-wavelengths spin waves can be excited in small patterned samples. In the small-amplitude approximation, the linearized version of equation of motion of the magnetization provides sufficiently exact description of properties of the normal spin wave modes. At higher power of the external field and, as a result, at large amplitudes of the precessional motion of the magnetization vector (high occupation number of a magnon state), these normal modes are no longer orthogonal but are coupled together by the terms proportional to the transverse component of the magnetization.

Spin waves are correctly represented by normal modes only if dipolar interactions are neglected. Otherwise, spin waves are coupled [25, 34]. If excitations of

these modes are small, the equations can be linearized by neglecting products of the mode amplitudes, diagonalizing the interaction between spin waves and, after a transformation, getting the normal modes again. If spin wave excitation is large, the modes are coupled by nonlinear terms and cannot be diagonalized [23, 53].

This is an example of an intrinsic nonlinearity when the system supporting the modes is altered by those modes.

2.4.2 Linear microscopic theory.

Excited states of a magnetic system can be described by the quantum mechanical approach. Spins are localized at assigned lattice sites in the Heisenberg model but the theory can include metals with well-localized magnetic moments [26, 30-35]. Let us apply the Holstein-Primakoff transformation [25] on the Hamiltonian of the spin system and transform the form of the Hamiltonian in an oscillatory one. In the Holstein-Primakoff treatment the initial Hamiltonian of a spin system includes the exchange, Zeeman and dipole-dipole energy terms. With the condition of a spin plane-wave solution the Hamiltonian [14] has the form

$$H = -2\sum_{i\neq j} J(\boldsymbol{R}_{ij})\, \boldsymbol{S}_i \cdot \boldsymbol{S}_j - \sum_i g\, u_B\, H\, \boldsymbol{S}_i + \tfrac{1}{2}\sum_{i\neq j} (g\, u_B)^2/(R_{ij})^5 [R_{ij}^2\, (\boldsymbol{S}_i \cdot \boldsymbol{S}_j) - 3(\boldsymbol{R}_{ij} \cdot \boldsymbol{S}_i)(\boldsymbol{R}_{ij}\, \boldsymbol{S}_j)] \,. \qquad (2.48)$$

The components of spin $\mathbf{S}_i$ satisfy commutation relations $[S_{ix}, S_{jy}] = i\, S_{iz}\, \delta_{ij}$. This form of the Hamiltonian can be transformed into a form $H = -\sum_k h\, \omega_k\, c_k^+\, c_k$ using magnon variables c_k, c_k^+. The spin operators $\boldsymbol{S}_i$ also can be transformed into an expression with magnon variables c_k's. The result is the dispersion relation for magnons and the

expansion of magnetization in terms of creation and annihilation operators. The dispersion relation has the form

$$\hbar\omega_k = [(Dk^2 + \hbar\omega_i)(Dk^2 + \hbar\omega_i + \hbar\omega_m \sin^2\theta_k)]^{1/2} \tag{2.49}$$

$$\hbar\omega_m = 8\pi\,\mu_B(g/2)\,|M| \tag{2.50}$$

$$\hbar\omega_i = 2\mu_B(g/2)(H - 4\pi N_z\,|M|)$$

$$D = 2Ja^2/\hbar \tag{2.51}$$

where $ka<<1$, θ_k is polar angle of $\boldsymbol{k}$, S is the spin, J (positive for a ferromagnet) is the exchange integral and a is the lattice constant. See Fig. 2.5 for details of uniform precessional mode [14].

The consequence of demagnetization energy arises in the existence of a band of degenerate magnons having the same energies and different wave vectors. Then two-magnon interactions and the conversion of the uniform mode into degenerate mode at $\boldsymbol{k} \neq 0$ are allowed [14]. The details are shown in Fig. 2.6.

Long wavelength spin waves interact weakly in the exchange-coupled ferromagnet, the angles between neighboring spins are small and the probability that two spin waves will interact at the same lattice site is very small (but can still linearly superpose and "interfere"). In the spin system with domain walls or a strong crystalline anisotropy the Hamiltonian is more complicated and the approximations done through the Holstein-Primakoff transformations (the truncations in the expansions of spin operators and the dropping of terms in the Hamiltonian) lead to poor convergence in cases where a stronger interaction between the spin waves is required.

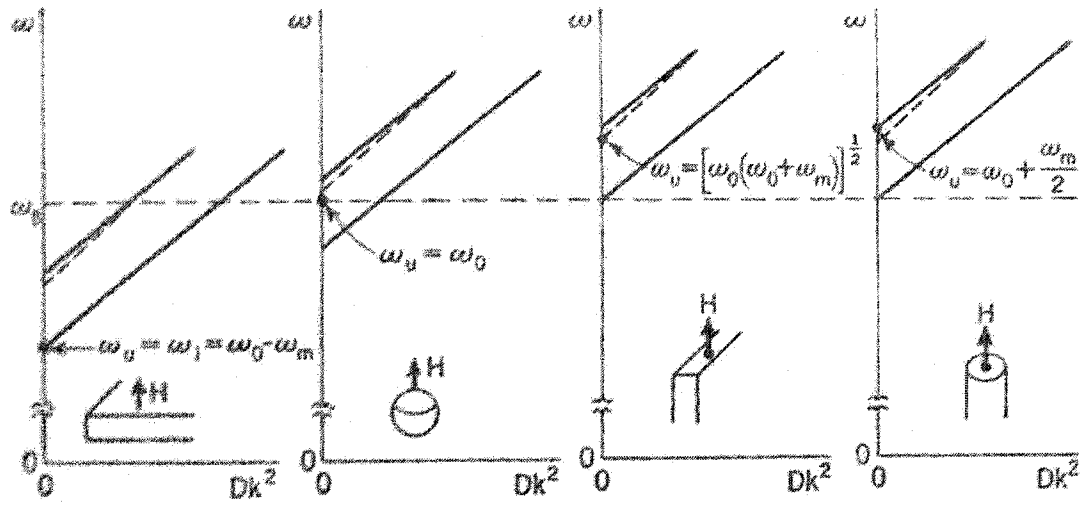

Fig. 2.5 The frequency ω_u of the uniform precession mode relative to the magnon spectrum for various sample geometries [14] under applied field H_0. Dashed lines represent the solution of the dispersion equation for $\hbar\omega_k$ (for $\theta_k=\pi/2$), while solid lines represent the approximate magnon dispersion formula $\hbar\omega_k \sim Dk^2 + \hbar\omega_i + \hbar\omega_m \sin^2\theta_k$ for sufficiently large k (for $\theta_k=0$ and $\pi/2$).

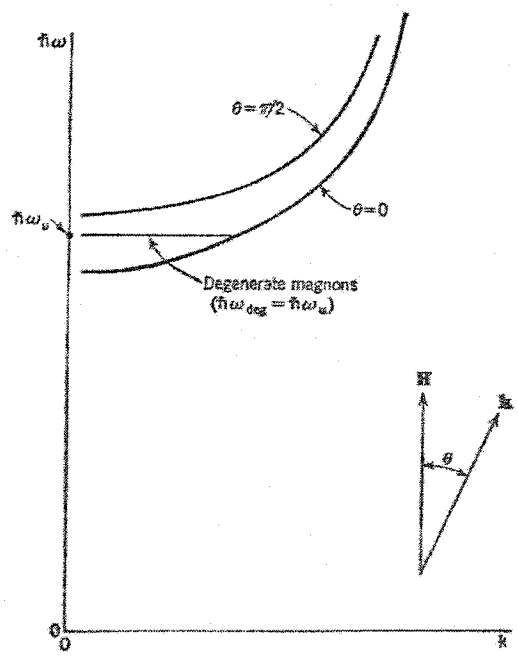

*Fig. 2.6 The magnon dispersion relation as a function of **k**, with exchange, Zeeman and dipole-dipole energies included [14].*

Inhomogeneous systems, like magnetic states containing domain walls, have ground states with spins varying from site to site. Dyson's approach[26] can also be used to investigate interactions between spin wave modes. The spin wave theory discussed above is based on the analysis of the equilibrium and excited states of a magnetic system. Such a system is described by a spin Hamiltonian and specific microscopic considerations of the spins located on lattice sites are assumed. A single spin is on the average only rarely deviated. This spin wave theory works best for long wavelengths where the probability of short- range interactions between spin waves is small.

2.4.3 Linear phenomenological theory.

When a classical, continuous magnetic medium is considered the magnetization vector at every point characterizes it. Spin wave wavelengths are much larger than lattice spacing, a typical assumption for the nature of a linear theory. The magnitude of the magnetization of an exchange-coupled spin system placed in a static magnetic field is a function of temperature and the moment $\boldsymbol{M}$ is oriented along the direction of the effective applied field. The magnitude $|\boldsymbol{M}|$ is assumed to be constant and less than the saturation magnetization M_0. The dependence of the magnitude $|\boldsymbol{M}|$ on the applied field (or the parallel susceptibility) is assumed to be negligibly small. From the point of view of the statistical mechanics of the system, the spin waves excited by thermal fluctuations at a temperature T have energies up to k_BT. The width of the spin wave band is of order of J and the Curie temperature T_c of the material depends on the exchange integral J. At small T/T_c this ratio determines the fraction of thermally excited wave numbers k. It can be estimated that the average $\boldsymbol{M}$ from a volume ~ $1/(Nk)^3$ will be directed along the

direction of the effective magnetic field H_{eff} from that region. Let us assume that the spatial changes of H_{eff} are very small. If changes of the H_{eff}, in direction or amplitude, are slow when compared to thermal relaxation rates, then M has a constant magnitude, the torque acting on it is proportional to $M \times H_{eff}$ and the thermal equilibrium is preserved.

When the anisotropy and the dipole terms are left out the LLG equation can be linearized using the following approximations

$$\boldsymbol{M(r,t) = M_0 + m_1 \exp[i(\omega t + k.r)]} \tag{2.52}$$

$$\boldsymbol{H_{eff}(r,t) = H_{0eff} + h_1 \exp[i(\omega t + k.r)]}\ . \tag{2.53}$$

$\boldsymbol{m_1}$ and $\boldsymbol{h_1}$ are neglected in quadratic and product terms. The exchange energy is proportional to $|grad\ \boldsymbol{M}|^2$. For the case of an ellipsoid, the analytical treatment yields [36]

$$i(\omega/\gamma)\ \boldsymbol{m_1} = \boldsymbol{M_0} \times (\boldsymbol{h_1} - B\ \boldsymbol{k}\ .\ \boldsymbol{k}\ \boldsymbol{m_1}) - \boldsymbol{H_i}\ x\ \boldsymbol{m_1} + (\alpha_{damp} / \gamma\ |\boldsymbol{M_0}|)\ \boldsymbol{M_0} \times i\omega\ \boldsymbol{m_1} \tag{2.54}$$

augmented by Maxwell equations, where $\boldsymbol{H_i}$ is the internal DC magnetic field. After similar transformation of an electric field

$$\boldsymbol{e_{eff}(r,t) = e_{0eff} + e_1 \exp[i(\omega t + k.r)]} \tag{2.55}$$

where $\mathbf{e}_1$ is small, the Maxwell equations are simplified into the forms

$$\boldsymbol{k\ x\ e_1} = -\ (\omega/c)\ (\boldsymbol{h_1} + 4\pi\ \boldsymbol{m_1}) \tag{2.56}$$

$$\boldsymbol{k\ x\ h_1} = -\ (\omega/c)\ \varepsilon_r\ \boldsymbol{e_1}$$

The resulting dispersion relation has, in general, the form

$$1/(k_x^2 + k_y^2) + (1/2)\ [\ (\boldsymbol{k}\ .\ \boldsymbol{k} - k_0^2)\ /\ 4\pi M_0)\ (\omega/\gamma - i\ (\omega/\gamma)\ \alpha_{damp} + H_i + \tag{2.57}$$

$$M_0 B\ (\boldsymbol{k}\ .\ \boldsymbol{k})) - k_0^2]^{-1} + (1/2)\ [\ (\boldsymbol{k}\ .\ \boldsymbol{k} - k_0^2)\ /\ 4\pi M_0)\ (-\omega/\gamma - i\ (\omega/\gamma)\ \alpha_{damp} +$$

$$H_i + M_0 B\ (\boldsymbol{k}\ .\ \boldsymbol{k})) - k_0^2]^{-1} = 0$$

where $k_0^2 = (\omega/c)^2\ \varepsilon_r$.

In the more general case of a metallic ferromagnet, solving the Maxwell equations together with the LLG equation in the small amplitude approximation, Soohoo in [56] and Ament and Rado in [46] found corresponding dispersion curves. Taking further into account the effect of the propagation of electromagnetic waves, the conductivity of the material and the effects of the exchange interaction, the resulting dispersion equation is biquadratic in k. This $(k^2)^2$ dependence comes from the dynamic representation of the electromagnetic fields instead of the magnetostatic approximations. The result is valid for a ferromagnetic ellipsoid of any size and conductivity.

2.4.4 Uniform mode.

In the approximation of long wavelength oscillations ($k_0^2=0$, the uniform precession with the propagation in Maxwell equations transformed into demagnetization effects) the dispersion relation [32, 14] is represented by

$$(\omega/\gamma)^2 = [\,((\boldsymbol{k}\,.\,\boldsymbol{k} - k_0^2)/4\pi M_0)\,(-i\,(\omega/\gamma)\,\alpha_{damp} + \qquad (2.58)$$

$$H_i + M_0 B\,(\boldsymbol{k}\,.\,\boldsymbol{k})) + 4\pi M_0 \sin^2\theta]$$

where $\sin^2\theta = (k_x^2 + k_y^2)/(\boldsymbol{k}\,.\,\boldsymbol{k})$.

Maxwell equations reduced into a form

$$curl\ \boldsymbol{h}_1 = 0 \qquad (2.59)$$

$$div\,(\boldsymbol{h}_1 + 4\pi\,\boldsymbol{m}_1) = 0$$

have for the unbounded thin film (after the Fourier transform) the solution for the magnetic field in the form

$$\boldsymbol{H}_1(\boldsymbol{k}) = -4\pi\,\{[\boldsymbol{k}\,.\,\boldsymbol{m}_1(\boldsymbol{k})]/(\boldsymbol{k}\,.\,\boldsymbol{k})\}\,.\,\boldsymbol{k}\,. \qquad (2.60)$$

This expression is represented as the demagnetizing field (normal to $\boldsymbol{k}$) inside the thin film (under the condition that $2\pi/|\boldsymbol{k}|$ is large compared to the sample dimensions).

The term $(k_x\ m_{1x} + k_y\ m_{1y}/(\boldsymbol{k}\ .\ \boldsymbol{k})\ k_{x,y}$ describes the effect of coupling the left and right circularly polarized components of magnetization in the same way as the annihilation and creation operators do in the microscopic treatment of spin waves.

The equation (2.58) allows the extension of the validity to other important specific shapes like a sphere, a disc or a thin film. If the damping factor is ignored, this equation gets the form of equation (2.49) from Holstein-Primakoff microscopic linear treatment of spin waves with dipole-dipole interactions included. The frequency vs. k^2 dependence of the uniform oscillations is shown in Fig. 2.5.

2.4.5 Magnetostatic modes.

The magnetostatic modes are specific magnetic excitations in a magnetically ordered material. Their wavelengths are of the same order of magnitude as the linear dimensions of the sample. On the other hand, regular spin waves have wavelengths that are comparable with the exchange length. The magnetostatic modes can be regarded as normal modes of oscillations of the magnetization vector $\boldsymbol{M(r,\ t)}$. Walker [32,36] gave the theory of magnetostatic modes for spheroidal bodies. A large amount of experimental work on the study of magnetostatic modes in ellipsoidal specimens has been done.

The dispersion relation in lossless form can be written in the form

$$\Omega^2 = (\Omega_M + B\ (\boldsymbol{k}\ .\ \boldsymbol{k})\ /4\pi)\ (\Omega_M + B\ (\boldsymbol{k}\ .\ \boldsymbol{k})\ /4\pi + \sin^2\theta) \qquad (2.61)$$

where $\Omega = \omega/(\gamma\ 4\pi\ M_0)$, $\Omega_M = H_i/(4\pi\ M_0) = (H_0 - N_z\ M_0)/(4\pi\ M_0)$, with the external DC magnetic field H_0 and the demagnetizing factor in the z direction.

In the region where the exchange term is small ($\lambda > 10^{-6}$ m) and $2\pi/|k|$ is large compared to the sample dimensions the dispersion relation for the magnetostatic modes has the form

$$\Omega^2 = \Omega_M (\Omega_M + \sin^2\theta) . \qquad (2.62)$$

The theory of magnetostatic modes was developed for several specific sample shapes and orientations, for example for spheroids, cylinders and plane slabs. These normal modes are natural modes of a magnetic dipolar continuum immersed into a uniform external magnetic field. The modes depend on the shape of the sample and have no size dependence while having temperature dependence. The expression for an eigenfrequency ω_0 of an ellipsoid in the external field H_0 directed along an axis of an ellipsoid has the form

$$\omega_0 = \gamma \{[H_0 + (N_x - N_z) M_0] [H_0 + (N_y - N_z) M_0]\}^{1/2} \qquad (2.63)$$

where demagnetization factors N_x, N_y, N_z for various magnetic body examples are described in Section 2.1.2.

Damon and Eshbach [37] adapted Walker's theory for infinite films assuming that the slab or film is homogeneous and laterally infinite, with a thickness d, the magnetocrystalline anisotropy is neglected, the saturating external magnetic field is parallel to the surface of the film, and the pinning conditions are the same at both surfaces of the film.

The dispersion equation in such approximation has the form

$$\omega_{DE}^2 = \gamma H (H + 4\pi M_s) + (2\pi M_s)^2 (1 - \exp(-2k_{//} d)) \qquad (2.64)$$

where H is the in-plane magnetic bias and $k_{//}$ is the in-plane spin wave vector.

For a simple case of an infinitely thin plate magnetized in plane the eigenfrequency is

$$\omega_0 = \gamma\,[H_0\,(H_0 + 4\pi\,M_0)]^{1/2}. \tag{2.65}$$

Including the uniaxial anisotropy and the demagnetizing factor $N_z^u = -2K_{1u}/M_0^2$ for tangentially magnetized film the eigenfrequency is

$$\Omega_0 = \gamma\,[(H_0 + 2K_{1u}/M_0)(H_0 + 4\pi\,M_0 + 2K_{1u}/M_0)]^{1/2} \tag{2.66}$$

Storey in [42b] calculated frequencies of magnetostatic modes in rectangular 12μm thick YIG specimens by allowing the wave vectors to be related to the finite dimensions of the sample as

$$\boldsymbol{k} = (n_d\,\pi/d,\ n_b\,\pi/b,\ n_c\,\pi/c) \tag{2.67}$$

where $n_{d,b,c}$ are the mode numbers, b, c are the lateral dimensions of the rectangle. This approach neglects the existence of non-uniform internal fields in a finite unsaturated sample. The resonance frequencies are related to the resonance field, which are proportional to the square of the wave vector as, according to the equation (19) in Ref. [42b]

$$\boldsymbol{H} = \boldsymbol{H}_0 - const\,\boldsymbol{k}^2. \tag{2.68}$$

Decreasing the thickness of the film, the exchange-related modes (bulk spin waves) emerge and the exchange interaction is included in the analysis to explain new resonances in the ferromagnetic resonance spectrum.

2.4.6 *Magnetostatic-exchange modes.*

Most of the known solutions concern ellipsoidal, infinite bodies or thin films of saturated ferromagnetic material. Relatively recently, Kalinikos and Slavin [43] developed a theory for spin waves in a very long magnetic slab of the thickness d and width w, taking into account the dipole-dipole and the exchange interactions. The important result is the dispersion relation in the form

$$\omega_p^2 = \gamma\,(H + (2A/M_s)\,k^2)\,(H + (2A/M_s)\,k^2 + 4\pi M_s F_{pp}(k_{//}\,d)) \qquad (2.69)$$

where H is the in-plane applied magnetic field, $k^2 = k_{//}^2 + k_z^2 = k_{//}^2 + (p\pi/d)^2$, $k_{//}$ is the in-plane spin wave vector ($k_{//}=n\pi/w$ in the slab geometry) and p is the quantization number for the perpendicular standing spin waves. For the thin (15nm) films used in our experiments the parameter p is null. $F_{pp}(k_{//}\,d)$ is the matrix element of the dipole-dipole interaction given by the formula [43]

$$F_{pp}(k_{//}\,d) = 1 + [4\pi M_s/(H+(2A/M_s)\,k^2)]\,P_{pp}(k_{//},d)[P_{pp}(k_{//},d)]\,. \qquad (2.70)$$

For the spin waves propagating perpendicularly to the magnetic bias H, with $p=0$ and assuming unpinned spins at both surfaces of the magnetic film, the P_{00} is given by

$$P_{00}(k_{//},d) = 1 - [\exp(-k_{//}\,d)]/(k_{//}\,d)\,. \qquad (2.71)$$

This equation will give a dispersion relation similar to the Damon and Eshbach one, in (2.64), assuming long wavelengths ($k\rightarrow 0$) and neglecting the exchange interaction ($A\rightarrow 0$).

In finite structures, nonuniform internal fields exist. Their non-uniformity creates potential wells for the spin waves (for example near an edge of a thin wire). The demagnetization fields in finite wires are strong and inhomogeneous along the width of the wire (mainly near the edges); see Schlöman in [38] and Bryant and Suhl in [81].

For the potential well for spin waves created near the edges the existence conditions for the eigenfrequencies can be determined (assuming the profile of the internal field across the magnetic structure is known) from the quantization condition, (Jorzick [49]),

$$\int k[H(z), \omega]\, dz = n\,\pi \qquad (2.72)$$

where $k\,[H\,(z), \omega]$ is found from (2.69) and n is an integer. The integration is done over the width of the wire. Hillebrands, Demokritov and Jorzick [29a, 29b, 42, 43, 47-50] realized the experiments using Brillouin light scattering. This experimental approach (so-called a "Fourier microscope") offers an effective method for the study of spin waves.

Different spin wave modes can be investigated with high sensitivity over a large range of spin wave vectors, in applications where ultrathin films are involved [41, 51, 52]. Fig. 2.7a shows the geometry of the sample and magnetic field and the resulting types of magnetostatic spin waves. Assuming $d<<w$, the spectrum of long-wavelength magnetic excitations can be calculated approximately using the theory of dipole-exchange spin waves. The spin dispersion curves are displayed in Fig. 2.7b. The analysis shows that the spin waves are the non-uniform eigenmodes of the system and their properties directly reflect the dimensionality of the system. The spin wave system of wires (magnetized along their axis) is determined by the quantization due to confinement in a wire.

There are other examples where quantization in dots yields an anisotropic nature of the spin wave dispersion due to non-homogeneous internal fields. In the case of arrays of wires or dots, the interaction between them is due to long-range magnetic dipole

interaction. The strength of the interaction depends on the geometrical properties of the elements. In addition, the static and dynamic couplings play an important role in the inter-element interactions and alter the magnetization excitations from normal to coupled spin wave modes.

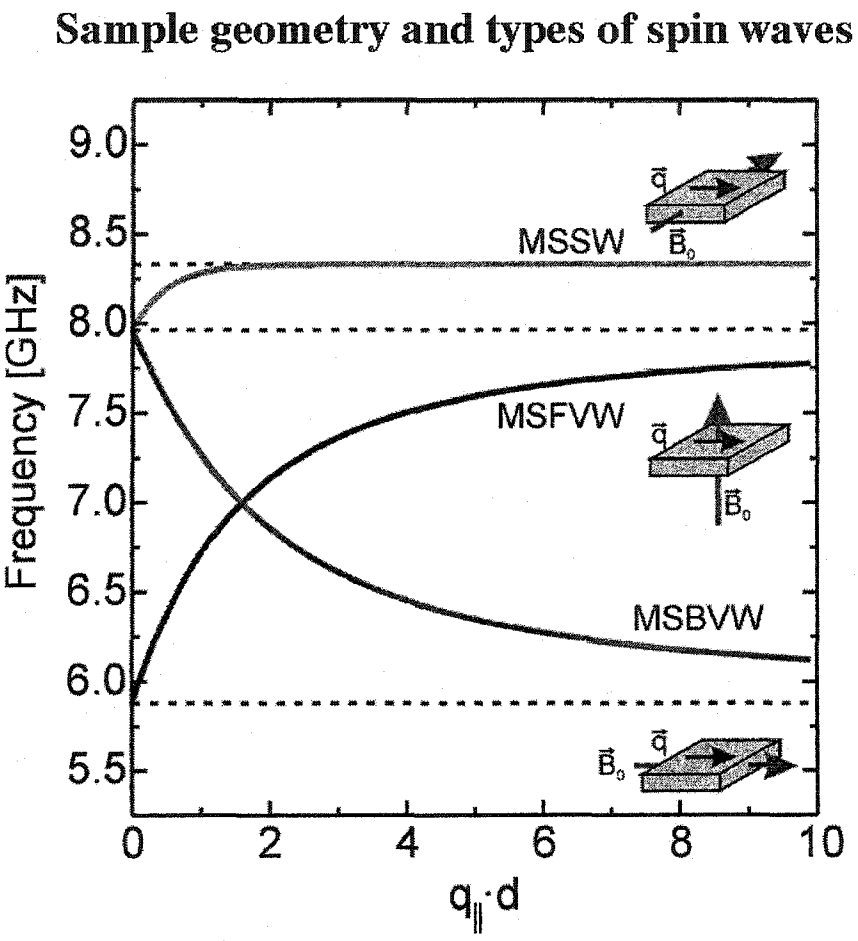

Fig.2.7a Types of spin waves are different for various relative orientations of the thin film sample and magnetic field vector B_0 [41]. MSSW (magnetostatic surface mode), MSFVW (magnetostatic forward volume mode) and MSBVW (magnetostatic backward volume mode) have dispersion curves dependent on the in-plane wave vector times the thickness of the sample quantity ($A=1x10^{-11}J/m$, $M_s=64.6kA/m$ for $Ni_{81}Fe_{19}$ [29a, 48]).

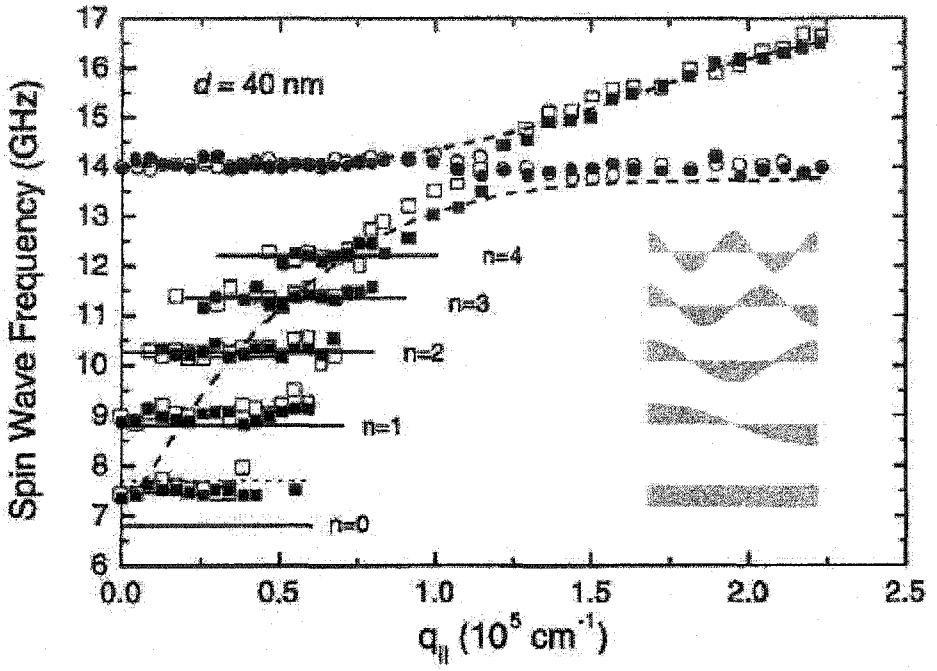

Fig.2.7b Spin wave dispersion curves, from [41], for an array of wires (wire thickness 40nm, a width of 1.8μm and a period 2.5μm (open symbols) and 2.2μm (solid)). The external field was applied along the wire axis at 3.98kA/m. The solid horizontal lines indicate the results of a calculation using equation (11) in Ref. 41 (with neglected exchange constant and quantized values of spin wave vector). The dotted horizontal lines show the result of calculations using Kittel formula [16]. Hybridized dispersion of the Damon-Eshbach mode [37] (dashed line) and the first perpendicular standing spin wave mode were calculated numerically for the continuous film of $Ni_{81}Fe_{19}$ (as in Fig. 2.7a). The mode profiles are illustrated on the right-hand side.

An important investigation of spin wave modes in a rectangular tangentially magnetized thin-film magnetic element has been published recently in the work of Guslienko et al. [72]. The dipole-exchange spectrums of quantized spin wave modes are

analyzed using a method of tensorial Green's functions. The internal fields along the magnetization direction are strongly inhomogeneous (these are the results of the magnetostatic solutions of Maxwell equations) and lead to the localization of the spin wave modes either at the edges (the exchange localization) or at the center (the dipolar localization) of the magnetic element. The mode intensity distributions along the other in-plane direction are determined by the dipolar boundary conditions and have the usual *cos()* form.

The dispersion equation has the form (equation (7) in [72]),

$$\omega_{mn}^2 = (\omega_H^{mn} + D\,\omega_M\,\kappa_{mn}^2)\,(\omega_H^{mn} + D\,\omega_M\,\kappa_{mn}^2 + \omega_M\,F_{mn}(\kappa_{mn})) \qquad (2.73)$$

where $\omega_H = \gamma H$, $\omega_M = 4\pi\gamma M_s$, $\omega_H^{mn} = \omega_H - \omega_M N_{mn}$, D is the exchange constant, H is the DC magnetic bias and N_{mn} are the effective demagnetization factors of the spin wave mode (m,n). $F_{mn}(\kappa_{mn})$ is a quantity depending on matrix elements of the dipole-dipole interaction [72, 43]. The interaction between spin waves is neglected in this approach.

From a deeper theoretical point of view, the classical equation of motion of the magnetization in a ferromagnet lead to an equation similar to the Schrödinger equation, as shown by Tsukernik [54].

2.5 ***Magnon-magnon interactions.***

The precession of spins in an uniform mode is highly correlated because of the exchange forces (assuming the uniform pumping over all area of the sample) [10, 11, 14, 23, 24, 34, 35, 37-39, 40a, 40b]. Above a certain threshold, pump power a spontaneous transfer of motion into higher order spin waves occurs. These spin wave motions are

coupled to the uniform precession by the demagnetizing fields (such as domain walls close to the edges of the sample). They grow exponentially with time at the expense of the uniform mode until the precession angle of the last one is decreased below the value at threshold. The spin waves excited in this way have amplitudes of a large non-thermal value. They can be represented as dissipative terms (intrinsic damping) in the equations of motion of the uniform mode and spin waves [10]. The energy is redistributed because of spin-spin relaxation processes. These processes involve or do not involve $k=0$ magnons, interactions with conduction electrons and spin-lattice relaxation processes (creation of phonons). The increase of the signal field causes primarily the greater excitation of the uniform spin wave mode, which results in the increased excitation of $k\neq 0$ coupled modes [34]. If the rate of energy transfer to the $k\neq 0$ mode spin wave exceeds the rate at which the energy can be transferred from that spin wave, the amplitude of the spin wave increases exponentially (until the uniform mode is significantly depleted). The condition of the instability depends on the rate (proportional to the threshold $\Delta H_k = 1/\gamma\tau_\kappa$, where τ_κ is the lifetime of the $\boldsymbol{k}$ magnon) at which the energy can be dissipated from the particular $k\neq 0$ spin wave.

There are two types of such nonlinear processes. One process is the "first-order Suhl instability", which is the process (dominating at lower frequencies) where the energy from a single $k=0$ magnon is transferred to two magnons. These new magnons have equal and opposite $\boldsymbol{k}$ and half the frequency/energy each (which, for example, in spheroidal samples can be satisfied only if $\omega_0 \leq 2M\gamma N_t$, where N_t is the transverse demagnetization coefficient).

In the second process (a 2nd order process possible at both low and high frequencies), two $k=0$ magnons decay into two magnons of the same frequency but with equal and opposite $\boldsymbol{k}$ (a degenerate magnon of direction $\boldsymbol{k}$ parallel to the applied field). By measuring the threshold ΔH_k at various frequencies, it is possible to obtain the information about relaxation of spin waves in different regions of the spin wave spectrum. Applying the signal field parallel to the direction of the *DC* magnetic bias the longitudinal *AC* field couples to the spin waves precessing in an elliptical cone and propagating in a direction perpendicular to the *DC* field (preserving the momentum and the energy).

Another kind of spin wave resonance has nodes at the surface of a thick magnetic film. The perpendicular component of this spin wave vector is $k_z = m\pi/d$, where d is the film thickness and m is an integer.

2.5.1 *Classification of relaxation processes.*

Many relaxation mechanisms exist in which the magnetization oscillations can be transformed from one mode to another and to transfer the energy and momentum of the spin wave into other vibrational modes of the lattice. The length of the characteristic time of the ferromagnetic relaxation (or the damping time) is determined by the interactions between various spin wave modes (uniform and nonuniform), between spin waves and phonons, conduction electrons and the electromagnetic radiation [33]. A flow chart and other details of these processes are displayed in Figs. 2.8 and 2.9.

a) *Magnon-magnon scattering involving k=0 magnons*

1. Two-magnon process ($k=0$ magnon destroyed, to conserve momentum these processes are possible in polycrystalline samples, disordered crystals or ordered crystals with surface imperfections).

2. Splitting process ($k=0$ magnon destroyed creating two $k\neq0$ magnons with half the energy and equal (opposite) $\boldsymbol{k}$).

3. Four-magnon process (two $k=0$ magnons destroyed creating two $k\neq0$ magnons with the same energy and equal (opposite) $\boldsymbol{k}$).

4. Four-magnon process (single $k=0$ magnon scatters creating three $k\neq0$ magnons).

5. Four-magnon process ($k=0$ and $k\neq0$ magnons destroyed creating two magnons $\boldsymbol{k}', \boldsymbol{k}'-\boldsymbol{k}$).

6. Four-magnon process ($k=0$ and two $k\neq0$ magnons $\boldsymbol{k}'$, $\boldsymbol{k}$ destroyed creating one magnon $\boldsymbol{k}+\boldsymbol{k}'$).

b) *Magnon-magnon scattering not involving k=0 magnons*

1. Two-magnon process (one magnon destroyed, one magnon created, possible in non-periodic crystals to conserve momentum).

2. Three-magnon splitting process.

3. Three-magnon confluence process.

4. Four-magnon process (**k** magnon scatters creating three **k** magnons).

5. Four-magnon process ($\boldsymbol{k}, \boldsymbol{k}' \rightarrow \boldsymbol{k}'', \boldsymbol{k}+\boldsymbol{k}'-\boldsymbol{k}''$).

6. Four-magnon process ($\boldsymbol{k}, \boldsymbol{k}', \boldsymbol{k}'' \rightarrow \boldsymbol{k}+\boldsymbol{k}'+\boldsymbol{k}''$).

c) *Magnon-phonon scattering*

1. Magnon-phonon scattering both having equal energy and momentum

2. Magnon-phonon scattering in non-periodic crystals with different momenta

3. Two-magnons one phonon process ($k \rightarrow k + p$ or $k + p \rightarrow k$)

4. Two-phonons one magnon process ($k \rightarrow p + p$ or $k + p \rightarrow p$)

5. Ion system with strong exchange and spin-orbit interactions

d) *Magnon-conduction electron scattering*

1. Eddy current damping in very thin (thickness << skin depth) metallic films (more details in Section 2.5.4 below)

2. The direct coupling of the localized magnetic and conduction electrons (with or without a flipping of the spin of the electron and an absorption or creation of a magnon) is an additional channel, through which the energy of the magnetic system can dissipate.

The two-magnon processes are forbidden in an ideal crystal by the momentum-conservation law. If non-uniformities, such as the heterogeneity of the chemical composition, the disorder of the ion distribution, the variation of the crystal axes in polycrystals, the stresses caused by dislocations, pores, a surface roughness, exist they can scatter magnons. In that case, the two-magnon k - k processes (including 0 - k process for the uniform mode) are allowed.

Arias et al. in [109] developed a theoretical approach to explain the damping processes and the frequency shift based on the two-magnon scattering by defects and interfaces. The conditions of the resonance are changed and the consequences of these non-uniformities can be observed via broadening and shifting of the ferromagnetic resonance lines. In ferromagnets, the dipole-dipole and the exchange interactions lead to a strong coupling of the magnetization oscillations. These oscillations are coupled and

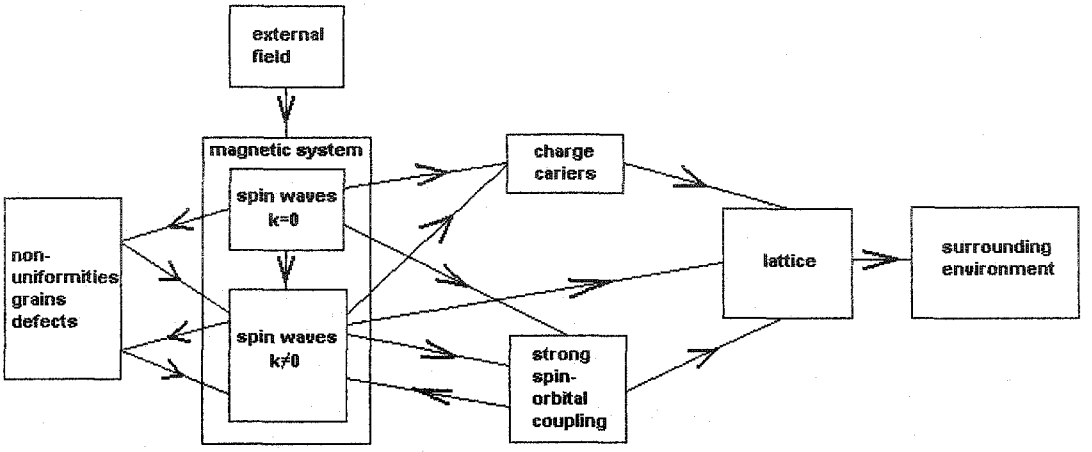

Fig. 2.8 Chart of energy flow in a magnetically ordered substance [10].

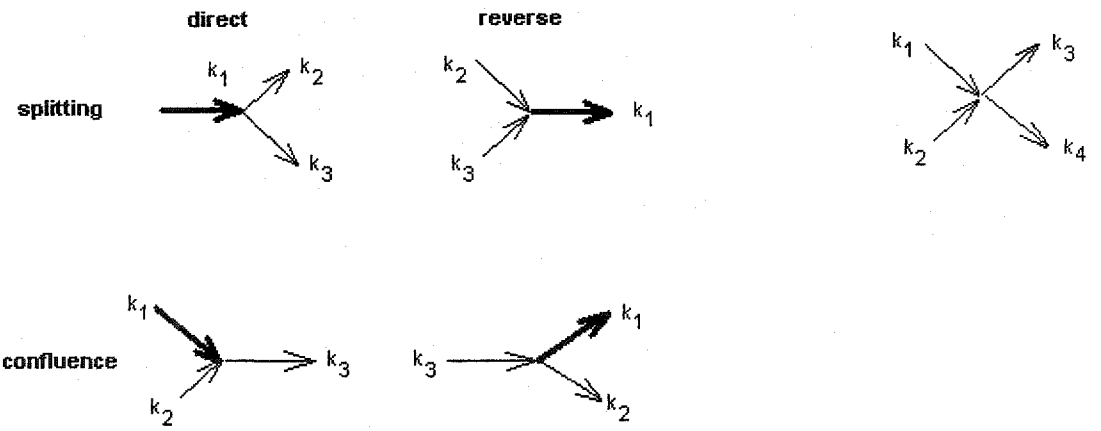

Fig. 2.9 Chart of elementary relaxation processes [10]. Splitting and confluence is shown on the left, and the 4-magnon process on the right.

they create a continuous group of modes near every uniform mode. Other relaxation channels exist if there are strong spin-orbital couplings such as indirect spin-lattice interactions or charge carriers. The coupling between the uniform and the higher modes

of the sample leads to the energy transfer from the initial mode (excited by the external field) to the higher modes, which is interpreted as a non-dissipative relaxation mechanism. Brief quantum-mechanical analysis of magnon-magnon interactions is shown in Appendix 2.

Akhiezer in [35] did the exact quantum-mechanical analysis of the relaxation processes in ferromagnets and shows the formulas for the spin wave lifetimes, the magnon decay and the coalescence probabilities, the magnon-magnon scattering probabilities or the probabilities of magnon-phonon interactions (e.g. the emission of a phonon by a magnon).

2.5.2 *Magnon-magnon interactions and non-uniform internal fields.*

Schlömann [38] showed results from an analysis of the coupling of microwave power into a ferromagnetic rod, including the nonuniform *DC* magnetic field inside the ferromagnetic body. The homogeneous part of the equation of motion has the form of the Schrödinger equation; the theoretical analysis is in Ref. [54]. The non-uniform (demagnetizing) fields inside the ferromagnet introduces nonlinear penalty for the spin wave behaviour (because of interactions between the spin wave modes), as described in Refs. [10, 23, 34, 53]. In finite structures with a nonuniform internal magnetization, the coupling of normal (spin wave) modes to these inhomogeneities creates potential wells for spin waves for example near the edge of a thin wire. This process has been analyzed theoretically and experimentally in Refs. [47-52].

The manner in which a nonuniform in-plane field can change the dispersion characteristics of magnetostatic surface spin waves was shown in [40]. The linearized

equations of motion of the magnetization provide a sufficiently exact description of the properties of the normal modes. If the dipolar interactions cannot be neglected the spin waves are coupled [25, 34]. If the excitations of these modes are small, the equations can still be linearized and transformed into the normal modes. If the spin wave excitation is large, the modes are coupled by nonlinear terms and cannot be linearized. An analysis of a spin wave dispersion spectrum in a ferromagnetic plate with a domain structure was shown in [55] and results in a band structure of the spin wave spectra. Suhl [23] showed an analysis of interactions between uniform and $\boldsymbol{k} \neq 0$ spin waves including the dipolar fields. The analysis related to the damping constant in [58] showing the energy transfer between various modes of magnetization oscillations.

Dobin and Victora in [39] extended the analysis of Suhl in [23] by taking into the account the advanced demagnetizing field formulas from Mansuripur's work [19]. They found a good agreement of their analytical theory with the numerical simulations [59]. The four-magnon scattering (while assuming the three-magnon processes are prohibited) in a thin metallic ferromagnetic film was primarily taken into account. They found a weak temperature dependence of the four-magnon damping mechanism in the temperature interval $30°K<T<600°K$. In addition, the importance of the magnetostatic interactions for the case of a thin film and periodic boundary conditions (assuming four-magnon scattering only in Permalloy and Nickel) was emphasized. The small damping constant $\alpha=0.005$, coming from this four-magnon scattering, gives similar results as the analysis in [60] where $\alpha=0.037$ was used without the four-magnon processes. A requirement to have the damping constant with the numerical value inside this interval

suggests that another damping mechanism is needed. This could be the scattering by conduction electrons [62], or magnon-phonon scattering [58, 61].

Solving Maxwell's equations only for some planar structures such as soft ferromagnetic thin film discs with the in-plane magnetic field, the internal domain walls were found by Bryant and Suhl in [81, 82]. Che and Suhl discuss the formation of domain structures by a self-organizing process in [83], see also the references therein. Knowledge of domain structure and the resulting non-uniform internal fields in a finite ferromagnetic element are essential for the exact analysis of magnon-magnon interactions.

The nature of the LLG equation of motion of magnetization is nonlinear. This nonlinearity and its consequences were expressed in analytical form as the many-soliton solution of the imaginary-time sine-Gordon equation, by Chui et al. in [63, 64]. Including the exchange, dipolar and anisotropy interactions in two-dimensions between spin sites, many domain structures typical for thin ferromagnetic films can be expressed in a form of the analytical soliton solutions. The two-soliton solutions include, for example, the 90° and 180° domain walls and the vortex structures. The inclusion of fourfold (or uniaxial) anisotropy and the exchange energy result in a edge domain configuration, as shown in Fig. 2.10. The common soliton solutions of the nonlinear sine-Gordon equation for different problems such as crystal dislocations, superconductivity and ferromagnetic domains are studied in more detail in [66]. Deeper insight exists in the reviews about magnetic solitons [65,68] and nonlinear waves [67].

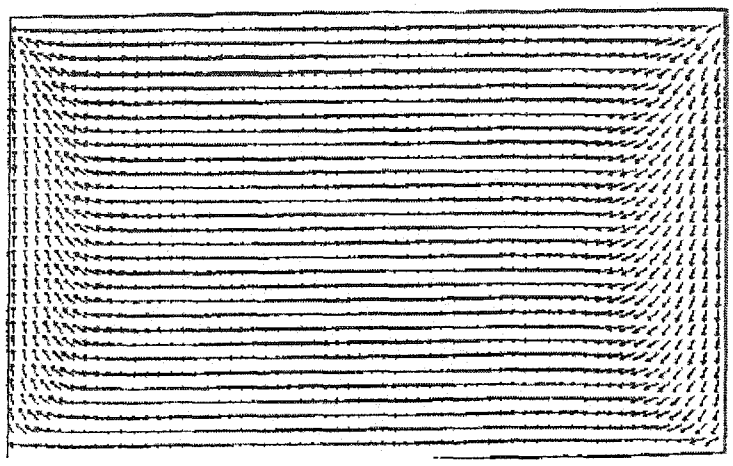

Fig. 2.10 The edge domain structure as the result of two-soliton solution of sine-Gordon equation in zero magnetic field.

The importance of the demagnetizing field in a finite-size structure, especially in the ferromagnetic thin films with weak (uniaxial) anisotropy can be shown using numerical simulations. The demagnetizing fields can be calculated following the equations (2.8)-(2.11) from Mansuripur [19].

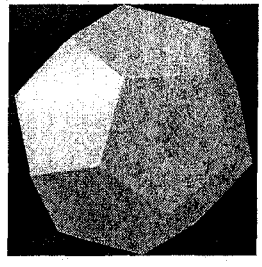

Fig. 2.11 A shape of a dodecahedron.

Beleggia and De Graef in [69] showed an approach based on Fourier analysis to calculate the demagnetizing field tensor of uniformly magnetized particle of arbitrary shape such as a faceted particle e.g. Fig. 2.11. The expressions for important configurations can be derived analytically. In this analysis the magnetization $\boldsymbol{M(r)}$ is written as $M_0\, D(\boldsymbol{r})\, \boldsymbol{m}$, where $D(\boldsymbol{r})$ is a shape function. Then the Fourier image of the demagnetizing tensor is

$$N_{ij}(\boldsymbol{k}) = D(\boldsymbol{k})\, k_i k_j / k^2. \qquad (2.74)$$

This is the direct connection between the shape of a particle and the demagnetizing tensor. Such an expression can be used in further analytical study of the magnetization of complicated (many-particle) structures.

2.5.3 Spin waves in patterned magnetic structures.

The experiments related to the magnetostatic modes represent an important source of information about the behaviour of magnetization in patterned thin films. The ability to excite and control spin waves in patterned Permalloy thin films was demonstrated in [74]. Modified by the uniaxial anisotropy and the demagnetizing fields, with pinned boundary conditions, the close agreement between measured and predicted absolute frequency (using the Damon–Eshbach dispersion relation) was obtained.

Covington et al. in [77] studied experimentally and numerically the propagation of spatially localized spin waves in Permalloy thin film structures. The spin wave packet distribution is predominantly driven by the spatial non-uniformity of the in-plane pumping field. Barman et al. in [78] studied the fourfold anisotropy (due to internal fields) and the spatial non-uniformity of magnetization oscillations of 10μm Permalloy square element. The damping in their measurements depended on the direction of the in-plane static magnetic field and was higher when the biasing field was parallel to the diagonals of the square.

Park et al. in [96] investigated the localization (due to the internal field profile as a result of the applied external field) of spin wave modes in thin film ferromagnetic wires. Distinct modes were detected at the edges of the Permalloy wires and the crossover of two edge modes into a single mode was shown via spatially resolved

spectra. In addition, the remanent states of individual micron scaled ferromagnetic squares and circles were studied, the excitations in inhomogeneously magnetized microstructures demonstrated and two classes of excitations resolved (Park et al. [95]). The first is the precession about the local demagnetizing field and the second is the excitation localized at the domain walls. Bayer et al. in [79] observed experimentally similar behavior of spin waves in inhomogeneous internal fields of thin narrow long ferromagnetic wires. The spin wave modes detected were interpreted as the multiple spin wave eigenstates of the effective potential wells. Boerner et al. in [80a] considered the relaxation processes in the ferromagnetic thin films using numerical LLG simulations. The role of the phenomenological damping that allows a drain of the energy from the magnetic system and the relaxation toward equilibrium configuration was investigated. Assuming the magnetic platelets are large enough (compared to the exchange length), the authors concluded that the external energy (due to the applied field) could be absorbed by the excitation of the magnetostatic nonuniform exchange spin wave modes without the damping term. Sandler et al. in [80b] also discussed the damping constant and the rate of energy dissipation in NiFe films.

Novosad et al. in [75] studied the importance of the magnetostatic interaction in an array of circular dots. The dependence of the vortex state stability on the interdot distance was shown. Guslienko et al. in [76a, 76b] discussed theoretically the fields, the vortex state evolution and the spin wave spectrum in an array of dots. The simple analytical form of the approximate discrete dispersion equation was derived and the quantization effect due to finite dot radius was shown by Guslienko and Slavin in [76b].

2.5.4 Spin waves in polycrystalline metallic magnetic thin film structures.

The outer shell *s* electrons in the iron group (Fe, Co, Ni)form an electron liquid under the interaction with a lattice of positive ions [62]. The ions have unfilled 4*f* shells and electrons, which can be treated as localized. In *3d* transition metals an indirect exchange interaction, via conduction *s* electrons and the Ruderman-Kittel-Kasuya-Yoshida (RKKY) interaction, plays an important role in the magnetic ordering. Assuming the magnetic moments of *3d* and *4f* shells are only partly localized, then the de-localized magnetic moment density of conduction electrons has to be taken into account. The conduction electrons in the (rare earth) metals act as the medium through which the coupling is established between the 4*f* electrons localized on the ions. The RKKY coupling has an influence on both the spin waves in the ferromagnetic phase and on the conduction electrons themselves. The indirect-exchange interaction has effects in limiting the lifetimes of the spin waves and in polarizing the conduction electrons. Enhancement of the effective mass of conduction electrons by the dynamical magnetic fluctuations can take place. Modification of the electrical resistivity by the exchange interaction and by scattering of the conduction electrons from the spin wave excitations can also take place. Herring and Kittel [30] showed the influence of the magnetic ordering on the conduction-electron band structure.

As from above, in ferromagnetic metals, the charge carriers can have a determinative impact on all dynamic magnetic processes. Taking the complex dielectric constant $\varepsilon - i\sigma/\omega$, (for example, $\sigma_{Fe}=1.03\text{x}10^7$ and $\sigma_{Ni}=1.46\text{x}10^7\ \Omega^{-1}\text{m}^{-1}$).

The skin depth is given by the formula

$$\delta = (2/\sigma\omega\mu)^{1/2}. \tag{2.75}$$

Usually $d<<\delta$ in the microwave regime for a thin magnetic film. The permittivity ε is usually a complex tensor quantity dependent on the frequency and the wave vector. The relative permeability $\mu>>1$ for ferromagnets and comes from the solution of Landau-Lifshitz equation. Because of the skin effect the AC magnetization near the surface could be very nonuniform but in the case of $d<<\delta$ this effect is also negligible. The magnetic dissipation parameter α in metals is practically independent of the frequency and has a weak temperature dependency in perfect samples [39, 61, 62].

Two-magnon processes caused by the nonuniform anisotropy can be strong in polycrystalline samples. In addition, the nonuniform elastic stresses can be the cause of strong two-magnon processes. The electron-magnon processes are caused by interactions of electron's orbital moment $\boldsymbol{p}$ and conduction electron spin $\boldsymbol{s}$ with the magnetization $\boldsymbol{M}$ of the magnetic system. The first interaction is described by the first term and the second by the other two terms in the interaction Hamiltonian

$$H = -2\mu_B \boldsymbol{A}.\boldsymbol{p} - 2\mu_B \boldsymbol{H}.\boldsymbol{s} - 2(J/M_0)\boldsymbol{M}.\boldsymbol{s} \tag{2.76}$$

where A is the vector potential of an electromagnetic field and J is the exchange integral describing the interaction of the s electrons with the magnetic system. After the transformation of the Hamiltonian into an expression with creation and annihilation operators, the higher order terms correspond to the creation and annihilation of magnons (for example the splitting and the confluence). In these interactions only, the electron's moment and spin could change. In the *sd* or *sf* exchange interactions within the magnetic system the spin of interacting particles is conserved.

From the point of view of the phenomenological theory of spin waves in metals, the general dispersion relation describes the spectrum of ellipsoidal bodies, see, for example, the analysis in Refs. [32, 46, 56].

Patton in [97] analyzed the spin wave dispersion for the allowed normal modes of excitations in planar ferromagnetic metal surface considering the effect of the exchange field on the damping term. The contribution of two-magnon scattering to the damping effect in Permalloy was the subject of an investigation in [98] by Patton. Using the ferromagnetic resonance technique, the contributions of large inhomogeneities to magnon scattering were identified.

Pincus in [99] studied the effects of the eddy currents on the spin wave damping. Eddy current damping of thin film domain walls were studied (via solving Landau-Lifshitz and Maxwell equations) by Yuan and Bertram in [106]. For Permalloy films thinner than 300nm, the eddy current damping can be neglected in wall dynamics, while this effect will be the dominating loss mechanism for film thickness higher than 1000nm. The two-magnon interactions and the uniform spin wave mode scattering into degenerate modes in metals with irregularities (voids, pores of various size and volume fractions, combined with an uniaxial anisotropy and an oblique magnetic bias field direction) were subject of the theoretical investigation of Hurben and Patton in [100].

Spin wave spectra in ferromagnetic multilayers have also been the subject of intensive research, for example, in the work of Grünberg and Mika [73]. The dipolar-magnetostatic limit was used (in the case of the in-plane magnetization) and spin wave branches were found (depending on the number and the thickness of the magnetic and non-magnetic layers). Hillebrands (including the interface anisotropies) did a similar

analysis including the exchange contributions and the interlayer exchange coupling [91, 92].

Nikitov studied spin waves in periodic magnetic structures (magnonic crystals) in [93a], particularly the propagation and reflection of the spin waves through a periodic multilayered magnetic structure (where the structure consists of ferromagnetic layers having the same thickness but different magnetizations). The spin wave spectrum contains forbidden zones because of the periodicity. Vasseur in [93b] theoretically studied the existence of magnon bandgaps of a two-dimensional composite of ferromagnetic cylinders embedded in a ferromagnetic matrix.

2.5.5 ***Review of past experimental work.***

Relaxation effects (ferromagnetic resonance damping) has been observed in the time domain by means of optical pump–probe spectroscopy in thin film Fe samples by Hicken et al. in [87], and, in addition, the ultrafast spin dynamics in a polycrystalline nickel thin film has been explored at saturation in [88]. Hiebert et al. in [89] studied the magnetic relaxation in a small Permalloy disk immersed in an in-plane biasing magnetic field. The nonuniform magnetic oscillations were excited and detected by the sub-nanosecond pulses of the perpendicular field. The result shows a good agreement of the experimental and simulated (via LLG) modal frequencies of the oscillations.

A comparison of experimental and numerical micromagnetic dynamics in coherent precessional switching and modal oscillations is shown in [90]. The high-frequency spin wave generation was inferred by apparent reduction in the magnetization vector length. Small angle (<1°) non-equilibrium modal oscillations in the ferromagnetic

resonance are compared and show a considerable agreement in the long-wavelength magnetic spatial structure.

The spin excitations of magnetic vortices in ferromagnetic dots (fabricated from Permalloy, 60nm thick and 800nm in diameter) were studied in [94]. Two excitation modes were observed experimentally in the vortex state. Numerical and analytical calculations of the dynamic magnetization based on the Landau-Lifshitz equation of motion show that the higher and lower frequency modes correspond to dipole-dominated spin excitations localized inside the dot and at the dot edges, respectively.

Stamps et al. in [101] studied spin wave propagation and reflection in imperfect ultrathin films (with occasional bumps and holes of size of few atoms). They found, in [102], that in very thin films the lifetime of long-wavelength spin waves is relatively insensitive to scattering from a large number of irregularities.

Hicken et al. in [105] investigated the rise and the damping of spin excitations in $Ni_{81}Fe_{19}$ films with thickness 5, 50 and 500nm. The damping constant was smallest in the 50nm sample and the variations in the rise time and the damping were attributed to the presence of the eddy currents and the structural disorder in the films.

The images of precessional motion of the magnetization vector in 20nm thick 6μm large cobalt disc show an evolution of the non-uniform precessional mode of the magnetic membrane, according to Acremann in [108]. Gerrits et al. in [84] investigated the spin wave dynamics in a thin Permalloy film (in in-plane fields). Coherent precession was observed when the duration of the in-plane pulses was shorter than the typical relaxation times of the magnetic system. Gubbiotti et al. in [85] reported a study of static domain configurations in micron-sized Permalloy squares. The magnetic "initial state"

Kerr patterns in zero magnetic fields show images of typical domain structures (four-, seven-domain and non-solenoidal closure patterns for 2μm squares). Merton et al. in [107] observed by MFM the effects on magnetostatic structure of the adding a hole in the middle of a patterned Permalloy element. The existence of remanent "cusp" structure (consisting of four domain walls that extend from the hole out toward but not reaching the edge of the element) was seen.

2.6 Summary of the chapter.

Spin waves are the normal modes of magnetization oscillations. Ferromagnetic materials in ellipsoidal, cylindrical and spherical forms, or as infinite thin films (in saturating external fields), have been intensively studied. The important solutions (after proper linearization) and characteristics of these magnetic systems such as the dispersion curves are well known in analytical forms. If the shape of the element is complicated, the demagnetizing fields inside the body are not uniform, the spin waves are not the eigenmodes of the magnetic system and, frequently, it is impossible to find the analytical solution. This non-uniform internal field distribution (the presence of closure domains, domain walls and stray fields) causes the spin waves interact with each other, and linearization of the equations brings unacceptable errors. A similar complication in finding the correct solutions arises with the application of very high pumping power. When crude approximations are made, the approximative solutions can explain some of the experimental results.

Magnetization oscillations have wavelengths in the range from approaching the lattice constant (the exchange spin waves), through the sizes comparable with the sample dimensions (magnetostatic oscillations) to "infinite" (uniform modes). The properties of these oscillations depend on the shape and the size of the sample; on the material properties such as the saturation magnetization, the anisotropy field and the exchange constant; on the magnitudes of the *AC* and *DC* external fields and on the relative orientations of all vectorial quantities involved. In the finite (patterned) thin film case, these spin waves interact with each other. A typical example is the excitation of the uniform mode by the uniform pumping field and the scattering of this uniform mode into the non-uniform spin wave modes by the non-uniform internal magnetic fields. The numerical solution of the equations of motions (such as Landau-Lifshitz-Gilbert under the condition the magnitude of the magnetization stays constant and is equal to the saturation magnetization) gives insight into the dynamics of the ultrafast processes in micron and sub-micron ferromagnetic elements.

Following experimental chapters show, how the non-uniform internal magnetic fields were realized using the microfabrication process (a patterning of thin magnetic films) and how the magnetization oscillations were imaged by the ultrafast optical scanning. The last chapter will discuss experimental results and a comparison with numerical simulations.

Biblography.

[1] Jackson J.D., "**Classical Electrodynamics**", John Wiley&Sons, Inc, New York 1962

[2] Chikazumi S., "**Physics of Magnetism**", John Wiley&Sons, Inc, New York 1959

[3] Marder M.P., "**Condensed Mater Physics**", John Wiley&Sons, Inc, New York 2000

[4] Yosida K., "**Theory of Magnetism**", Springer-Verlag, Berlin 1996

[5] Kittel Ch., "**Introduction to Solid State Physics**", John Wiley&Sons, Inc, New York 1971

[6] Van Vleck J.H., "**Theory of Electric and Magnetic Susceptibilities**", Oxford University Press, London 1932

[7] Schiff L.I., "**Quantum Mechanics**", McGraw-Hill, 1968

[8] White R. M., "**Quantum Theory of Magnetism**", McGraw-Hill, New York 1970

[9] Aharoni A., "**Introduction to the Theory of Ferromagnetism**", Oxford University Press 2000

[10] Gurevich A.G., "**Magnetization Oscillations and Waves**", CRC Press, Boca Raton 1996

[11] Soohoo R.F., "**Magnetic Thin Films**", Harper&Row, New York 1965

[12] Masuripur, M., "**The Physical Principles of Magneto-optical Recording**", Cambridge University Press 1995

[13] Hubert A. and Schäfer R., "**Magnetic domains: the analysis of magnetic microstructures**", Springer 1998

[14] Sparks M., "**Ferromagnetic-Relaxation Theory**", McGraw-Hill 1964

[15a] Landau L and Lifshitz E., "**Dispersion of Magnetic Permeability in Ferromagnetic Bodies**", Phys. Zeitschrift der Sowjetunion, 8, 153, 1935

[15b] Gilbert T.L., "**A Lagrangian Formulation of the Gyromagnetic Equation of the Magnetization Field**", Phys. Rev. 100, 1243, 1955

[15c] Bloembergen N., "**On the Ferromagnetic Resonance in Nickel and Supermalloy**", Phys. Rev. 78, 572, 1950

[16] Kittel Ch., "**On the Theory of Ferromagnetic Resonance Absorption**", Phys. Rev. 73, 155, 1948

[17] Osborn J.A., "**Demagnetizing Factors of the General Ellipsoid**", Phys. Rev. 67, 351, 1945

[18] Mansuripur M., "**Magnetization reversal dynamics in the media of magneto-optical recording**", J. Appl. Phys 63, 5809, 1988

[19] Mansuripur M. and Giles R., "**Demagnetizing field computation for dynamic simulation of the magnetization reversal process**", IEEE Trans. on Magnetics 24, 2326, 1988

[20] Nakatani Y. et al.,"**Direct Solution of the Landau-Lifshitz-Gilbert equation for Micromagnetics**", Jap. J. Appl. Phys. 28, 2485, 1989

[21] Kittel Ch., "**Physical Theory of Ferromagnetic Domains**", Rev. of Mod. Phys. 21, 541, 1949

[22] Cowburn R. et al., "**Domain wall injection and propagation in planar Permalloy nanowires**", J. Appl. Phys. 91, 6949, 2002

[23] Suhl, H., "**Ferromagnetic Resonance at High Signal Powers**", J. Phys. Chem. Solids. 1, 209-227, 1957

[24] Callen H.B., "**A Ferromagnetic Dynamical Equation**", J. Phys. Chem. Solids. 4, 256-270, 1958

[25] Holstein T. and Primakoff H., "**Field Dependence of the Intrinsic Domain Magnetization of a Ferromagnet**", Phys. Rev. 58, 1098, 1940

[26] Dyson J.F., "**General Theory of Spin wave Interactions**", Phys. Rev. 102, 1217, 1956

[27] Mallinson J.C., "**On Damped Gyromagnetic Precession**", IEEE Trans. on Magnetics 23, 2003, 1987

[28] Gerrits Th., "**Coherent Control of fast Precession Dynamics in Magnetic Thin Films**", PhD Thesis, November 2003

[29a] Hillebrands B. and Ounadjela K., eds, "**Spin Dynamics in Confined Magnetic Structures I**", Springer 2002

[29b] Hillebrands B. and Ounadjela K., eds, "**Spin Dynamics in Confined Magnetic Structures II**", Springer 2003

[30] Herring C. and Kittel Ch., "**On the Theory of Spin waves in Ferromagnetic Media**", Phys. Rev. 81, 869, 1951

[31] Rado G.T. and Suhl H., eds, "**Magnetism; a treatise on modern theory and materials**", Academic Press, New York 1963

[32] Walker L.R., "**Spin waves and Other Magnetic Mode**", in [31]

[33] Haas C.W. and Callen H.B., "**Ferromagnetic Relaxation and Resonance Line Width**", in [31]

[34] Damon R.W., "**Ferromagnetic Resonance at High Power**", in [31]

[35] Akhiezer A.I, Baryakhtar V.G. and Pletminskii S.V., "**Spin waves**", North Holland, 1968

[36] Walker L.R., "**Magnetostatic Modes in Ferromagnetic Resonance**", Phys. Rev. 105, 390, 1957

[37 Damon R.W. and Eschbach J.R., "**Magnetostatic Modes of a Ferromagnet Slab**", J. Phys. Chem. Solids. 19, 308, 1961

[38] Schlömann E., " **Generation of Spin waves in Nonuniform magnetic Fields. I. Conversion of Electromagnetic Power into Spin wave Power and Vice Versa**", J. of Applied Phys., 35, 159, 1964

[39] Dobin A.Yu. and Victora R.H., " **Intrinsic Nonlinear Ferromagnetic Relaxation in Thin Metallic Films**", Phys. Rev. Lett., 90, 167203-1, 2003

[40a] Stancil D.D. and Morgenthaler F.R., " **Guiding magnetostatic surface waves with nonuniform in-plane fields**", J. Appl. Phys. 54, 1613, 1983

[40b] Storey D.D. et al., "**The determination of the frequencies of magnetostatic modes in rectangular thin films of ferrimagnetic yttrium iron garnet**", J. Phys. C: Solid State Phys. 10, 875, 1977

[41] Demokritov et al., "**Brillouin Light Scattering Studies of Confined Spin waves: Linear and Nonlinear Confinement**", Phys. Rep. 348, 441-489, 2001

[42] Demokritov et al., "**Confined Dynamic Excitations in Structured Magnetic Media**", IEEE Trans. Magn. 38, 2502, 2002

[43] Kalinikos B.A. and Slavin A.N.,"**Theory of dipole-exchange spin wave spectrum for ferromagnetic films with mixed exchange boundary conditions**", J. Phys. C: Solid State Phys. 19, 7013-7033, 1986

[44] Kittel Ch., "**Interaction of Spin waves and Ultrasonic Waves in Ferromagnetic Crystals**", Phys. Rev. 110, 836-841, 1958

[45] Rado G.T. and Weertman J.R., "**Spin wave Resonance in a Ferromagnetic Metal**", J. Phys. Chem. Solids. 11, 315-333, 1959

[46] Ament W.S. and Rado G.T.,"**Electromagnetic Effects of Spin wave Resonance in a Ferromagnetic Metal**", Phys. Rev. 97, 1558-1566, 1955

[47] Hillebrands B., "**Spin wave calculations for multilayered structures**", IEEE Trans. Magn. 38, 2502, 2002

[48] Jorczik et al., "**Spin wave quantization and dynamic coupling in micron-size circular magnetic dots**", Applied Phys. Lett. 75, 3859-3861, 1999

[49] Jorczik et al., "**Spin wave Wells in Nonellipsoidal Micrometer Size Magnetic Elements**", Phys. Rev. Lett 88, 047204, 2002

[50] Jorczik et al., "**Spin wave quantization in laterally confined magnetic structures (invited)**", J. of Appl. Phys. 89, 7091-7095, 2001

[51] Jorczik et al., "**Quantized spin wave modes in micron size magnetic disks**", J. of Appl. Phys. 87, 5082-5084, 2000

[52] Jorczik et al., "**Brillouin light scattering from quantized spin waves in micron-size magnetic wires**", Phys. Rev. B 88, 15 194-15 200, 1999

[53] Anderson P.W. and Suhl H., "**Instability in the Motion of Ferromagnets at High Microwave Power Levels**", Phys. Rev. 100, 1788-1789, 1955

[54] Tsukernik V.M., "**Quantum Mechanics of a Spin wave in a Ferromagnet**", Soviet Physics: Solid State 10, 795-798, 1968

[55] Baryakhtar V.G. et al., "**Spin waves in ferromagnets with domain structure**", Soviet Physics: Solid State 21, 1729-1734, 1979

[56] Soohoo R.F., "**General Spin wave Dispersion Relation**", Phys. Rev. 120, 1978-1982, 1960

[57] Suhl H., "**Ferromagnetic Resonance in Nickel Ferrite Between One and Two Kilomegacycles**", Phys. Rev. 97, 555-557, 1955

[58] Suhl H., "**Theory of the magnetic damping constant**", IEEE Trans. on Magnetics 34, 1834-1838, 1998

[59] Boerner E.D. et al., "**Dynamic relaxation in thin films**", J. of Appl. Phys. 87, 5389-5391, 2000

[60] Back C.H. et al., "**Minimum Field Strength in Precessional Magnetization Reversal**", Science 285, 864-867, 1999

[61] Kambersky V., "**On the Landau-Lifshitz relaxation in ferromagnetic metals**", Can. J. Phys. 48, 2906-2911, 1970

[62] Abrahams E., "**Interaction between Spin waves and Conduction Electrons in Ferromagnetic Metals**", Phys. Rev. 98, 387-390, 1955

[63] Chui S.T. and Ryzhov V.N., "**Soliton and 2D Domains in Ultrathin Magnetic Films**", Phys. Rev. Lett. 78, 2224-2227, 1977

[64] Castro J. et al., "**Domains structures in ferromagnetic ultrathin films with in-plane magnetization**", Phys. Rev. B 60, 10 271-10 279, 1999

[65] Kosevich A.M. et al., "**Magnetic Solitons**", Physics Reports 194, 117-238, 1990

[66] Dodd R.K et al., "**Solitons and Nonlinear Wave Equations**", Academic Press, London 1982

[67] Witham G.B., " **Linear and nonlinear waves**", John Wiley&Sons, New York 1974

[68] Mikeska H.J. and Steiner M., "**Solitary excitations in one-dimensional magnets**", Advances in Physics 40, 191-356, 1991

[69] Beleggia M. and De Graef M., "**On the computation of the demagnetization tensor field for an arbitrary particle shape using a Fourier space approach**", J. Magn. Magn. Mater. 263, L1-L9, 2003

[70] Chandrasekhar S., "**Stochastic Problems in Physics and Astronomy**", Rev. Mod. Phys. 15, 1, 1943

[71] Garanin D.A., "**Fokker-Planck and Landau-Lifshitz-Bloch equations for classical ferromagnets**", Phys. Rev. B 55,1, 1997

[72] Guslienko K.Yu.. et al., "**Dipolar localization of quantized spin wave modes in thin rectangular magnetic elements**", Phys. Rev. B 68, 024422, 2003

[73] Grünberg P. and Mika K., "**Magnetostatic spin wave modes of a ferromagnetic multilayer**", Phys. Rev. B 27, 2955, 1983

[74] Crawford T.M. et al., "**Time-domain excitation of quantized magnetostatic spin wave modes in patterned NiFe thin film ensembles**", Phys. Rev. B 67, 024411, 2003

[75] Novosad V. et al., "**Effect of interdot magnetostatic interaction on magnetization reversal in circular dot arrays**", Phys. Rev. B 65, 060402-1, 2002

[76a] Guslienko K.Yu. et al., "**Field evolution of magnetic vortex state in ferromagnetic disks**", Appl. Phys. Lett. 78, 3848, 2001

[76b] Guslienko K.Yu. and Slavin A.N., "**Spin waves in cylindrical magnetic dot arrays with in-plane magnetization**", J. Appl. Phys. 87, 6337, 2000

[77] Covington M. et al., "**Time-Resolved Measurement of Propagating Spin waves in ferromagnetic Thin Films**", Phys. Rev. Lett. 89, 237202-1, 2002

[78] Barman A. et al., "**Anisotropy, damping, and coherence of magnetization dynamics in a 10 mm square Ni81Fe19 element**", Appl. Phys. Lett. 82, 3065, 2003

[79] Bayer C. et al., "**Spin wave wells with multiple states created in small magnetic elements**", Appl. Phys. Lett. 82, 607, 2003

[80a] Boerner E.D. et al., "**Dynamic relaxation in thin films**", J. Appl. Phys. 87, 5389-5391, 2000

[80b] Sandler G.M. et al., "**Determination of the magnetic damping constant in NiFe films**", J. Appl. Phys. 85, 5080, 1999

[81] Bryant P. and Suhl H., "**Thin-film magnetic patterns in an external field**", Appl. Phys. Lett. 54, 2224, 1989

[82] Bryant P. and Suhl H., "**Magnetization and domain structure of cylinders and spheres in subsaturating fields**", Appl. Phys. Lett. 54, 78, 1989

[83] Che X. and Suhl H., "**Scaling of critical self-organized magnetic-domain formations**", Phys. Rev. B 44, 155, 1991

[84] Gerrits Th. et al., "**Magnetization dynamics in NiFe thin films induced by short in-plane magnetic field pulses**", J. Appl. Phys. 89, 7648, 2001

[85] Gubbiotti G. et al., "**Finite size effects in patterned magnetic Permalloy films**", J. of Appl. Phys. 87, 5633, 2000

[86] Guedes I. et al., "**Magnetization reversal in an Fe film with an array of elliptical holes on a square lattice**", Phys. Rev. B 67, 024428, 2003

[87] Hicken R.J. and Wu J., "**Observation of ferromagnetic resonance in the time domain**", J. Appl. Phys. 85, 4580, 1999

[88] Wilks R. et al., "**Investigation of ultrafast spin dynamics in a Ni thin film**", J. Appl. Phys. 91, 8670, 2002

[89] Hiebert W.K. et al., "**Direct Observation of Magnetic Relaxation in a Small Permalloy Disk by Time-Resolved Scanning Kerr Microscopy**", Phys. Rev. Lett. 79, 1134, 1997

[90] Hiebert W.K. et al., "**Comparison of experimental and numerical micromagnetic dynamics in coherent precessional switching and modal oscillations**", Phys. Rev. B 65, 140404-1, 2002

[91] Hillebrands B., "**Calculation of spin waves in multilayered structures including interface anisotropies and exchange contributions**", Phys. Rev. B 37, 9885, 1988

[92] Hillebrands B., "**Spin wave calculations multilayered structures**", Phys. Rev. B 41, 530, 1990

[93a] Nikitov S.A. et al., "**Spin waves in periodic magnetic structures-magnonic crystals**", J. Magn. Magn. Mater. 236, 320, 2001

[93b] Vasseur J.O. et al., "**Magnon band structure of periodic composites**", Phys. Rev. B 54, 1043, 1996

[94] Novosad V. et al., "**Spin excitations of magnetic vortices in ferromagnetic nanodots**", Phys. Rev. B 66, 052407, 2002

[95] Park J.P. et al., "**Imaging of spin dynamics in closure domain and vortex structures**", Phys. Rev. B 67, 020403(R), 2003

[96] Park J.P. et al., "**Spatially Resolved Dynamics of Localized Spin wave Modes in ferromagneticWires**", Phys. Rev. Lett. 89, 277201-1, 2002

[97] Patton C.E., "**Classical theory of spin wave dispersion for ferromagnetic metals**", Czech. J. Phys. B 26, 1976

[98] Patton C.E., "**Direct Evidence for a Two-Magnon Contribution to the FMR Relaxation in Ni-Fe Thin Films**", IEE Trans. Magn. Mater, page 760, Sept 1971

[99] Pincus P., "**Excitation of Spin waves in Ferromagnets: Eddy Current and Boundary Condition Effects**", Phys. Rev. 118, 658, 1960

[100] Hurben M.J. and Patton C.E., "**Theory of two magnon scattering microwave relaxation and ferromagnetic resonance linewidth in magnetic thin films**", J. Appl. Phys. 83, 4344, 1998

[101] Stamps R.L. et al., "**Reflection of spin waves by atomic steps**", Phys. Rev. B 46, 836, 1992

[102] Stamps R.L. et al., "**Spin wave propagation on imperfect ultrathin ferromagnetic films**", Phys. Rev. B 47, 5072, 1993

[103] Gopar V.A. et al., "**Electronic transport through domain walls in ferromagnetic nanowires: Coexistence of adiabatic and nonadiabatic spin dynamics**", Phys. Rev. B 69, 014426, 2004

[104] Dantas A.L. et al., "**Local modes of thin magnetic films**", Phys. Rev. B 62, 8625, 2000

[105] Wu J. et al., "**Investigation of the rise time and damping of spin excitations in $Ni_{81}Fe_{19}$ thin films**", J. Appl. Phys. 89, 6692, 2001

[106] Yuan S.W. and Bertram H.N., "**Eddy Current Damping of Thin Film Domain Walls**", IEEE Trans. Magn. 29, 2515, 1993

[107] Merton C. et al., "**Magnetic reversal of tapered Permalloy bars with holes in the center**", J. Appl. Phys. 85, 4601, 1999

[108] Acremann Y. et al., "**Imaging precessional motion of the magnetization vector**", Science, 290,492, 2000

[109] Arias R. and Mills D.L., "**Extrinsic contributions to the ferromagnetic resonance response of ultrathin films**", Phys. Rev. B 60, 7395, 1999

[110] Ballentine G.E., "**Comparison of Time- Resolved Micromagnetic Dynamics Experiments on $Ni_{80}Fe_{20}$ and Landau-Lifshitz-Gilbert Micromagnetic Simulation**", Ph.D. Thesis, University of Alberta 2002

3. Fabrication and characterization of magnetic microstructures.

3.1 Preparation of thin films

A long history of successful experiments using basic techniques for the fabrication of magnetic microstructures and nanostructures has been documented [61-76]. Deposition of thin films by sputtering and evaporation, and patterning using optical lithography and electron beam lithography [1-4] followed by etching and lift-off procedures, create the closed process of pattern transfer [45-60]. The microfabrication process used in this work was chosen because the essential instruments such as DC magnetron sputtering (Lesker), the scanning electron microscope (SEM LEO440 with W and LaB_6 filaments), the electron beam writing system (NPGS, the Nanometer Pattern Generator System by J. Nabity [7]) and optical lithography were readily accessible. In the existing microfabrication facilities, these deposition and patterning technologies (augmented by the data design packages such as AutoCAD 2000, and DesignCad) were used to design, optimize, and finalize the planar magnetic structures with micron and sub-micron features. Microfabrication procedures such as the preparation of single and double layers of an electron beam resist, the detailed description of the SEM alignment, the writing procedures, the development of the e-beam resist and lift-off procedures, were developed during the work on this thesis and are described in Appendix 4. For a successful pattern formation and its transfer into a thin film system, many parameters and procedural steps are required. These include, for example, an appropriate choice of

material properties (such as the clean surfaces with small roughness), a proper chemical processing, a careful geometrical data design, and proper parameters for the electron beam. The thickness, homogeneity and uniformity of the metallic thin films and resist layers, the SEM gun and beam alignment, the time and the temperature of the resist development and the lift-off processes are critical. Their final (resulting) values were chosen in series of trials and test experiments and are described below.

3.1.1 Titanium and gold thin film deposition

The metallic thin films (gold with titanium as the adhesion layer were chosen for simple processing and to keep the continuity with previous experiments) were deposited on silicon (Si) and sapphire substrates. These thin film depositions were created using the Lesker *DC* magnetron sputter system (at NanoFab, the UofA Microfabrication Facility) and the e-beam evaporation system (at the Department of Physics) . To minimize the roughness of the metallic surfaces deposition tests of Ti/Au thin films were done. In these trials, the appropriate values of parameters like pressure and temperature were found using sputtering, evaporation and thermal annealing of thin film. The usual rotation of substrates during the sputtering process was cancelled to reduce by approximately four times the deposition time. The pressure of Argon gas (Ar) was initially 7.0×10^{-3}Torr and was later decreased to investigate an influence of the Ar pressure on thin film properties. The lowest reachable Ar pressure was set by the maximum allowed gun voltage 550V. Approaching this voltage limit, the sputtering discharge could stop anytime and a voltage of approximately 530V (at the Ar pressure approximately 1.0×10^{-3}Torr) was set as the lowest, reliable working point. The base

pressure for the Ti/Au sputtering process was usually $1.0x10^{-6}$Torr. The titanium layer was the adhesion layer for the gold thin film. The thickness of the Ti was typically 30nm thick. The film was sputtered at 300W power for 5min with no rotation of the substrate. The substrate size was typically $10x10mm^2$ and the deposition, ten pieces maximum at once, was realized using 3inch targets (for both the Ti and Au). After this optimization of the sputtering parameters, the average roughness value was 1.1nm (at Ar pressure 0.8mTorr).

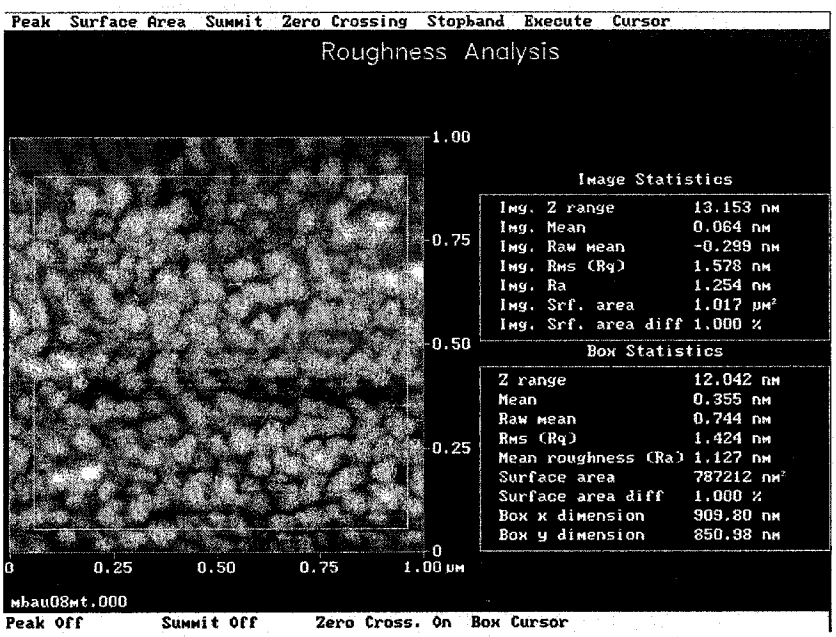

Fig. 3.1 The roughness analysis of a sputtered Ti/Au film (of the thickness 30/300nm and deposited at 0.8mTorr of the Ar pressure) shows the mean roughness 1.1nm (measured by atomic force microscope).

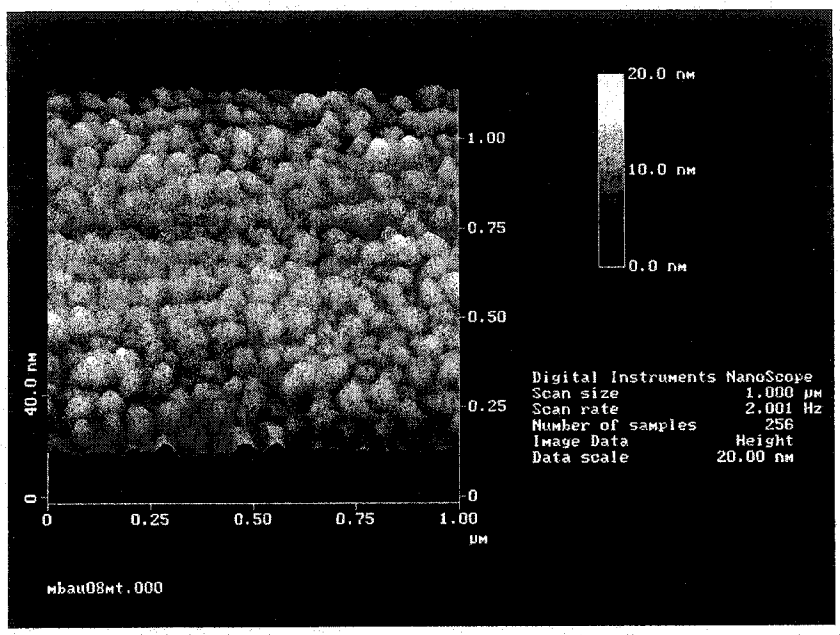

Fig. 3.2 The surface analysis of the sputtered Ti/Au film (30/300nm, 0.8mTorr).

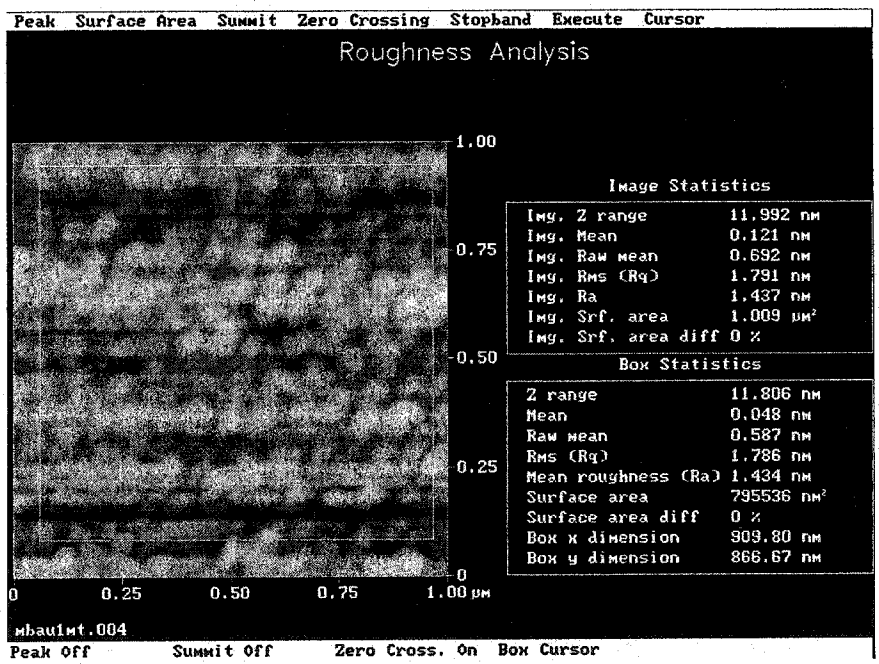

Fig. 3.3 The roughness analysis of the sputtered Ti/Au (30/300nm, 1mTorr) shows the mean roughness 1.8nm.

The next layer (the 300nm thick Au) was deposited with a deposition time of 10 min at 75W power and at the gun voltage 500V. The scans from Digital Instruments atomic force microscope (AFM) of Au surfaces (the roughness and surface analysis) are in Figs. 3.1-3.5. This analysis shows the dependence of the mean roughness value on the Ar pressure. The lowest possible Ar pressure during deposition assists in reaching decreased roughness of the gold film. Thermal heating of the substrates during deposition was applied to increase the mobility of the Au atoms on the substrate's surface. A heating lamp was installed inside the vacuum chamber just above the position of the substrate. The AFM scans in Fig 3.6 conclude that after heating the roughness was significantly worse.

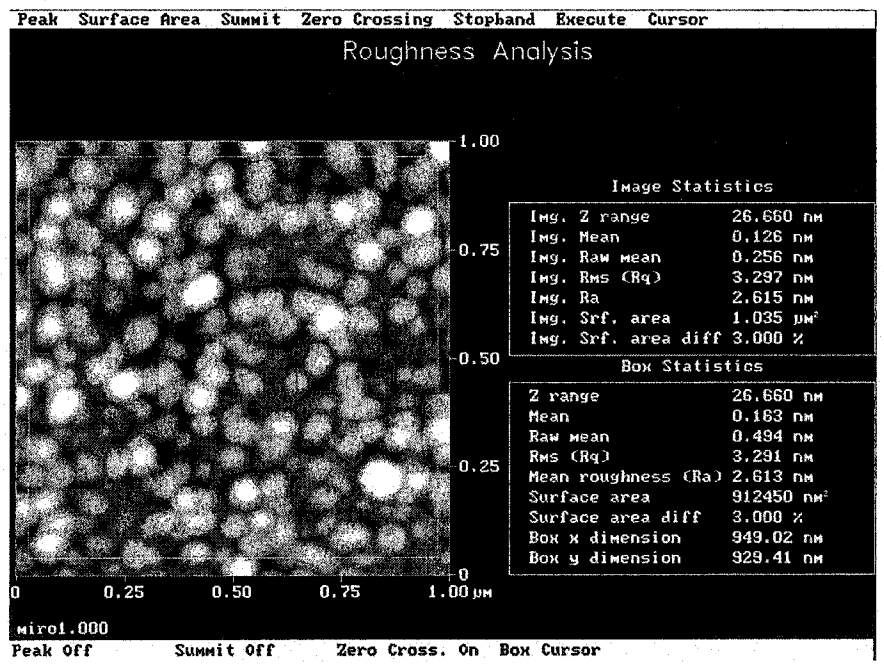

Fig. 3.4 The roughness analysis of a sputtered Ti/Au (30/300nm, 7mTorr) shows the mean roughness 2.6nm.

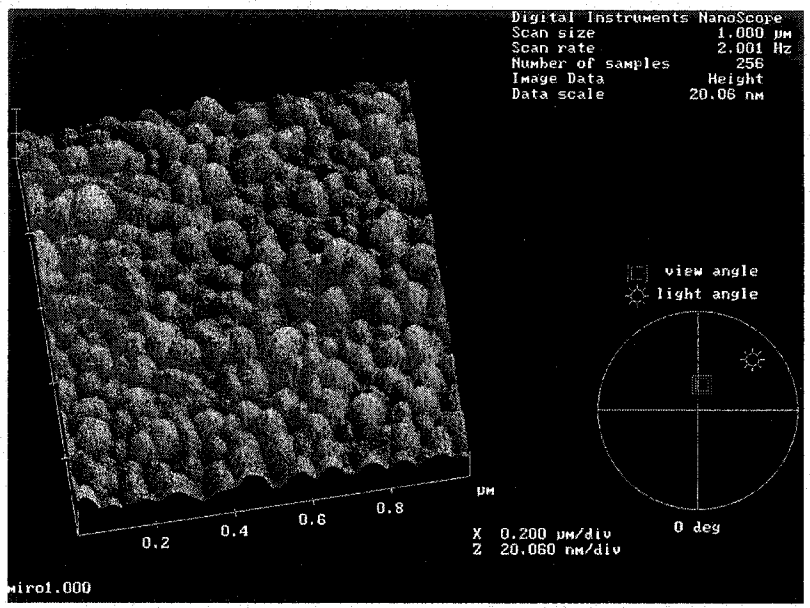

Fig. 3.5 The surface analysis of a sputtered Ti/Au (30/300nm, 7mTorr).

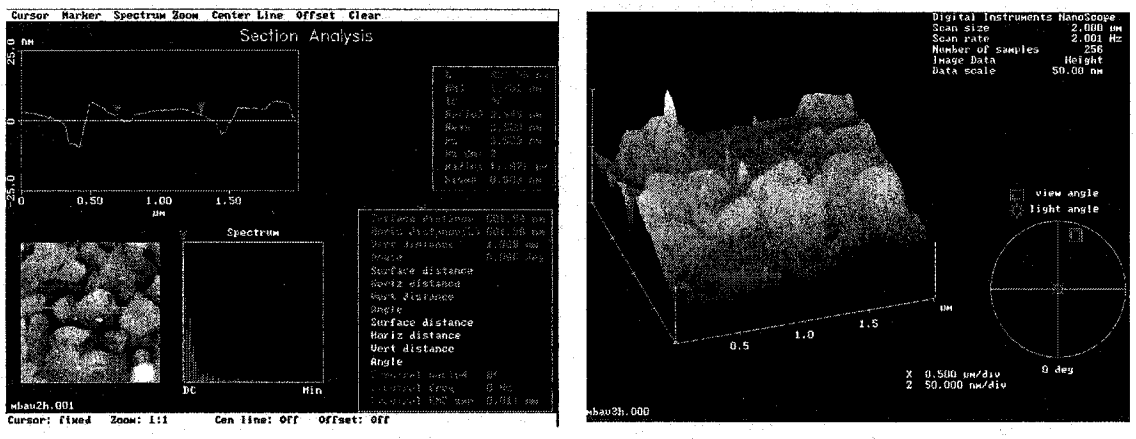

(a) *(b)*

Fig. 3.6 The roughness and the surface analysis in (a) and (b) respectively. The Ti/Au sputtered film at 1mTorr of the Ar pressure was heated and rotated (10rpm) during the sputtering process. The deposition time of Ti was 20min with the heater power 925W (80% of the maximal power and at 112V). The sputtering time of Au was 40min at the heater power 600W (60% and at 84V). The estimated temperature of the substrate during deposition was 125°C. The surface roughness was significantly increased.

The estimated temperatures of the Si substrates during the sputtering process were in the range of 100°C to 160°C but the thermal processing of the thin gold film didn't improve the flatness or roughness of the surface. Following the sputtering process, the annealing of Ti/Au layers was accomplished using the high temperature furnace (for 5min at 400°C) and the hotplate (for 5min at 300°C). Fig. 3.7 shows that the increase in the mobility of the Au atoms did not lead to decreased roughness. After the annealing on the hotplate, the Au films cracked because of the temperature gradients and resulting mechanical stresses in the thin film.

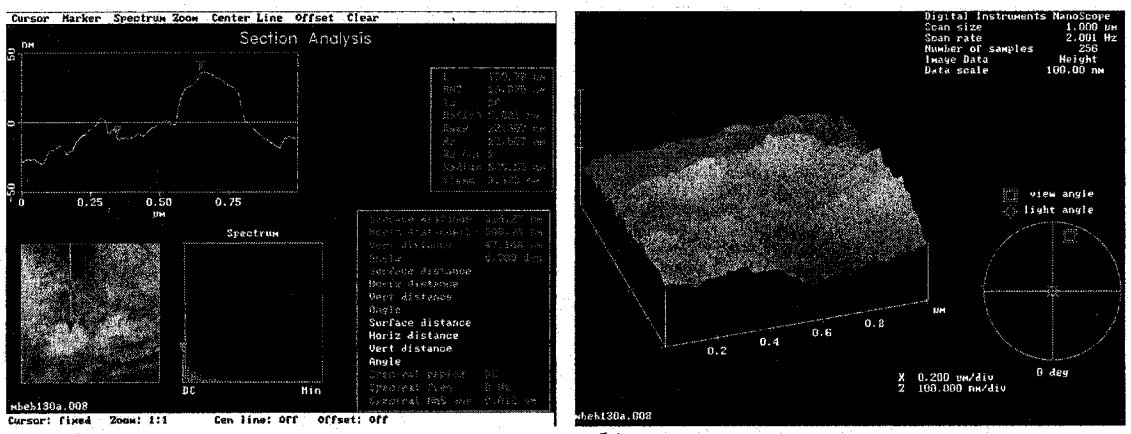

(a) *(b)*

Fig. 3.7 The images from the AFM surface scan. The section and surface analysis in (a) and (b) respectively show the 300nm thick Au films after 5min long annealing in a high temperature furnace at 400°C.

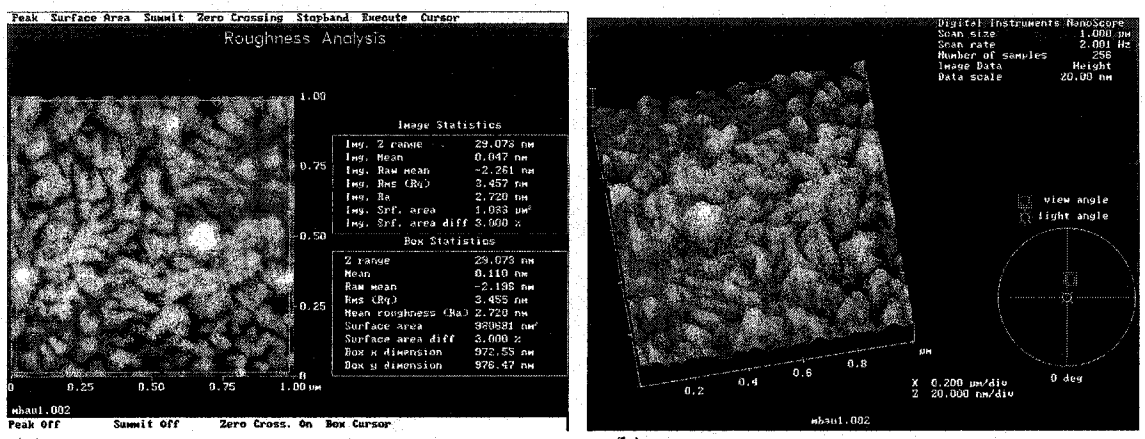

(a) *(b)*

Fig. 3.8 The roughness (a) and surface analysis (b) of the e-beam evaporated Au thin film. The mean roughness value is 2.7nm.

The Au thin films were deposited in the e-beam evaporation process using regular base pressure 1.0×10^{-6}Torr. The details in Fig. 3.8 show that the mean roughness value (2.7nm) was higher than the value of the sputtered films (1.1nm).

3.1.2 Deposition of Permalloy magnetic thin films.

3.1.2.1 DC Magnetron sputtering.

The Permalloy ($Ni_{80}Fe_{20}$) was chosen as the magnetic material important in many spintronic and magnetic storage applications, and to keep the continuity with previous experiments. The Permalloy thin films were deposited on the silicon and the sapphire substrates using the Lesker dc magnetron sputter system and the e-beam evaporator. A low-base pressure was achieved (with a typical value from $8.0x10^{-8}$Torr to $1.0x10^{-7}$Torr) to reduce the amount of oxygen and other impurities in the $Ni_{80}Fe_{20}$ film. The lowest base-pressure $3.0x10^{-8}$Torr was reached using overnight pumping and Ti pre-sputtering (for 5min). Fig. 3.9 provides the AFM analysis of the Permalloy film on Ti/Au layer (sputtered at the Ar pressure $7x10^{-3}$Torr).

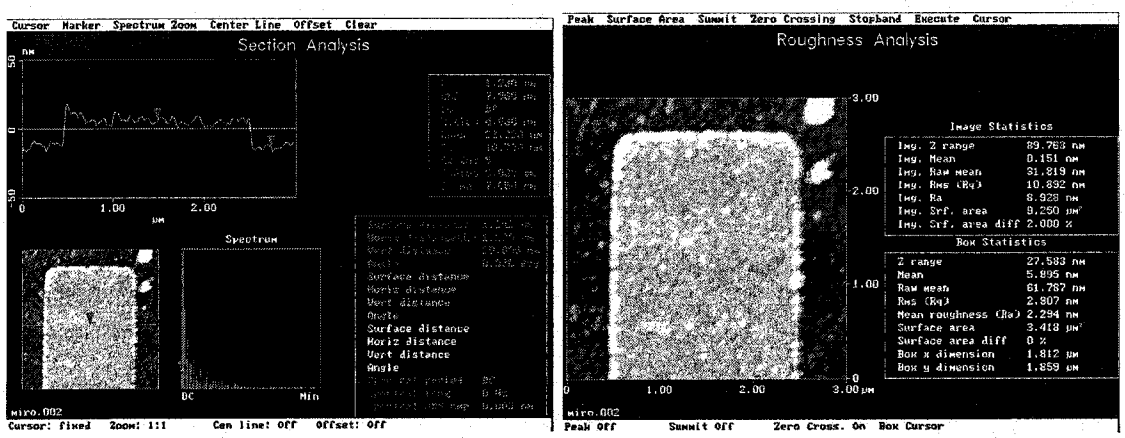

(a) *(b)*

Fig. 3.9 Section (a) and roughness analysis (b) of the 15nm thick sputtered Permalloy rectangle on gold (7mTorr). The mean roughness value is 2.2nm.

After the e-beam writing and resist development processes were completed, a 100mm x 15mm collimation tube [73] was placed between the target and the substrate to avoid covering the resist walls during deposition and to improve the lift-off process. The tube improved the collimation of the beam of Ni/Fe ions as shown in Fig 3.10.

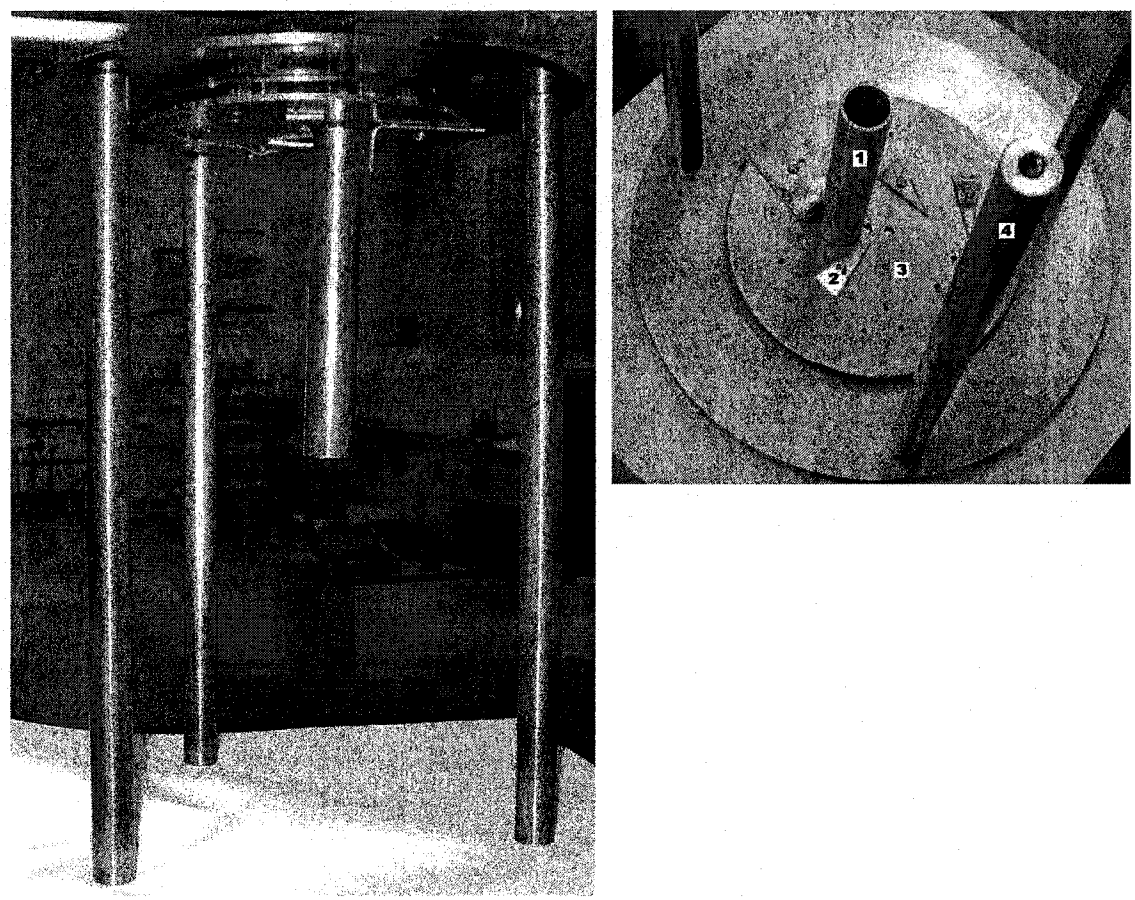

Fig. 3.10 The larger view (left) of the sample holder used for the DC magnetron sputtering of thin magnetic films with the in-plane magnetic bias field. The details (right) show the collimating tube (1), and the small holder (2) used to hold the substrate at the surface (3). The plate (3) was placed beneath the biasing magnet bars. The legs (4) define the distance between the holder and the sputtering target.

This solution reduced the divergence angle of the Ni/Fe beam sputtered from the target. The magnetic material did not cover the resist walls once these had an appropriate undercut of the profile. Acetone lifted the resist film leaving the patterned structures on the substrate. The edges of the thin film structures were clean and smooth.

The bulk and thin film Permalloy was investigated using the transmission electron microscope. The thin film sample was taken from the lift-off bath. The second, the reference sample, was prepared by grinding a splinter of Permalloy cut from the sputtering target. The diffraction analysis (details are in Appendix 3) shows the polycrystalline phase of the Permalloy thin film sample. The energy dispersive spectroscopy (EDS) also reveals the differences in the compositions of the two samples (details are in Appendix 3).

3.1.2.2 E-beam evaporation.

The other available deposition method was the e-beam evaporation. The 15nm-thick Ni film was deposited and used to test the lift-off process. The chamber pressure of the e-beam evaporation process was 1.0×10^{-5} Torr. The base pressure was 4.0×10^{-6}Torr and was later increased as the consequence of the outgassing of the chamber walls. The deposition rate was 1.6Å/s. The lift-off process of the thin film structures was not an easy one. The edges of the thin film patterned structures were rough; Section 3.3 details the experimental results of the electron beam lithography and the lift-off. All previous magneto-optical experiments used *DC* magnetron sputtering for the microfabrication of magnetic thin film structures. For continuity with those experiments, *DC* magnetron sputtering was chosen as the magnetic thin film deposition procedure.

3.2 Fabrication of micro- and nano-structures.

3.2.1 Optical lithography - fabrication Ti/Au wires.

The patterning by optical lithography was done on Si (for test purposes) and sapphire substrates. To produce a variety of Ti/Au wires a new mask was designed using AutoCAD 2000, and fabricated by a Nortel Networks electron beam writer. A set of five wires with the lengths from 60 to 200μm, the period 2mm and with linewidth/gap ratios from 20/20 to 1/2μm were designed for the area of substrate 10x10 mm^2 .The details are shown in Fig. 3.11.

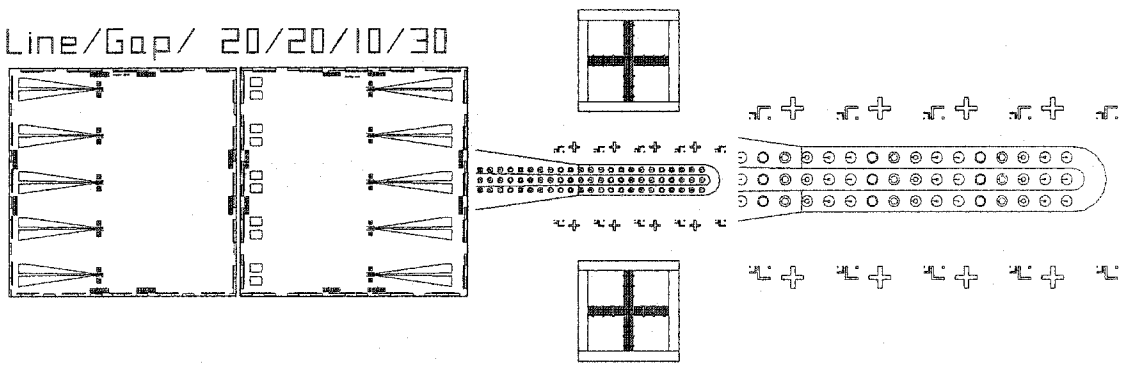

(a) *(b)* *(c)*

Fig. 3.11 Details of the mask design for the transmission line fabrication by optical lithography and wet etching. In (a), the Ti/Au wires have of spacing 2mm and large contact pads. In (b), the linewidth/gap have ratios 20/20μm with large square marks for the optical alignment and, in (c), the electron beam lithography alignment marks along 250μm long Ti/Au wire are shown. Blue, red and yellow circles represent structures for the e-beam writing.

Additional alignment marks for the e-beam lithography writing form lines and cross

structures, 4, 2, 1μm in size along the Au wire. The alignment marks are 80μm away from each other and at least 25μm away from the e-beam writing area to avoid any unwanted exposure of the e-beam resist during the alignment procedure. Fig. 3.11b shows a set of wires and e-beam lithography marks and Fig. 3.11c gives details of the 20μm Au wire with the circular structures to be written by the e-beam. After the standard optical lithography procedure was completed the wet etching of Au (using the standard gold etchant) and Ti (using a 5% solution of hydrofluoric acid, HF) were used to fabricate the Au transmission lines with contacts and alignment marks.

3.2.2 Electron beam lithography.

3.2.2.1 Physical and mathematical models of electron scattering.

A primary electron entering the resist or substrate, transfers part of its energy to the atomic electrons, resulting in their excitation, ionization and a generation of high-energy radiation [4-5]. Electron–electron collisions with a large energy transfer will generate secondary electrons with a kinetic energy ranging from near zero or up to half of the energy of the incident primary electrons. The slow secondary electrons (with energies 2-50eV) are not so important because they travel only a few nanometers from their position of generation. The exception is when a size of wanted structures and thin film thickness are within a range of a few nanometers. The fast secondary electrons with relatively low energy (for example, a primary 20 keV electron entering the resist generates a secondary electron with the energy of a few keV along its path) have a moderate influence on the spatial distribution of the energy deposition in the polymer

film or the substrate; their typical radius of influence is ~50nm. According to, Bethe's theory [5a-d], this secondary electron has approximately ten times more energy deposition efficiency per unit path length than the 20keV electron.. The secondary electrons can travel in a perpendicular direction to the primary electron path and this behavior of the secondary electron causes an additional spatial spread of the absorbed energy. This spread affects the spatial resolution in the electron lithography. In addition, backscattered electrons have lateral influence out to a radius of several microns and contribute significantly to the proximity effect.

3.2.2.2 Electron collisions.

An electron undergoes an angular deflection and energy loss when a succession of distinct scattering events affects the trajectory of the incident electron within the resist and the substrate. The angular distribution of the scattered electrons is dependent on the assumed Thomas-Fermi potential [4]

$$V(r) = (Ze^2 / r)\ exp\ (-0.745\ r\ Z^{1/3}/a_0) \qquad (3.1)$$

where Z is the atomic number of the element, r is the radius, a_0 is the Bohr radius. The Thomas-Fermi potential assumes that an incoming electron sees the atomic charge of the nucleus screened by the electron cloud of the atom. By using the atomic potential $V(r)$, the differential elastic cross section in the first Born approximation, is

$$d\sigma/d\Omega = Z_i(Z_i+1)e^4/(4m^2v^2(sin^2(\theta/2) + \alpha^2_i)^2) \qquad (3.2)$$

where θ is an angle, Z_i is the atomic number of the i-th element, m and v are the electron mass and velocity respectively, $\alpha_i = 2.33\ Z_i^{1/3}$, $E^{-1/2}$ is the atomic screening parameter, and E is the energy of the incident electron.

The electrons travel in straight lines (the mean free path) between the elastic scattering events with the energy loss. The continuous slowing down approximation formula, accordingly the Bethe energy loss theory, approximates the energy loss (per unit distance) as

$$dE/dx|_B = -2\pi e^4 \Sigma_i n_{ei} Z_i/E \ ln(aE/I_i) \qquad (3.3)$$

where n_{ei} is the density of the atomic electrons, $I \sim 1.15\ 10^{-2}$, *[keV]* is the mean excitation energy, and a=1.166 is a constant.

The Mott-Moller formula for the differential cross-section of the inelastic electron scattering (in the Born approximation, for non-relativistic electrons) is

$$d\sigma/d\varepsilon = (B/E)\ (\ 1/\varepsilon^2 + 1/(1-\varepsilon)^2 - 1/(\varepsilon(1-\varepsilon))\ ) \qquad (3.4)$$

where $\varepsilon = dE/E$ and $B = 2\pi e^4\ mv^2$. After the introduction of ε_c (the cut-off value for the energy transfer) the energy losses for the secondary electrons are given by

$$dE/dx|_S = \Sigma_i n_{ei} Z_i \int_{\varepsilon c}^{1/2} E\ \varepsilon\ (d\sigma/d\varepsilon)\ d\varepsilon . \qquad (3.5)$$

The trajectory of the secondary electrons can be calculated (by the Monte Carlo integration) from the formula

$$dE/dx|_{BS} = dE/dx|_B - dE/dx|_S . \qquad (3.6)$$

3.2.2.3 Proximity effect.

The description above gives a brief mathematical model of interactions on an atomic level. From an experimental point of view, the distribution of the deposited energy described by the two-Gaussian kernel (the point spread function) is valid for most substrates, and can be modified by adding a third Gaussian or an exponential function, for example, GaAs substrates. The function *K(r)* describing the distribution of

the energy in a 2-D resist layer (assuming a point source of electrons) is given by [1, 5b]

$$K(r) = (1/\pi(1+\eta))\,[(1/\alpha^2)\exp(-r^2/\alpha^2) + (\eta/\beta^2)\exp(-r^2/\beta^2)] \qquad (3.7)$$

where α and β are the forward and backward scattering parameters respectively, that define the beam broadening effects (the area of the energy deposition can be several times larger than the area directly hit by the primary electrons), and $\eta = I_f/I_b$ is the ratio of the electron densities coming from the forward I_f and the backward I_b scattering. These three parameters can be derived from experiment or from Monte Carlo simulations. After the exposure of a finite area A by the electron distribution $D(r)$ the final dose (absorbed energy) $Q(r_0)$ can be expressed as

$$Q(r_0) = \int\int_A K(r_0 - r)\, D(r)\, dr^2 \qquad (3.8)$$

Several models were developed to extract proximity parameters from experiments as described, for example, in [21-38]. Most of them work well for standard patterns in the poly(methylmetacrylate) (PMMA)-based resists in the 2D approximation. The point exposure test can be used with small structures [24] or with different models for chemically amplified resists [34]. For thicker 3D resists or low energies of electron beam, newer models were developed [34-38]. The "intra-proximity effect" reflects the deformations of an exposed structure (for example a wide line or a rectangle).

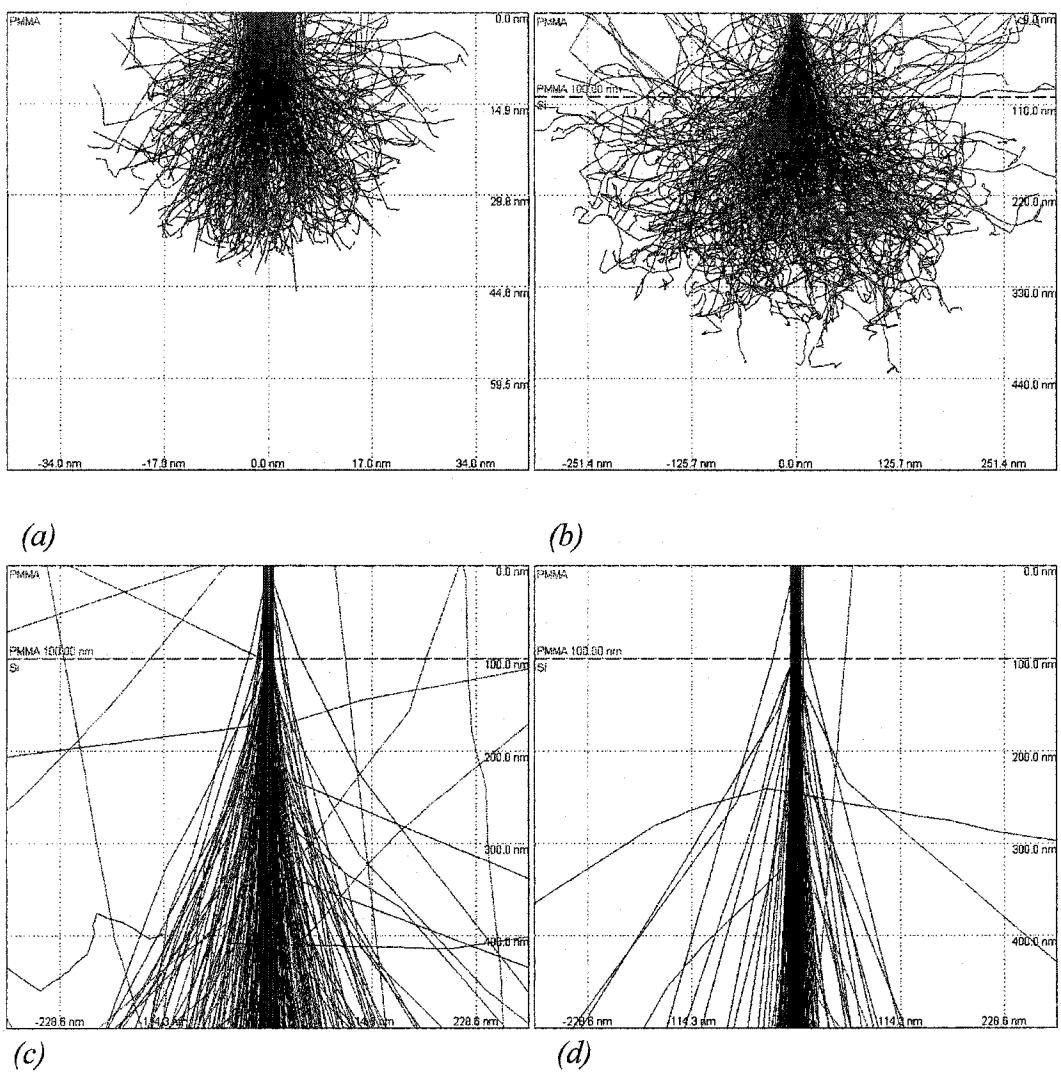

Fig. 3.12 The Monte Carlo simulations (the 10nm beam diameter) with Casino2 simulator [9]. The electron trajectories for energies 1keV (a), 5keV (b), 40kV (c) and 100keV (d) are shown (100nm thick PMMA resist, $C_5O_2H_8$ with the density 1.188 g/cm^3) on Si substrate (the density 2.33 g/cm^3). In (a) the electrons do not have enough energy to penetrate the resist, the influence of the substrate is negligible and the resolution in a resist layer is limited by the fast secondary electrons. The plots in (b) and (c) show significant influence from the backscattered electrons. The highly energized primary electrons do penetrate very deeply into the substrate as shown in (d).

The inter-proximity effect expresses the common influence (deformations) between two or more separated geometrical patterns. Gaussian blurring (via intra- and inter-proximity effects) is a major obstacle when writing complicated patterns onto a substrate that produces a strong backscattering at high electron energies (~30-40kV for example). The dependence (3.8) is linear and time-independent unless heating effects come into account [39]. In the latter case, the time sequence of individual writing events plays an important role because the temperature of the substrate/resist system is changed during writing and, hence, the sensitivity of the resist is (significantly in some cases) increased. The temperature change is large only at very high writing currents (by several orders of magnitude higher than currents used in the current SEM-based e-beam exposures).

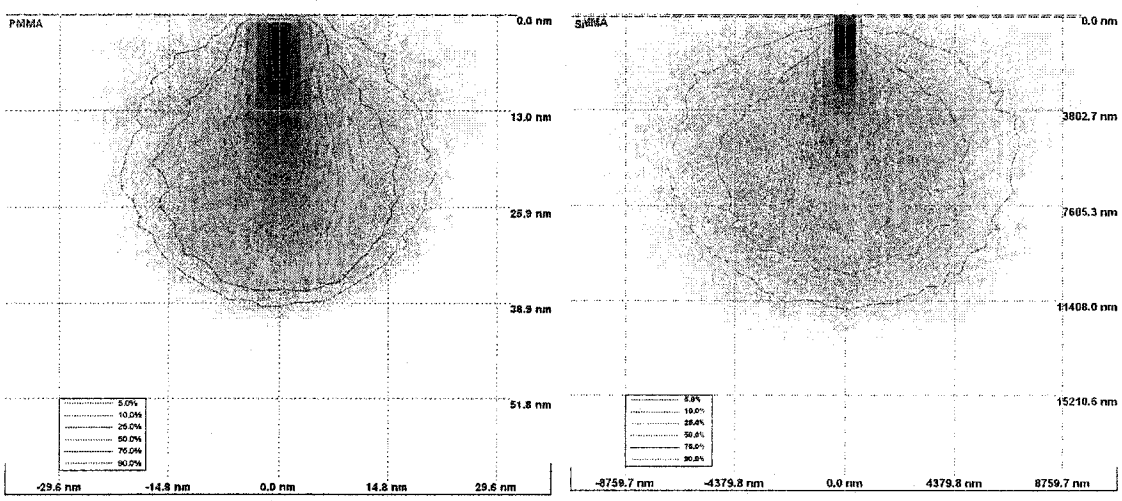

(a) *(b)*

Fig. 3.13 The Monte Carlo simulations of an energy deposition at 1keV (a) and 40keV (b) in 100nm thick PMMA on Si substrate. The area (volume) where the energy is deposited is significantly smaller at a lower electron energy causing weaker backscattering and better spatial resolution.

Backscattering causes sharp features such as corners on the desired pattern to become rounded, and gaps and linewidths can change or disappear. The exposure at low electron energy (~1keV), the energy of backscattered electrons is small to cause significant chemical changes in the resist. Fig. 3.12 shows the plots of the Monte Carlo simulations using the Casino2 simulator [9] in PMMA on silicon at various electron energies. The radius of the backscattered electrons is large, the energy is deposited uniformly over a large area and the proximity effect is reduced. For this reason, the very low and very high-voltage electron sources offer the best resolution.

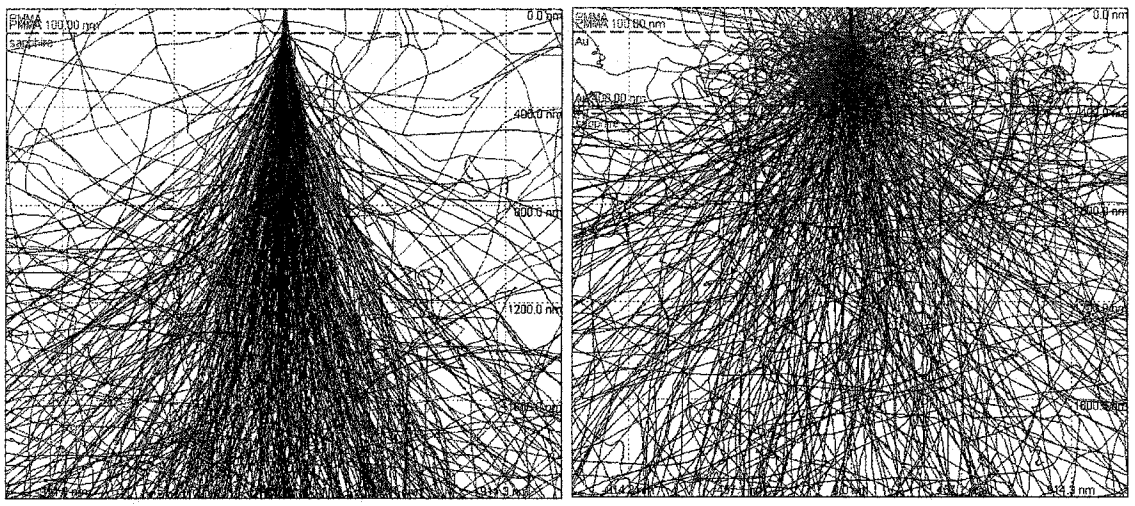

(a) *(b)*

Fig. 3.14 The Monte Carlo simulations show the difference between the electron scattering in (a) PMMA on sapphire (density 3.98 g/cm^3) and (b) PMMA on Ti/Au (the thickness 30/300nm and the density 4.6 / 19.3g/cm^3). The backscattering from the Au layer is much stronger than the one from the sapphire because of the heavier Au atoms, which explains why the (experimental) exposure doses required to open the resist on the sapphire are approximately 1.5x larger than the doses required for the gold substrate.

Fig. 3.13 shows the significant differences in the energy deposition at 1 and 40 keV. Fig. 3.14 gives a comparison of the backscattering from the sapphire and the gold substrates at 40keV. Other non-PMMA resists with much better sensitivities (but usually accompanied by worse spatial resolution) are used for the e-beam patterning [10-20]. A wide spectrum of processing procedures working with PMMA-based resists exist to improve the properties of the thin film resist structures, such as the long pre-bake at high temperatures or the ultrasonically-assisted development [40-44].

3.2.2.4 SEM imaging and exposure parameters.

In this section, a brief summary of the influences of different SEM parameters on the SEM imaging and the e-beam exposure (related to the SEM LEO440 and NPGS) is summarized [1, 4, 88]. By changing one SEM (e-beam writing system) parameter to improve the quality of an image (writing), another property of the system is changed. Hence, often a compromise is required when looking for an optimal SEM alignment. Below are examples of relations between important SEM parameters (the opposite values of SEM parameters have the opposite consequences):

- A short *working distance* gives a higher *resolution* and a shorter *focus depth*.
- A low *acceleration voltage* causes a shorter *penetration depth*, less *damage*, a weaker *charging* and *edge effect*, a lower *resolution* and a higher *resist sensitivity*.
- A small *aperture* provides a lower *current* (and less heating), a higher *depth of focus*, a higher *resolution* and higher *noise*.

The optimized exposure parameters (for the exposure of fine features with smooth

edges of the exposed structures and a shorter writing time) affect each other.

- A high *acceleration voltage* e.g. 40keV provides higher *resolution* but stronger *backscattering*, a lower *resist sensitivity* and longer *writing time*.
- A small (5-10pA) *writing current* (that is proportional to the *beam size*) has a larger *depth of focus* and causes weaker *Coulomb interactions* but requires a longer *writing time*.
- A small *writing field size* (~100μm and less) produces better *resolution* and *stitching* precision but requires a bigger number of writing fields for larger patterns.
- For a small *step size* (~10nm), the recommended value is less than 20% of the minimal feature size causes a *longer writing time*.
- A perfect *beam alignment* requires careful *focusing*, an *astigmatism* correction and an *aperture* alignment.
- A proper *settling time* for 'best line' *smoothness* causes a longer *writing time*.
- the numerical rounding during exposure data calculations affects the proper ratio of the desired *structure size* and the *writing step size*, so a careful data design is required.
- A small overall *exposure time* requires a short *settling* time, a *meander* mode, a higher writing *current*, a lower *acceleration voltage*, larger *writing fields* and properly designed *pattern* data.

For a good placement and stitching of the structures, a reasonable waiting time after the stage has stopped is recommended. In addition, the stability of the high voltage source (EHT), the gun and the electron optics can significantly affect the resulting

patterns. Exposure to a thick resist causes a larger undercut because of the forward scattering. The overexposure in time and the overdevelopment (respectively to the time and the temperature of the development bath) are also sources of distorted structures.

3.3 Microfabrication and experimental results.

The major procedures used in the microfabrication process were the lithographic patterning and the lift-off. Other ways exist in which the optical and electron beam lithography are followed by other etching methods based on the reactive-ion etching or ion-milling [77-87]. Some of these approaches require chlorine-based mixtures (not available in the microfabrication facility at this time) to improve etching rate of low volatile magnetic (Permalloy) materials.

3.3.1 Tests structures for critical doses.

The important part of the e-beam exposure is a determination of a sufficient dose required for the full opening of the exposed area (after the development process). A critical dose is the dose when macromolecular bonds (hit by the electrons) are broken or cross-linked (the bond scission and cross-linking exist in resists with positive and negative tonality respectively).

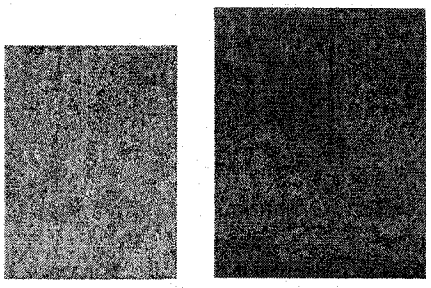

Fig. 3.15 The test for a critical dose for the 10μm square (on the left) in PMMA 950k on Si substrate. The doses were in the range from 230μC/cm^2 to 290μC/cm^2. The resulting critical dose was 280μC/cm^2. The correctly exposed squares are at the bottom of the array. On the picture on the right is the exposure test in PMMA 950k on Si with 15nm Permalloy film exposed with the doses from 140μC/cm^2 to 280μC/cm^2. The resulting critical dose is 255μC/cm^2. A stronger backscattering from Ni atoms is lowering the required effective dose. The critical doses on silicon, sapphire and gold are in Appendix 4.

The liquid developer can completely remove the resist and open the exposed area in positive resist such as PMMA. The value of the critical dose depends on the acceleration voltage, the writing conditions and the composition of the substrate and resists. The important condition to avoid the resist swelling and the narrow line closure is the sufficiently baked resist. The resist swelling and narrow line closures are caused by mechanical properties of insufficiently baked resist film and by the influence of strong intermolecular forces in sub-10nm fine structures [60b]. The dry and hard resist film has also a good adhesion to the substrate. The hard baked resist requires a longer etch time during the lift-off.

The typical writing conditions for the 120nm thick PMMA resist (pre-baked on hotplate for 5 minutes at 180°C, covered by 5nm thick gold layer on the top if non-conductive sapphire substrates) were:

- The magnification 1000X, the EHT voltage 40kV and the writing current 10pA.

- The working distance (the focus) ~7mm.
- The Center-to-Center Distance (ccd), the smallest distance between two neighboring points measured from the center of the Gaussian e-beam spot, and Line-to-Line Spacing (lls) approx. 10nm (the smallest value for NPGS 100μm writing field).
- The typical development of the exposed resist (in MIBK:IPA 1:3) for 40sec and additional two baths (in IPA and water) for 20sec were followed by the post-bake on the hotplate for ~2min at 100°C.

A typical test pattern with a matrix of 10μm squares exposed with different doses is in Fig. 3.15 (with details about the exposure). Such test writings were regularly exposed and critical doses were determined for each new combination of substrate, resist and parameters of the SEM and the data design.

Fig. 3.16 shows the differences in structure dimensions fabricated on different films (using two layer resist for a better undercut of the resist, and collimated deposition, see 3.1.2.1). After the development process, the areas with sufficient level of the deposited energy are clearly recognized (brighter squares on the top image). A stronger backscattering from the Ti/Au layers (see the Monte Carlo simulations in Fig. 3.14) results in the sufficiently exposed resist and the right size of the Permalloy structures on the gold film. However, the edges of the Permalloy squares on sapphire are rounded, witnessing that the exposure dose was low. The asymmetry of the middle element (in the bottom image) is the consequence of the resist thickness non-uniformity. The non-uniformity at that area is caused by the change of the height at boundary between the sapphire and the 300nm thick gold wire.

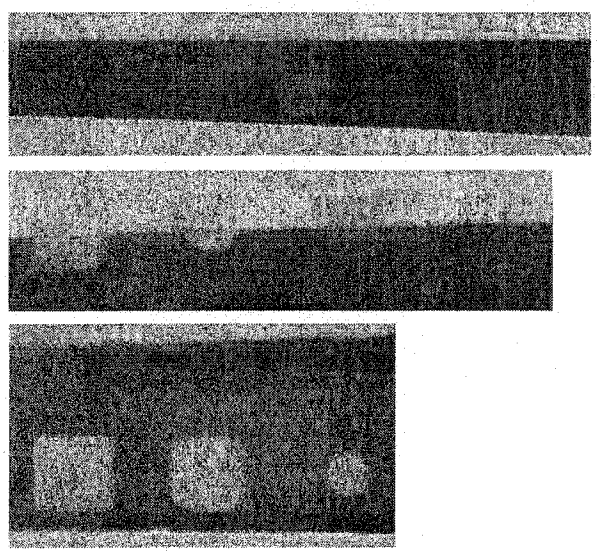

Fig. 3.16 The study of critical doses on sapphire with and without 30/300nm Ti/Au wires (bright in the image). The two-layer resist system was composed of the copolymer-EL6, 130nm thick and PMMA950k-C, 100nm thick. In the middle and bottom, the images are the same data patterns after the deposition of 15nm of Permalloy (the gray patterns) and the lift-off. The critical doses (for a mix of copolymer and PMMA950kC) are 95μC/cm^2 for gold and 170μC/cm^2 for sapphire. The images of the exposed areas before and after the lift-off clearly show the consequence of the different electron scattering and the proximity effect in different materials.

The comparison of the dose values for a single resist layers of the copolymer and the PMMA950k shows that the top PMMA resist layer penetrated the first copolymer layer during the spinning procedure. Hence, the higher effective sensitivity of the 2-layer resist system is the result. This effect of mixing was removed once PMMA in Anisole instead in Chlorobenzene was used.

The composition of the substrate material is important for the exposure process. Heavier atoms cause the backscattering of electrons into wider angle; the backward constant β has values in range up to several micrometers. This is the major contribution to the resist irradiation because the forward parameter α has a small value of the order

50nm. Exposing appropriate arrays of small elements (lines, circles, donuts) with a variable dose and measuring the lateral dimensions, the proximity parameters can be found as a numerical fit using expressions (3.7) and (3.8). Such a test array of rectangles is shown in Fig. 3.17. A similar point-like test exposure (an array of dots with increasing doses resulting in the increasing diameter of the dots) was also done. This kind of test offers an opportunity to measure curves proportional to the point spread function *K(r)*. Nevertheless, it has the disadvantage because the high dose required and the heating effects could change the resist sensitivity for different elements of the test array.

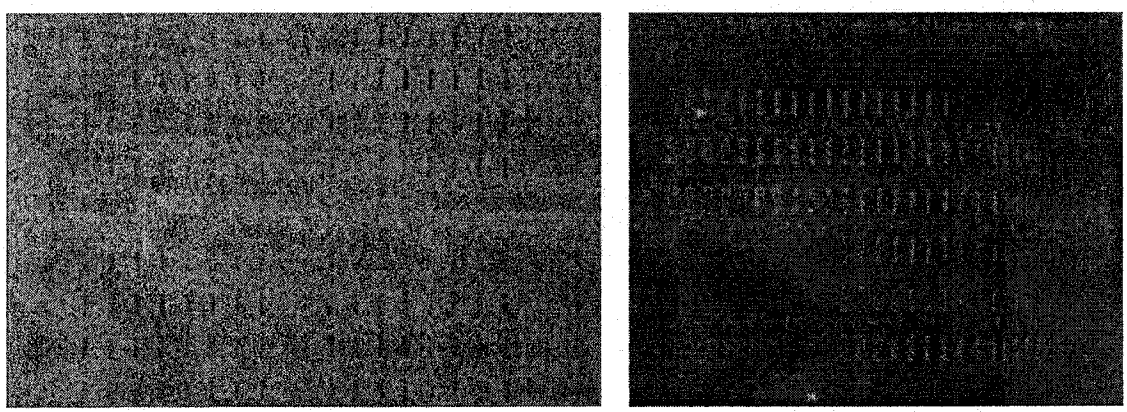

Fig. 3.17 The test structures, on the left the 160nm of PMMA950k on sapphire with gold. On the right is the test pattern on the silicon with the gold and the copolymer. This test was exposed as the matrix of 5μm x W rectangles (W goes from 30nm to 950nm) with doses from 53.4μC/cm^2 (10μsec, 5pA) in the 1st top row to 935μC/cm^2 (175μsec, 5pA) in the bottom 7th row. The numbers are 2μm high (designed as "zero width" lines or a single beam pass) written with line dose 4.985nC/cm (482.1μsec) resulting in 200nm linewidths.

The linewidths and diameter measurements are lengthy and several resist combinations were tested to find the proper one for a good lift-off. For this reason the determination of the proximity parameters has not been finished. It is a common way to write a matrix of the same patterns with different doses and choose the correct dose, which gives the right dimensions of the structures. An example of the line pattern (with a constant dose for each row and with decreasing designed linewidths from left to right) for proximity parameter determination is in Fig. 3.17.

3.3.2 Rectangular Permalloy structures.

The lift-off process was the final procedure of the fabrication process. This process was realized using the Acetone (preferred) or Acryl Striper baths with mild manual agitation at the room temperature ~22°C for 2min (or more if needed). It was followed by the ultrasonic bath, if the thin film did not peel off after several minutes. The Acryl Striper is very strong solvent and in 3 hours was able to completely dissolve 15nm thick sputtered Permalloy film. This property of the Acryl striper helped to finish the lift-off relatively quickly (in 3-4 minutes), however, the Acetone has been later used for the lift-off process. The resistance of the Permalloy film was dependent on the properties of the Permalloy sputtering target. Only sputtering from the specific Permalloy target (PureTech Inc.) produced thin magnetic films sufficiently resistant respectively to the "etching" in the Acryl Striper bath.

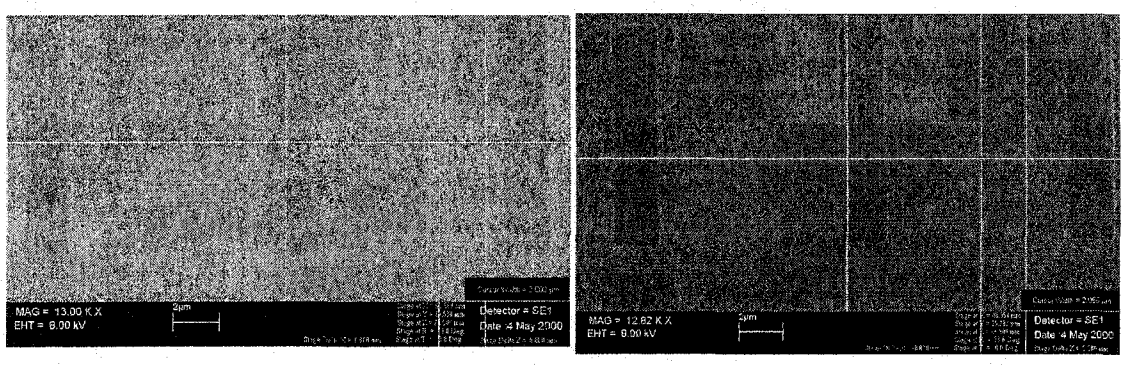

Fig. 3.18 The e-beam exposure in the 150nm thick PMMA950k on sapphire with the Ti/Au film with the doses 280-320μC/cm^2. The designed patterns are identical but Permalloy thin film deposition processes are different. The DC magnetron sputtering was used on the left and the e-beam evaporation on the right. The lift-off produced glowing edges (burrs). The development time in MIBK: IPA was 15sec.

Magnetic films sputtered from the Angstrom's Permalloy target had very weak adhesion to the substrate and were dissolved in the Acryl striper bath in approx.30 min.

First magnetic structures were produced by a lift-off from a single layer of the PMMA 950k resist, as shown in Fig. 3.18. The profile of a typically 100-150nm thick resist had not the right undercut and the magnetic material covered the resist walls during the deposition process.

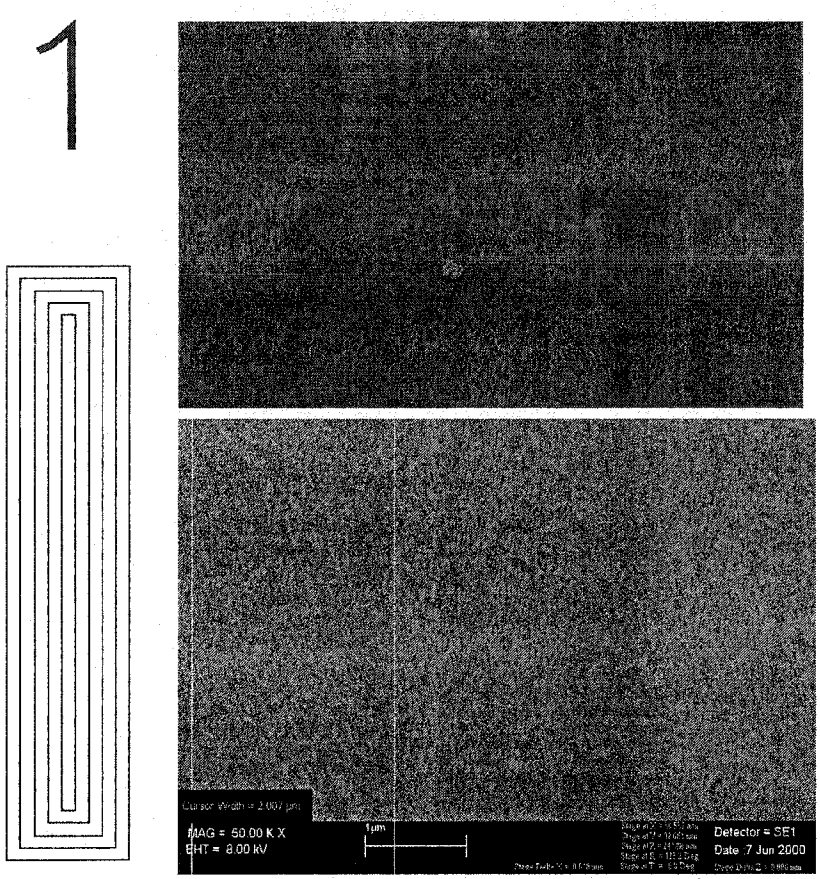

Fig. 3.19 An example of the data design is on the left. On the right, top image is the array of rectangles and on the bottom image is the detail of a single structure. The "burrs" were significantly lower. The doses for the inner and outer lines were 2.991 nC/cm^2 and 3.49nC/cm^2 respectively. The writing current was 10pA. The exposure was realized on sapphire with Ti/Au and PMMA950k 150nm thick. The development time in MIBK : IPA was 15sec.

The use of the lift-off bath with the ultrasonic agitation (in Acetone or in Acryl Striper) helped to finish the successful lifting of the magnetic film. However, the edges of the magnetic structures had "burrs" [48] (residual magnetic material at the edges of the magnetic element rising high above the surface of the sputtered film). The change in the geometrical data design (Fig. 3.19 left) and the new exposure dosage with a better collimation of the sputtering beam helped decrease the amount of "burrs" (see sputtering

in the Section 3.1.2). The 10x2μm Permalloy rectangles are shown in Figs. 3.19 and 3.20. The new design had the central part of the structure separated from the boundary parts. All lines were exposed using a single pass beam.

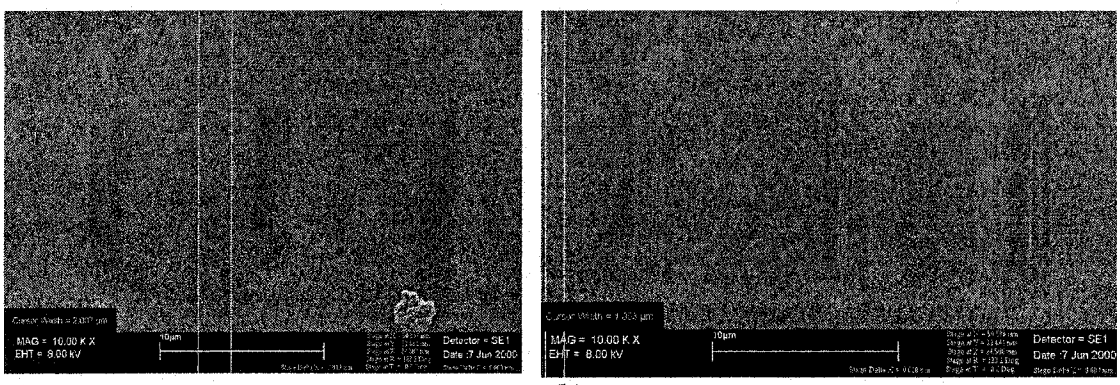

(a) *(b)*

Fig. 3.20 The Permalloy structures in (a) and (b). For the inner lines the doses were 2.992nC/cm^2 in (a) and 1.994nC/cm^2 in (b). For the boundary lines the doses were (from left to right) 3.988, 4.487, 4.985nC/cm^2 for (a) and 5.484, 5.982, 7.478nC/cm^2 in (b). The structures in (b) show the underexposed line structure of the inner areas. The boundary of the rectangle was written by the single line writing. This approach had to minimize the proximity effect and increase the undercut at the edges of the element. The numbers were written as 100nm wide lines (0.997nC/cm^2) resulting in 150nm linewidths. The development time was 15sec.

This approach came from the experimental results that the lift-off of the very narrow (single pass) line was good (the linewidths ~50-70nm) and the structure had no burrs (the evidence of the sufficient undercut of the resist). Nevertheless, the exposures into a single layer resist (following by the lift-off) were complicated and did not provide burrs-less results reliably. The two-layer resist system was chosen to transfer the patterns into

the magnetic thin film.

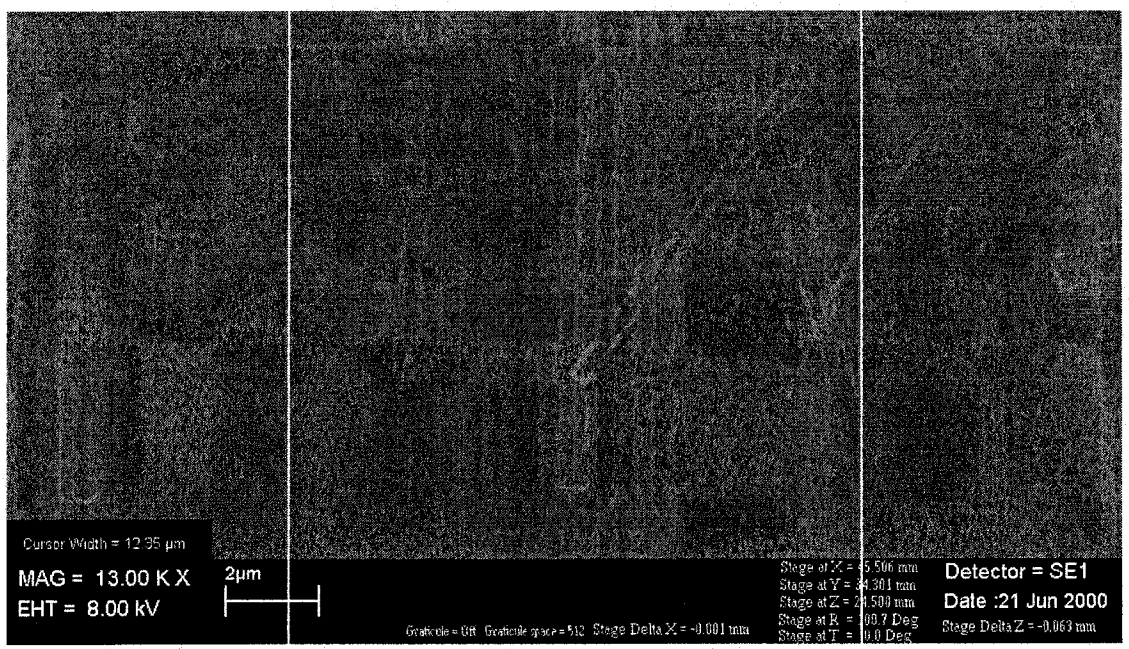

Fig. 3.21 The fabrication of "free" Permalloy wires. The patterns and exposure parameters are similar as shown in Fig. 3.20. The resist was underexposed and after the lift-off the single 100nm wide, 10μm long, 15nm thick Permalloy wires (both closed and open) were left stuck on the sapphire substrate.

3.3.3 Circular Permalloy structures.

The study of fabrication of Permalloy dots in arrays with varying diameter and period is shown in Figs. 3.22 - 3.24 with size/period ratios 125/200nm, 183/400nm and 400/800nm. The matrix of dots in Fig.3.22 was designed as an exposure of the filled rectangle with relatively large step size (*ccd=lls=400nm and 200nm).*

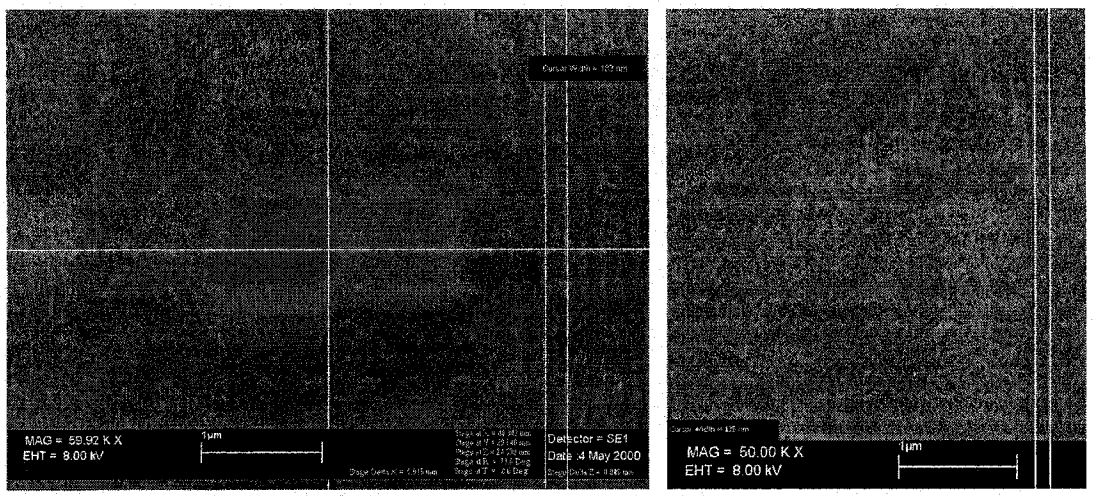

(a) (b)

Fig. 3.22 The Permalloy dots in rectangular arrays. In (a) and (b) are the arrays written as multiples of 10µm squares with large writing step ccd/lls (a point-like exposure with the current 10pA and the voltage 40kV). The array of Permalloy dots (a) has the period 400nm. The dot diameter designed/measured was 200/183nm respectively and the exposure dose was 298µC/cm^2. This magnetic film was deposited by the e-beam evaporation. Burrs are almost completely missing. The period of the array in (b) was 200nm and the dot diameter 125nm.

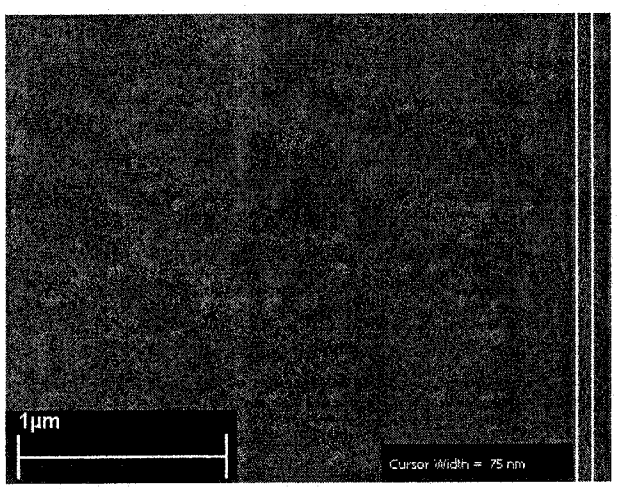

Fig. 3.23 The Permalloy array with the period/diameter 150nm/75nm. The exposure data designed as multiple of four rectangles (written at the same place) with the effective dose 88.276µC/cm^2. The sapphire substrate with Ti/Au thin films was covered with 160nm thick PMMA 950k resist. The development time was 15sec.

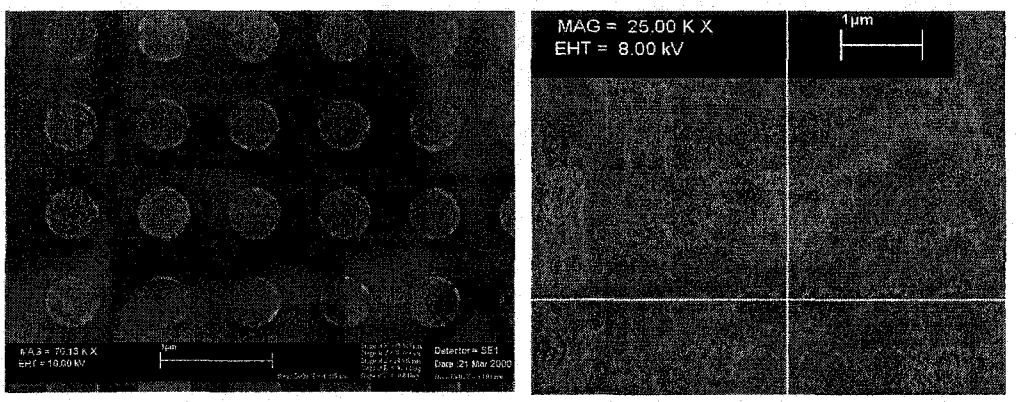

Fig. 3.24 The arrays of 15nm thick Nickel discs. The dots in (a) have diameter 450nm (designed as 200nm wide arcs with 400nm diameter) and the period is 800nm. The deposition was done by the e-beam evaporation. The exposure dose on the Si substrate was 596.4µC/cm^2 at the current 5pA. In (b) is the 5µm large square array of 400nm in diameter dots. The dots were designed as 100nm wide arc lines with the diameter200nm and the period 800nm resulting in the dot diameter 550nm (the exact dose is unknown). The proximity effect causes the size of dots in the center of the array to be larger and the profile of 160nm PMMA950k resist on the sapphire with Ti/Au layer has worse undercut and, hence, stronger "burrs" than the dots close the boundary of the array.

Another way how to adjust the profile of the resist is to change the time of the development process (from typical 40-60sec to 15sec long bath in MIBK:IPA). This way the undercut of the single resist layer was improved as documented in [48]. In our experiments, the improvement of the lift-off (smaller "burrs") was not proved. The collimation of the sputtering beam was still low that overrides the influence of the improved undercut by the shorter development time. In addition, the substrate in [48] was GaAs with stronger backscattering than the one from our sapphire (Al_2O_3).

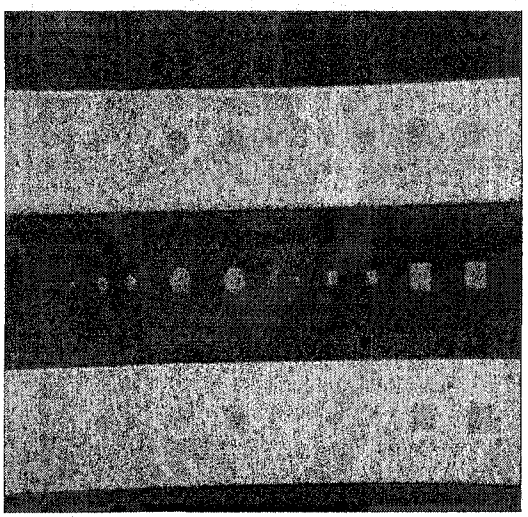

Fig. 3.25 The Permalloy squares and circles on the 20μm wide Ti/Au wire and on the sapphire in the 20μm gap between two yellow wires. The sizes are 1, 2 and 4μm for the circles and the squares (both with and without the hole in the center).

The designed diameter of the pinhole on the sapphire was in the range from 200nm in the smallest 1μm element to 250nm in the largest 4μm one. The area doses for 4,2,1μm elements were 320, 340, 360μC/cm^2 respectively at the 5pA writing current into the copolymer EL6 + PMMA 950k A2 double resist system. The measured diameter of the hole in the 4μm square was 240nm. The diameter and the area doses for 1, 2, 4μm large elements on Ti/Au wire were 300, 375, 375nm and 240, 215, 195μC/cm^2 respectively. The development time in MIBK: IPA was 40sec.

3.3.4 ***Permalloy structures using double layer resist system.***

After lengthy lift-off tests with single resist layers the double layer resist system was used to pattern the thin film magnetic structures. The first (bottom) layer was the copolymer EL6 130nm thick. The second (the defining high resolution thin film) resist was ~70nm thick PMMA 950k. The sensitivity of the copolymer (the 1st layer) was higher than of the 2nd PMMA resist layer and, after development, a larger portion of the copolymer was removed creating sufficient undercut respectively to the 2nd layer of

PMMA. The results from the two-layer resist system are shown in Fig. 3.26.

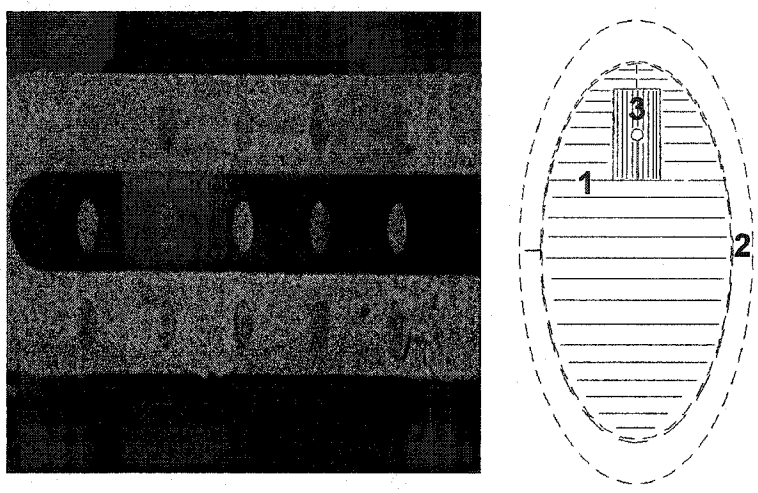

Fig. 3.26 The set of Py ellipses is shown with the sizes 2.5x5μm and the hole having 250nm in diameter. The designed pattern, shown on the right, was written into 2-layer resist, a mix of copolymer+PMMA950k-C with the structured exposure doses (on the sapphire) (1)-198μC, (2)-180μC and (3)-180μC.

The top resist, dissolved in the Chlorobenzene, penetrated the bottom resist and a thick intermediate layer of the resist mixture was created. This resist mixture had changed the sensitivity. In addition, the thickness of that mixed layer is hard to control. Despite this obstacle, the Permalloy elements with various shapes and sizes on both the gold wires and the sapphires were fabricated. The donuts and squares are shown in Fig. 3.27 and small lines and dots in Fig. 3.28 with exact details about the exposure parameters.

The use of PMMA solved in Anisole is recommended because the Anisole is weak solvent and its penetration is negligible. The experiments with the 2-layer system PMMA 495k and PMMA 950k (both in Chlorobenzene) did not give good lift-off results. However, the use of the PMMA49k and PMMA950k in Anisole is still promising, because the result was affected by the strong mixing of the two resists.

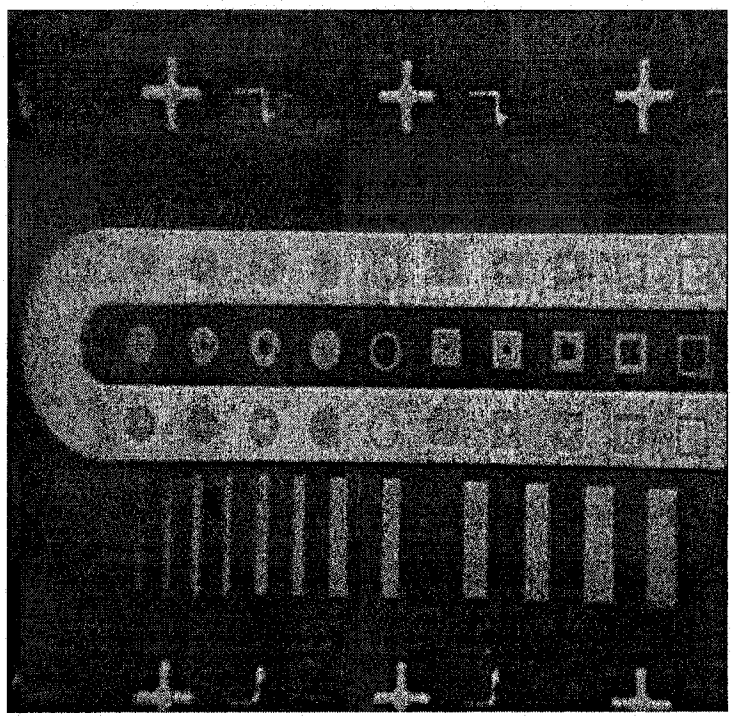

Fig. 3.27 The set of 10μm large donuts and squares with window size 8, 6, 4, 2 and 1μm from left is shown. The actual structure outer/inner dimensions are 9.9/8.05μm, 9.85/6.2μm, 9.75/4.3μm, 9.45/2.4μm, 9.25/1.6μm for donuts and 9.85/8.1μm, 9.8/6.2μm, 9.7/4.4μm, 9.45/2.4μm, 9.25/1.65μm for squares respectively. The doses for a mix of copolymer+PMMA950k-C for the gold and the sapphire were in the range from 112 to 153μC/cm^2 and from 185 to 263μC/cm^2 respectively. The single pass lines (with the line dose 0.3nC/cm) featured the edges of each of the elements. The missing 6μm window in one of the donut is caused by an error in the data file.

The fabrication of the rectangular and circular structures on sapphire with and without Ti/Au was done using both mixing and non-mixing resist systems. The rectangular and circular Permalloy structures on the sapphire and the gold wire, which were used in magneto-optical measurements, are shown in the SEM scanning on Fig. 3.29. The details about the parameters for the e-beam writing are in the Fig. 3.30.

Fig. 3.28 The set of the lines and rectangles (height/width ratio was 5:1) and circles with sizes 2, 1, 0.5, 0.25, 0.125, 0.1μm, 80, 60, 50nm, and less. The doses for a mix of the copolymer and PMMA 950k-C were in the range from 228μC/cm^2 to 596μC/cm^2 on sapphire. The numbers (designed as 100nm wide lines) and triangular areas were written with doses 348μC/cm^2 and 497μC/cm^2 respectively.

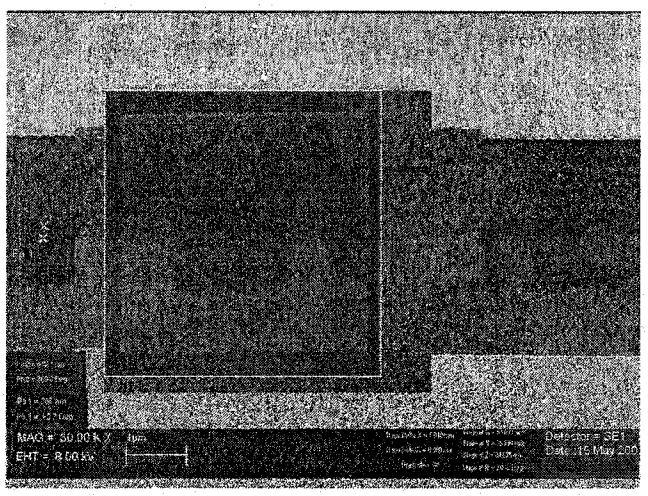

Fig. 3.29 The SEM image of the Permalloy square on sapphire. The 4μm square with 240nm in diameter hole in the center was the magnetic element used in magneto-optical Kerr measurements.

The images of various ellipses and ellipse-related structures ("bullets") are shown in Fig 3.31. The Permalloy elements on the sapphire and on the gold wire were prepared using the double layer resist systems.

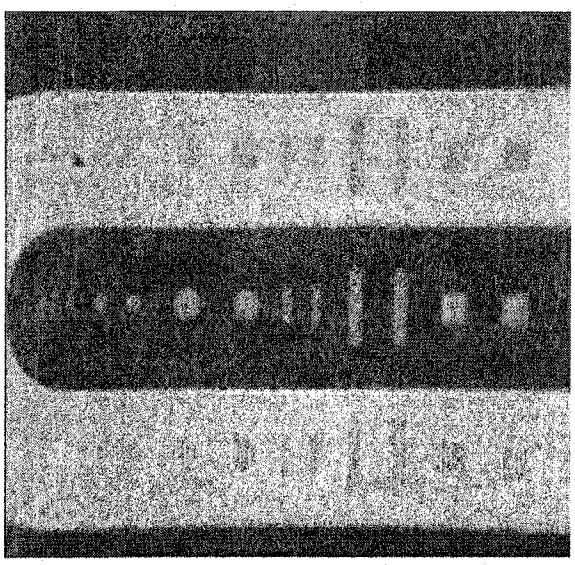

Fig. 3.30 The optical images of the Permalloy structures. For the non-mixed 2-layer resist (copolymer +PMMA950k-A2) on sapphire the designed exposure parameters for 4μm squares, circles were (size/defect-diameter/dose) 3.85μm /380nm/342.4 μC/cm^2. For the 2μm and 1μm elements the parameters were 1.95μm/330nm/363.8μC/cm^2 and 0.98μm/300nm/ 385.2μC/cm^2 respectively. On the Ti/Au wires the corresponding parameters were (size/defect-diameter/dose) were 3.85μm/380nm/204μC/cm^2, 1.95μm/330nm/224μC/cm^2 and 0.98μm/300nm/255μC/cm^2 respectively.

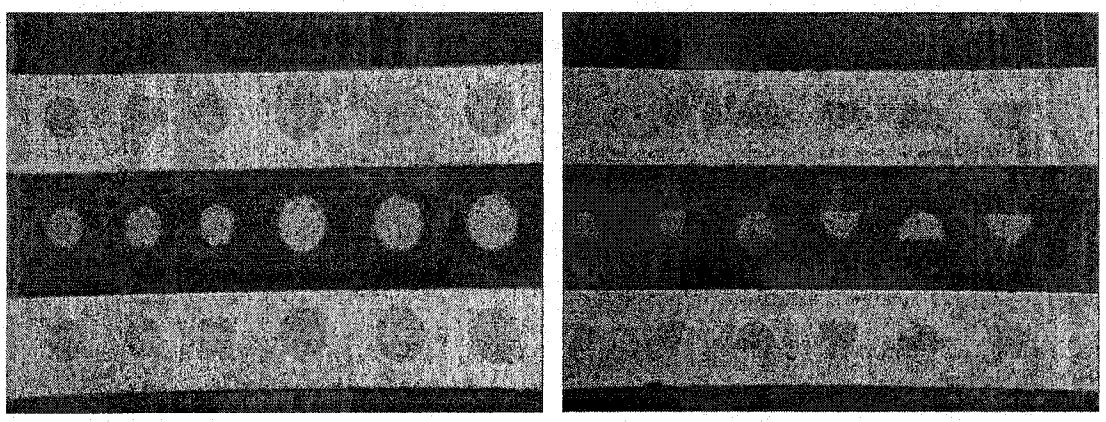

(a) *(b)*

Fig. 3.31 The ellipses with and without the holes in (a) and half-ellipses or "bullets" in the part (b). The exposure parameters for structures in (a) were 190/180/180μC/cm^2, 192/183/183μC/cm^2 and 188.4/183.5/174μC/cm^2 for 10x8.66μm/450nm, 5x4.33μm/450nm and 5x2.5μm/270nm ellipse size/defect size respectively. The doses are for the outer, inner and (around) defect parts of the ellipse (see Fig. 3.24b) (for exposure on sapphire+Ti/Au with non-mixed 2-layer resist system). The same structures on sapphire had doses 288/282/282μC/cm^2, 290/285/285μC/cm^{2}and 315/300/300μC/cm^2. In (b) are the bullets 10x8.6μm, 10x7μm and 10x5μm with outer/inner doses 187/177μC/cm^2 for large, 193/183μC/cm^2 for medium and 197/187μC/cm^2 for small sized elements respectively. The writing current and development time were 5pA and 40sec respectively.

3.3.5 *Narrow lines and arrays of dots.*

Various test patterns were designed to test the limits of the e-beam writing system (relative to the materials and methods used, and other limits). One of such testing pattern, how small structures can be fabricated, was the university logo. The result of such single pass beam exposure is on Fig. 3.32. In this complex pattern, various narrow lines far and close each other are shown. The structures are in resist (after development lift-off) and they document 50nm and sub-50nm capability, Fig. 3.33, of the used SEM+NPGS system writing capability.

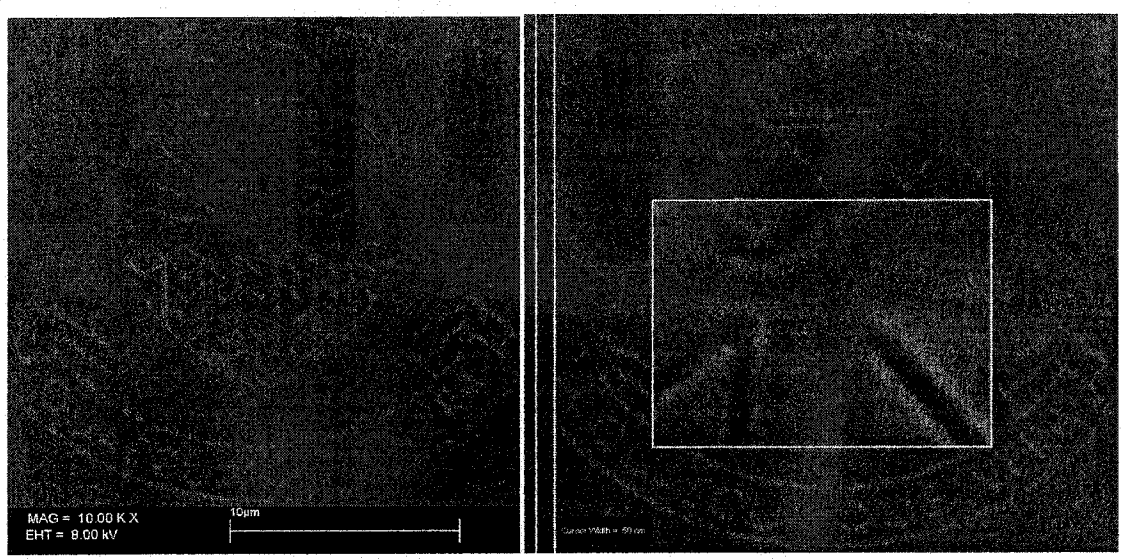

(a) *(b)*

Fig. 3.32 The narrow lines and small areas on the UofA logo pattern. The exposure was realized on sapphire with Ti/Au and 160nm PMMA950k resist. The linewidths were 50nm (with the line dose 1.75nC/cm) and 100nm (2.625nC/cm). All areas where the crossing lines created the overlaps, or were mistakenly doubled as reveals the left central part of (a), the overdose is clearly visible. The development time in MIBK: IPA was 15sec.

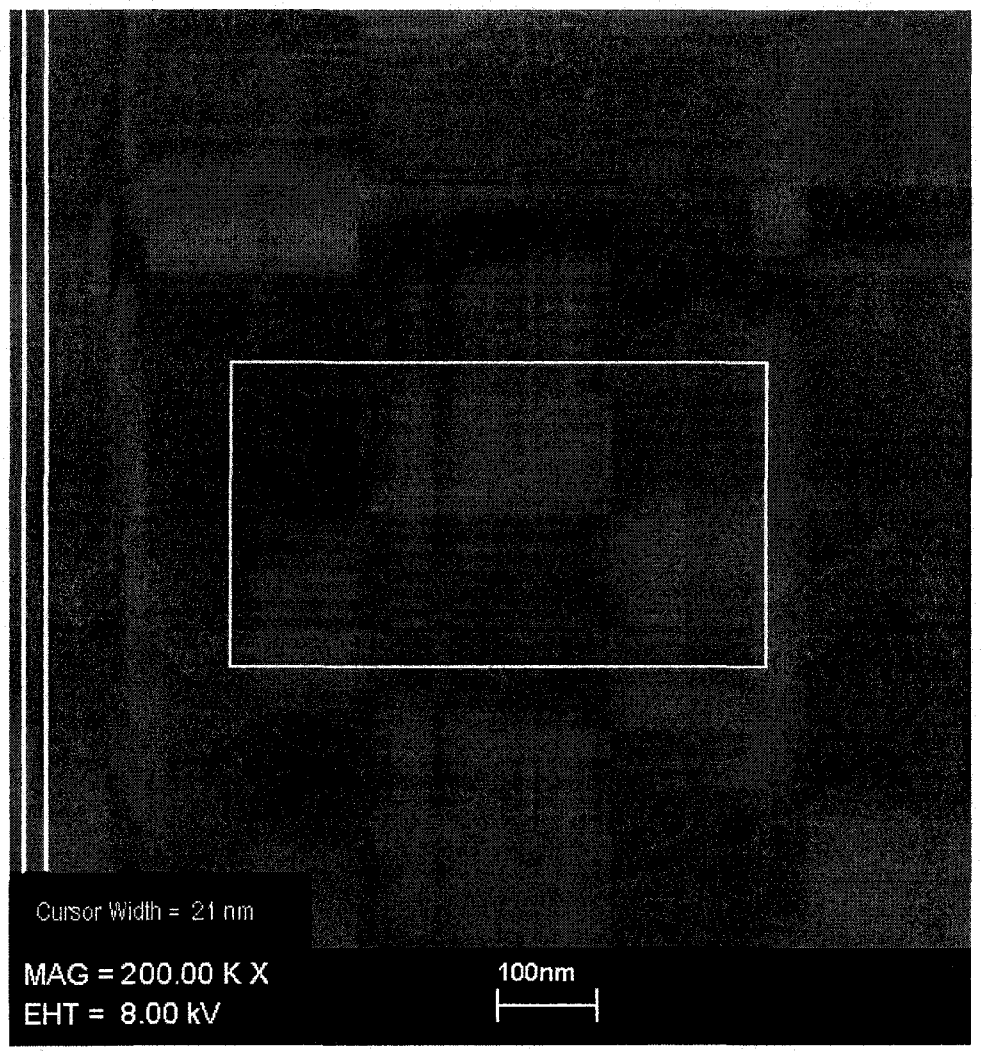

Fig. 3.33 The picture shows the result of the lift-off of the Permalloy film. The mix of copolymer + PMMA950k-C on Si was exposed by the line dose 2.094nC/cm. The lift-off of the Permalloy in some areas has not been fully completed. The example is seen in the zoom window or in some small closed geometrical patterns e.g. the letters at the bottom.

The two-layer resist method is still a promising approach to the 50nm features when non-mixing resists are used. In addition, the application of LOR (Microchem) resist (as the bottom resist layer) and the ultrasonically assisted lift-off (at a higher temperature of

the Acetone bath) offer an improvement of the lift-off process.

The SEM image in Fig. 3.34 displays the set of lines and dots (in resist) with the description and triangular marks. The pattern includes the insert with details of the rare writing error, when a part of designed data were decomposed into long matrix of dots covering area more than 100μm long.

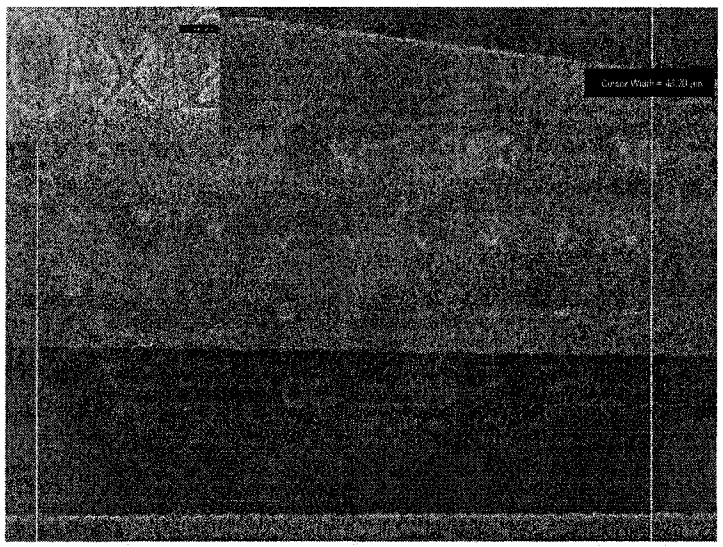

Fig. 3.34 The set of rectangles (the height/width ratio 5:1) with the sizes 2, 1, 0.5, 0.25, 0.125, 0.1μm, 80, 60, 50nm, and less. The SEM image of the pattern includes the insert with details of a writing error.

For non-mix resist system of copolymer + PMMA950k-A2 the 5pA writing current and the 40sec development time were used. The doses on gold for rectangles 2μm, 1μm, 500nm, 250nm, 125nm, 100nm, 80nm, 60nm, 50nm and 100nm text line structures were 210, 240, 250, 300, 350, 370, 400μC/cm^2, 550nC/cm, 0.68nC/cm and 310μC/cm^2 respectively. The doses on sapphire were approx. 1.5x higher.

Square arrays of holes, on the sapphire (w/ and w/o Ti/Au film) after sputtered 15nm Permalloy film, are displayed in Fig. 3.35. The square has size 5x5μm^2 and the period of each matrix is 100nm with the dot diameter 50nm or less. The array in the middle and the insert below show the consequences of the inner proximity effect.

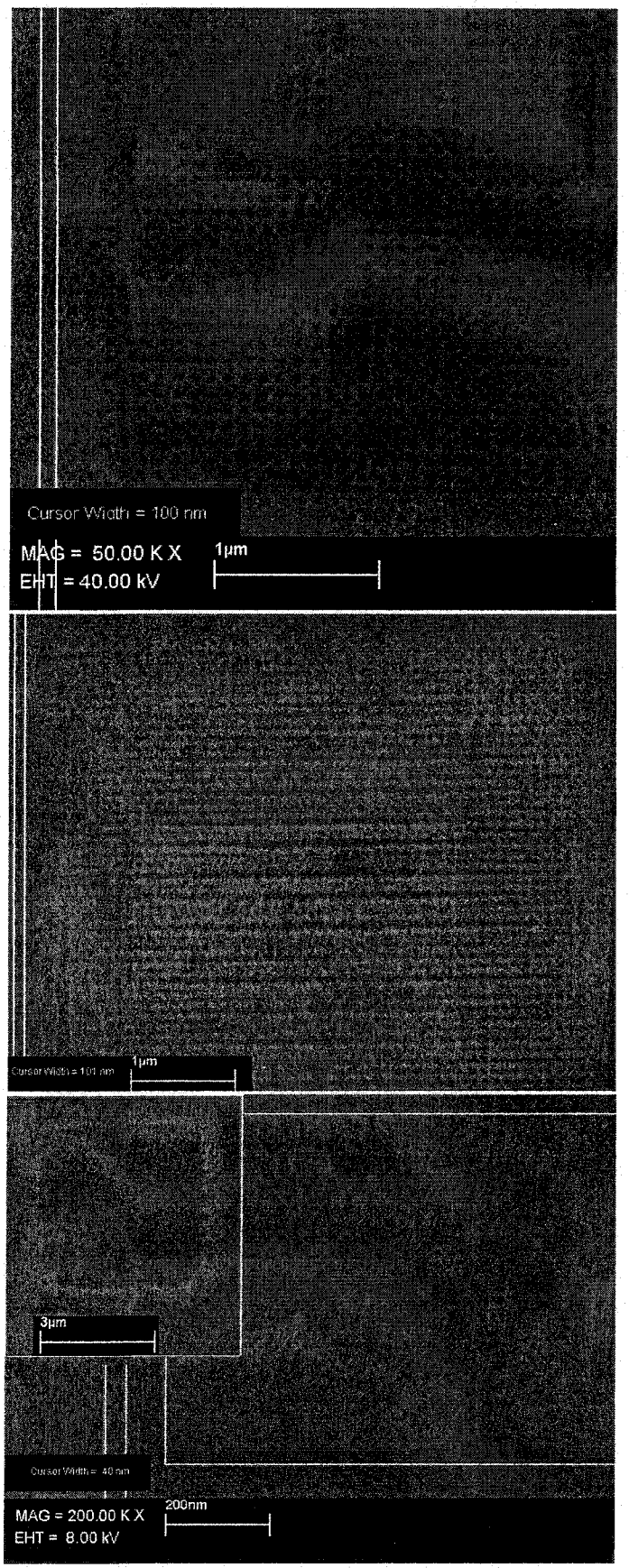

Fig. 3.35 The rectangular arrays of dots written into 160nm PMMA950k. On the top image is the 5µm large dot array on sapphire designed as a filled rectangle with ccd/lls 100nm. The diameter of dots is 50nm. The array was exposed with the dose 238.4µC/cm^2 (at 10pA). The exposures in the middle and bottom are on the Ti/Au thin film. The dose on the middle was 158.9µC/cm^2. The 160nm thick (>50nm wide) resist walls were undercut after the development and shifted (or tilted). The inner proximity effect is clearly visible in the central part. The bottom image shows the 35nm holes (the dose 79.5µC/cm^2) and the insert with overexposed square (the dose 198.6µC/cm^2). The development time was 15sec.

In the Fig 3.36, the AFM and SEM scanning results are displayed; the dense dot arrays in a single layer resist. The AFM scans show in details the PMMA resist layer after the e-beam writing and development processes. The data were designed as single lines (arcs). The 20nm thick and 150nm high resist walls in the overexposed array of dots are displayed.

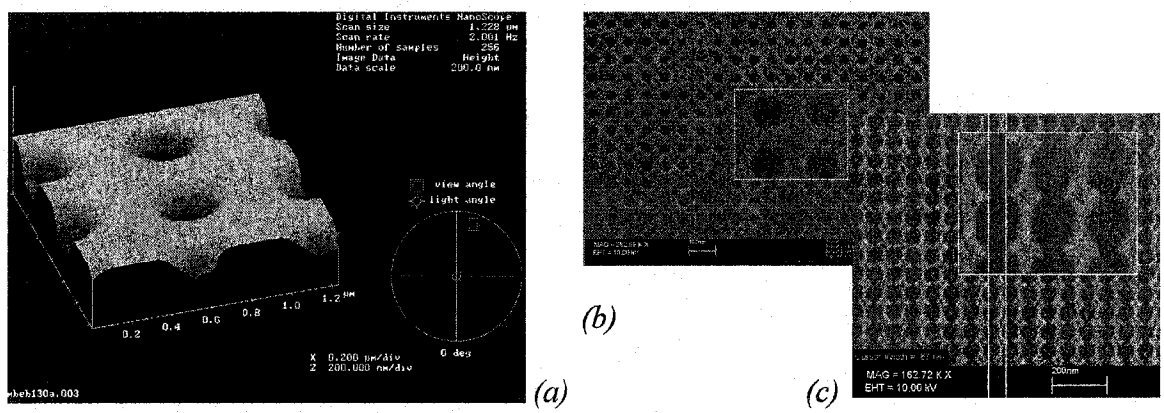

Fig. 3.36 The AFM scanning of dots in PMMA resist on the left, in (a). The dots shown in (b), were exposed with the line dose 1nC/cm on the Si + 150nm thick PMMA950k resist. The structures were designed as full arcs (with 50nm wide lines) of the radius 25nm. The 2x2 subset of dots (with 100m diameter) is shown in the zoom window. The smaller 2x3 dot pattern close the left upper corner is caused by a dirty substrate reducing the backscattering and effectively decreasing the resulting dot diameter. In (c) is the same pattern but with higher dose 2.5nC/cm. The 20nm thick resist walls and 60nm gaps are clearly visible. The writing was done with the writing current 5pA. The development time was 20sec.

3.3.6 *"Pillar" structures in resist on Si.*

To fabricate pillars of a sub-100nm diameter the method of the overexposure of the single resist layer was chosen, see Figs. 3.37 - 3.39. Overexposed resist material can withstand the removal process in developer MIBK:IPA or even the stronger resist removal bath such as the Acetone. The overdosing of the 200nm thick PMMA950k resist layer causes the cross-linking of organic macromolecular bonds. After a standard development process the exposure on the left results in the array of holes with a diameter 100nm while the overexposed resist on the right gives 75nm diameter pillars surrounded

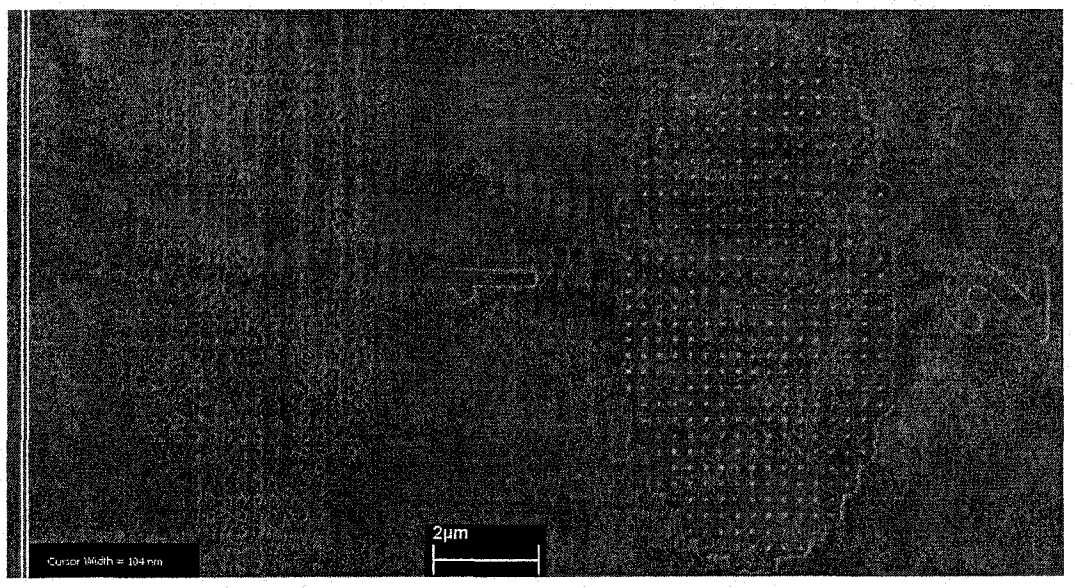

Fig. 3.37 The results of the microfabrication of arrays of dots and pillars in 200nm thick PMMA950k single resist layer on Si. On the left is the elliptical pattern of point-like exposures with the period 480nm written by the point dose 8fC. On the right is the same pattern but written with the dose 32fC. The numbers were designed as 200nm wide lines and exposed with the dose 1.8nC/cm.

by the silicone area without the resist. The area surrounding the ellipse is still covered by the unexposed resist film. A more detailed SEM image of the area of pillars is in the Fig. 3.38. The zoom window shows the 100nm diameter pillars at three different magnifications starting from the lowest at the bottom.

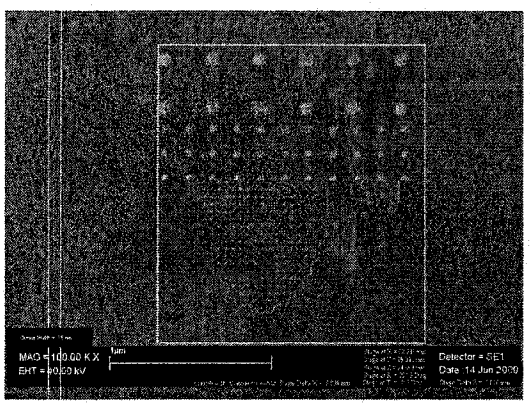

Fig. 3.38 The composition from the SEM scans (with different magnifications the lowest at the bottom). The elliptical pattern is the same as in Fig. 3.37.

The SEM stage required more than 1min of the settling time. Otherwise its drifting causes the deformations of the exposed patterns, as shown in Fig. 3.39. The first written point is at the lower left down corner and the direction of the writing is up. The pillar arrays of various periods (from 150 to 1200nm) were fabricated by the same method as in Fig. 3.37.

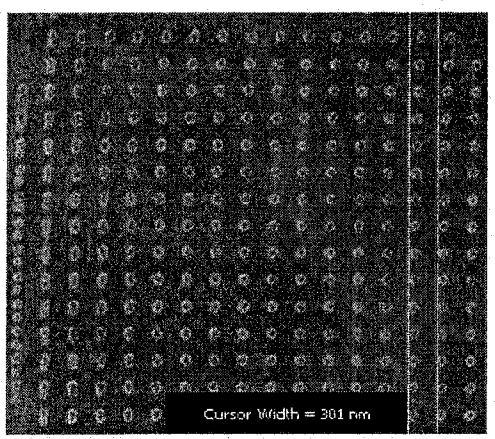

Fig. 3.39 Similar structures as in Fig. 3.37. This SEM image shoes the drift of the SEM stage. The exposure starts in the left lower corner and goes up.

The entire area dose for the 900nm and 1200nm period arrays (at the bottom of Fig 3.40) was not sufficient to allow the backscattering process to work and to expose the resist between the points of the matrix.

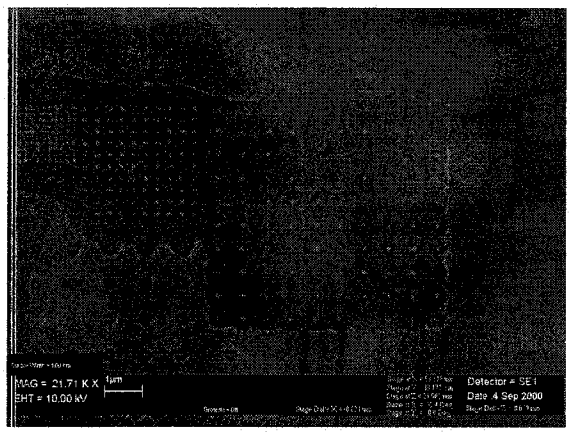

Fig. 3.40 The arrays of 100nm diameter pillars with period/point dose (from the top left corner to the right) 150nm/11.2fC, 300nm/12.8fC and 600nm/14.4fC respectively. The pillars with the period 900nm/16fC and 1200nm/20fC were exposed with an insufficient dose. The developer did not remove the resist from the areas between the pillars. The description numbers (designed as 50nm wide lines) were exposed with the dose 402μC/cm^2.

3.4 Summary of the microfabrication process.

The experimental results of this chapter show how complex and deep the technology of the micro- and nano-fabrication is. The microfabrication of small magnetic structures using lift-off requires proper sputtering process and the right choice of the resist system. The hard and long baking of the substrate/resist is important for a good adhesion of the resist film and stable mechanical properties of the resist film after the development. The last condition is important when sub-50nm features are fabricated. The set of exposure and post-exposure parameters (a development, baking, etc.) is important also to get right profile of the resist. In both single and double layer resists, the thickness of the resist and

the deposited film, the properties of the electron beam and proximity effects in a substrate and a resist determine the range of the spatial resolution and the density of resulting microstructures (arrays). A double layer consisting from 100nm thick copolymer-EL6 and 70nm thick PMMA950k-A2 gives resolution approx. 60-70nm. The next experiments can also be done using the combination of PMMA495k-A and PMMA950k-A resists followed by very long pre-bake duration and ultrasonically assisted resist development. Promising chances for good control of the resist undercut brings the Microchem LOR resist as the bottom layer.

Bibliography.

[1] Rai-Choudhury P., Editor, "**Handbook of Microlithography, Micromachining and Microfabrication**", SPIE 1997, Vol. 1,2

[2] Marrian Ch. R. K. and Tennant D. M., "**Nanofabrication**", J. Vac. Sci. Technol. A 21(5), S207-S215, Sep/Oct 2003

[3] Chang T. H. P. et al., "**Nanostructure technology**", IBM J. Res. Develop. 32(4), 462-493, July 1988

[4] Brodie I. and Muray J. J., "**The Physics of Micro/Nano-Fabrication**", Plenum Press, London 1993

[5a] Bethe H. A., Rose M. E. and Smith L. P., "**Multiple scattering of electrons**", Am. Philos. Soc. Proc. 78(4), 573-585, 1938

[5b] Kyser D. F. and Murata K., "**Quantitative Electron Microprobe Analysis of Thin Films on Substrates**", IBM J. Res. Develop. 18(4), 352-363, July 1974

[5c] Murata K. et al., "**Effects of the Introduction of the Discrete Energy Loss**

Process into Monte Carlo Simulation of Electron Scattering", Scanning 17, 228-234, 1995

[5d] Gauvin R. et al., "**Casino: A New Monte Carlo Code in C Language for Electron Beam Interaction-Part I: Description of the Program**", Scanning 19, 1-14, 1997

[6] Broers A. N., "**Resolution limits for electron-beam lithography**", IBM J. Res. Develop. 32(4), 502-513, July 1988

[7] http://www.jcnabity.com, Nanometer Pattern Generation System Manual, Help and Tutorial

[8] http://www.microchem.com, MicroChem Corp. Resist products description and MSDS sheets

[9] http://www.gel.usherb.ca/casino/index.html, Monte **CA**rlo **SI**mulation of electro**N** trajectory in s**O**lids, Université de Sherbrooke, Québec, Canada

[10] Kozawa T. et al., "**Relation between spatial resolution and reaction mechanism of chemically amplified resists for electron beam lithography**", J. Vac. Sci. Technol. B 21(6), Nov/Dec 2003

[11] Tilke A. et al., "**Low-energy electron-beam lithography using calixarene**", J. Vac. Sci. Technol. B 17(4), 1594-1597 Jul/Aug 1999

[12] Yasin S. et al., "**Nanolithography using ultrasonically assisted development of calixarene negative electron beam resist**", J. Vac. Sci. Technol. B 19(1), 311-313, Jan/Feb 2001

[13] Lin E. K. et al., "**Direct Measurement of the Reaction Front in Chemically Amplified Photoresists**", Science Vol. 297, 372-375, 2002

[14] Whelan C. S. et al., "**Low energy electron beam top surface image processing using chemically AXT resist**", J. Vac. Sci. Technol. B 15(6), 2555-2560, Nov/Dec 1997

[15] Tanenbaum D. M. et al., "**High resolution electron beam lithography using ZEP-520 and KRS resists at low voltage**", J. Vac. Sci. Technol. B 14(6), 3829-3833, Nov/Dec 1996

[16] Glezos N. et al., "**Aqueous base development and acid diffusion length optimization**", J. Vac. Sci. Technol. B 18(6), 3431-3434, Nov/Dec 2000

[17] Robinson A. P. G. et al., "**Polysubstituted derivatives of triphenylene as high resolution electron beam resists for nanolithography**", J. Vac. Sci. Technol. B 18(6), 2730-2736, Nov/Dec 2000

[18] Manako S. and Ochiaia Y., "**High-purity, ultrahigh-resolution calixarene electron-beam negative resist**", J. Vac. Sci. Technol. B 18(6), 3424-3427, Nov/Dec 2000

[19] Kedzierskia J. et al., "**Calixarene G-line double resist process with 15 nm resolution and large area exposure capability**", J. Vac. Sci. Technol. B 18(6), 3428-3430, Nov/Dec 2000

[20] Fujita J. et al., "**Sub-10 nm lithography and development properties of inorganic resist**", J. Vac. Sci. Technol. B 13(6), 2757-2761, Nov/Dec 1995

[21] Shaw C. H., "**Proximity parameters determination for electron beam lithography using a novel technique**", J. Vac. Sci. Technol. 19(4), 1286-1290, Nov/Dec 1981

[22] Kratschmer E., "**Verification of a proximity effect correction program in**

electron beam lithography", J. Vac. Sci. Technol. 19(4), 1264-1268, Nov/Dec 1981

[23] Eisemann H., Waas T. and Hartmann H., "**PROXECCO-Proximity effect correction by convolution**", J. Vac. Sci. Technol. B 11(6), 2741-2745, Nov/Dec 1993

[24] Rishton S. A. and Kern D. P., "**Point exposure distribution measurement for proximity correction in electron beam lithography on a sub-100nm scale**", J. Vac. Sci. Technol. B 5(1), 135-141, Jan/Feb 1987

[25] Lee S-Y. and Cook B. D., "**PERMALLOYRAMID-A Hierarchical, Rule-based Approach Toward Proximity Effect Correction-Part I: Exposure Estimation, Part II: Correction**", IEEE Trans. On Semiconductor Manufacturing 11(1) 108-128, 1998

[26] Greeneich J. S., "**Proximity effect correction using a dose compensation curve**", J. Vac. Sci. Technol. 19(4), 1269-1274, Nov/Dec 1981

[27] Tan Z. C. H. et al., "**Characterization of a positive resist and the application of proximity effect correction in electron-beam direct write**", J. Vac. Sci. Technol. B10(6), 3099-3103, Nov/Dec 1992

[28] Haslam M. E. and McDonald J. F., "**Transform based proximity corrections: Experimental results and comparisons**", J. Vac. Sci. Technol. B 4(1), 168-175, Jan/Feb 1986

[29] Dubonos S. V. et al., "**Evaluation, Verification and Error Determination of Proximity Parameters α, β and η in Electron Beam Lithography**", Microelectronic Engineering 21, 293-296, 1993

[30] Cui Z. and Prewett P. D., "**Proximity Correction of Chemically Apmplified Resists for Electron Beam Lithography**", Microelectronic Engineering 41/42, 183-186, 1998

[31] Dobisz E. A. et al., "**Thin silicon nitride films for reduction of linewidth and proximity effects in e-beam lithography**", J. Vac. Sci. Technol. B 10(6), 3067-3071, Nov/Dec 1992

[32] Hofmann U., Crandall R. and Johnson L., "**Fundamental performance of state-of-the-art proximity effect correction methods**", J. Vac. Sci. Technol. B 17(6), 2940-2944, Nov/Dec 1999

[33] Satyalakshmi K. M. et al., "**Charge induced pattern distortion in low energy electron beam lithography**", J. Vac. Sci. Technol. B 18(6), 3822-3825, Nov/Dec 2000

[34] Olkhovetsa A. and Craighead H. G., **"Low voltage electron beam lithography in PMMA**", J. Vac. Sci. Technol. B 17(4), 1366-1370, Jul/Aug 1999

[35] Kudryashov V. A. et al., "**Low Energy Electron Beam Lithography: Pattern Distortion by charge trapped in the resist**", Microelectronic Engineering 35, 165-168, 1997

[36] Stauff J. M. et al., "**Electron beam writing of continuous resist profiles for optical applications**", J. Vac. Sci. Technol. B 10(6), 2526-2529, Nov/Dec 1992

[37] Dubonos S. V. et al., "**Proximity Correction for 3D Structures**", Microelectronic Engineering 27, 195-198, 1995

[38] Kudryashov V. A. et al., "**Process Latitude for 3D Structure Formation in E-Beam Lithography**", Microelectronic Engineering 35, 487-490, 1997

[39] Groves T. R., "**Theory of beam-induced substrate heating**", J. Vac. Sci. Technol. B 14(6), 3839-3844, Nov/Dec 1996

[40] Dobisz E. A. et al., **"Effects of molecular properties on nanolithography in PMMA**", J. Vac. Sci. Technol. B 18(1), 107-111, Jan/Feb 2000

[41] Hasko D. G. et al., "**Influence of developer and development conditions on the behavior of high molecular weight electron beam resists**", J. Vac. Sci. Technol. B 18(6), 3441-3444, Nov/Dec 2000

[42] Khoury M. et al., "**Effect of molecular weight on poly(methyl methacrylate) resolution**", J. Vac. Sci. Technol. B 14(1), 75-79, Jan/Feb 1996

[43] Lee K. L. et al., "**Ultrasonic and dip resist development processes for 50 nm device fabrication**", J. Vac. Sci. Technol. B 15(6), 2621-2626, Nov/Dec 1997

[44] Lavallee E. et al., "**Electron beam lithography of nanostructures using 2-propanol water and 2-propanol:methyl isobutyl ketone as developers for poly-methylmethacrylate**", J. Vac. Sci. Technol. B 16(3), 1255-1257, May/Jun 1998

[45] Candeloro P. et al., "**Patterned Magnetic Permalloy and Nickel Films-Fabrication by Electron Beam and X-Ray Lithographic Techniques**", Japanese Journal of Applied Physics, 41(8), 5149-5152, 2002

[46] Novosad V. et al., "**Spin excitations of magnetic vortices in ferromagnetic nanodots**", Physical Review B 66, 052407, 2002

[47] Park Y. D. et al., "**Comparative study of Ni nanowires patterned by electron-beam lithography and fabricated by lift-off and dry etching techniques**", J. Vac. Sci. Technol. B 18(1), 16-20, Jan/Feb 2000

[48] Lohau J. et al., "**Electron-beam lithography using a scanning transmission electron CM12 (Philips)**", J. Vac. Sci. Technol. B 16(3), 1150-1154, May/Jun 1998

[49] Ross C. A. et al., "**Fabrication of patterned media for high density magnetic storage**", J. Vac. Sci. Technol. B 17(6), 3168-3176, Nov/Dec 1999

[50] Moreau C. E. et al., "**Fabrication and magnetic characterization of single**

domain $Co_{91}Fe_9$ nanostructures", J. Appl. Phys., Vol. 87, No. 9, 6316-6318, 2000

[51] Farhoud M. et al., "**Fabrication of 200 nm period nanomagnet arrays using interference lithography and a negative resist**", J. Vac. Sci. Technol. B 17(6), 3182-3185, Nov/Dec 1999

[52] Merton C. et al., "**Magnetic reversal of tapered Permalloy bars with holes in the center**", J. Appl. Phys., Vol. 85, No. 8, 4601-4603, 1999

[53] Yang X. et al., "**Fabrication of FePt nanoparticles for self-organized magnetic array**", J. Vac. Sci. Technol. B 22(1), Jan/Feb 2004

[54] Tsoi M. et al., "**Magnetic domain wall motion triggered by an electric current**", Appl. Phys. Lett., Vol. 83, No. 13, 2617-2619, 2003

[55] Gubbiotti G. et al., "**Finite size effects in patterned magnetic Permalloy films**", J. Appl. Phys., Vol. 87, No. 9, 5633-5636, 2000

[56] Cowburn R. P. et al., "**Sensing magnetic fields using superparamagnetic nanomagnets**", J. Appl. Phys., Vol. 87, No. 9, 7082-7084, 2000

[57] Heyderman L. J. et al., "**Nanoscale ferromagnetic rings fabricated by electron-beam lithography**", J. Appl. Phys., Vol. 93, No. 12, 10011-10013, June 2003

[58] Liu X. and Itoh F., "**Magnetic properties of Sr-ferrite dot arrays by electron beam lithography**", J. Appl. Phys., Vol. 93, No. 10, Parts 2 & 3, 7423-7425, 2003

[59] Zhao Y. et al., "**Submicron Co(TaC) line array produced by electron-beam direct writing**", J. Appl. Phys., Vol. 93, No. 10, Parts 2 & 3, 7417-7419, 2003

[60a] vanDelft F. C. M. J. M. et al., "**Method for manufacturing nanoscale structures in transition metal layers**", J. Vac. Sci. Technol. B 20(6), 2763-2767, Nov/Dec 2002

[60b] Cumming D. R. S. et al., "**Fabrication of 3 nm wires using 100 keV electron beam lithography and poly(methylmethacrylate) resist**", Appl. Phys. Lett. 68 (3), 322-324, 1996

[61] Liu K. et al., "**Simple fabrication scheme for sub-10 nm electrode gaps using electron-beam lithography**", Appl. Phys. Lett., Vol. 80, No. 5, 865-867, 2002

[62] Dial O. et al., **"Fabrication of high-density nanostructures by electron beam lithography**", J. Vac. Sci. Technol. B 16(6), 2887-3890, Nov/Dec 1998

[63] Namatsu H. et al., **"Fabrication of sub-10-nm silicon lines with minimum fluctuation**", J. Vac. Sci. Technol. B 13(4), 1473-1476, Jul/Aug 1995

[64] Ocola L. E. et al., "**Lithography for sub-60 nm resist nanostructures**", J. Vac. Sci. Technol. B 17(6), 3164-3167, Nov/Dec 1999

[65] Crandall R. et al., **"Contrast limitations in electron-beam lithography**" J. Vac. Sci. Technol. B 17(6), 2945-2947, Nov/Dec 1999

[66] Malac M. et al., "**Fabrication of submicrometer regular arrays of pillars and helices**", J. Vac. Sci. Technol. B 17(6), 2671-2674, Nov/Dec 1999

[67] Dick B., Brett M. J., Smy T., Belov M., and Freeman M. R., **"Periodic submicrometer structures by sputtering**", J. Vac. Sci. Technol. B 19, 1813 (2001)

[68] Chen W. and Ahmed H., "**Fabrication of high aspect ratio silicon pillars of sub10 nm diameter**", Appl. Phys. Lett. 63 (8), 1116-1118, 1993

[69] Subramanian V. R., DeCorby R. G., McMullin J. N., Haugen Ch. J., Belov M., "**Fabrication of aperiodic gratings on Silicon-On-Insulator (SOI) rib waveguides using e-beam lithography**", Proceedings of SPIE 2002, San Jose, CA

[70] Tada T. et al., "**Fabrication of silicon nanostructures with a poly(methylmethacrylate) single-layer process**", J. Vac. Sci. Technol. B 13(6), 2801-2804, Nov/Dec 1995

[71] Tsutsumi T. et al., "**Fabrication technology of a Si nanowire memory transistor using an inorganic electron beam resist process**", J. Vac. Sci. Technol. B 18(6), 2640-2645, Nov/Dec 2000

[72] Gomez R. D. et al., **"Domain configurations of nanostructured Permalloy elements**", J. Appl. Phys., Vol. 85, No. 8, 6163-6165, 1999

[73] Rossnagel S. M. et al., "**Collimated magnetron sputter deposition**", J. Vac. Sci. Technol. A 9(2), 261-265, Mar/Apr 1991

[74] Chen W. and Ahmed H., **"Fabrication and physics of ~2 nm islands for single electron devices**", J. Vac. Sci. Technol. B 13(6), 2883-2887, Nov/Dec 1995

[75] Chen W. and Ahmed H., **"Fabrication of 5-7 nm wide etched lines in silicon using 100 keV**", Appl. Phys. Lett. 62 (13), 1499-1501, 1993

[76] Yoshizawa M. and Moriya S., "**Quantitative factor analysis of resolution limit in electron beam lithography using the edge roughness evaluation method**", J. Vac. Sci. Technol. B 18(6), 3105-3110, Nov/Dec 2000

[77] Kim S. D. et al., **"Assessment of dry etching damage in Permalloy thin films**", J. Appl. Phys., Vol. 85, No. 8, 5992-5994, 1999

[78] Smith Ch. et al., "**Use of polymethylmethacrylate as an initial pattern transfer layer in fluorine- and and chlorine-based reactive-ion etching**", J. Vac. Sci. Technol. B 17(1), 113-117, Jan/Feb 1999

[79] Jung K. B. et al., "**Relative merits of Cl_2 and $CONH_3$ plasma chemistries for dry**

etching of magnetic random access memory device elements", J. Appl. Phys., Vol. 85, No. 8, 4788-4790 1999

[80] Jung K. B. et al., "**Development of chemically assisted dry etching methods for magnetic device structures**", J. Vac. Sci. Technol. B 17(6), 3186-3190, Nov/Dec 1999

[81] Jung K. B. et al., **"Patterning of Cu, Co, Fe, and Ag for magnetic nanostructures**", J. Vac. Sci. Technol. A 15(3), 1780-1784, May/Jun 1997

[82] Hsiao R. et al., "**Response surface study of resist etching in high density oxygen plasma and interactions of O_2 plasma with NiFe, Cu, Ta, and Al_2O_3**", J. Vac. Sci. Technol. A 14(3), 1028-1032, May/Jun 1996

[83] Khamsehpour B. et al., "**High resolution patterning of thin magnetic films to produce ultrasmall magnetic elements**", J. Vac. Sci. Technol. B 14(5), 3361-3366, Sep/Oct 1996

[84] Chen Y. et al., "**Fabrication of magnetic submicron-wire channels for the investigation of magnetization reversal**", J. Vac. Sci. Technol. B 16(6), 3830-3834, Nov/Dec 1998

[85] Khamsehpour B. et al., "**Fabrication of NiFe thin film elements by dry etching using $CH_4/H_2/O_2$**", Appl. Phys. Lett. 67 (21), 3194-3196, 1995

[86] David C. et al., "**Low-distortion electron-beam lithography for fabrication of high-resolution germanium and tantalum zone plates**", J. Vac. Sci. Technol. B 13(6), 2762-2766, Nov/Dec 1995

[87] Nakatani I., "**Ultramicro fabrications on Fe-Ni alloy films using electron-beam writing and reactive-ion etching (abstract)**", J. Appl. Phys. 79 (8), 5067, 1996

[88] Raith GmbH, **The tutorial and software manual for Raith 150 Ultra-high Resolution E-beam Lithography and Metrology Tool**, University of Alberta NanoFab, February 2004

4. *Ultrafast scanning magneto-optic Kerr effect imaging setup*

4.1 Introduction.

Magneto-optical effects are intensively used in scientific measurements and in the probing of a variety of materials, bulk or thin film. Freeman and Choi recently published a survey [9] of advances in stroboscopic magneto-optic Kerr effect (MOKE) microscopy. The MOKE experiments were also the focus of the work of Freeman and Hiebert [7], where the experimental details of the ultrafast magnetization dynamics studies were discussed. The details of the MOKE setup were described in details in Hiebert's thesis [33]. There are a great variety of methods and approaches to utilizing the magneto-optical effect. Pico-second and femto-second pulses have been used in detecting and characterizing of ultrafast processes in magnetic thin films for a long time, starting from the pioneering works [8,10]. The spatial resolution is important for imaging of spatially non-uniform magnetization of thin film structures [12]. Other experimental approaches such as detection of Brillouin light scattering also exist [13]. This experimental setup offers less spatial resolution but it has the capability to excite spin wave modes in a narrow range of spin wave vectors. As a result, the measurement of the dispersion curves with an excellent spectral resolution is possible [14].

Except the direct (differential) detection of the Kerr signal other methods, such as 2^{nd} harmonic signal detection, (for example Silva et al. in [16] and Gerrits in [18]), or inductive measurements, Silva et al. in [17], offer other opportunities for the

characterization and imaging of the magnetization dynamics. Another important difference between various experimental setups is the method of excitation of the non-equilibrium magnetization in a thin film. Some approaches use direct photoexcitation as well, (see van Kampen [19]). The source is often the ultrafast photodiode. In this method, which is used in our experiments, the optical pulses with a rise time of few hundreds pico-seconds, are launched by the ultrafast laser pulses. An ultrafast photo-switch fabricated on GaAs or Si substrates, (see for example results of recent experiments done by Gerrits [20]), generates excitation pulses with a rise time of tens of pico-seconds or less. This ultrafast pulse usually has a several hundred picosecond long exponentially decreasing tail [21-23]. An electronic pulse generator with an electronic delay line can produce several nanosecond long pulses with a rise time of tens of picoseconds. This source of ultrafast pulses has a large jitter.

In the MOKE experimental setup, all three components of magnetization can be detected by proper configuration of a couple of quadrant detectors [26-27]. The measurement of one component (the polar one) requires a single detector, or two if the noise subtraction scheme is used. This detection scheme is used in this thesis (as described below). The magnetization of a patterned thin film is confined (by the external *DC* magnetic bias) in the plane of the thin film and excited by a transient out-of-plane external magnetic field.

In the following two parts of this chapter, the fundamentals of the magneto-optical Kerr effect are briefly introduced and the parameters of the ultrafast scanning magneto-optical Kerr microscope setup are described.

4.2 *Magneto-optical Kerr effect, Gaussian beams.*

A linearly polarized electromagnetic wave of amplitude E can be represented as a sum of right and left circularly polarized waves. Let the wave has a wave vector k_0, and an oblique angle of incidence on a planar magnetic surface [1-5]. The reflected wave has a rotated polarization plane.

The relative orientations of the electric field vector and the magnetization vector are in Fig. 4.1.

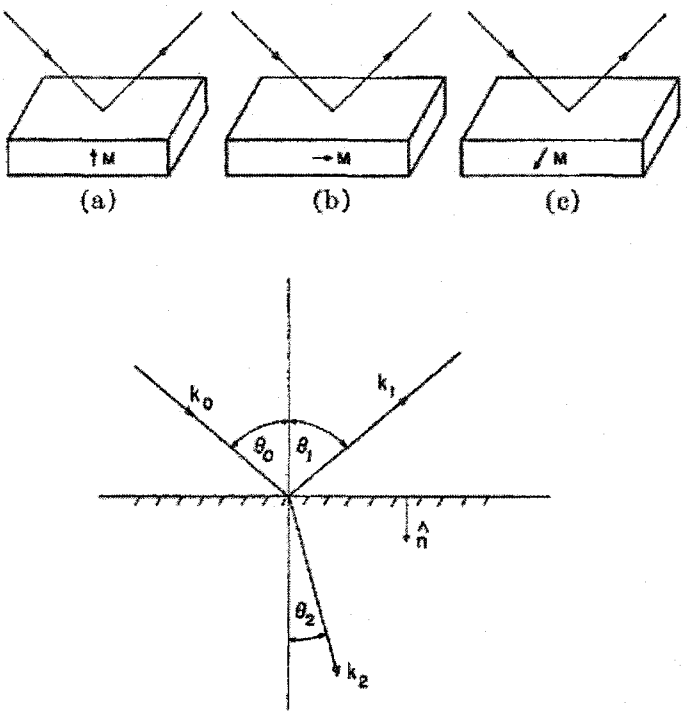

Fig. 4.1 Three basic configurations of the relative orientations of the electric field vector of the optical wave and the magnetization vector of the thin magnetic film [6]. In (a) is the polar, in (b) the longitudinal and in (c) the transverse configurations. Below is the orientation of $\boldsymbol{k}$ *vectors and angles with respect to the normal* $\boldsymbol{n}$ *of the interface of the air (top) and the magnetic (absorbing) medium.*

In general, the reflected wave is elliptically polarized, because of the existence of a Kerr vector component and a different absorption of the two orthogonal components of

the vector $\boldsymbol{E}$ [6, 11, 15]. The right and left-polarized light components have a different complex index of refraction and the phase shift between them is proportional to the difference of these two indices. Let the magnetic material have the magnetization $\boldsymbol{M}$ and complex dielectric tensor ε

$$\varepsilon = 1 - (\sigma/\omega) \tag{4.1}$$

where σ is the complex conductivity tensor. The conductivity tensor includes the ionic polarization, the free carrier currents, and the magneto-optical term dependent on the magnetization. The last term is derived from the equation of motion of the electron in the time-dependent electric field and the magnetic field and is proportional to the vector multiplication of electron's velocity and magnetic field or the Lorentz force, [6]. In a general system of arbitrary multilayers with appropriate boundary conditions, one derives the reflection and transmission coefficients for a plane wave with arbitrary angle of incidence. Solving Maxwell equations with appropriate boundary conditions at the interfaces of different materials/films, the Fresnel coefficients can be derived, [6, 29-31].

Using the standard notation (*p* for the in-plane polarization and *s* for the perpendicular polarization with respect to the plane of incidence), the Kerr reflection coefficients at the simple interface of two media are

$$r_{pp} = (n_0\gamma - \gamma')/(n_0\gamma + \gamma') \tag{4.2}$$

$$r_{ss} = (\gamma - n_0\gamma')/(\gamma + n_0\gamma') \tag{4.3}$$

$$r_{sp} = r_{ps} = \kappa_2 n_0/(\gamma - n_0\gamma')(\gamma + n_0\gamma') \tag{4.4}$$

where $\gamma = \cos(\theta_0)$ *and* $\gamma' = [1 - \sin^2(\theta_0)/n_0^2]^{1/2}$, κ_2 is the off-diagonal component of the dielectric tensor ε and n_0 is the index of refraction in the absence of $\boldsymbol{M}$. The dielectric

tensor is represented by the 3x3 matrix with $\kappa_{11}=\kappa_{22}$, $\kappa_{33}=\kappa_3$, $\kappa_{12}=\kappa_2$ and $\kappa_{21}=-\kappa_2$ nonzero components. The component κ_2 is an odd function and κ_1, κ_3 are even functions of the magnetic field **H** or the magnetization **M** respectively.

In the case of optical multilayers, the advanced general formulas for the reflection coefficients can be derived, [11, 29, 31]. The Kerr rotation angle θ and the ellipticity η (each for *p* and *s* polarizations) are then defined as [29]

$$\theta_s = - Re(r_{ps}/r_{ss}) \tag{4.5}$$

$$\theta_p = Re(r_{sp}/r_{pp}) \tag{4.6}$$

$$\eta_s = Im(r_{ps}/r_{ss})\, Re(r_{ps}/r_{ss}) \tag{4.7}$$

$$\eta_p = Im(r_{sp}/r_{pp})\, Re(r_{sp}/r_{pp})\,. \tag{4.8}$$

The analysis above was realized for the plane wave representation of an electromagnetic radiation.

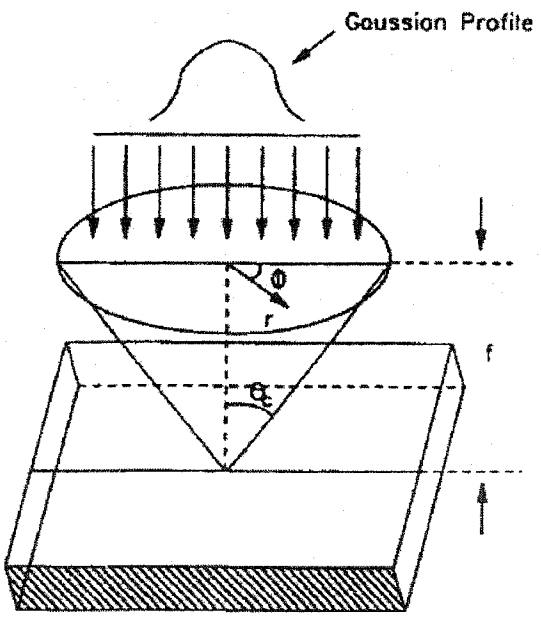

Fig. 4.2 Schematic picture of the Gaussian distribution of a convergent beam. Φ is the azimuth angle and θ the angle of incidence. The largest angle θ_c is the angle defined by the NA of the focusing objective [27].

In a typical MOKE experiment the probing beam are Gaussian beams and are

focused by a focusing objective with a high numerical aperture (NA). Based on the analysis by Mansuripur et al. in [28] and Parker et al. in [27], one can describe how the focusing of the beam affects the Kerr signal. As seen from the picture in Fig. 4.2, summing the amplitude over Φ and θ angular coordinates gives the signal at the focus of the convergent beam. Assuming linear polarization, the elements (r, Φ) of the beam arrive in phase at the waist but each of these elements is subjected to individual amplitude and phase change depending on its relative orientation to the magnetization vector (of the film or the substrate). The Gaussian spot acts as phase object and all complex components of the reflected beam can be integrated to produce a complex effective reflectance [27]. This kind of calculation opens an opportunity for signal to noise ratio (SNR) improvement, as described by Yang in [29]. With multiple dielectric layers, the Kerr signal detection can be improved by matching the phases of reflected beams from interfaces between dielectric films (by changing the index of refraction and the thickness of thin films, and, as a result, the reflection and transmission coefficients), Mansuripur [4] and Chen [24].

Let us assume a plane wave focused by a microscope objective with the circular input aperture of diameter D_{Aper}, the focal length f and numerical aperture NA. The Airy formula for the diameter W of the focus spot, from Born and Wolf [1], is given as

$$W_{Airy}=2.44 f\lambda / D_{Aper}. \tag{4.9}$$

Similarly, for a focused Gaussian beam with radius r_e (measured to $1/e$ of the maximum amplitude, the distribution of which is $exp[-(r/r_e)^2]$) [4],

$$W_{Gaussian}= 2 f\lambda / D_{Aper}. \tag{4.10}$$

At 99% of "captured" power of the Gaussian beam the diameter $W_{G99\%}= \lambda/NA = 2f$

$\lambda/(1.517\ r_e)$, after Mansuripur [4]. For $f=0.72mm$, $\lambda=780nm$, $NA=0.9$ and $D_{Aper}=2mm$ the focus spot W_{Airy} is 685nm, $W_{Gaussian}$ is 560nm and $W_{G99\%}$ is 870nm.

3.3 Optical detection scheme.

Based on the Kerr rotation and the ellipticity parameters defined above, the polar component of magnetization can be detected using the two-detector scheme and a Wollaston polarization beamsplitting prism.

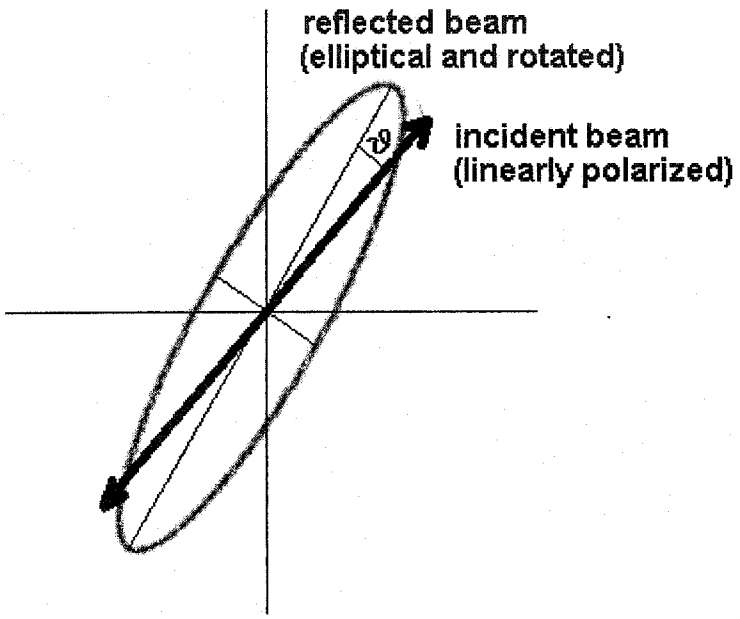

Fig. 4.3 Polarization vector analysis of the linearly polarized incident beam, after reflection from the surface and carrying a Kerr rotation θ and ellipticity η. The ellipticity η is the ratio of the minor and major axes of the polarization ellipse).

The prism is rotated by 45° with respect to the reference direction of the polarization[1] (the polarization axis of a reflected beam with zero Kerr contribution), Fig. 4.3. The Wollaston prism then divides the beam carrying Kerr information into two

[1] At this angle of the prism, the detection system has maximal sensitivity to small polarization changes.

beams with opposite phase. The subtraction of the optical signals (the optical intensities) from both detectors brings common-mode noise reduction. The values θ_s and θ_p of the Kerr rotation are doubled. In a similar way, using quarter-wave-plate, the ellipticity η can be detected [4] or [30]. In current work, only the Kerr rotation related to the out-of-plane component of the magnetization was detected.

4.4 ***Sources of noise.***

Working with the laser source, one has noise from fluctuations of the amplitude, phase, wavelength and polarization of the optical beam. Below a couple of hundreds Hertz one has noise related to the noise in the environment of the laser itself, including the temperature drift. Generally, in solid-state pumped femtosecond laser systems the fluctuations of the output are not the limiting factor.

Shot noise comes into play in the process of photodetection. The statistics of optical energy arriving in discrete units as photons is the origin of the shot noise. In terms of noise current per Hertz of bandwidth one can write, $I_{sh}^2 = 2\ e\ h_s\ P_d = 2\ e\ I_{dc}$, where h_s is the quantum efficiency of the detector, e is elementary charge, P_d is the incident power on the detector and I_{dc} is the *dark* current of the detector. Shot noise (approx. 10nV at 2nA dark current), is white noise, has a constant noise power per Hertz of bandwidth and a direct proportionality of noise power to laser power.

The electronic noise of the photodetector is also significant. This consists of Johnson noise, dark current noise and base current noise. The Johnson noise has thermal origin and the only principal means for its reduction is lowering of the temperature (approx. 4nV at room temperature).

The noise relevant to our measurements is in kHz range. In practice, the most challenging source of noise was the mechanical vibrations, directly coupled from the rotating mechanical chopper. Isolating the chopper from the optical table and surrounding it by a small enclosure resolved this problem. The settings of the lock-in amplifier to extract the Kerr related signal at the 1kHz chopping frequency were optimized to have appropriate compromise between the noise of the final signal and the required scanning time (integration constant of the lock-in was typically 30-100ms).

4.5 Experimental ultrafast scanning Kerr microscope.

4.5.1 Details of the microscope.

The optical pulses, both the pump and probe, are generated by the mode-locked Ti-sapphire femtosecond laser (Spectra Physics Tsunami) that is pumped with the "green" laser Millenia V. The Ti-sapphire laser was tuned to the wavelength 780nm and the pulse repetition rate was 80MHz. The output laser pulses were 80-100fs long (based on measurement of a spectral width) and the output optical power was typically 700mW. The maximum optical power of the probe beam was in 30mW. The diameter of the Gaussian beam was 2mm. The beam was expanded 5 times and the optical power was measured in front of the achromatic microscope objective. Effectively about 12% of the initial probing power entered the focusing objective. Assuming 5% reflection losses related to the focusing objective (numerical aperture NA=0.9), the maximum power of

the focused probe beam was approximately 3.5mW. Details of the MOKE scheme are in Fig. 4.4.

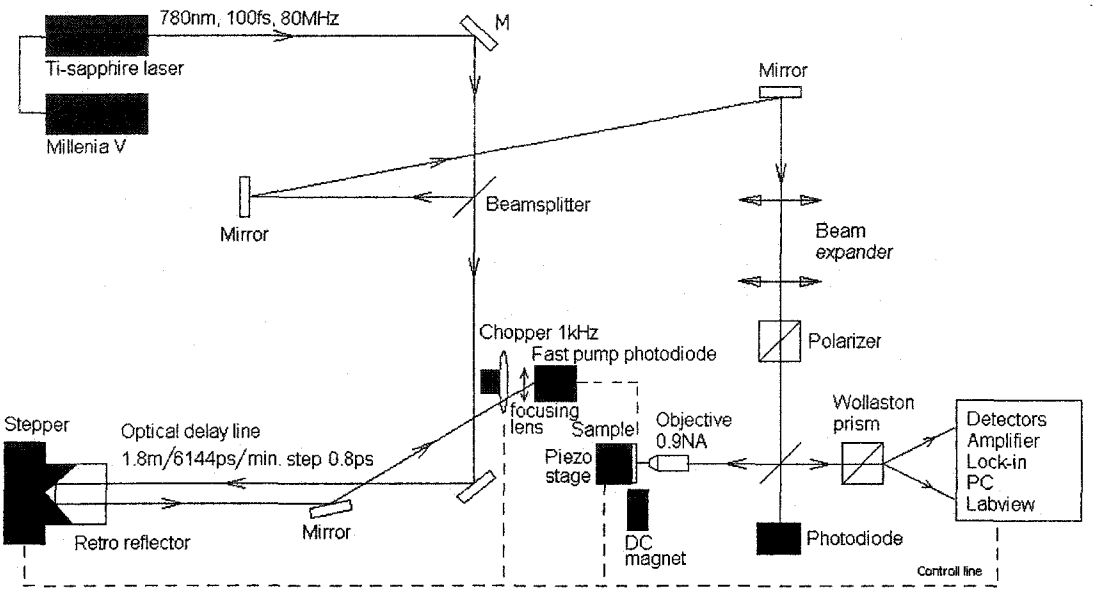

Fig. 4.4 The scheme of the ultrafast scanning magneto-optical Kerr effect microscope.

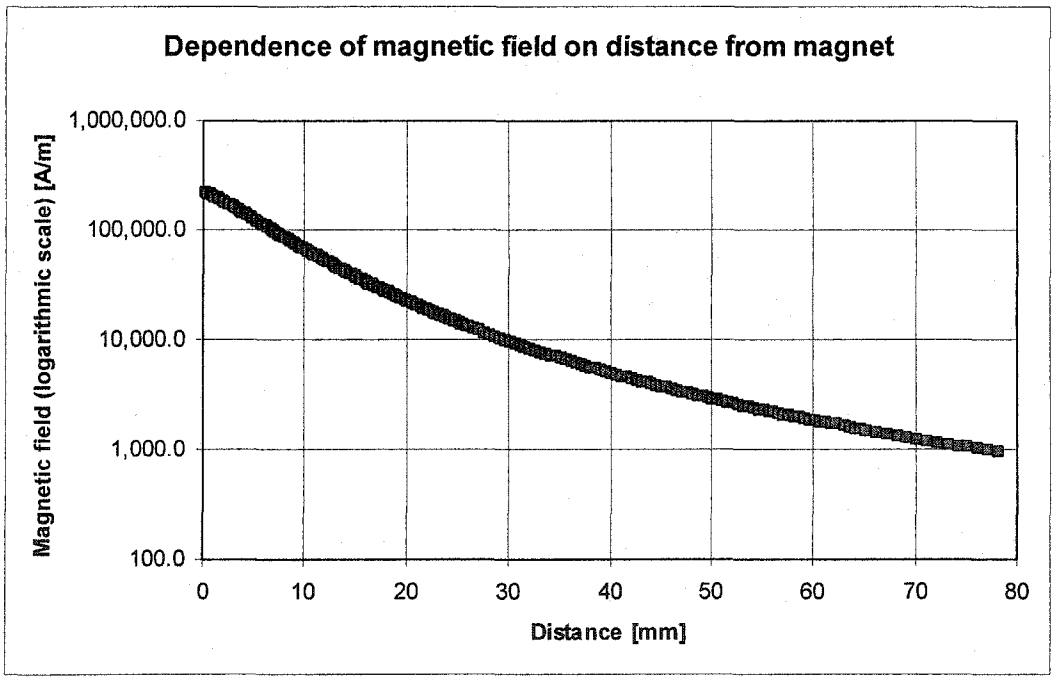

Fig. 4.5 The dependence of the magnetic field (on a logarithmic scale) on the distance from the DC magnet.

The intensities of the two optical signal beams emerging from the Wollaston prism were detected by a matched pair of two optical detectors (UDT-555D from UDT Sensors Inc., with 100mm^2 large sensitive area and with integrated amplifiers), and subtracted using a low-noise differential amplifier (SR560 Stanford Research). A digital lock-in amplifier (SR830 DSP) processed the signal flow from the differential amplifier. A PII 400MHz computer with Labview 6 software and procedures designed for this system controlled the experiment.

The sample was magnetized by the field from a permanent magnet, in the plane of the sample and perpendicular to the long axis of the gold wire. The *DC* magnetic field could be set to values from zero to 0.05T, and to a single value 0.125T using two magnets. The permanent magnet (25x25x12.5mm NdFeB) was attached to a holder moved by a manual XYZ stage (with smallest step 10 micrometers), and calibrated using a gaussmeter. Fig. 4.5 shows the dependence of the magnetic field on the distance from the magnet.

Despite the sufficiently precise calibration of the *DC* magnet field dependence versus the distance, the measurement of distance from the magnetic bar to the location of the magnetic wire (with magnetic elements) was accompanied with uncertainty ±0.5mm. The corresponding uncertainty of the magnitude of the DC magnetic bias was about 400A/m.

The 10x10mm sapphire substrate with five sets of 300nm thick and 20μm wide Ti/Au wires with 20μm gap between them was attached to the holder. Fig. 4.6 shows the details of the holder for the sapphire substrate. The holder was attached to the XYZ piezo stage, which was controlled by the computer and had a minimum scanning step

size of 10nm.

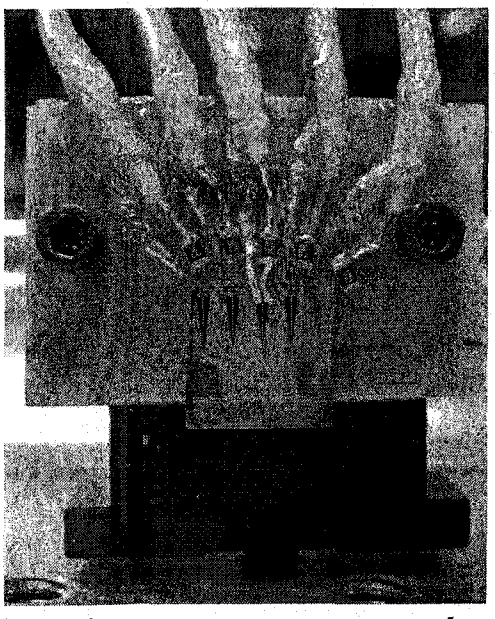

Fig. 4.6 The substrate holder for the MOKE scheme. The coax cable is glued to a fibreglass support for the sapphire substrate, and connected to the pumping photodiode with 2V output. The cable is attached via ~37Ω resistor to the (middle) planar wire. The circuit resistance is ~50Ω. The probe beam (perpendicular to the plane of the substrate) is focused on magnetic structures at the end of the wire.

The gold wires were connected using indium bonds to the coaxial cable. The other end of the coaxial cable was connected to the output of pump photodiode. The fast photodiode Thorlabs SV2-FC has ~2GHz bandwidth, 2V output and produced 300ps FWHM current pulse with the 200ps rise time. The current pulse induced the transient magnetic field around the planar gold wires. With 10mW of average power from the pump beam focused on the area of the photodiode, the out-of-plane magnetic pulses of magnitude 640A/m were produced[2]. The magnetic field was calculated using the Biot-Savart formula. The point of the calculation lies between two wires (10μm from each one) carrying a current of 40mA. The distribution of the field in the gap is uniform because of the symmetry of the wire design[3].

[2] This was the limiting power before the photodiode was driven into saturation.
[3] The deviation of the field amplitude at the edges and at the top surface of the magnetic element,

The profile of the pumping pulse is shown in Fig. 4.7. The insert in the figure shows the ferromagnetic response (at DC magnetic bias 100kA/m oscillating at the frequency close to 10GHz) taken at the center of the 4μm magnetic square.

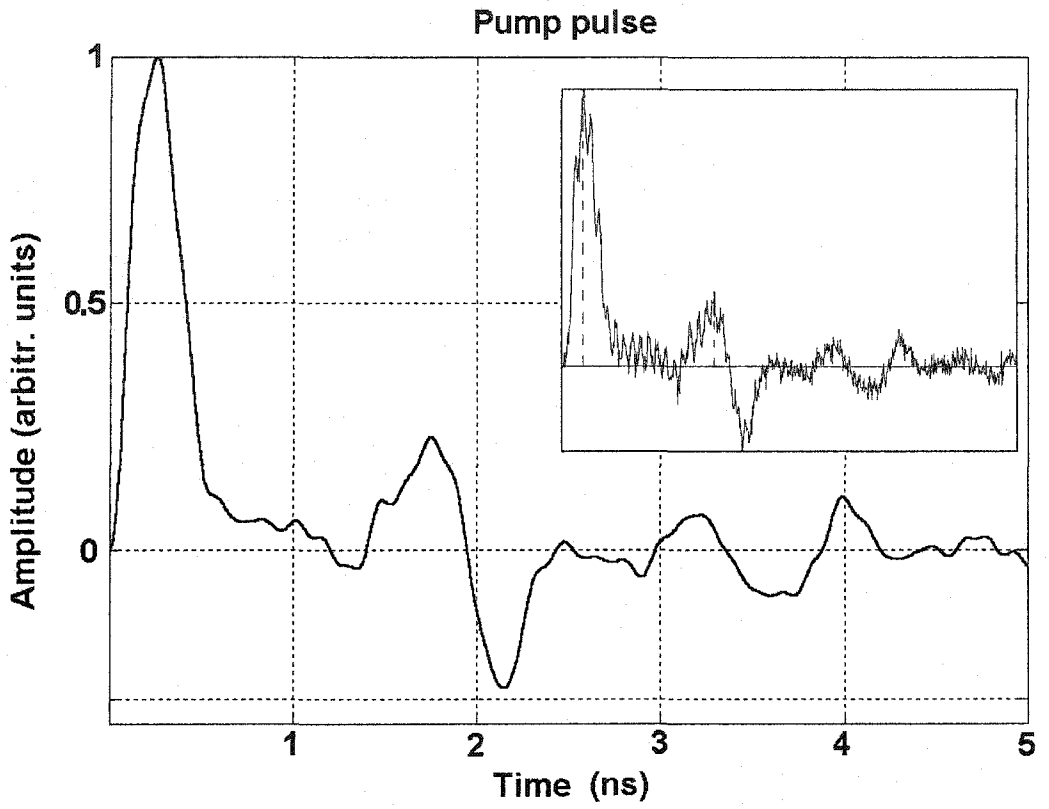

Fig. 4.7 The pumping pulse profile shows the reflections (the first reflected pulse comes after 1.56ns) caused by an imperfect circuit design. The insert displays the broadband ferromagnetic resonance response at a 100kA/m DC magnetic bias as the source data for the pump pulse profile derivation. The period of these relatively high frequency magnetization oscillations, taken from the center of the platelet, is 100ps that correspond to the frequency 10GHz. The pumping pulse profile is the source shape used in the numerical simulations.

---

respectively to the central (bottom) point, is small (less than 1%, based on numerical integration over the 200x20x0.3μm two parallel conductors with 4x4x0.015μm structure placed symmetrically between them).

This data curve was used as the source curve for the derivation of the pump pulse profile. The derivation was accomplished through the Fourier transformation of the experimental data curve into the frequency domain. In the next step, the high-frequency components

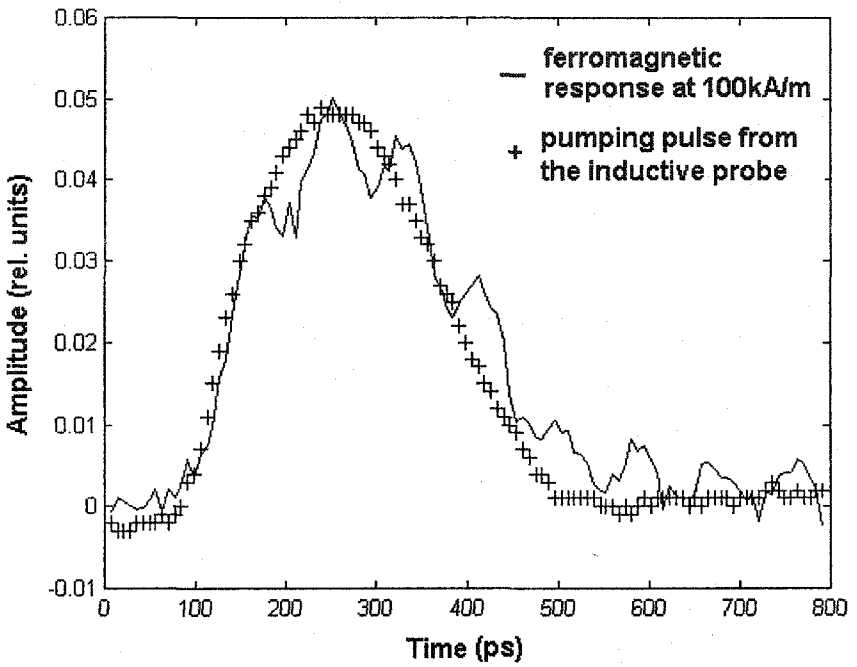

Fig. 4.8 The "+" curve shows the pumping pulse as detected by a Hewlett Packard 20GHz memory oscilloscope with a CT-6 inductive probe. The FWHM of the pulse is 300ps. The solid line displays the broadband ferromagnetic resonance response (at DC magnetic bias 100kA/m) on the transient pumping pulse excitation.

were cut and the back Fourier transformation produced the curve representing the profile of the pump pulse in Fig. 4.7. The imperfect impedance adjustment between the fast photodiode and the gold coil is the cause of the electrical reflections. The time interval between the major pump pulse and the first reflected pulse is 1.56ns. The first and second reflected pulses (after 3.8ns measured from the zero point), affect the

magnetization oscillations by an additional excitation and, consequently, change the magnetization dynamics and the damping in this pool of spin waves. Fig. 4.8 shows with a CT-6 inductive probe both the pumping pulse and the broadband ferromagnetic resonance response from the Hewlett Packard 20GHz oscilloscope.

The relative optical delay between the probe and pump pulses was controlled by the optical delay line (ODL). The ODL was built from an optical rail with a retro-reflector attached to stage that was moved by a stepping motor (controlled by the computer). The total length and the smallest temporal step of the ODL were *6ns* and *0.8ps* respectively (calculated using the rail effective length $1.800 \pm 0.001m$, the speed of light in air $2.998 \times 10^8 m/s$ and the required number of steps of the stepping motor to move the stage along the ODL's path). The chopper was placed at the end of the ODL and modulated the 80MHz train of pumping pulses at the frequency of 1kHz.

The entire opto-mechanical setup was built on a Newport optical table with pneumatic vibration isolation. The piezo stage with the attached sample holder was mechanically isolated from the table using rubber pads. The chopping frequency was empirically selected from the interval from 100Hz to 6kHz to produce the lowest noise. The power of the probe beam was adjusted to a safe level below the damage threshold of the sample. To probe the damage level and heating in a film, a small area about $0.5\mu m^2$ was scanned while the probe power was increased over a trial of test experiments. At the highest available probe power, approx. 3.5mW, the damage limit has not been reached.

4.5.2 Parameters of the scanning process.

A temporal step of the scanning process (ferromagnetic curves or X-t scans)

depends on the magnetic bias field magnitude that determines a period of magnetization oscillations, and was typically 8-12ps for higher bias above 20kA/m and 12-24ps for lower bias fields. The 2-D imaging is a very time-consuming process (~45min per 2-D frame). The temporal steps from 20 to 48ps were usually chosen in a 2-D scanning process (generating up to 100 frames). To reduce the scanning time a low level of noise is required. The noise depends on many parameters such as the power of the probe beam, the chopping frequency, mechanical isolation (using rubber pads) of the piezo stage from the optical table, the electronic amplifications (a differential and a lock-in amplifier), and the lock-in integration and waiting constants. The typical parameters were: a probe power 0.5-1mW (less power caused too much noise, more power would heat the monitored sample); a chopping frequency of 1kHz (with a 60 blade wheel); and a 10x differential amplification. The important settings of the lock-in were the following: an external reference frequency source from the chopper (with a zero phase), a sensitivity of 50mV, a normal (or low) reserve, a time constant 10ms(30ms) with a slope/oct 12dB and 100ms(300ms) longer waiting time. Other parameters that have significant impact on scanning results were: the alignment and focusing of the focused probe beam on the surface of the magnetic element, the balance of the photodiodes, the uniformity of the pumping beam power along the delay line path (1.8m) and the stability of the room temperature. The alignment (auto-centering and auto-focusing) procedures were repeated after each 2-D frame was finished. The pumping power was monitored by an extra photodiode during the scanning and in addition, the probe power was continuously monitored and recorded using a separate channel. The typical spatial steps of the piezo-stage in X-t and 2-D scannings were 40nm and 62nm respectively. To accelerate the

scanning, the scanning rate was increased, while scanning outer non-magnetic areas, by decreasing the waiting time ~10x (via auto-detecting the edges of the magnetic sample using the amplitude channel).

4.6 Summary of the chapter.

The ultrafast scanning MOKE microscope was built and successfully used in the imaging of the magnetization dynamics of micrometer-sized magnetic elements. The experimental setup was built using a femtosecond laser, optical delay line, fast optical pumping photodiode, XYZ stage controlled by piezo-actuators, a two-detector probe beam scheme with low-noise differential amplifier followed by a digital lock-in amplifier. A computer with Labview software controlled the opto-mechanical setup. The temporal and effective spatial resolutions of the microscope were 0.8ps and 200nm (limited by the size of the Gaussian probe) respectively. The polar components of the magnetization and their spatial and temporal evolution are detected using this MOKE microscope.

Bibliography.

[1] Born M. and Wolf E., "**Principles of Optics**", Pergamon Press 1980

[2] Jackson J.D., "**Classical Electrodynamics**", John Wiley&Sons, Inc, New York 1962

[3] Argyres P.N., "**Theory of the Faraday and Kerr Effects in Ferromagnetics**", Phys. Rev. 97, 334-345, 1955

[4] Masuripur, M., "**The Physical Principles of Magneto-optical Recording**", Cambridge Univ. Press 1995

[5] Masuripur, M., "**Classical Optics And Its Applications**", Cambridge Univ. Press 2002

[6] Freiser M.J., " **A Survey of Magnetooptic Effects**", IEEE Trans. Magn. 4, 152, 1968

[7] Hillebrands B. and Ounadjela K., eds. "**Spin Dynamics in Confined Magnetic Structures I**", Springer 2002

[8] Freeman M.R. et al., "**Pico-second pulsed magnetic fields for studies of ultrafast magnetic phenomena**", IEEE Trans. Magn. 27, 4840, 1991

[9] Freeman M.R. and Choi B.C., "**Advances in magnetic microscopy**", Science 294, 1484, 2001

[10] Freeman M.R. and Smyth J.F, "**Pico-second time-resolved magnetization dynamics of thin-film heads**", J. Appl. Phys. 79, 5898, 1996

[11] Qiu Z.Q. and Bader S.D., "**Surface magneto-optic Kerr effect**", Rev. of Sci. Instrum. 71, 1244-1255, 2000

[12] Hiebert W.K. et al., "**Ultrafast imaging of incoherent rotation magnetic switching with experimental and numerical micromagnetic dynamics**", J. Appl. Phys 92, 392, 2002

[13] Demokritov et al., "**Brillouin Light Scattering Studies of Confined Spin Waves: Linear and Nonlinear Confinement**", Phys. Rep. 348, 441-489, 2001

[14] Jorczik et al., "**Brillouin light scattering from quantized spin waves in micron-size magnetic wires**", Phys. Rev. B 88, 15 194-15 200, 1999

[15] You Ch. And Shin S., "**Generalized analytic formulae for magneto-optical Kerr effects**", J. Appl. Phys. 84, 541, 1998

[16] Silva T.J. et al., "**Detection of coherent and incoherent spin dynamics during**

the magnetic switching process using vector-resolved nonlinear magneto-optics", Appl. Phys. Lett. 81, 2205, 2002

[17] Silva T.J. et al., "**Inductive measurement of ultrafast magnetization dynamics in thin-film Permalloy**", J. Appl. Phys. 85, 7849, 1999

[18] Gerrits Th., "**Coherent Control of fast Precession Dynamics in Magnetic Thin Films**", Ph.D. Thesis, November 2003

[19] van Kampen M. et al., "**All-Optical Probe of Coherent Spin Waves**", Phys. Rev. Lett 88, 227201-1, 2002

[20] Gerrits Th., "**Ultrafast precessional magnetization reversal by pico-second magnetic-field pulse shaping**", Nature 418, 509, 2002

[21] Keil U.D. and Dykaar D.R., "**Ultrafast Pulse Generation in Photoconductive Switches**", IEEE of Quantum Electronics 32, 1664, 1996

[22] Elezzabi A.Y. and Freeman M.R. "**Ultrafast magneto-optic sampling of pico-second current pulses**", Appl. Phys. Lett. 68, 3546, 1996

[23] Keil U.D. et al., "**High-Speed Coplanar Transmission Lines**", IEEE of Quantum Electronics 28, 2333, 1992

[24] Chen L., et al., "**Enhancement of magneto-optical Kerr effects**", J. of Appl. Phys. 67, 5337, 1990

[25] Choi B.C. et al., "**Ultrafast Magnetization Reversal Dynamics Investigated by Time Domain Imaging**", Phys. Rev. Lett 86, 728, 2001

[26] Stankiewicz A, "**Time-resolved scanning Kerr microscopy in magnetic dynamic investigations**", Crit.Rev. CR72, 181, 1999

[27] Parker M.R. et al., "**Analysis of magneto-optic Kerr effect signals from**

convergent Gaussian beams", IEEE Trans. Magn. 25, 4024, 1989

[28] Mansuripur M. et al., "**Signal and noise in magneto-optical readout**", J. Appl. Phys. 53, 4485, 1982

[29] Yang Z.J. and Scheinfein M.R., "**Combined three-axis surface magneto-optical Kerr effects in the study of surface and ultrathin-film magnetism**", J. Appl. Phys. 74, 6810, 1993

[30] Zvezdin A.K. and Kotov V.A., "**Modern magnetooptics and magnetooptical materials**", Institute of Physics Publishing, Bristol 1997

[31] Mansuripur M., "**Analysis of multilayer thin-film structures containing magneto-optic and anisotropic media at oblique incidence using 2x2 matrices**", J. Appl. Phys. 67, 6466, 1990

[32] McDaniel T.W. and Victora R.H., "**Handbook of magneto-optical data recording**", Noyes Publications, New Jersey 1997

[33] Hiebert W.K., "**Experimental Micromagnetic Dynamics: Ultrafast Magnetization Reversal Using Time Resolved Scanning Kerr Effect Microscopy**", Ph.D. Thesis, University of Alberta 2001

5. *Magnetization dynamics: experimental results and comparison with numerical simulations*

5.1 *Magnetization oscillations of a Permalloy squares.*

Results presented in this chapter emerged from a motivation by photonics bandgap structures. Once spin waves are generated in an internally patterned element, "a magnonic crystal" (for example an array of pinholes inside of micron sized thin film magnetic platelet), the (periodic) non-uniformity of an internal magnetic field can modify their propagation in an intended way. The simple step had to be realized first; a single lithographic pinhole created inside a magnetic square, magnetization oscillations of such magnetic systems (with and without a pinhole) imaged and compared relatively each other, and with numerical simulations.

The broadband magnetization dynamics (BMD) of lithographic, polycrystalline thin film ferromagnetic $Ni_{80}Fe_{20}$ elements were studied experimentally using time-resolved ultrafast scanning Kerr microscopy (MOKE). The spatiotemporal evolution of the polar component of magnetization responding to a small out-of-plane transient magnetic pulse is imaged in the presence of an in-plane static bias field. Recent results show that the geometrical form of an ultrathin magnetic film can significantly affect the oscillations of the magnetization vector. The results of ultrafast stroboscopic scanning Kerr microscopy experiments presented here show in detail the interactions between various modes of magnetization oscillations. Square and elliptical samples, each with and without a small pinhole, were investigated. How the structure determines both the

spatial and temporal characteristics of the broadband magnetization dynamic is shown and discussed.

The complete process of microfabrication and the description of the MOKE microscope were described in Chapters 3 and 4 respectively. The samples were fabricated from 15-nm-thick polycrystalline $Ni_{80}Fe_{20}$ films deposited by DC magnetron sputtering onto a sapphire substrate and patterned using electron beam lithography and lift-off. Fig. 5.1 shows an optical micrograph of the specimen hosting a family of independent elements, and a scanning electron micrograph "close-up" of a 4.00±0.05μm

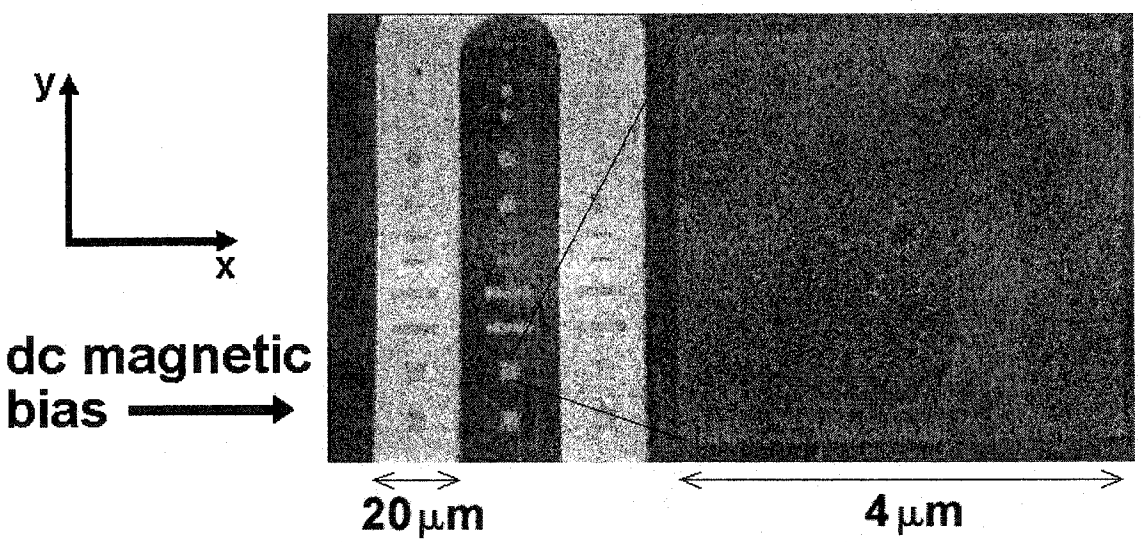

Fig. 5.1 Optical and electron microscopy (zoom) images of the 15nm thick $Ni_{80}Fe_{20}$ sample, with the coordinate system for the field geometry on the left. The transient out-of-plane magnetic field is generated by a current flow through the elongated 300nm thick gold loop (bright in the optical image). The hole in the center of the 4μm ferromagnetic platelet on the right has a 240nm diameter.

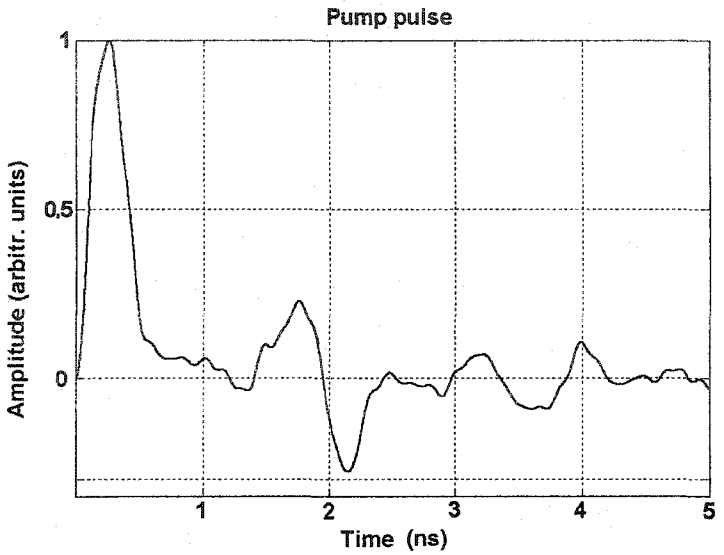

Fig. 5.2 The pumping pulse profile with the reflections (the first reflected pulse comes after 1.56ns).

square with the 240±10nm-diameter central pinhole investigated in this study. The structures are within an elongated loop of 300nm thick, 20μm wide gold wire that carries fast current pulses. The measurements are performed by a conventional pump-probe optical method, using 100 femtosecond pulses from an 80 MHz mode-locked Ti: sapphire oscillator tuned to a 780nm wavelength. The sample is biased along the *x*-direction (perpendicular to the axis of the wire) by the external DC magnetic field.

The response of the patterned magnetic elements is strongly spatially dependent and a careful alignment procedure is required before the actual scanning process is started. The stability of the position of the magnetic element during several-minutes to many hours scanning is important; otherwise, the resulting experimental signal is an average value over an area dependent on the drift of the scanning stage (mainly due to temperature change), in addition to the averaging over the area of the focused probe beam.

5.1.1 *Temporal behavior of the magnetization.*

The sample is DC biased in the plane of the magnetic film and its initial state shows three different domain areas, the central domain and two closure domains. The orientation of the closure domains depends on the magnitude of the DC bias (as will be seen later from the spatial frames and confirmed by numerical simulations). Typically, a "C" or "S" configuration can be formed, the first for the magnitude of the DC bias less than 8kA/m and the second for higher values of the DC bias magnitude. A weak transient pulse (less than 1/5 of the DC bias magnitude, with a steep rising slope) excites the magnetic system and the magnetization starts to move in an out-of-plane direction and rotate about the vector of the effective magnetic field.

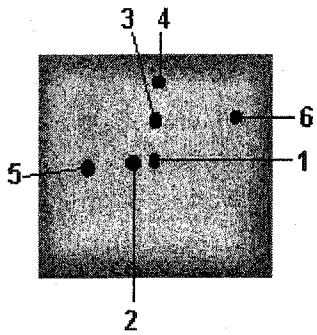

Fig. 5.3 The experimental Kerr image (at 180ps of time delay) of the 4μm square in DC magnetic bias 4.62kA/m (oriented horizontally) with closure domain structure, domain walls and a 240nm-diameter pinhole in the center. Numbers and lines represent locations of the probe spot where full time-domain curves were constructed (at each location, an average of 3 pixels was used). The magnitude of the pulse excitation was 640A/m and the rise time 200ps.

The polar component of the magnetization is small compared to the magnitude of the in-plane components and its angle, relative to the plane of the magnetic film, is a fraction of a degree. The rise time 200ps of the pumping pulse excites responses up to

several GHz (see the ferromagnetic response at high DC bias fields ~100kA/m below in Fig. 4.7 inset, Chapter 4). The initial state of the in-plane biased magnetization is shown in Fig. 5.4. As confirmed by the numerical simulations (shown below) the "*C*" configuration (Fig. 5.4) for weak DC magnetic bias (~4kA/m) and "*S*" configuration for

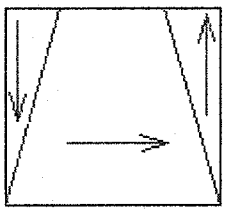

Fig. 5.4 The "C" state at low (~4kA/m) in-plane DC magnetic bias fields shows the orientation of the magnetization vector in the central and closure domains.

stronger fields (~15kA/m) yield good match to the observed distributions of the magnetization vector of the magnetic platelet.

The oscillations strongly depend on the local magnitude value of the effective internal magnetic field. These local fields are determined by the domain wall structure, which is a result of the competition between exchange, anisotropy, magnetostatic and Zeeman energies. In time domain responses (see, for example, the line curve in the first graph in Fig. 5.5), the first peak of curve includes the parametric response to the excitation pulse. The polar component of the magnetization is small compared to the magnitude of the in-plane components and its angle, relative to the plane of the magnetic film, is a fraction of a degree.

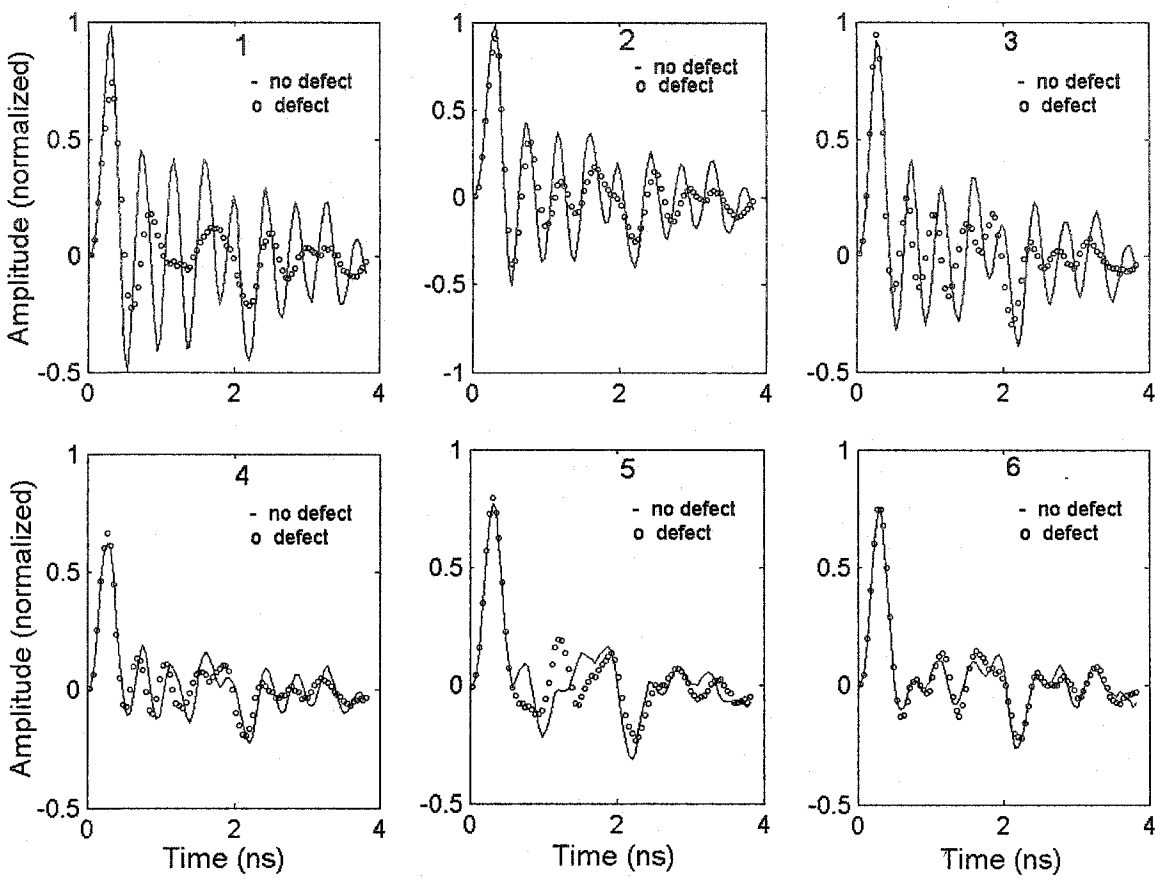

Fig. 5.5 Experimental broadband magnetization dynamics curves at different points of the magnetic platelets (with and without a pinhole, see the map in Fig. 5.3). The frequency of oscillations in and around the center (points #1, #2 and #3) of the uniform sample is 2.3GHz. Similar frequency was found at some points at the center of the sample with a pinhole (see Appendix 6 for more details). The oscillations at points #5 and #6 (and at some points around the pinhole) have complicated shape. At these points, no single frequency can be identified (possibly because of the probe spot is overlapping more than one mode, or this could be an evidence that in highly non-uniform internal fields around the defect the modes aren't spatially localized). The bias field magnitude was 4.6kA/m.

During the initial peak, the magnetization vector is lifted from its in-plane state by a fraction of a degree and then equilibrates back when disturbed by two weaker reflections (approximately 1.5ns and 3.8ns later) of the initial pumping pulse. These two reflected pump pulses are weak but still strong enough to affect oscillations of the magnetization vector by changing the magnitude and phase (see the exceptionally strong "negative" peak just after the second nanosecond after the excitation started). The qualitative response of a uniform magnetization to a broadband-pulsed excitation can be visualized by separating the spectral content of the excitation into three frequency bands. The parametric response of the magnetization oscillations is a response at frequencies below the resonance frequency (the Larmor frequency proportional to the amplitude of the local magnetic field). The magnetization parametrically follows the excitation field. At the same time, the frequency content of the pulse overlapping the ferromagnetic resonance frequency causes an initial precession of the magnetization about the excitation field axis (the resultant field in the rotating frame). During the parametric response (or the growth of the pumping pulse), the vector of the internal (local) field is changing and, consequently, the frequency of the precessional motion, which is always present, is shifted. A change in the magnetization vector is orthogonal to the parametric response. The high frequencies (beyond the value set by the magnetic bias field) are attenuated. After the pumping pulse ended the precession of the magnetization vector follows the evolution of the local magnetic field vector. If the amplitude of the bias field is low, ~4.6kA/m, the precessional response of the magnetic system is slow and the oscillations start after the pumping pulse stopped. At high magnetic bias field, see for example the insert in Fig. 4.7 inset, Chapter 4, showing the oscillations at 100kA/m, the response of

the magnetic system is very fast and the precessional motion is superposed on the parametric response. The relative delay of the polar magnetization response at the closure domain boundaries implies a lower local resonant frequency and a proportionally stronger resonant response at those locations.

The oscillations of the polar component of magnetization measured at various points of the samples (see Fig. 5.5) with curves for both the uniform and with central pinhole platelets) are normalized to the height of the initial peak. See the map in Fig. 5.3 for the exact point locations (Appendix 6 offers more details about magnetization oscillation curves). Each curve was extracted from the set of 92 spatial frames (scanning grid 96x96 points over the 6x6μm area) with the temporal step 45ps. Each data point on the curves is an average over an area of seven (from –3 to +3) neighboring scanning points. This represents an effective area the magnetic signal was taken (assuming the effective diameter of the Gaussian beam at the focus ~500nm). The number of oscillations is small, affected by the reflected pulses and there are not enough data points for a precise Fourier analysis. The Fourier analysis was done on reduced sets of points (without initial pumping and reflected pulses that were excluded from the data set).

The frequency of the oscillations (between the initial and first reflected pulses) over a large area of the central domain (the uniform sample) is ~2.3 GHz. The situation close to the pinhole (Fig. 5.5, dotted curves) is different. The "cusp" structures around the pinhole form a small domain wall (based, for example, on the MOKE spatial frames below). Consequently, the central domain is divided by quadrupolar symmetry of these "cusp" domain structures. A significant effect has the finite size of the probe beam. In comparison with the 240nm pinhole area, when averaging over a relatively large area,

(approx. 800nm in diameter) the tiny domain structures around the hole are mostly blurred. The dotted curve in #1 in Fig. 5.5 is an average signal from all complicated domain structures at the perimeter of the pinhole. Based on the analysis in Appendix 6, the oscillations on the left and right of the pinhole are close to the frequency of the uniform sample (~2.3GHz). Frequencies at points above and below the pinhole are shifted down to ~1.5GHz (a consequence of magnons launched from the lithographic pinhole).

The analytical expression (2.66) for the ferromagnetic resonance frequency of the infinite thin film (the Kittel formula) gives the value 2.13GHz (with the external in-plane DC bias 4.6kA/m, the saturation magnetization M_0 = 57kA/m and with the anisotropy field 477.6A/m).

Close the domain walls (points #5 and #6 in Fig. 5.5), a period of oscillations is longer than in the uniform magnetic areas, because of lower effective internal fields. In addition, the spot size is much larger than the width of the domain wall and no single frequency can be determined. There is not exact symmetry between oscillations at left and right domain structures (some asymmetry is seen also in X-t scans below; more, numerical simulations don't show such an asymmetry). The reason can be found in a small defect from the microfabrication process (below a spatial resolution of the MOKE microscope). The resonance curves in the closure domains are very similar, albeit the Fourier analysis offers a larger spectrum of frequencies (a small magnetic area and relatively large probe size). The similarity of resonance curves shows that the domain walls produce sufficient "isolation" and that the influence of the pinhole (located in the sample's center) on the magnetization oscillations at closure domains is minimal.

5.1.2 Spatial (2-D) distribution of magnetization.

The experiments were conducted at room temperature far below the Curie temperature of the magnetic material used. In addition, the effective microwave frequencies ~2GHz are assumed to be low enough to satisfy the low temperature regime, $\hbar\omega/k_B \sim 0.01\ K$, where k_B is the Boltzmann constant. The magnetic system (the spin wave or magnon pool) is assumed to be in thermal equilibrium. The occupational numbers of all the thermally excited magnons are maintained at thermal-equilibrium by the other relaxation processes. Initially, the magnetic bias field and the magnetization vector lie in the plane of the magnetic thin film, with the exception of the closure domain walls near the edges of the magnetic squares, as seen in Fig. 5.3. The orientation of the initial state vector of the magnetization is shown in Fig. 5.5. In the uniform square platelet, the spatial response is strongly controlled by the nonuniform magnetization distribution associated with the closure domains transverse to the bias field direction. For low amplitude transient excitations, the closure domain structures yield a static, spatially non-uniform magnetization and effective field that plays a dominant role both in the initial response and the subsequent small angle evolution of the magnetization. The existence and the form of the domain's form in the structure is a result of the competence of the exchange interaction between individual magnetic moments (assuming the spin-orbital interaction is negligible) and the demagnetizing field. The demagnetizing (dipolar) field is a consequence of the shape of the patterned magnetic thin film. The anisotropy of the Permalloy thin film is very small compared with the saturation magnetization, and its influence is assumed weak.

Two-dimensional images of the polar magnetization change across the entire uniform specimen are shown in Fig. 5.6 for different instances (frames were re-normalized to show details) during the oscillation. At the time around 200ps, on the initial peak, strong spatial contrast has developed along the closure domain boundaries (the static magnetization is arranged in a "*C*"-state) with an inclination towards $+y$ and $-y$ in the left and right closure domains, respectively, while the central magnetization is along $+x$, in Fig. 5.4. The gray color of the response (in the gray scale) corresponds to no change (witness the border around the specimen.).

By the time the central magnetization has reached its initial peak, the significant change along the domain boundaries (the parametric response) is delayed, Fig. 5.6 (the frames at 90ps, 180ps and 360ps) and Fig. 5.7 (1-D rendering across the sample). Qualitatively, the response of a uniform magnetization to a broadband-pulsed excitation was discussed in Section 5.1.1. The response to the pumping pulse of the large central domain and two smaller closure domains is uniform by a fraction of a degree (a small angle excitation, ~0.1°). All spins in those areas of the magnetic platelet are lifted by the pumping magnetic field. The internal magnetic fields are non-uniform because the existing magnetic domains and the relative delay of the polar magnetization response at the closure domain boundaries imply a lower local resonant frequency (and a proportionally stronger resonant response at those locations). The 4μm size of these structures is large enough that such a decomposition of the initial response into locally different behaviors is still viable. The combination of magnetostatic and spin wave characteristics of the eigenmodes of the system creates a hybridized character. These excitations exist on well-separated length scales in this geometry, and it is possible to

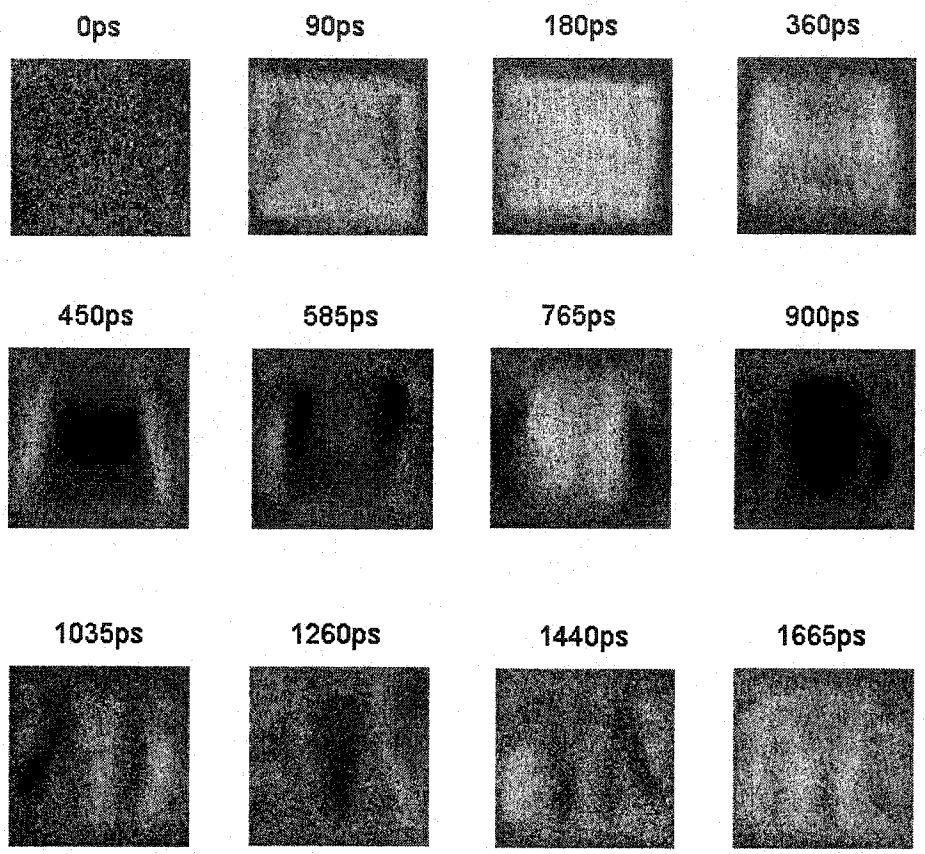

Fig. 5.6 Selected experimental images of magnetization dynamics evolution in 4μm square, at dc magnetic bias (in +x, horizontal right direction) 4.62kA/m, during and after short out-of-plane pulse excitation. Gray corresponds to no change of magnetization. The spatial scale is 5.2μm.

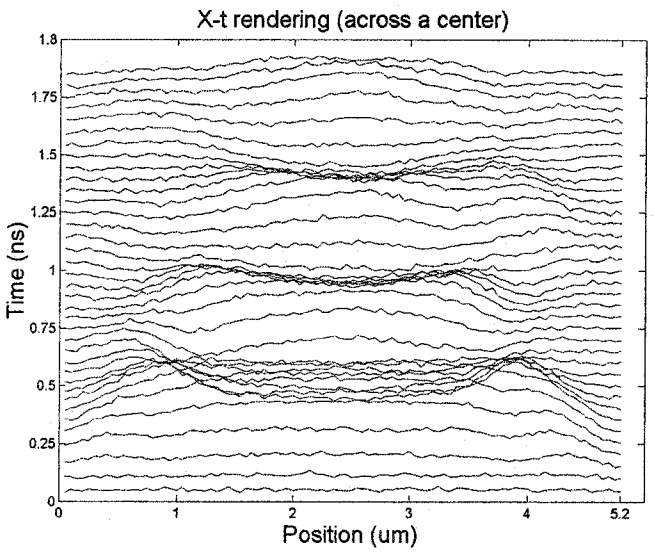

Fig. 5.7 1-D rendering of a set of 2-D frames (as in Fig. 5.6). Each curve represents a horizontal cut through a center of the magnetic platelet.

observe their interactions in the regions of spatially non-uniform magnetization. The result is the relaxation of the excited magnetic system and a decay of each of the wave-like oscillations. The central (uniform) excitation and two smaller (uniformly excited) areas at the closure domains interact with the non-uniform fields at the domain walls. If there were no domain walls, the initial excitation would be uniform ($k=0$) over all the area of the magnetic platelet. Then the relaxation processes that include the uniform mode (for example, the magnon-phonon, the two- or the three-magnon processes) would come into account but the magnitude of the magnetization vector is not preserved.

In the present case, the magnetic area was divided into three parts by the very thin domain walls (estimated thickness of the Nèel-like domain wall is 5nm). If these walls isolated the neighboring domains, each of those domains could be assumed as independent and the relaxation processes of the uniform spin wave mode ($k=0$) would work. However, the narrow "potential valleys" connect the large central and the small closure magnetic systems, which interact each other. From the point of view of the complete magnetic square, the initial set of magnons (excited by the spatially uniform pumping) has non-zero wave vectors ($k\neq0$) and in a following relaxation, $k\neq0$ magnons will decay into other $k\neq0$ magnons (while $|\mathbf{M}|$=const). In general, the energy and the momentum in these decay processes must be conserved. The two-magnon process requires a polycrystalline sample or a sample with defects but if the $k=0$ magnon is involved the resulting $|\mathbf{M}|$ is not constant. The three-magnon confluence process does not preserve $|\mathbf{M}|$ if $k\neq0$ magnons are involved. This last process cannot also relax the uniform ($k=0$) precession for the reason that both the energy and wave vector must be preserved (for the non-local dipole-dipole induced interaction and the weak local

anisotropy field). The three-magnon splitting process that includes the $k=0$ magnon is possible for a field not exceeding the saturation field. The four-magnon process can relax the non-uniform magnons as well (in a large angle excitation).

Other dissipative channel, the magnon-conduction electrons interactions and eddy currents, depend on material parameters of the metallic film. Let us assume the conductivity of the Permalloy film is $5x10^6$ Ωm, $\mu_0=4\pi\ 10^{-7}$ H/m and relative permeability $\mu_{rel}=2000$ (maximal estimated value, could be, especially at high microwave frequencies much smaller). For microwave frequencies ~2GHz the skin depth (accordingly formula 2.75) is ~110nm. The thickness of the magnetic film is 15nm and, consequently, a microwave field (with a wavelength significantly larger than d) uniformly penetrates entire thin film sample and resulting influence of eddy currents is very small. If the magnetization distribution is non-uniform across the thin film element, it could drive conduction electrons opening an additional channel for a dissipation of energy of a magnetic system. However, the resulting contribution of this interaction with conduction electrons depends on the change of the magnetization, which is small (a fraction of degree for the out-of-plane angle of the magnetization vector).

The following model can be proposed for a micron sized magnetic element. The platelet is composed of five membranes, each having its own spatiotemporal evolution and that interact with each other. Any of these areas have a finite size; the magnetization vector points in various directions; its temporal evolution is different and each represents a spin wave resonator (or a pool of traveling and reflected spin waves). The first is the largest (central) area, which is connected to the two, left and right, very narrow walls. The left and right edge domains are the last two areas connected to the narrow "wall"

domains. The narrow walls oscillate at lower frequency than the neighboring large domains and, because they are not in a phase, each low-frequency wave launches a new spin wave in the left and right spin wave reservoirs.

The system of magnons excited by this nonuniform magnetization distribution (with finite micron and sub-micron laterally sized features) is composed from magnons with a broad set of wave vectors (wavelengths). Therefore, wide spectrum of $\boldsymbol{k}\neq 0$ magnons exists (some, initially, having very low amplitudes); the energy and the momentum between these $\boldsymbol{k}\neq 0$ oscillations can be transferred. The pumping field excites the uniform-like mode $k\sim 2\pi/L$ (where the L, ~micron, is the typical lateral size of each domain) and the following magnon-magnon interactions transfer this energy into $\boldsymbol{k}>>0$ magnons. The following processes are the interactions with phonons and conduction electrons that definitely take away the energy from the magnetic system into the crystal lattice. This representation preserves the magnitude $|\boldsymbol{M}|$ that accordingly Sparks [2-23] is given by the formula as $|\boldsymbol{M}|=M_0V-(g\mu_B/2)\sum_{k\neq 0}n_k$, where M_0 is the saturation magnetization, V is the volume and n_k is the number of magnons with a wave vector $\boldsymbol{k}$.

When a sub-micrometer pinhole is patterned in the center of the platelet, the static magnetization accommodates itself to the change by forming cusp-like structures (structures with quadrupolar symmetry with four domain walls pointing along the diagonals into the corners of the square) at the edges of the hole normal to the bias field direction. See Kerr images in Fig. 5.8 and Fig. 5.7 (1-D rendering across the sample). A resulting effect allows the magnetization to streamline around the hole, Fig. 5.8 (the frame at time 450ps), causing the spatial pattern of magnetization oscillation response.

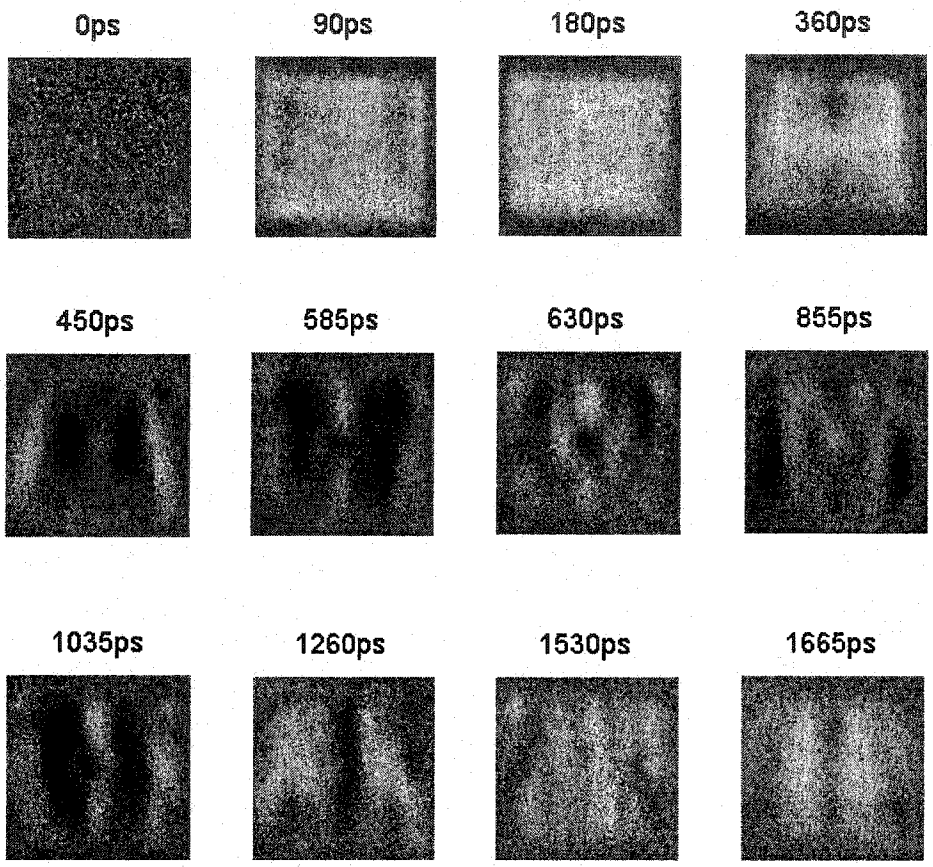

Fig. 5.8 Selected experimental images of magnetization dynamics evolution in a 4μm square with a small 240nm diameter hole in the center, at dc magnetic bias (in +x, horizontal right direction) 4.62kA/m, during and after short out-of-plane pulse excitation. Gray corresponds to no change of magnetization. The spatial scale is 5.2μm.

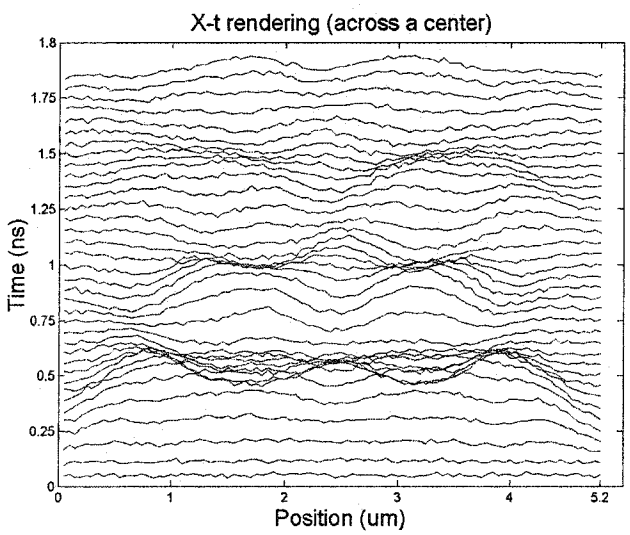

Fig. 5.9 1-D rendering of a set of 2-D frames (similar as in Fig. 5.8). Each curve represents a horizontal cut through a center of the magnetic platelet.

The sensitivity of this circular pinhole also depends on weaker variations of the static magnetization. Two-dimensional images of the polar magnetization that change across the entire non-uniform specimen are shown in the Fig. 5.8 and the cut through a center in Fig. 5.9. Such structures have been imaged by magnetic force microscopy for larger holes in Permalloy films [Ref. 107, Chapter 2]. The formerly uniform magnetization in the center of the platelet presented a flat effective field for a uniform mode of oscillation, whereas the new "potential surface" has a quadrupolar variation as a function of angle about the center. Interactions in a spin wave reservoir are similar to those of the uniform platelet, but including a central domain divided into four sub-domains with smaller sizes changes the model of the uniform platelet and the spectrum of magnons.

The existence of the pinhole allows us to use the approximative theory of Sparks [Ref. 23, Chapter 2]. This approach provides a calculation of the relaxation time for a magnon-scattering process caused by a pit in an infinite volume. Assuming that our 240nm diameter large hole at the center of the platelet can represent such a defect and that the angle θ_k between the magnon and in-plane magnetic field is very small, the equation $T_{pinhole}=2\pi^2 M_0 (V_{pinhole}/V)[3 \cos^2(\theta_k) - 1]/\cos(\theta_k)$gives a typical relaxation time 2-3ns. The degenerate magnons created in the scattering process have wavelengths approximately equal to the pinhole diameter. The values of the relaxation time and the wavelength are consistent with values typical in the current experiment and, consequently, the two-magnon processes in the magnetic element with the pinhole can take place. The investigation of the spatial distribution and temporal evolution of the magnetization in Fig. 5.8 (also seen in the movie) shows the 180°-phase shift between the peaks of the magnetization at areas between points #2-6 and #3-7 (in Fig. 1,

Appendix 6). It suggests that the energy of the magnons traveling from left to right, after the interaction with the pinhole, is transferred into the energy of magnons traveling in perpendicular directions.

5.1.3 One-dimensional X-t scans at DC magnetic biases 3, 3.6, 4.6, 7.6, 18.3, and 60kA/m.

A "one-dimensional movie" of the response is obtained by assembling horizontal cross-section or line-scan measurements for a high density of time-sampling points into single 2-D images, as in Fig. 5.10 and Figs. 1 - 6 in Appendix 7 (X-t scans at DC bias 3, 3.6, 4.6,7.6, 18.3, and 60kA/m). These "x vs. t" (X-t) renderings of the signal provide additional insight into the evolution of the non-equilibrium magnetization. A striking feature of these images is the apparent spatially non-uniform damping of the modal oscillation in the central domain. This situation represents a cleanly realized case of indirect damping of magnetization oscillations. The non-uniform magnetization at the closure domain boundaries gives rise to magnon-magnon scattering, converting energy from the "uniform" (longer wavelength) mode of the central domain into shorter spin waves where it disappears below the spatial resolution of the measurement. The Fig. 5.10 shows the differences between spatiotemporal responses of the structures with (left) and without (right) pinhole when low (top row) and high (bottom) magnetic bias fields are applied. The higher in-plane magnetic bias field suppresses the weak "cusp" structures around the pinhole. The result is that the creation of shorter wavelength magnons is suppressed and the magnon-magnon interactions are weak.

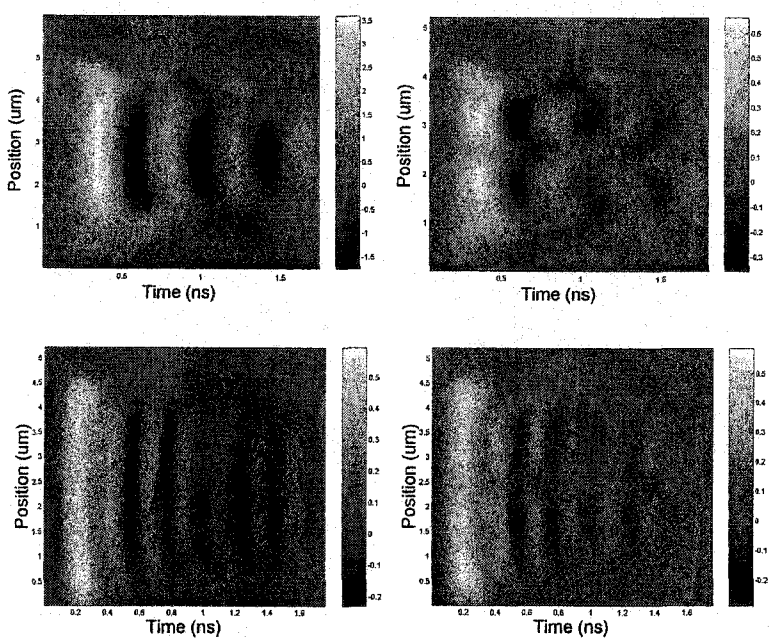

Fig. 5.10 One-dimensional X-t experimental scans of the magnetization dynamics similar to the Permalloy elements without (on left) and with (on right) the pinhole at the DC magnetic bias 4.62kA/m (upper row) and 18.3kA/m (at the bottom). The length of time interval is 1.75ns and 1.8ns respectively. The temporal step during scanning was 12ps. Each 6μm-long scanning line consists of 128 experimental points of the polar Kerr signal (x-direction is represented by the vertical axis).

Both samples, with and without pinhole, show the typical "V" and "double-V" profiles respectively (clearly visible in the right column of Fig 5.11 and Fig.5.12). The measurements of the slopes of without and with pinhole (at the bias 4.6kA/m), give the velocities 850m/s and 610m/s respectively of the spin wave propagation (launched from the domain walls). The first velocity value corresponds to the wave vector $2.5 \times 10^5 cm^{-1}$ or the wavelength 250nm. The velocity relative to the pinhole is about one half of those values (approximately 315m/s).

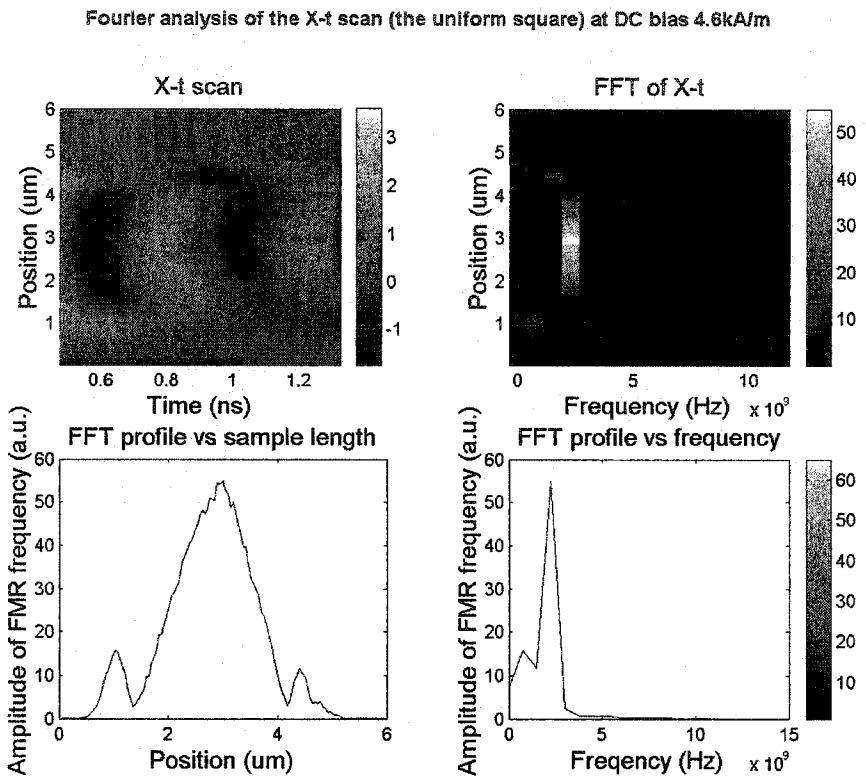

Fig. 5.11 The Fourier analysis of X-t scans of 4μm squares. A few periods of oscillations (left, up) were processed by the Fourier transform (right, up). Lower satellite frequencies at the domain walls emerged.

The Fig. 5.11, 5.12 and 5.13 show the details of the Fourier analysis of the X-t scans. The weaker internal magnetic fields at the domain walls and at the edges around the pinholes give a rise of the lower frequencies of magnetization oscillations. The number of experimental points used in the frequency analysis was decreased to eliminate the influence of the pumping and reflected pulses and resulting resolution is ~0.7-0.8Ghz. The Fig. 5.14 shows the result of a comparison of experimental frequencies with "Kittel" formula (2.66) and no difference between a frequency of the uniform and

internally patterned platelet. The satellite frequencies related to the magnons at the areas of the closure domain walls are shifted by ~0.7GHz down from the main frequency value.

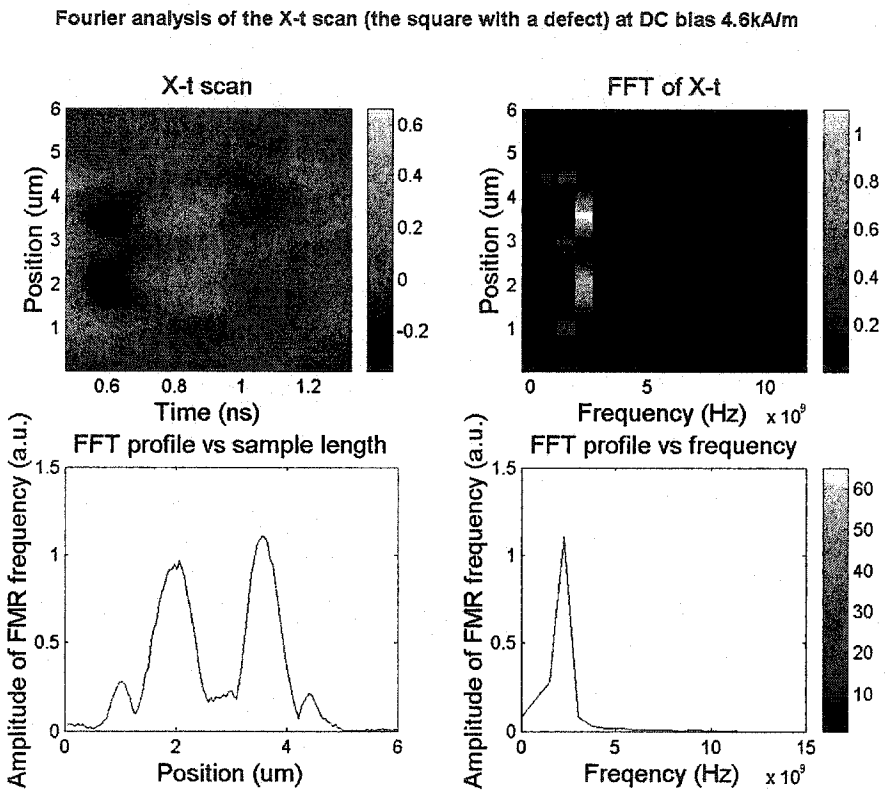

Fig. 5.12 The Fourier analysis of X-t scans of 4μm square with a pinhole. Additional satellite frequencies showed up at the area of the pinhole.

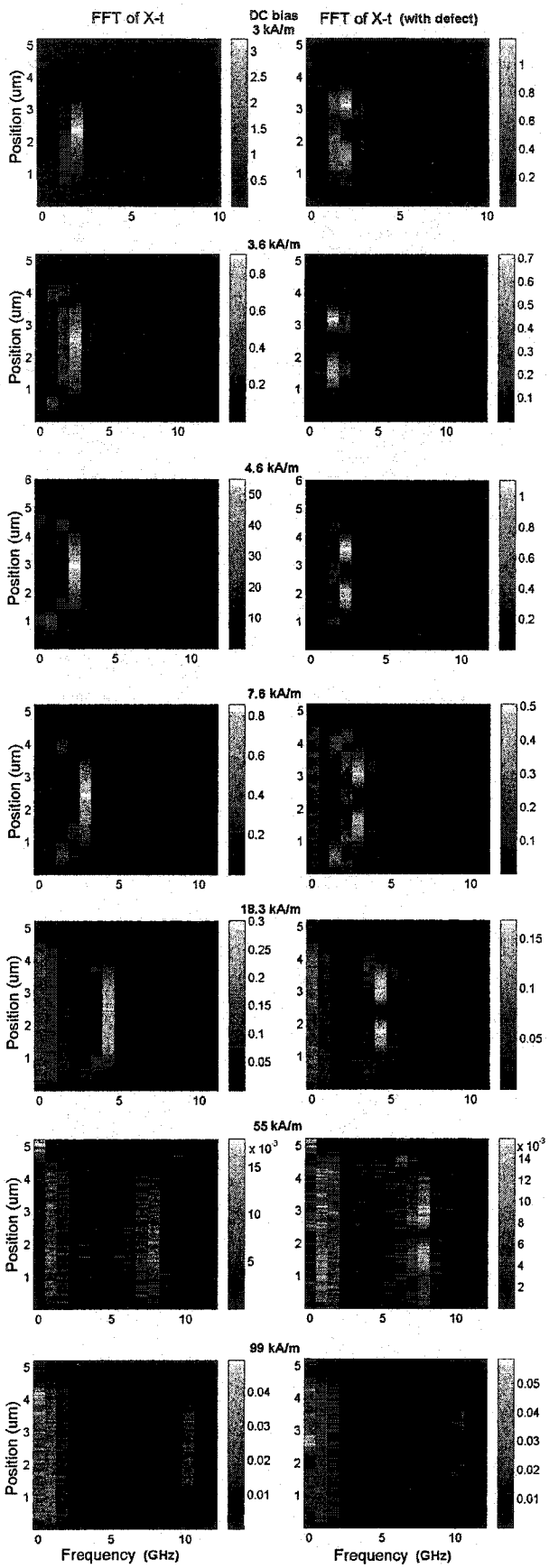

Fig. 5.13 The Fourier analysis of X-t scans of 4μm squares w/o (left) and w/ a pinhole (right). The frequencies of the ferromagnetic oscillations, excited by the pumping pulse, follow (from the top to the bottom) the increasing magnetic bias field. The lower frequency oscillations close to the edges of the platelet (at the domain walls) are visible providing the evidence of weaker internal fields in those areas. Applying higher bias field (≥18kA/m) suppresses the satellite frequencies at the edges of the pinhole.

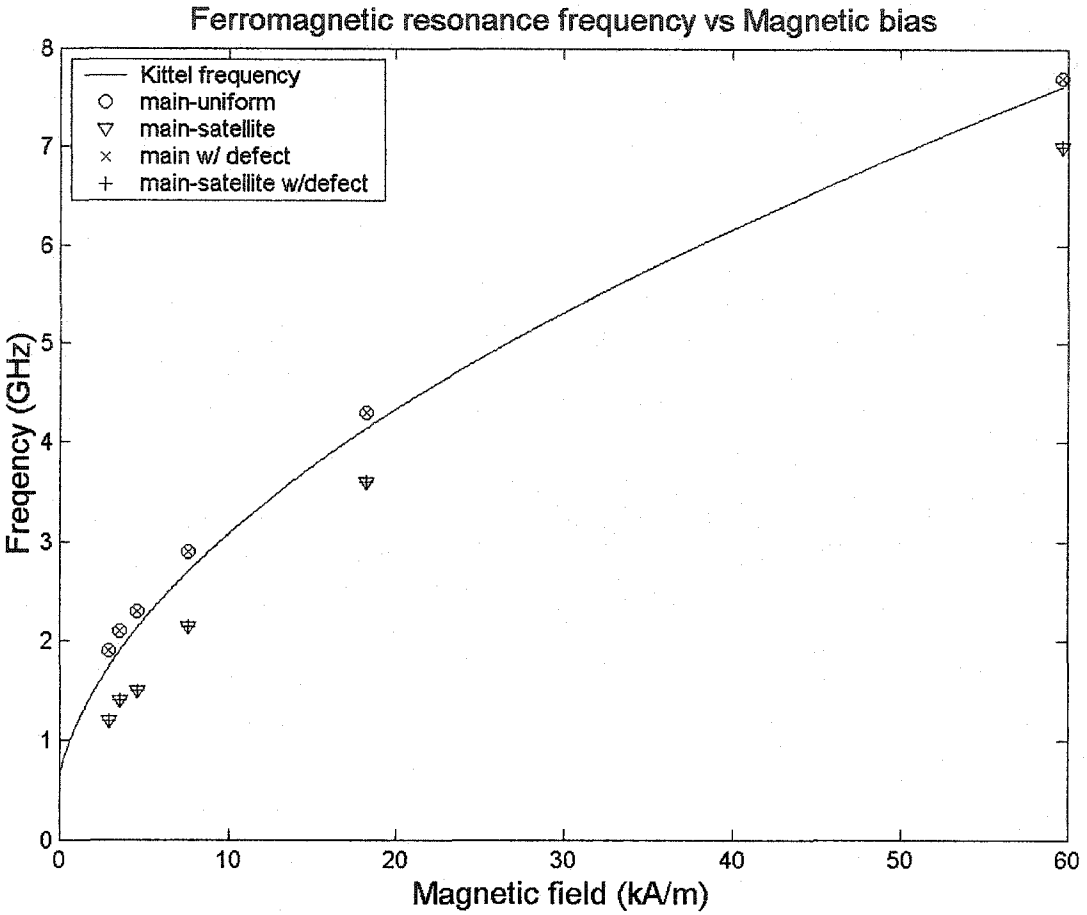

Fig. 5.14 The frequency dependence versus the magnetic field bias of the polar component of the magnetization at the center of the platelet, compared with the theoretical "Kittel" formula (solid line) for the uniform infinite film. The displayed experimental points are for the frequencies of the uniform and internally patterned 4μm squares (the same samples as analyzed in Fig. 5.13). The experimental error resulting from Fourier processing is approximately ±0.4GHz.

5.1.4 *Numerical simulations of rectangular elements and a comparison with the experimental results.*

The broadband magnetization dynamics of patterned polycrystalline thin film ferromagnetic $Ni_{80}Fe_{20}$ elements was studied numerically via micromagnetic simulation. The LLG model reproduces the observed modal oscillation symmetry and reveals in detail that the observation of spatially nonuniform damping in the experiment is a result of conversion of energy into shorter wavelength modes near the domain boundaries.

Fig. 5.4 shows the initial "C" state for the numerical simulation at low in-plane DC magnetic bias fields. The "S" initial state (not displayed) provides the starting point of the simulations for magnetic bias fields higher than 8kA/m. The following parameters were used in LLG equation [Chapter 2, Ref. 100]: exchange constant 1.05×10^{-11}J/m, saturation magnetization 57kA/m, anisotropy field 478A/m, dimensionless damping constant 0.013 (0.5 for an initial state computation), and a lateral cell size of 15.6 and 7.8nm (on 256×256 or 512×512 grids respectively). The single value of the damping constant was satisfyingly used at bias fields from 3 to 18kA/m and no further dependence of the damping constant on the magnitude of the bias field was investigated. Calculation results on both grids give very similar results (2% difference of average values over the area of the sample) and the 256×256 grid was used for most of the simulations. Convoluting with a Gaussian kernel of width 500nm to mimic the experimental view, albeit at a slightly higher spatial resolution, processed simulation data.

A series of test simulations and comparisons with the experimental ferromagnetic response curves at various magnetic bias fields was done to optimize the values for the

damping constant and saturation magnetization. As shown in Fig. 5.15, the values of the saturation magnetization and phenomenological damping constant 57kA/m and 0.013 respectively provide good qualitative agreement with the experimental curves[1]. The saturation magnetization value agrees with the experimental dc SQUID measurement done in Ref. 89, Chapter 2. The anisotropy field influence is very small and numerical simulations confirm this experimental observation. The slight discrepancy in the peak levels in the comparison between experiment and model for the first series of oscillations is attributable to a small difference in the shape between the actual transient magnetic pulse and the one extracted from the magnetization dynamics curve at DC bias 100kA/m.

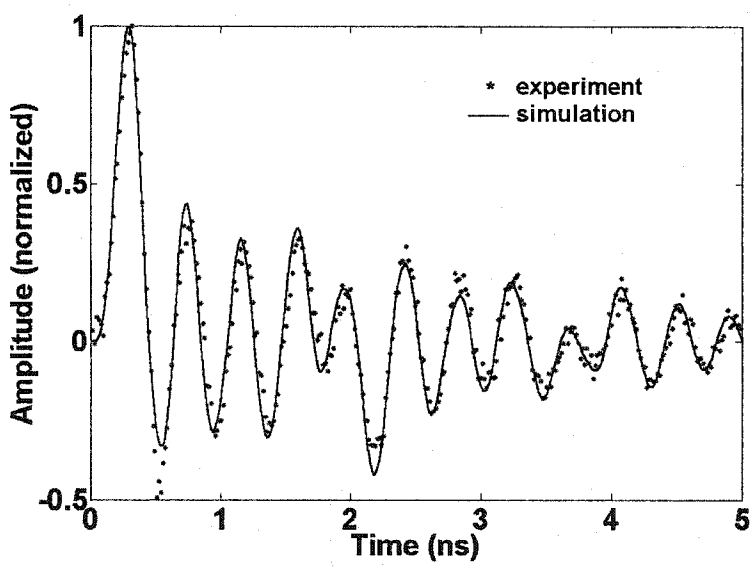

*Fig. 5.15 The local response of the polar component of the magnetization at the center of the platelet for the static magnetic field 4.6kA/m (*line), and the corresponding numerical simulation (solid line) are shown.* Details of the spatiotemporal responses of

[1] The experimental and simulation data (as bitmaps) were subtracted and the histogram of the resulting bitmap showed narrow distribution of pixels documenting the agreement between exper. and simul. data.

the polar magnetization components and related simulated distributions are compared in Fig. 5.16. The closure domain walls and their delayed response to the excitation pulse are clearly visible in both the uniform and non-uniform magnetic platelets biased with the in-plane field 5.6kA/m. The quadrupolar symmetry of the spatial magnetization distribution is a consequence of the pinhole in the center of the platelet (displayed in both, experimental and numerical frames).

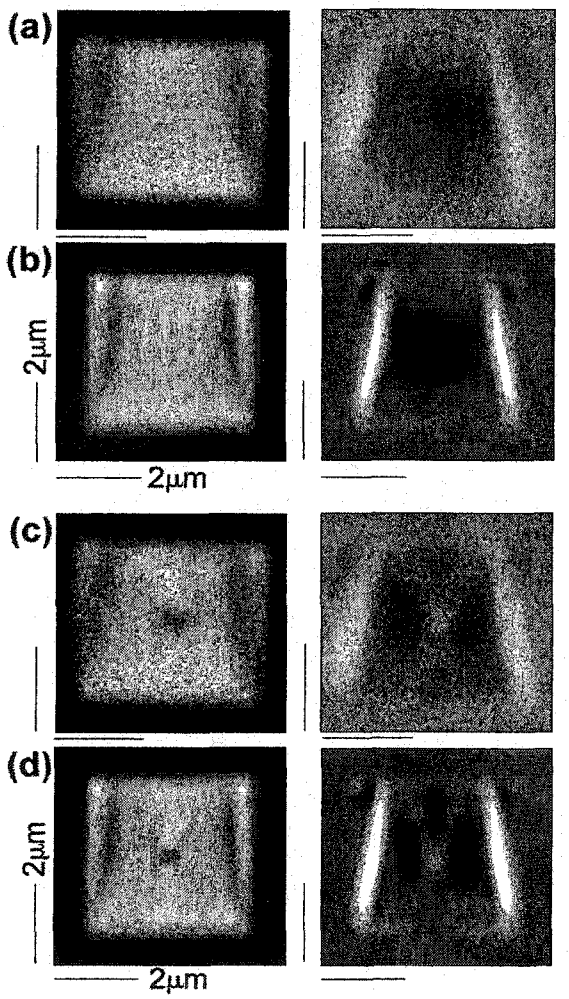

Fig. 5.16 The experimental (a, c) and simulation (b, d) spatial images of polar magnetization component at 225ps (left) and 450ps (right) from the start of the magnetic excitation. Cell size in the left and right simulation frames was 15.6 and 7.8nm respectively. The maximum (white) corresponds to the 0.1° angle of the polar magnetization component. The 4.6kA/m DC bias field direction is parallel with the horizontal axis of the squares. The frames in (c) and (d) show samples with the central pinhole. The simulated images were blurred by convolution with a Gaussian kernel.

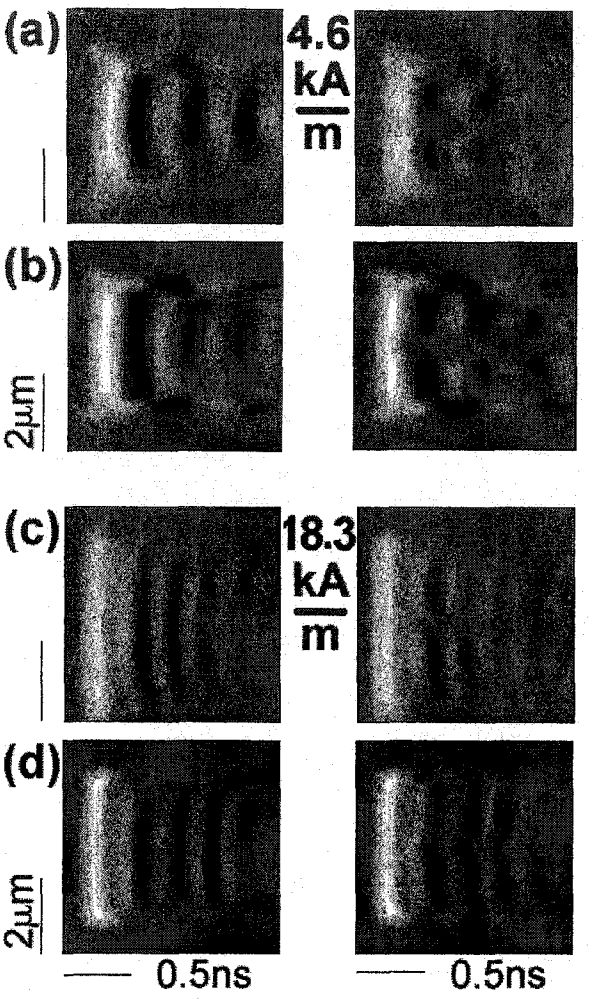

Fig. 5.17 The polar magnetization component images from the experiment (a,c) and the LLG equation (b,d) at DC bias 4.6kA/m (a,b) and 18.3kA/m (c,d) based on "X vs. t" signal rendering. The experimental cross-section, a 40nm step scanning line through the center of the platelet, is parallel with the DC bias field direction. The sample with the pinhole is on the right. The compilation of successive snapshots was obtained using 12ps steps and simulation data were processed by convolution with a Gaussian kernel.

The dominant spatial mode excited by the broadband magnetization excitation reflects this symmetry, as seen clearly in Fig. 5.16 (c, d) for both the experimental measurements and the micromagnetic simulations. Note, in comparison with Fig. 5.16 (a, b), that the other spatial features associated with the closure domains are identical, with and without a central pinhole.

The X-t renderings (Fig. 5.17) of the experimental and numerical data at low and high magnetic bias fields display the "V" (the uniform sample) and "double-V" (the sample with the pinhole) shapes.

Spatiotemporal responses extracted from non-convoluted numerical data at DC bias 4.6kA/m are shown in Fig. 5.18 (with the results from the sample with a pinhole on

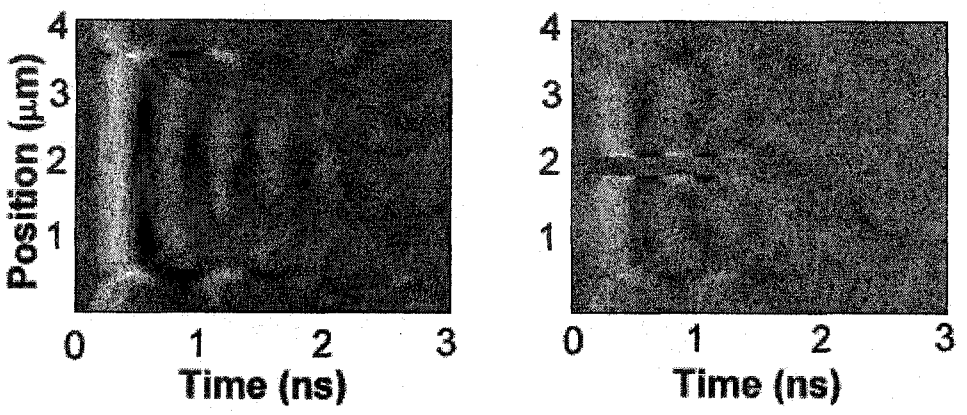

Fig. 5.18 The spatiotemporal evolution of magnon-magnon scattering at DC bias 4.6kA/m extracted from the numerical solution of LLG equation. The data were not processed by convolution with a Gaussian kernel.

the right). Turning off the Gaussian blur of the simulation makes this process very clear. The energy of the "uniform" mode is converted to shorter wavelength modes by magnon-magnon scattering in the non-uniform effective field near the domain boundary and around the pinhole (right, resulting in a "double-V" X-t profile). The influence of these interactions propagates across both specimens (with and without the pinhole) at velocities 800m/s and 590m/s respectively. The agreement with experimental values (Section 5.1.3) 850m/s and 610m/s is within a 20% error. The short wavelength modes are below the spatial resolution of our microscope, giving rise to a characteristic "V"-shaped envelope as they propagate at a constant speed toward the center of the specimen (along the direction of the in-plane magnetic bias field). Indirect damping due to magnon-magnon scattering along the domain boundaries results in the apparent

relaxation of accelerated precessional oscillation everywhere in the sample, although it is position dependent (discussed in part 5.1.3). Returning to the previous figure with blurred images (Section 5.1.3), the X-t scans at the bottom of Fig. 5.10 show that the magnetization at DC bias 18.3kA/m (with "S" initial state) is uniform near the hole, and, consequently, the magnon-magnon scattering is suppressed relative to that near the closure domains. The resulting relatively high DC magnetic bias is confirmed by the similar results of scanning at higher DC bias fields (discussed in part 5.1.3).

The temporal changes of the full magnetization vector (trajectory of in-plane and out-of-plane angles versus time) at two locations are illustrated by LLG simulation in Fig. 5.19 (assuming a reflection-free pulse for clarity). A characteristic disruption of the magnetization oscillations is seen at time 1.2ns in the left panel, corresponding to a position 1μm left of center.

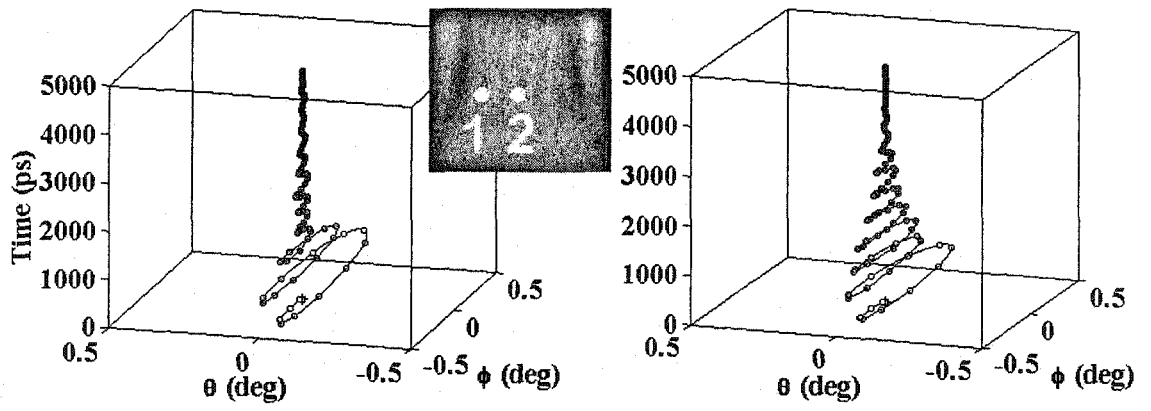

Fig. 5.19 Full trajectories of the small-angle changes in orientation of the magnetization vector at two different points of the platelet (1, a micron from the left edge, 2, at the center). The spherical coordinates (delta ϕ is in the plane of the specimen and delta θ is perpendicular to it) were taken from simulations with the DC bias field 4.6kA/m.

In contrast, the precession decays smoothly at the center of the specimen during the entire time interval shown.

The numerical simulations (based on two-dimensional model of an ideal crystal without any surface roughness, grains and grain boundaries or by patterning affected edges) show good agreement with the experimental results (relatively to the experimental spatial and temporal resolutions). Both experimental and numerical frames reveal a rich world of spatially non-uniform modes of the magnetization oscillations. The external, demagnetizing and the exchange energies determine these modes. The anisotropy energy of the thin Permalloy polycrystalline film is small when compared with the other interactions, as confirmed by simulations with a neglected anisotropy field. The magnetic system is excited by a small amplitude of the transient pulse and the intrinsically nonlinear character of the LLG equation is sufficient to support magnon launching, magnon-magnon scattering, and finally, the relaxation of the entire magnetically excited platelet back into the equilibrium. The competition between exchange and demagnetizing magnetostatic interactions causes the internal magnetic fields to be spatially and temporarily dependent.

The semi-classical LLG equation based on the condition of a constant magnitude of the magnetization provides qualitatively and quantitatively correct results when the important material constants (the saturation magnetization and the phenomenological damping constant) are properly chosen. The magnitude of the magnetization vector is preserved that implies three-magnon scattering and confluence do not play important role except the samples with lithographic pinholes when additional magnons with a

wavelengths at the scale of the pinhole's size can be generated. The two-magnon and magnon-phonon play important role in the scattering and decay processes.

5.1.4.1 Permalloy square at DC bias 4.6kA/m, 2-D frames.

The complete comparison of the experimental and simulation spatial frames (at magnetic bias field 4.6kA/m) and the temporal evolution (for the first 3 nanoseconds) is shown in Fig. 5.20 (a, b, c) for the uniform square and in Fig. 5.21 (a, b, c) for the internally patterned one. Similar comparison of the experimental and simulation spatial frames (at magnetic bias field 18.3kA/m) is shown in Fig. 5.22 and 5.23 for the uniform and internally patterned platelet. The experimental and simulation data are on the top and bottom rows respectively. The numerical simulations are in good qualitative agreement with experimental measurement (taking into account spatial resolution of the MOKE microscope). All-important features related to the initial states, the closure domain structures and small domain walls around the artificially created pinhole are reproduced numerically (on both the spatial and temporal scales). On the gray scale white corresponds to maximum value of the polar component of magnetization (gray corresponds to no change, witness the border around the specimen).

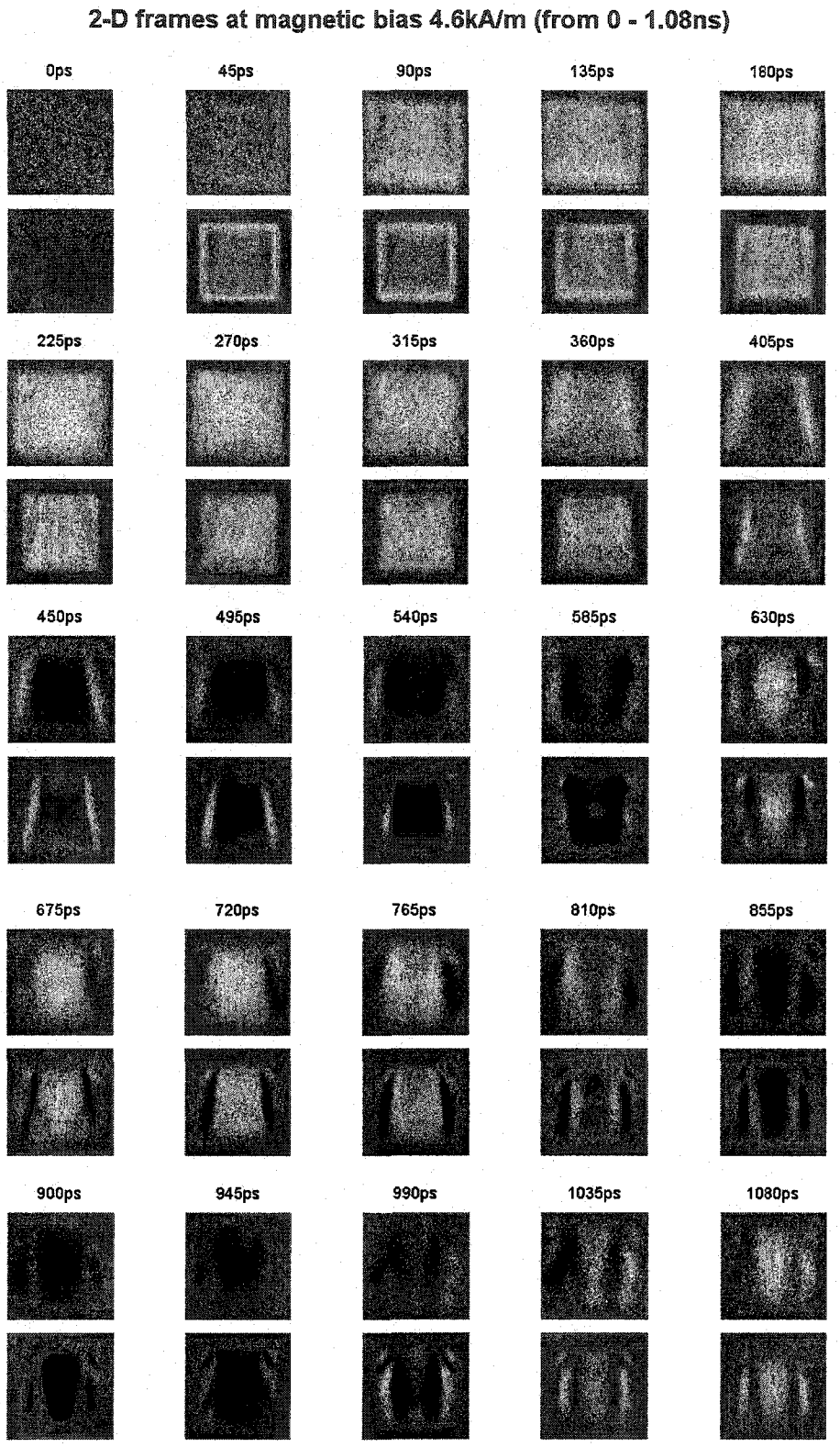

Fig. 5.20a Experimental (top) and numerical results of the 4μm platelet (1.1-2.2ns)

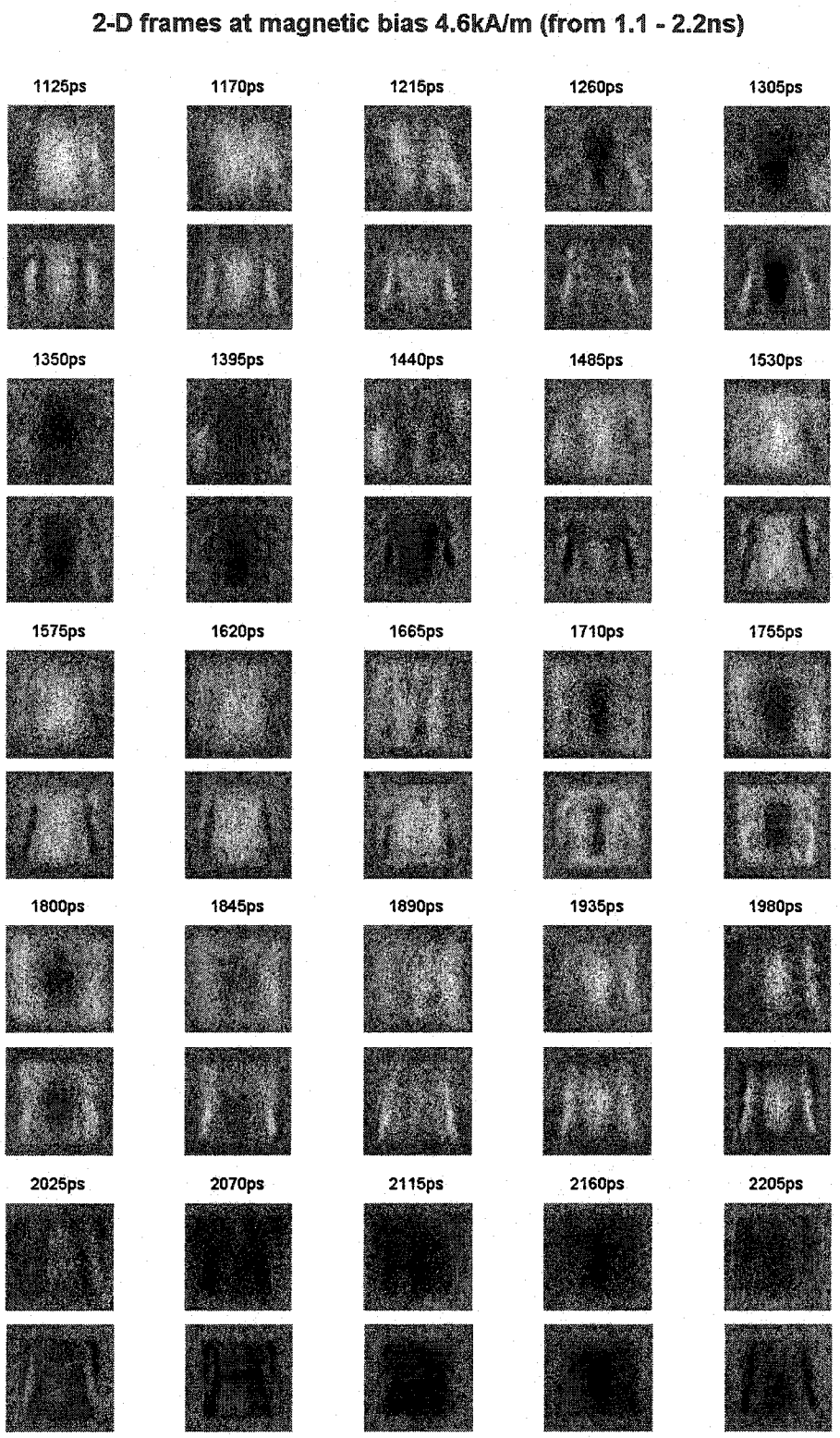

Fig. 5.20b Experimental (top) and numerical results of the 4μm platelet (1.1-2.2ns).

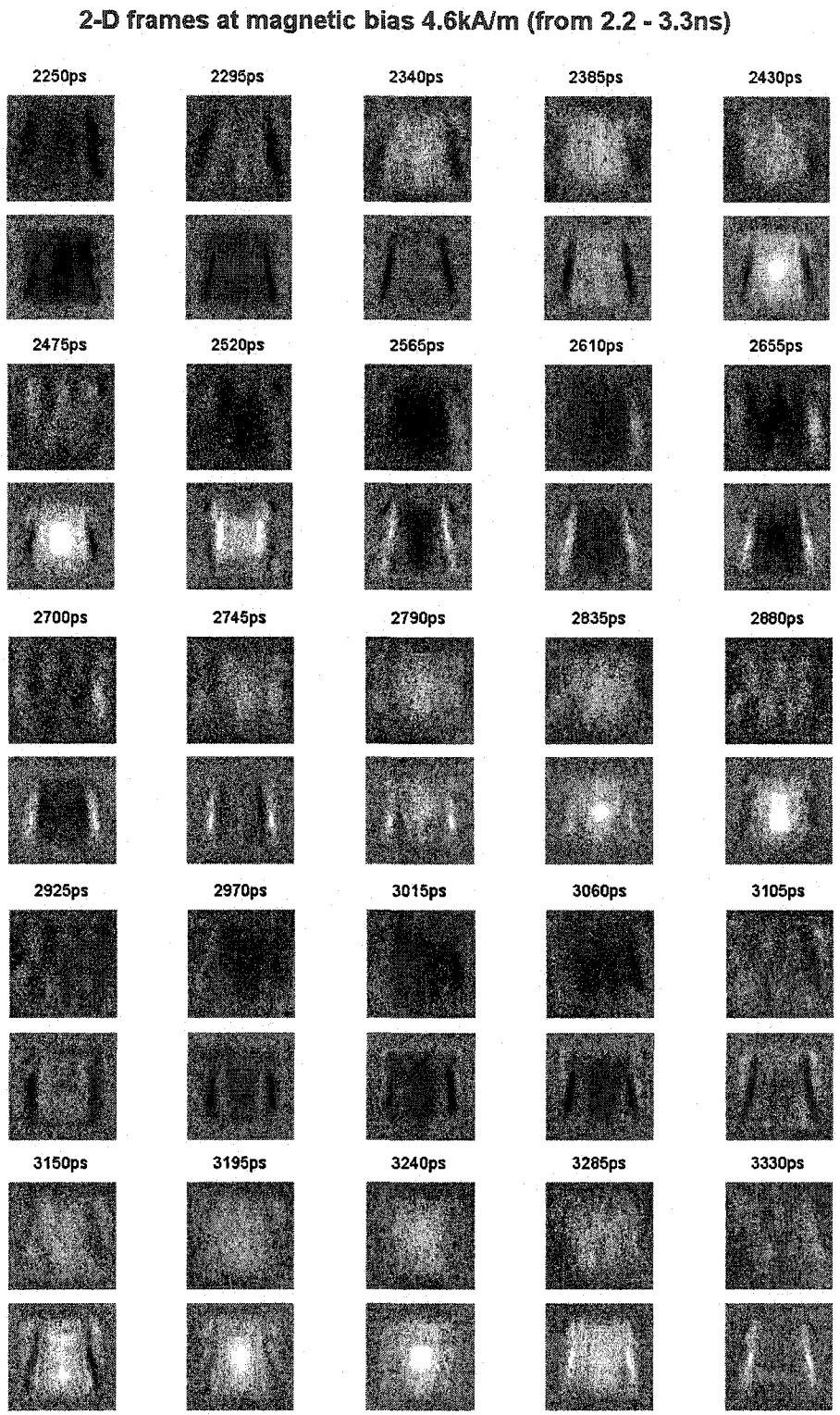

Fig. 5.20c Experimental (top) and numerical results of the 4μm platelet (2.2-3.3ns).

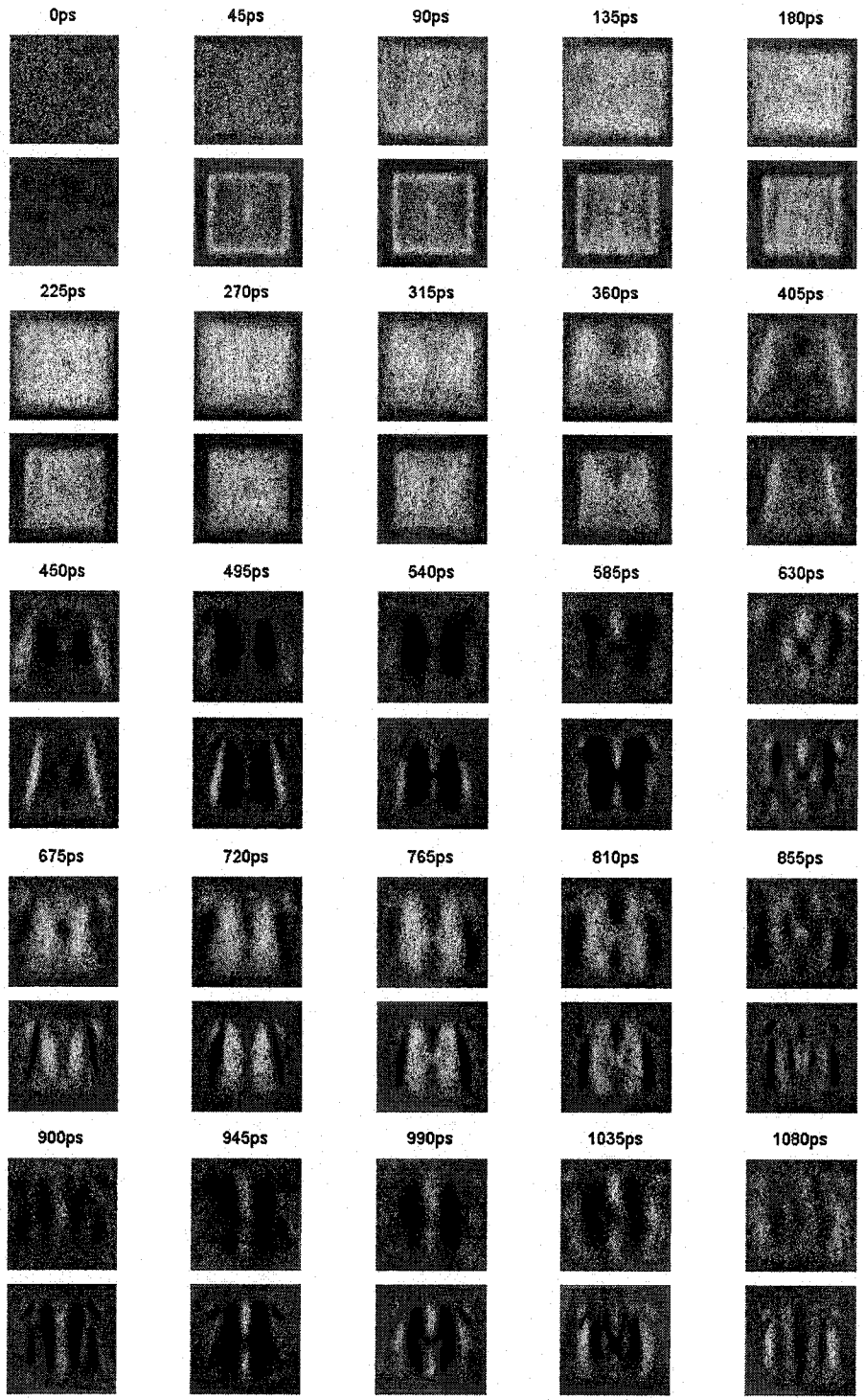

Fig. 5.21a Experimental (top) and numerical frames, 4μm platelet w/ pinhole (0-1ns).

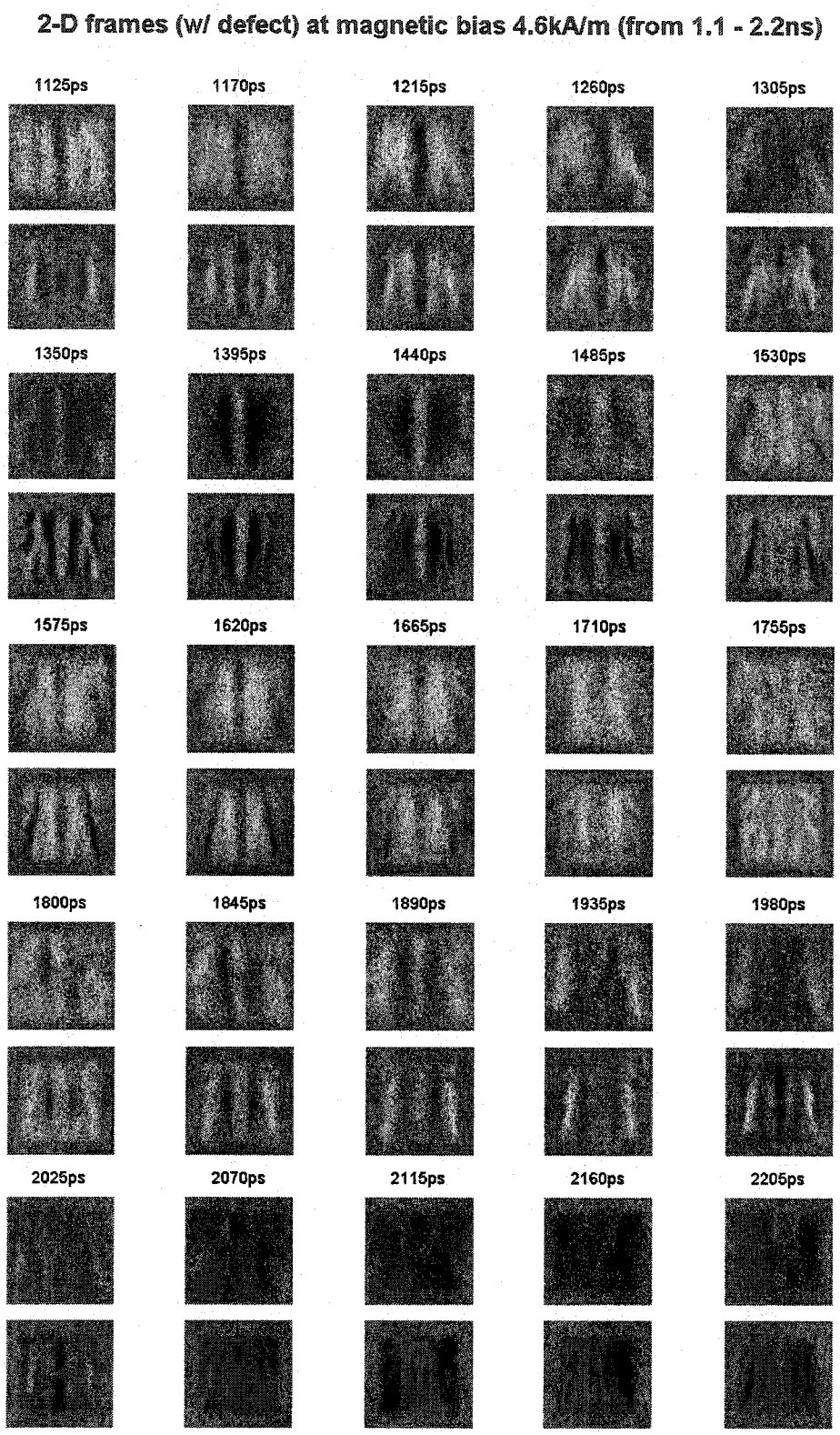

Fig. 5.21b Experimental (top) and numerical frames, 4μm platelet w/ pinhole (1-2ns).

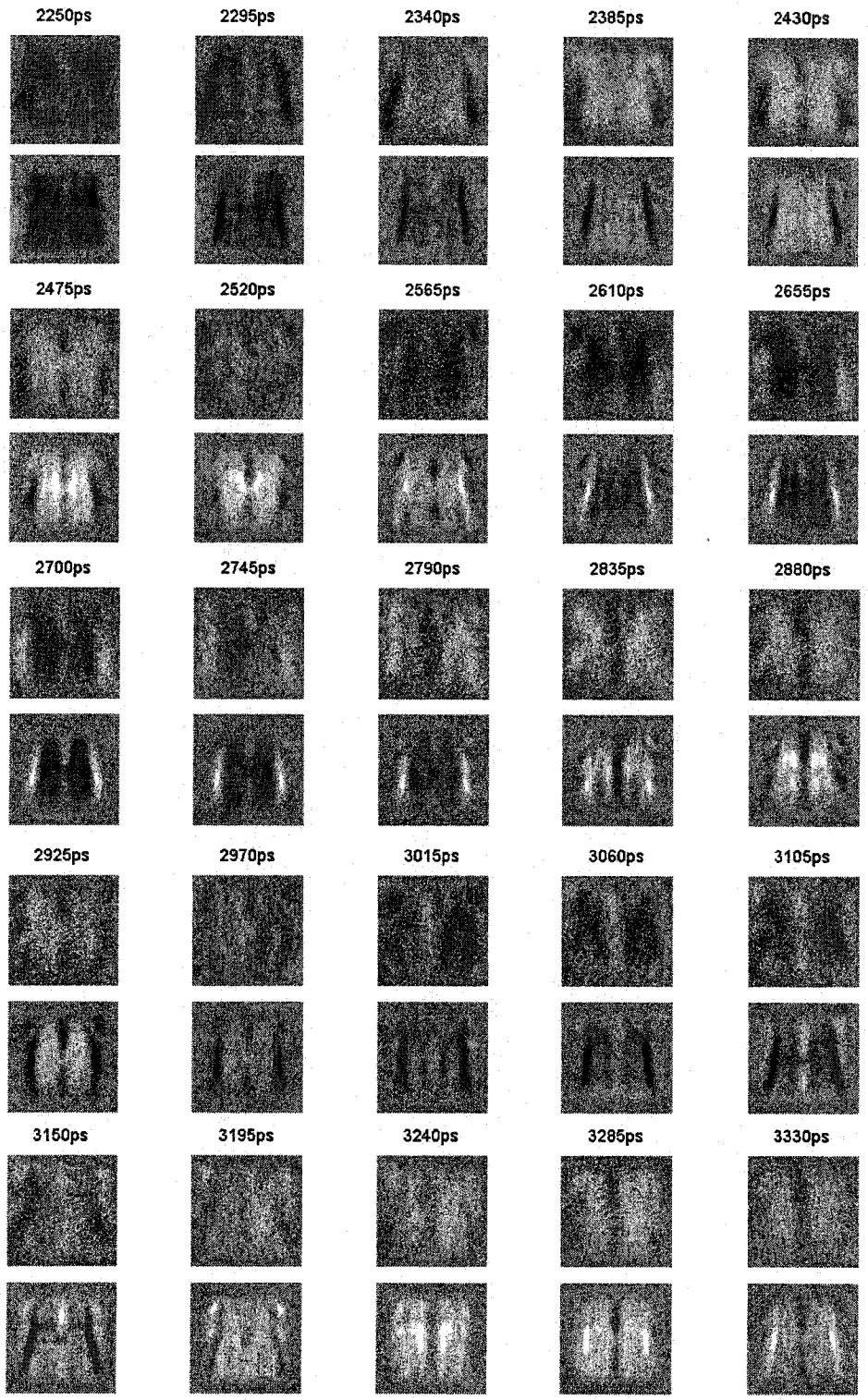

Fig. 5.21c Experimental (top) and numerical frames, 4μm platelet w/ pinhole (2-3ns).

5.1.4.2 Permalloy square at DC bias 18.3kA/m, 2-D frames.

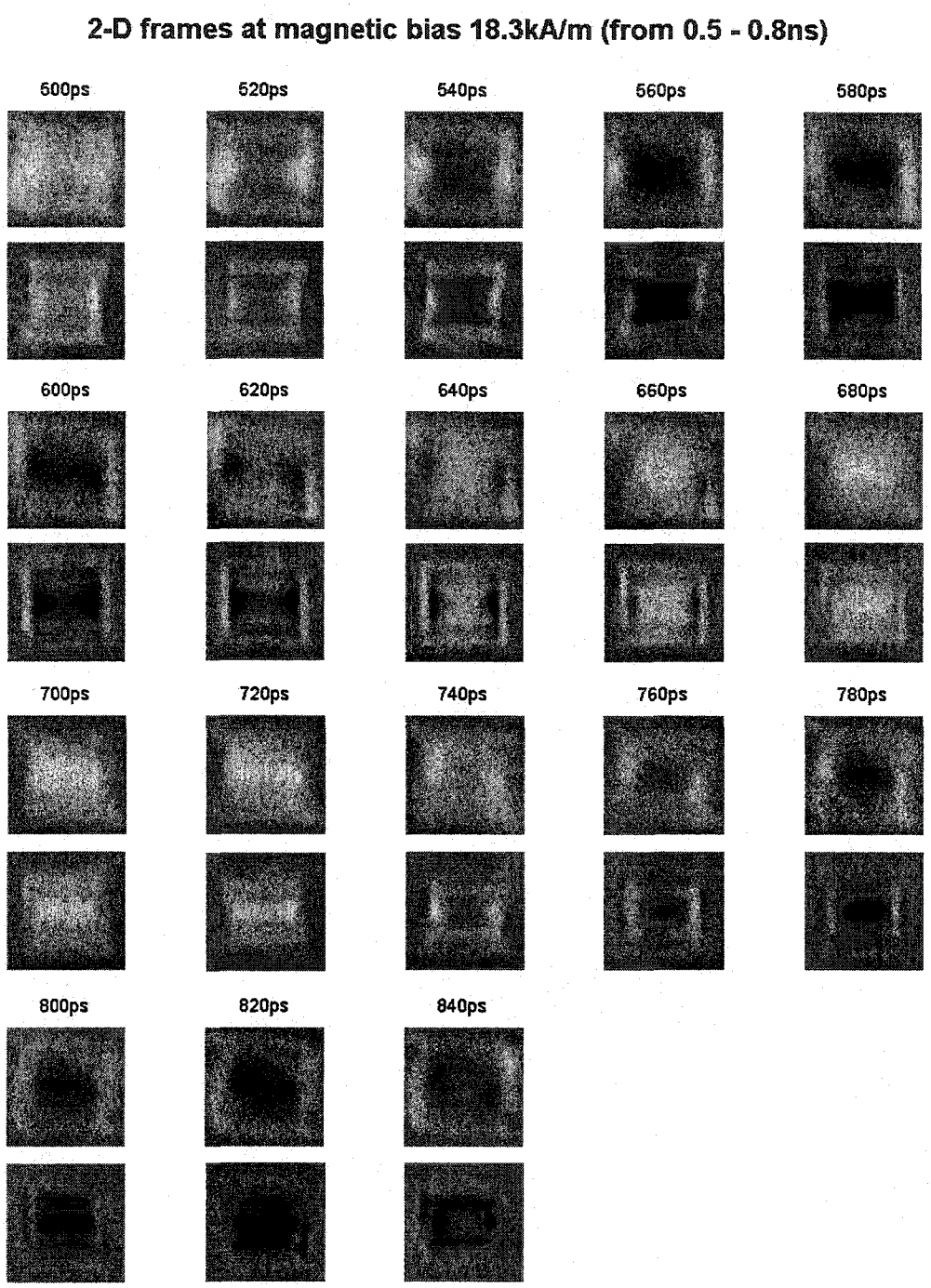

Fig. 5.22 Experimental (top) and numerical frames, 4μm platelet (0.5-0.8ns).

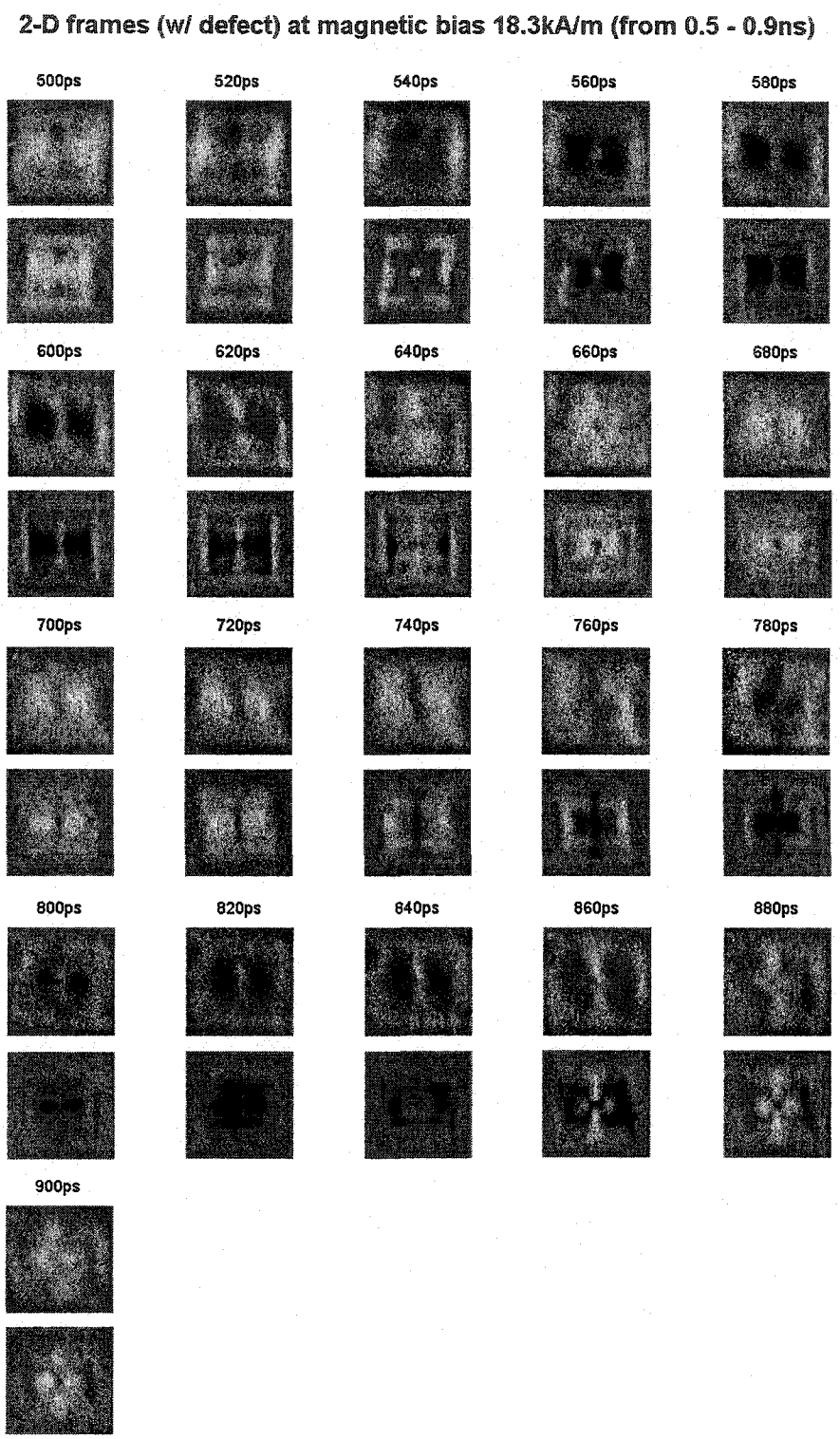

Fig. 5.23 Experimental (top) and numerical frames, 4μm platelet (0.5-0.9ns).

5.2 *Permalloy elliptical structures.*

The motivation for the fabrication and scanning of elliptical micromagnets (with and without a pinhole) came from the possibility that uniform fields inside the elliptical structures could allow the study propagation of spin waves launched by a pinhole at one focus. These spin waves could be focused at the other end of the ellipse (partly inspired by the "quantum mirage" of Fe atoms on Cu surface, see Nature, 403, p512, 2000). Other "bullet" like structures were fabricated for a similar experiment, (see Fig. 3.31b in Chapter 3) but no MOKE scanning was done on them.

The imaging of 10x5μm ellipses was achieved using the same experimental setup as for the magnetic squares, as described in Chapter 4. Each new sapphire substrate with ferromagnetic structures requires new installation components, such as a circuit board and a coaxial cable. The length of the electrical wire used to connect the pumping photodiode and the transmission line is different for each substrate. This change causes a delay in the reflected pulses' returns of approximately 20-30ps, and the timing of the excitation process during and after the first reflection changes. The measurement of the pump pulse profile (at high DC magnetic bias field) was realized with the 4μm magnetic square after the scanning of the elliptical structures finished.

The microfabrication of the elliptical structures was similar to the process used for the preparation of the rectangular structures. The sapphire substrate shows significant differences when used for the elliptical elements. The polishing (shown in Appendix 5) is insufficient and the resulting scratches modify the surface of the thin magnetic film. In addition, during the microfabrication process more pinholes appeared, mostly in the ellipse without artificial holes in one of the focuses. These unwanted pinholes are very

small and have little impact on the behavior of magnetization oscillations (as shown below).

The effect of high probe beam power (heating of the magnetic film) is discussed in Appendix 8.

5.2.1 Temporal response of the magnetization at DC bias 4.6kA/m.

The oval shape and the larger size of the ellipsoidal structures caused that the magnetization oscillations changed their properties. Missing strong internal fields (a consequence of closure domains) do not affect the creation of magnons and a magnon-magnon scattering. However, despite the elliptical shape, the magnetization inside the element is not uniform and these thin film magnetic elements have small domain structures at both ends of the ellipses. Magnetization oscillations that are unaffected by strong internal fields have lower damping. Fig. 5.24 shows the ferromagnetic response from the center of the magnetic structure, affected by the presence of reflected excitation pulses, but the oscillations are sustained for relatively longer periods (when compared with the similar ferromagnetic response of the 4μm square in Fig. 5.15). The delay of the reflected pulse depends on the electrical parameters of the electrical circuit (the contacts and the planar transmission line) and its value differs from the delay of the reflected pulse of the square sample (placed on a different substrate). The initial delay of the pumping pulse (from 0 to 800ps of the curve in Fig. 5.24) is given by opto-mechanical configuration of the probe&pump scanning setup.

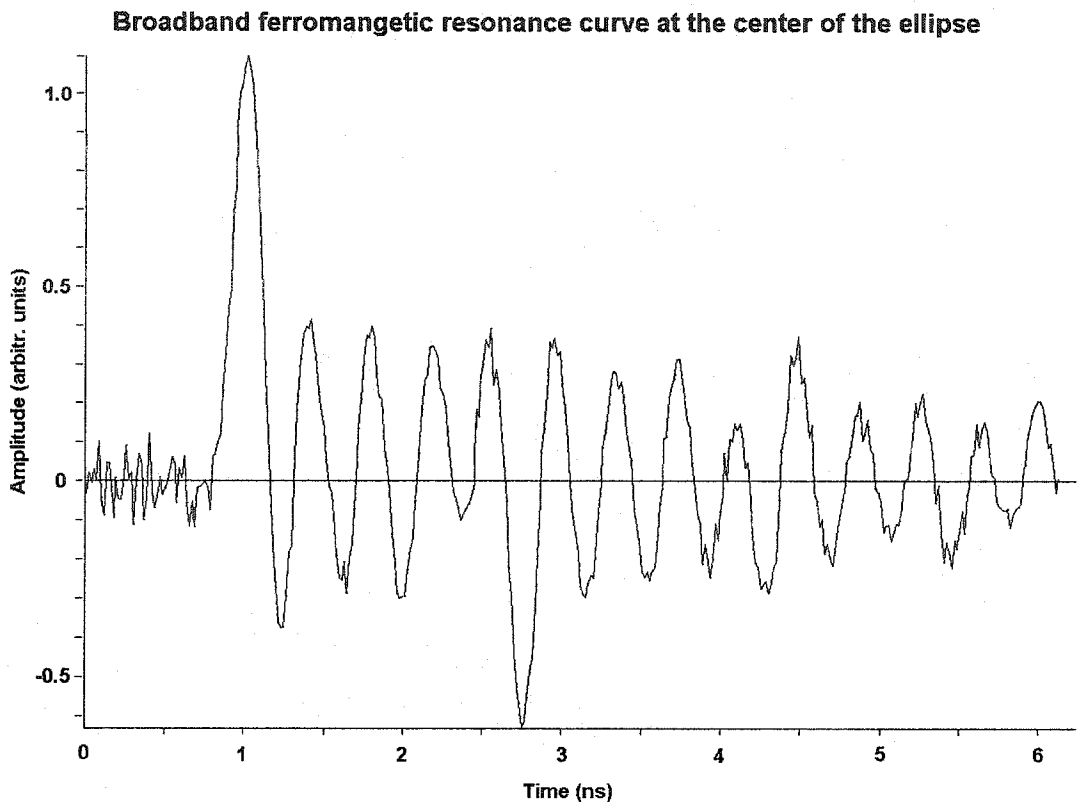

Fig. 5.24. A broadband ferromagnetic response 10x5μm in size and 15nm thickness of the Permalloy ellipse was taken from the center of the ellipse in the MOKE measurement. The probe beam power was 1.2mW and the temporal step of the scanning was 16ps. The peak of the first reflection pulse comes 1740ps after the peak of the major excitation pulse. The frequency of the magnetization oscillations is 2.5GHz.

5.2.2 *X-t scans and their Fourier transformation.*

The Fig. 5.25 shows the X-t scans of three ellipses (without and with a pinhole). The uniform distribution along the longer (easy) axis of each ellipse provides the evidence that large central areas are not affected by the pinholes at the end of an ellipse. Small domain structures at the (right or left) focus of the ellipse are sources of the non-uniform magnetic field distribution but these internal fields are weak and magnon-magnon scattering caused by them is also weak. The relatively low spatial distribution does not allow seeing of fine spin wave structures around a pinhole but the Fourier analysis of these X-t renderings shows that satellite frequencies do exist around the pinhole, Fig. 5.26.

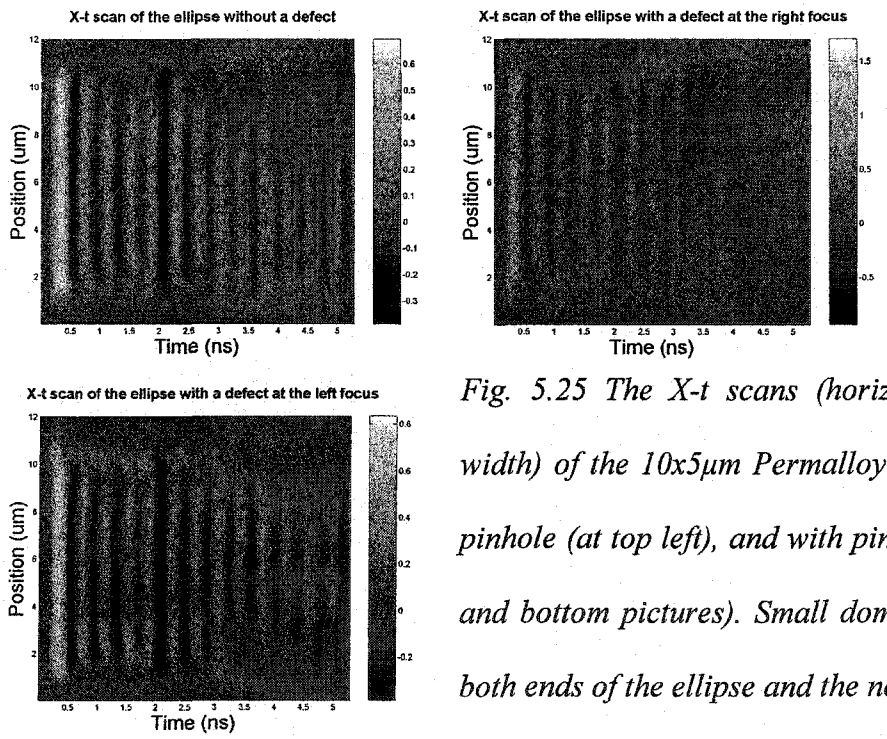

Fig. 5.25 The X-t scans (horizontally along the width) of the 10x5μm Permalloy ellipses without a pinhole (at top left), and with pinholes (at top right and bottom pictures). Small domain areas exist at both ends of the ellipse and the non-uniform internal fields create shorter wavelength magnons launched from the domain structures.

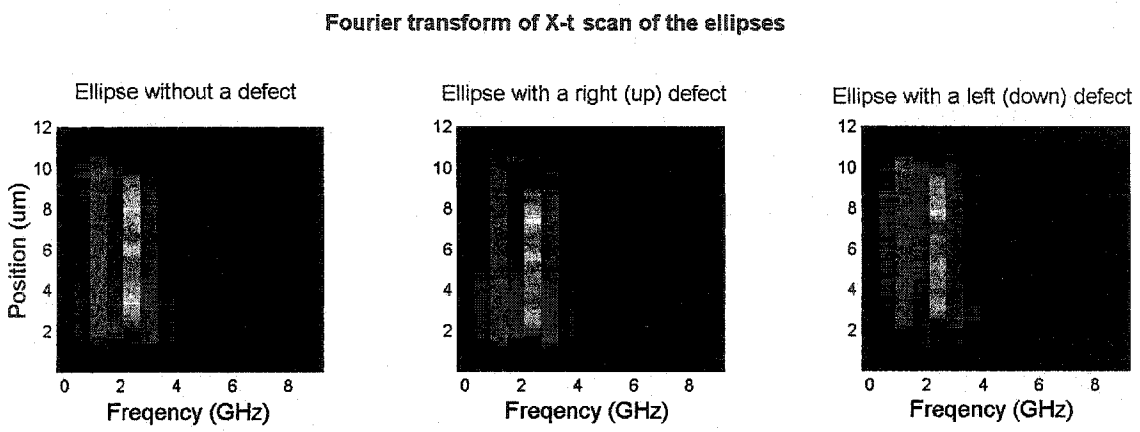

Fig. 5.26 The Fourier transforms of X-t scans of the Permalloy ellipses with and without pinholes. Satellite oscillations at lower frequencies (below 2GHz) that close the areas of lower internal fields around pinholes were detected.

5.2.3 ***Ellipse without a pinhole, 2-D frames.***

Horizontal stripes in Figs. 5.27 – 5.29 are the spin wave-like consequences of the shape and size of the ellipses. Existing small closure domains at the ends of the ellipses affect the magnetization oscillations. The symmetry of the spatial distribution of magnetization at both ends of the ellipse without a pinhole, Fig. 5.27, is disturbed by the 250nm pinhole at the right focus of the next ellipse, Fig. 5.29. The "cusp" structures (similar to the rectangular platelet) with resulting non-uniform magnetization distribution are relatively weak, the non-uniform internal fields cause magnon creation and affect close magnetic areas, but do not modify oscillations inside the ellipses. The spatiotemporal evolutions of the ellipses in Figs. 5.27 and 5.29 are very alike, except the areas of the focus. The detailed images of the left and right ends of ellipses in Fig. 5.28, 5.30 and 5.32 reveal the influence of a pinhole at a focus of an ellipse.

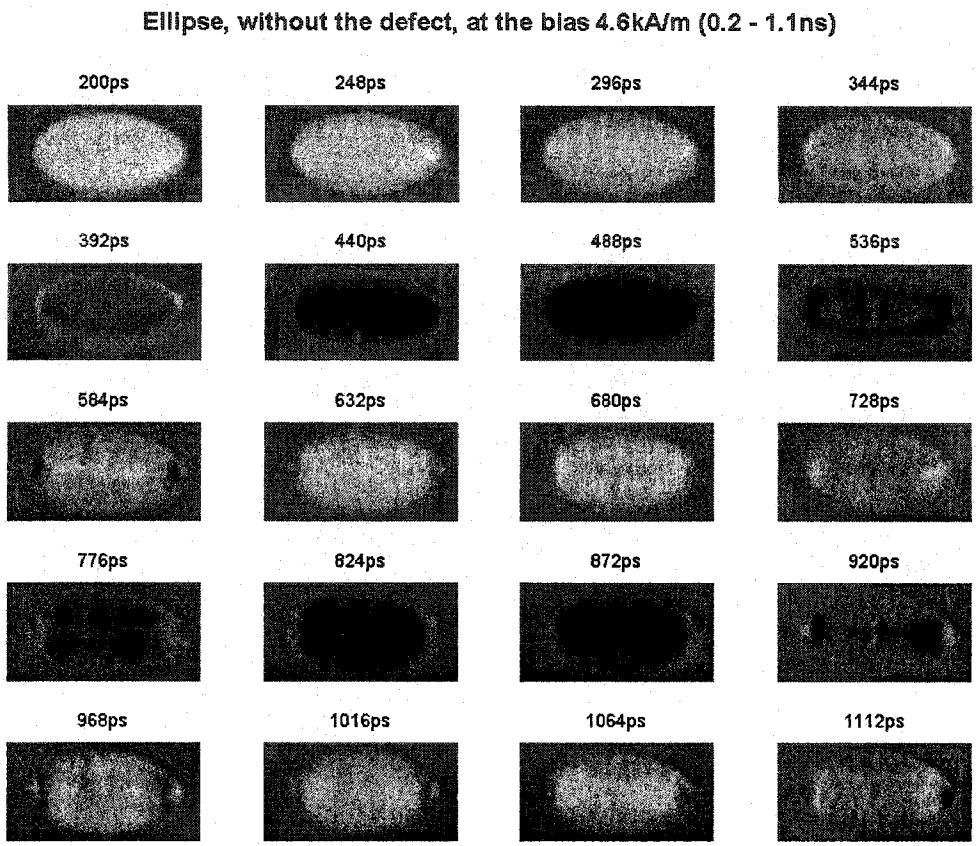

Fig. 5.27 The spatial ferromagnetic response (the polar component of the magnetization vector) of the Permalloy ellipse, 10x5μm in size and 15nm thick. Relatively small closure domain areas exist at both ends of the ellipse and the magnetostatic character of spin waves is affected by the creation and scattering of magnons.

The modal oscillations around a pinhole were changed and the oscillations at the other end of the ellipse were affected.

The surface of the elliptical structures is affected by surface roughness (details are shown in Appendix 5). The surface of a thin magnetic film is corrugated and, as a result, the vertical stripes (in all three sets of the Kerr images in Figs. 5.27, 5.29 and

5.31) are clearly visible. It can be deduced from the continuous character of the horizontal stripes that the magnetic film is not broken.

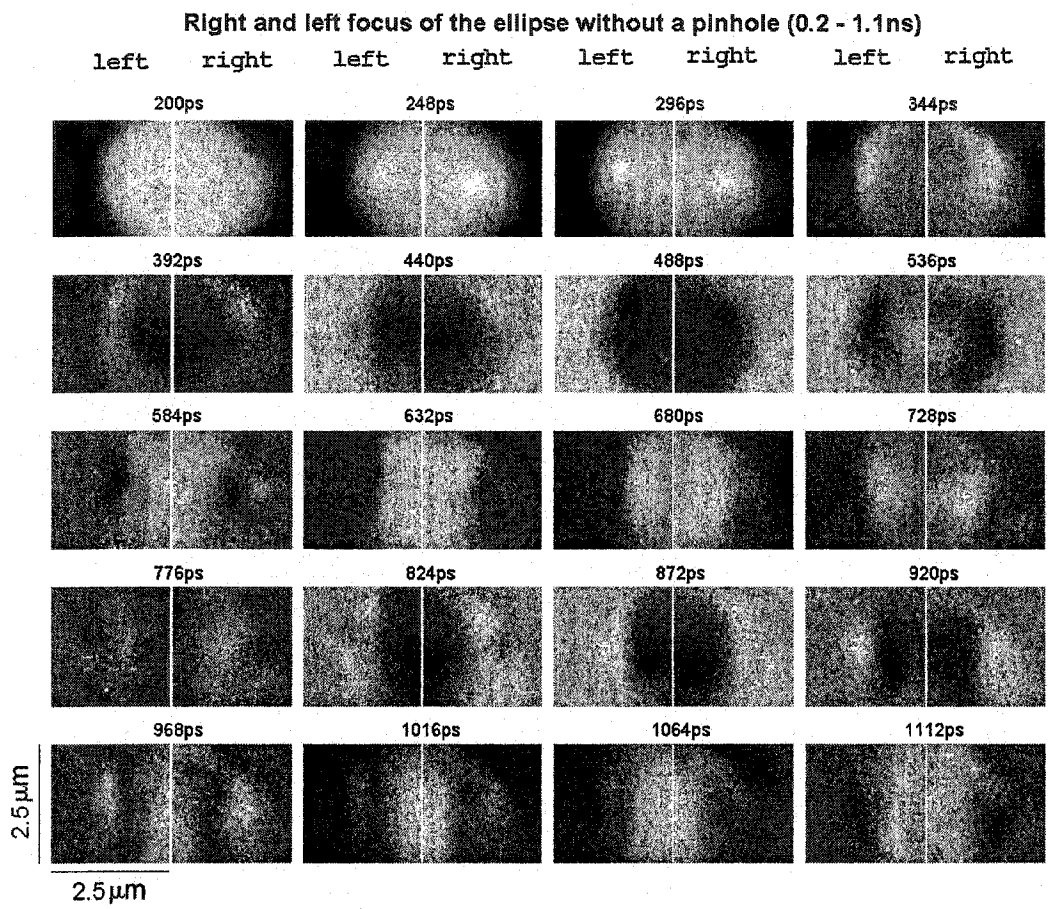

Fig. 5.28 The spatial ferromagnetic response (the polar component) of the Permalloy ellipse, 2.5µm square detail at both ends. Specimen was horizontally biased by in-plane field 4.6kA/m. Without a pinhole (at an end of the ellipse) the response of the magnetization vector on the out-of-plane magnetic pulse is symmetric (vertical axis of symmetry). The relative delay of the oscillations between the central part of the ellipse and both ends is clearly visible.

This observation provides evidence that the internal fields of the corrugated magnetic surface are not changed and that the magnetization moments have their vectors statically

tilted by a fraction of a degree respective to the plane of the magnetic film. In principle, these scratches can affect the uniformity of demagnetizing fields and cause a generation and a scattering of magnons, but the wavelengths of such magnons are below the spatial resolution of the MOKE microscope.

5.2.4 *Ellipse with a pinhole at the right focus, 2-D frames.*

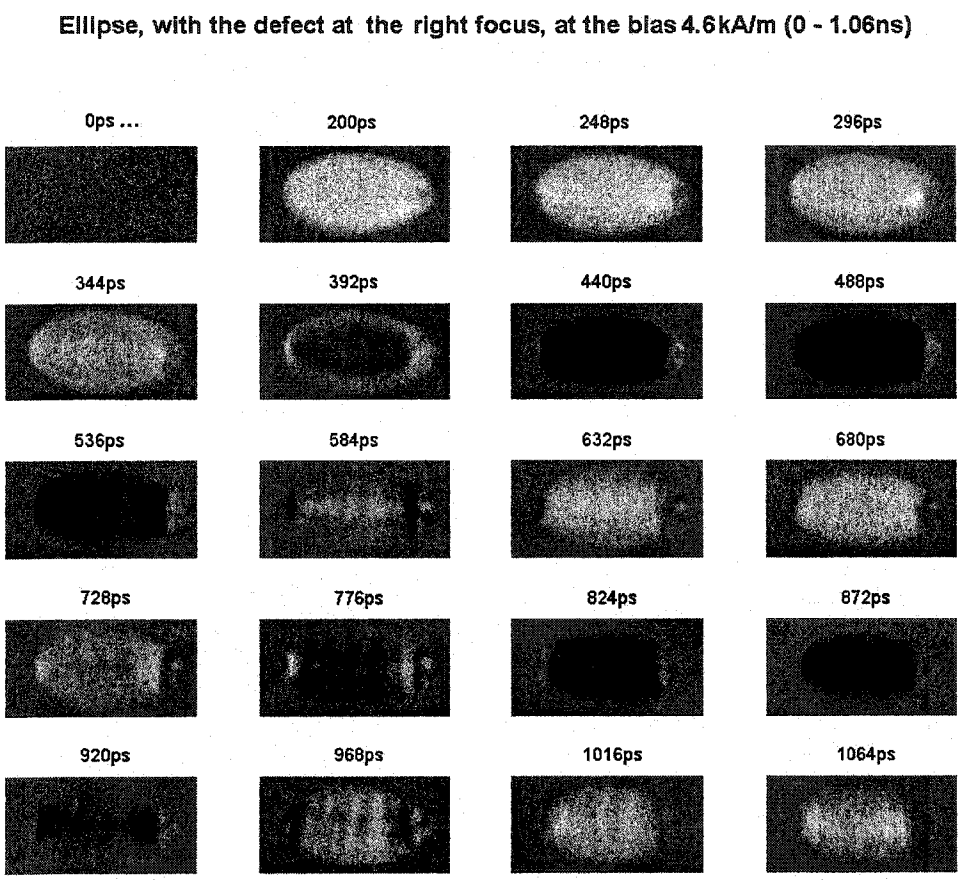

Fig. 5.29 The spatial ferromagnetic response of the Permalloy ellipse with a pinhole at the right focus. A relatively small closure domain areas exist at both ends of the ellipse and the magnetostatic character of the spin waves is affected by the creation and scattering of magnons.

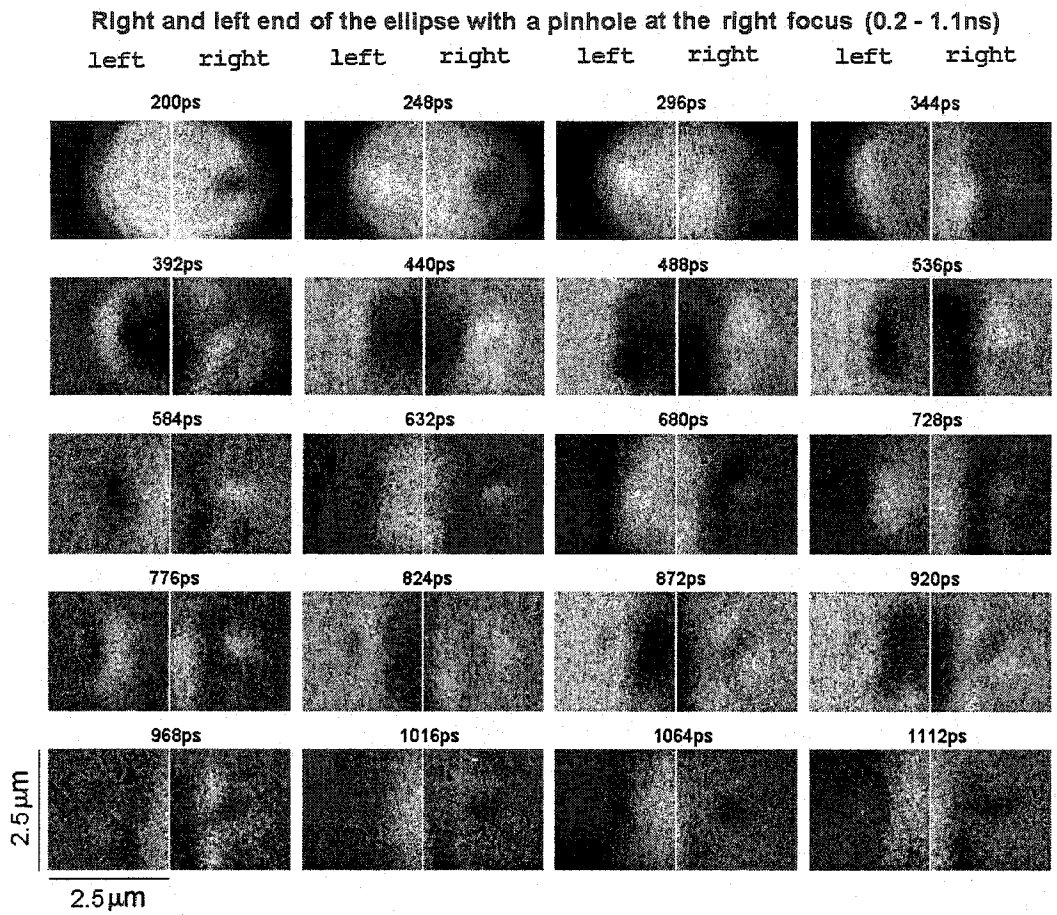

Fig. 5.30 The spatial ferromagnetic response of the Permalloy ellipse with a 250nm in diameter pinhole at the right focus, 2.5μm square detail at both ends. Specimen was horizontally biased by in-plane field 4.6kA/m. The pinhole significantly affects the response of the magnetization vector by creating non-uniform fields around the pinhole (similarly as "cusp" structures around the pinhole in the square element) and the symmetry of both focuses (recognized in Fig. 5.28) is lost. The relative delay of the oscillations between the central part of the ellipse and both ends is clearly visible. The comparison with Fig 5.28 (the ellipse without a pinhole) reveals that the oscillations at the end without a pinhole are affected by the pinhole at the opposite end of the ellipse (see, for example, bright spots, left, missing on 968ps frame and created in 1112ps one).

5.2.5 *Ellipse with a pinhole at the left focus, 2-D frames.*

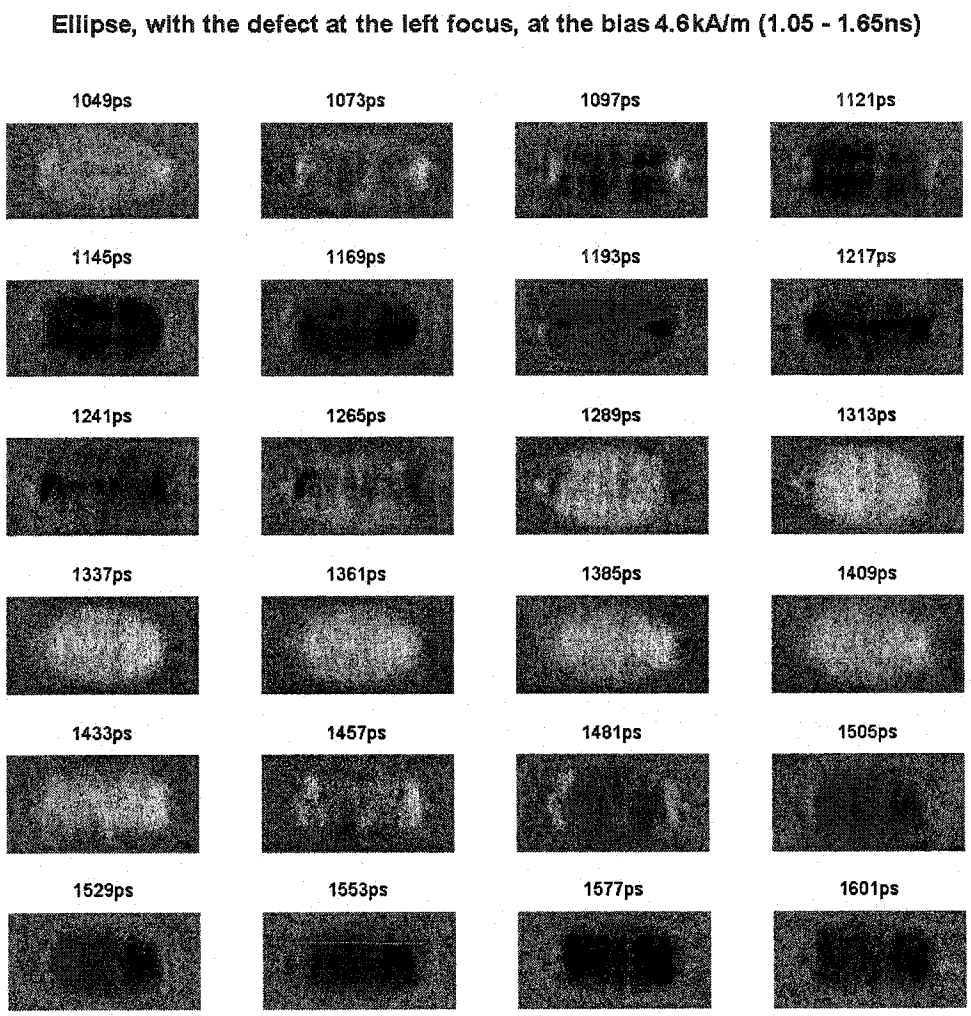

Fig. 5.31 The spatial ferromagnetic response of the Permalloy ellipse with a pinhole at the left focus. Relatively small closure domain areas exist at both ends of the ellipse and the magnetostatic character of spin waves is affected by the creation and scattering of magnons.

The "super-resolution" seen in Fig. 5.32 (the circles in the central part of the *right* end of the images scanned with high probe power) implies an influence of a

heating effect, which is sensitive to a probe position. The future SEM scanning of the edge of the magnetic ellipse also could show possible structural defects at that place.

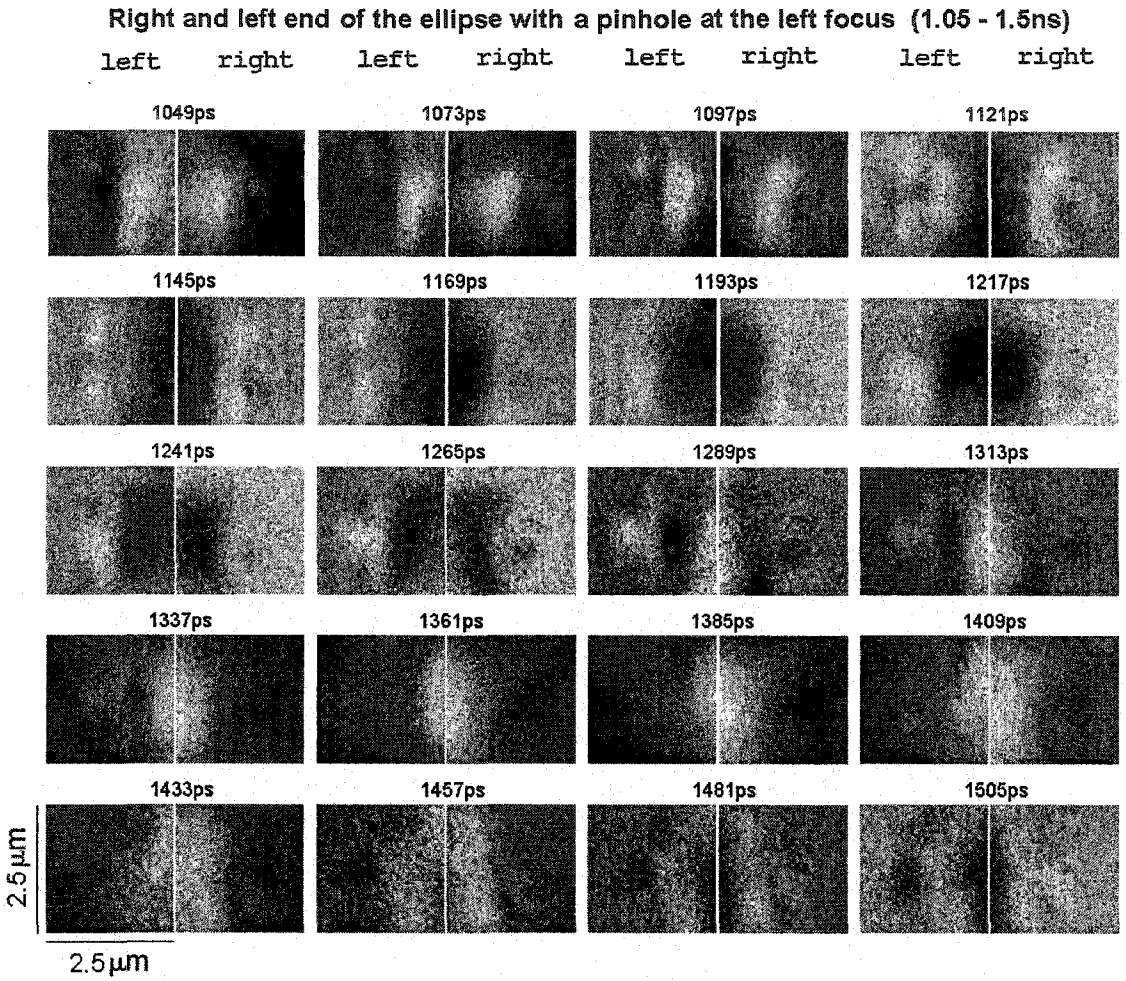

Fig. 5.32 The spatial ferromagnetic response of the Permalloy ellipse with a 250nm in diameter pinhole at the left focus, 2.5µm square detail at both ends (the ellipse biased by the field 4.6kA/m). The frames were shifted in time, showing the evolution of magnetization oscillations after 1ns. Similarly as in the ellipse in Fig. 5.30, the pinhole significantly affects the response of the magnetization vector by creating nonuniform fields around the pinhole. The comparison with the ellipse without a pinhole (in the interval from 1049ps to 1112ps) reveals that the modal oscillations at the left focus are significantly changed and strong oscillations around the pinhole were detected.

5.3 *Discussion of spatially dependent damping.*

Let us look at the uniform sample via the broadband ferromagnetic resonance curves in Figs. 5.5 (square sample) and the amplitudes of consecutive "ringing" peaks[2]. The oscillations in the center of the uniform square have the ratios of magnitudes of the 1st peak and the following "ringing" peaks different than those closer to the domain walls and the edges (their amplitudes decrease faster). The increased non-uniformity of demagnetizing fields and magnon-magnon scattering is responsible for the indirect damping becomes stronger.

At the centers of the edges (#10-#13, Fig. 5.7) the magnitude of the signals is lower that corresponds with the presence of a non-magnetic areas (the surface of the sapphire substrate) around the magnetic platelet. The non-uniform internal fields near the edges of the magnetic element and an effective pinning of the magnetization vector (see the discussion of magnetostatic-exchange modes in Chapter 2, Section 2.4.6). The experimental data from the edge points, and from the closure domains and Nèel domain walls, are affected by the large size of the optical probe (spot size~500nm) relatively to the size of domain structures (D_N~5nm). The effective damping varies strongly across these magnetically non-uniform areas. The spin wave structure of this small magnetic element is affected by the existence of both magnetostatic-exchange waves and propagating spin waves. Despite of the small amplitudes of the magnetic oscillations the existence of non-uniform internal fields is mandatory and allows interactions between normal spin wave modes.

[2] The existence of reflected pumping pulses complicates the analysis and their influence has to be taken into account.

The broadband ferromagnetic resonance curves of the platelet with the pinhole, Fig. 5.5, show that while the magnitudes of the 1st peaks are equal the amplitudes of "ringing" peaks are smaller in the central area. There are regions of nonuniform fields around the pinhole, they alter the temporal evolution and spatial distribution of the magnetization, and, consequently the indirect damping is stronger (than the damping in the uniform sample).

The resonance curves at the corners of the both platelets (#14 and #17 in Fig. 5, Appendix 6) show very small damping. These two corners are far from the central area and from closure domain walls, and a creation and interactions of magnons are weak.

The 1st pumping pulse excites whole sample uniformly except the areas of domain walls. The spin wave modes of the uniformly magnetized sample (see Chapter 2, part 1.4.4-1.4.5) are the normal modes but the existence of the non-uniform internal fields causes that these modes interact (as discussed in Chapter 2, part 1.5). A decay of uniform and non-uniform spin wave modes into $k \neq 0$ modes in thin metallic films is a regular mechanism of the ferromagnetic relaxation. The two-magnon scattering represents one important channel for the indirect damping observed in the experiments (while preserving the magnitude of the magnetization vector). The tipping angle of the excitation in our experiment is small and, as a result, the probability of four-magnon interactions are small (see Dobin and Victora about of four-magnon scattering in Ref. 39, Chapter 2). Ultimately the energy of the magnetic system is transferred into the lattice vibrations (via spin-orbit interactions). Effects of eddy currents are small (Section 5.1.2). The intrinsic damping (usually facilitated by an interaction with phonons, see discussion of Suhl in Ref. 58, Chapter 2) does involve also the magnon-conduction

electrons interaction (see Kambersky in Ref. 61, Chapter 2), which is related to spin moment transfer.

The reflection pulse arriving after approximately 1.5ns changes the temporal relations of the magnetization oscillations. The phase of the reflected pulse is not synchronized with the phase of the spin waves, which are suddenly forced to change their evolution. The first (the strongest) pumping pulse created *k~0* magnons, which during the following 1.5ns time interval partly relaxed (indirectly via two-magnon scattering or directly via an interaction with and conduction electrons). Then the reflected pulse (also uniform over the whole area of the magnetic element) started pumping the energy into the magnetic system again by creating magnons with large wavelength in a pool of already existing short-wavelength magnons. Details of the simulation of the X-t distribution of the uniform 4μm magnetic element convoluted by

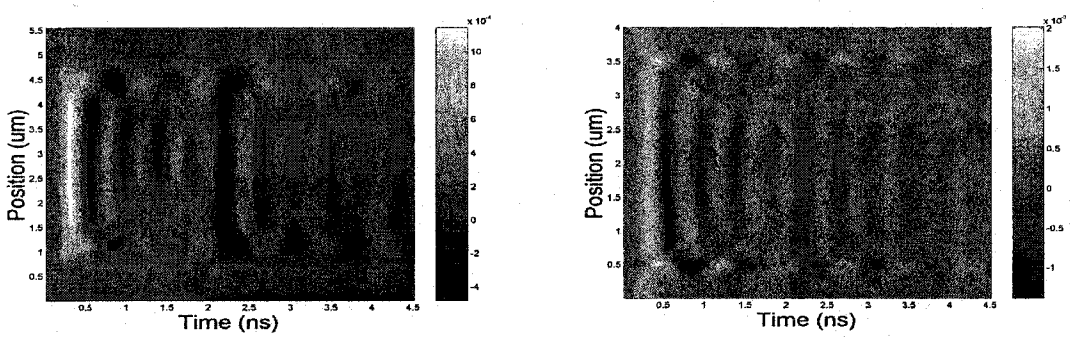

Fig. 5.33 Simulations of the 4μm magnetic square displaying the Gaussian-blurred X-t (left) rendering (a horizontal distribution through a center of the element) and raw data (right). The reflected pulse starts after the 1.5ns and affects existing short-wavelength magnons (displayed as thin 45° tilted line-like structures in the right picture) by exciting long-wavelength magnons. See also Fig. 5.18 for (non-blurred) details with the pumping without the reflections.

the Gaussian kernel are in Fig. 5.33 (left). Fig. 5.33 (right) shows the same simulation result but non-convoluted with the Gaussian kernel.

The important interactions in our magnetic system shows combined magnetostatic and exchange characteristics and the observed spatial and temporal evolution of excited eigenmodes of the system is of hybrid (magnetostatic/exchange) nature. A main part of a magnetic energy that (spatially uniform) excitation pumps into long-wavelength magnetostatic-like modes, is transformed (via decay caused by non-uniform internal field at closure domains or around a pinhole) into energy of short-wavelength spin waves. The indirect damping in elliptical elements is lower because of weaker internal fields (small domain structure localized at the ends of the ellipse). As a result, the creation and scattering of magnons (before a final dissipation of the magnetic energy into lattice via conductive electrons and phonons) is less intensive.

Because of a large probe size, the experimental data show an average value over a large magnetic area, but a similar effect brings the finite cell size (15.6nm) in our 2-D numerical simulations. Consequently, there could exist spin waves with wavelengths smaller than our cell size while not revealed by the numerical solutions of the LLG equation. These oscillations (and related interactions) would not enter the "indirect" damping, but affect the phenomenological Gilbert damping constant. However, the numerical simulations on finer grid (a cell size 7.8nm) did not show significant changes and the comparison of experimental and numerical broadband ferromagnetic resonance curves (taken from various points on the magnetic square) show good quantitative agreement.

5.4 *Summary of the chapter.*

A spatiotemporal study of broadband magnetization dynamics in internally patterned thin film $Ni_{80}Fe_{20}$ elements was conducted in order to elucidate (using time-resolved scanning Kerr microscopy and numerically via micromagnetic simulation) the excitation and decay of modal oscillations in microstructures. The spatiotemporal evolution of the polar component of magnetization in response to a small out-of-plane transient magnetic pulse is imaged in the presence of a weak in-plane static bias field. In a uniform square platelet, the spatial response is strongly controlled by the nonuniform static magnetization distribution associated with the closure domains transverse to the bias field direction. A circular pinhole is patterned in the center of a square platelet to show that the spatial pattern of magnetization oscillation response also depends sensitively on weaker variations of the static magnetization around that circular pinhole. Assuming a quadrupolar pattern around a small pinhole was shown that the primary mode of magnetization oscillations in the center of the platelet (biased in a weak longitudinal field) adapts to the configuration of static magnetization. The micromagnetic simulation highlights the quantitative agreement with the experimental results and confirms that the transfer of energy into shorter wavelength modes by magnon-magnon scattering (the indirect damping) in regions of nonuniform magnetization is responsible for the appearance of position-dependent decay of oscillations in the measurement. In the case when the in-plane magnetic bias field is strong enough, the non-uniform internal fields around the pinholes or the domain walls are suppressed, the short-wavelength magnon creation and scattering is weak and resulting effective damping constant smaller.

6. Summary of the thesis.

A spatiotemporal study of broadband magnetization dynamics in internally patterned thin film Permalloy platelets was conducted in order to elucidate the excitation and decay of modal oscillations in patterned magnetic microstructures.

In Chapter 2, magnetization oscillations of thin magnetic films are introduced in terms of spin waves and magnons. The importance of the shape of a microstructure and related non-uniform internal magnetic fields is discussed, based on latest theoretical and experimental results. The results in Chapter 3 show how complex the technology of the micro- and nano-fabrication is. The microfabrication of small magnetic structures using lift-off requires proper sputtering process and the right choice of the resist system for a lift-off. The hard and long baking of the substrate/resist is important for a good adhesion of the resist film and stable mechanical properties of the resist film after the development. The set of exposure and post-exposure parameters (a dosage, an alignment of the e-beam writer, a development, baking, etc.) are important to get right profile of the resist. In both single and double layer resists, the thickness of the resist and deposited film, the energy of the electron beam, the writing current and proximity effects in substrate and resist imply the range of the spatial resolution and the density of resulting (magnetic and non-magnetic) microstructures (arrays). In a single layer resist, sub-50nm structures were fabricated. Using a double layer the lateral resolution approximately 60-70nm. The next experiments can be done using other resist combinations followed by long pre-bake and ultrasonically assisted resist development.

Chapter 4. The ultrafast scanning MOKE microscope was built and successfully used in imaging of a magnetization dynamics of micrometer-sized magnetic elements.

The computer-controlled experimental setup was built using a femtosecond laser, an optical delay line, a fast optical pumping photodiode, XYZ stage moved by piezo-actuators, a two-detector scheme with a low-noise differential amplifier followed by a digital lock-in amplifier. Temporal and spatial resolutions of the stroboscopic scanning microscope were, respectively, 0.8ps and 200nm (effectively, determined by the size of the Gaussian probe and a noise of the scanning process). The out-of-plane component of the magnetization (a spatial and temporal evolution) was measured using the MOKE microscope.

A spatiotemporal study of broadband magnetization dynamics in internally patterned thin film $Ni_{80}Fe_{20}$ elements was conducted in order to elucidate the excitation and decay of modal oscillations in ferromagnetic microstructures (Chapter 5). The spatiotemporal evolution of the polar component of magnetization in response to a small out-of-plane transient magnetic pulse is imaged in the presence of a weak in-plane static bias field. In a uniform square platelet, the spatial response is strongly controlled by the nonuniform static magnetization distribution associated with the closure domains transverse to the bias field direction. If a lithographic pinhole is patterned in the center of a square platelet, the spatial pattern of magnetization oscillation responded sensitively on weaker variations of the static magnetization (with a quadrupolar symmetry) around that circular pinhole. It was shown that the primary mode of magnetization oscillations in the center of the platelet (longitudinally biased) adapts to the configuration of static magnetization. The micromagnetic simulation highlights the quantitative agreement with the experimental results and confirms that the transfer of energy into shorter wavelength modes by magnon-magnon scattering (the indirect damping) in regions of

nonuniform magnetization is responsible for the appearance of position-dependent decay of oscillations in the measurement. In a strong magnetic bias field, the non-uniform internal fields around the pinholes or the domain walls are suppressed and the short-wavelength magnon creation and scattering is weak. As a result, the damping of magnetization oscillations is lower.

This work is a step towards more elaborate manipulation of allowed magnetic modes ("magnonics"). These ferromagnetic "ripple tanks" will show how multiple defects, and the amplitude dependent response in this intrinsically nonlinear system affect spatial and temporal behaviour of spin waves. In addition, the excitation of magnetic films biased by spatially nonuniform magnetic fields and using clearer magnetic pulses with higher bandwidth and multiple peaks can open another way how to affect the magnetic modes. Spatial control of modal oscillations is also potentially of interest for spintronic applications and magnetic logic. The latest development in the field of photonics and photonics bandgap structures shows that a rich world of waves and oscillations can be sophisticatedly altered in artificially patterned complex thin film systems. An application to the area of micromagnetic systems suggests that "magnonic" structures can offer a control of magnetization oscillations at a similar level, significantly expanding opportunities in fields of computation and sensors.

Appendix 1. ***Fourier coefficients of a magnetization of a sample with finite dimensions. Maxwell equations.***

Below are the equations for the Fourier coefficients of magnetization $M(x,y)$. A sample of lateral dimensions L_x, L_y, thickness $h<<L_x,L_y$ is considered and periodic boundary conditions applied (in the XY plane). In the demagnetizing field of a thin film finite structure [Mansuripur, 12, 19], the Fourier coefficients of a periodic function $M(x,y)$ are

$$M_{mn} = (1/ L_x L_y) \int\int_0^{Lx\,Ly} M(x,y)\, exp[-i2\pi(mx/L_x + ny/L_y)]\, dxdy \qquad (1)$$

and the magnetization by

$$M(x,y) = \Sigma_{m=-\infty,+\infty}\ \Sigma_{n=-\infty,+\infty} M_{mn}\, exp[i2\pi(mx/L_x + ny/L_y)] \qquad (2)$$

The demagnetizing field is

$$H(x,y,z) = \Sigma_{m=-\infty,+\infty} \Sigma_{n=-\infty,+\infty} H_{mn}(z)\, exp[i2\pi(mx/L_x + ny/L_y)]. \qquad (3)$$

The Fourier components of the field $H_{mn}(z)$ are:

$$-4\pi\, [\, exp(2\pi fz)\, sinh(\pi fh)\, (M_{mn}\cdot\sigma_-)\sigma_-], \text{ for } z<-h/2 \qquad (4)$$

$$-4\pi\, \{\, (M_{mn}\cdot\sigma)\sigma - 1/2\, exp[(2\pi f(z-h/2)]\, (M_{mn}\cdot\sigma_-)\sigma_- - 1/2\, exp[(-2\pi f(z+h/2)] \qquad (5)$$

$$(M_{mn}\cdot\sigma_+)\sigma_+\} \text{ for } |z|<h/2$$

$$-4\pi\, [\, exp(-2\pi fz)\, sinh(\pi fh)\, (M_{mn}\cdot\sigma_+)\sigma_+], \text{ for } z>h/2 \qquad (6)$$

where $f = \sqrt{(f_x^2 + f_y^2)}$ $\sigma = (f_x/f)\, i_x + (f_y/f)\, i_y$ and $\sigma_\pm = \sigma \pm i\, i_z$.

After averaging through the film thickness the Fourier component of the demagnetizing field is, where $S(x) = [1-exp(-2\pi x)]/2\pi x$,

$$H_{mn}^{av} = -4\pi\, \{\, [1-S(hs)](M_{mn}\cdot\sigma)\sigma + S(hs)(M_{mn}\, i_z)\, i_z\} \qquad (7)$$

Maxwell equations.

From the classical electrodynamic theory of the electric and magnetic fields, the electric and magnetic inductions are

$$\boldsymbol{D} = \varepsilon_0 \boldsymbol{E} + \boldsymbol{P} = \varepsilon_0 \varepsilon_r \boldsymbol{E} \tag{8}$$

where $\varepsilon_r = 1+\chi_e$, and

$$\boldsymbol{B} = \mu_0(\boldsymbol{H} + \boldsymbol{M}) = \mu_0 \mu_r \boldsymbol{H} \tag{9}$$

where $\mu_r = 1+\chi_m$, respectively. The inductions $\boldsymbol{D}$ and $\boldsymbol{B}$ are controlled by Maxwell equations [1] (with the boundary conditions for electrical and magnetic fields)

$$\nabla . \boldsymbol{D} = \rho_{free} \tag{10}$$

$$\nabla . \boldsymbol{B} = 0 \tag{11}$$

$$\nabla \times \boldsymbol{E} = -\partial \boldsymbol{B}/\partial t \tag{12}$$

$$\nabla \times \boldsymbol{H} = \boldsymbol{J}_{free} + \partial \boldsymbol{D}/\partial t \tag{13}$$

where ρ_{free} is a density of free charges and

$$\boldsymbol{J}_{free} = \sigma \boldsymbol{E} \tag{14}$$

where $\boldsymbol{J}_{free}$ are free currents and σ is an electric conductivity. The permittivity of vacuum, ε_0, and the permeability of vacuum, μ_0, are constants. The tensor material parameters ε_r, μ_r, χ_e, χ_m are respectively the relative permitivity, the relative permeability, and the electric and magnetic susceptibility.

Appendix 2. ***Quantum-mechanical analysis of magnon-magnon interactions.***

Let us use the Hamiltonian of the form

$$H = U_0 + H_{Heis} + H_{p2} + H_p \tag{15}$$

where H_{Heis} is the Heisenberg Hamiltonian, H_{p2} and H_p contain higher order terms of creation a^+ and annihilation a operators for magnons. Let us assume the time-dependent quantum-mechanical perturbation theory for the transition probabilities. Then the number of transitions per unit time w_{lm} from the state l into the state m (with energy eigenvalues ε_l and ε_m respectively) and the Hamiltonian H_{p2} are respectively

$$w_{lm} = (2\pi/h)\,|\langle m|H_p|l\rangle|^2\,\delta(\varepsilon_l - \varepsilon_m) \tag{16}$$

$$H_{p2} = \Sigma_1\Sigma_2\Sigma_p\, H_k\, a_2^+ a_1\, \Delta(\boldsymbol{k}_2 - \boldsymbol{k}_1 - \boldsymbol{k}_p) + H.c. \tag{17}$$

where H_k is the amplitude of $\boldsymbol{k}_p$-th component of the effective field $\boldsymbol{H}_{eff}$. This approach also allows the investigation of the case when the non-uniformities are chaotic, which is the case related to the rough surfaces or to the polycrystals.

For an ideal crystal the form of the Hamiltonian H_p is given [10, 35] as

$$H_p = \Sigma_1\Sigma_2\Sigma_3\; \Psi_{1,23}\, a_1 a_2^+ a_3^+ \Delta(\boldsymbol{k}_1 - \boldsymbol{k}_2 - \boldsymbol{k}_3) + \tag{18}$$

$$\Sigma_1\Sigma_2\Sigma_3\Sigma_4\; \Psi_{1,234}\, a_1 a_2^+ a_3^+ a_4^+ \Delta(\boldsymbol{k}_1 - \boldsymbol{k}_2 - \boldsymbol{k}_3 - \boldsymbol{k}_4) +$$

$$\Sigma_1\Sigma_2\Sigma_3\Sigma_4\; \Psi_{12,34}\, a_1 a_2 a_3^+ a_4^+ \Delta(\boldsymbol{k}_1 + \boldsymbol{k}_2 - \boldsymbol{k}_3 - \boldsymbol{k}_4) +$$

higher terms + Hermitian conjugate

where Ψ are complex quantities caused by e.g. dipole-dipole interactions. Each term represents a certain elementary process. For example $a_1 a_2^+ a_3^+$ corresponds to a splitting (three-magnon process with one magnon annihilated and two others created) or $a_3 a_2 a_1^+$

to a confluence (reverse process), and $a_1 a_2 a_3^+ a_4^+$ to the scattering (four-magnon process with two magnons annihilated and two others created), as shown in Fig. 2.10. The Hermitian conjugate terms correspond to the reverse processes. The number of magnons for 3-magnon splitting is given by the equation

$$<n_1 - 1, n_2 + 1, n_3 + 1|H_p|n_1, n_2, n_3> = \tag{19}$$

$$\sqrt{(n_1, n_2 + 1, n_3 + 1)}\, \Psi_{1,23}\, a_1 a_2^+ a_3^+ \Delta(\boldsymbol{k}_1 - \boldsymbol{k}_2 - \boldsymbol{k}_3) .$$

The energy and momentum in an ideal crystal are conserved in each elementary process.

Appendix 3. ***Transmission electron microscopy of Permalloy samples.***

The transmission electron microscopy (TEM) together with an analysis of X-ray spectra (EDS) was applied and Permalloy samples were analyzed.

Lift-off procedure (in acetone) was used to lift a sputtered Permalloy thin film from the substrate and pieces of a thin film floating in the acetone bath were caught on a TEM copper grid. A second Permalloy sample was prepared from a little bulk piece of $Ni_{80}Fe_{20}$ sputtering target by grinding in Al_2O_3 dish (with acetone).

Using transmission electron microscope JEOL 2010 working at 200kV the bright field image of the surface of sputtered $Ni_{80}Fe_{20}$ film was taken (Fig. 1a).

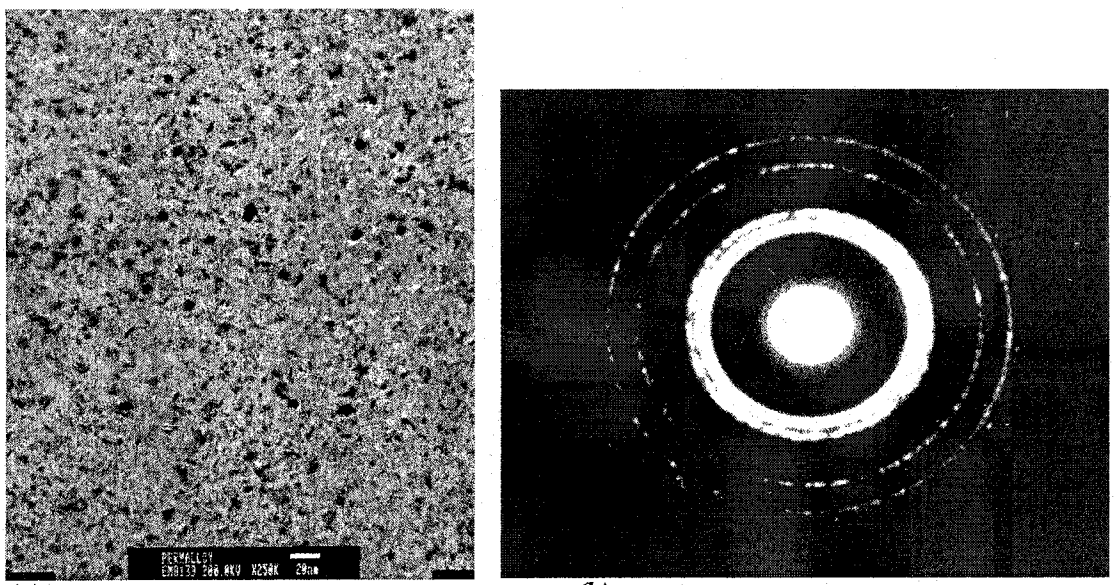

(a) *(b)*

Fig. 1. TEM image of a sputtered 15nm thick polycrystalline film is in (a) and its diffraction pattern in (b). Camera length was 1m.

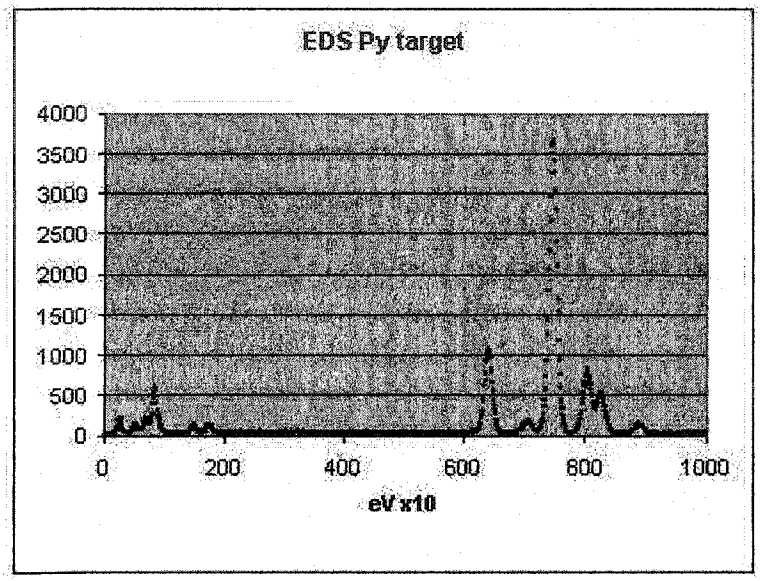

(a)

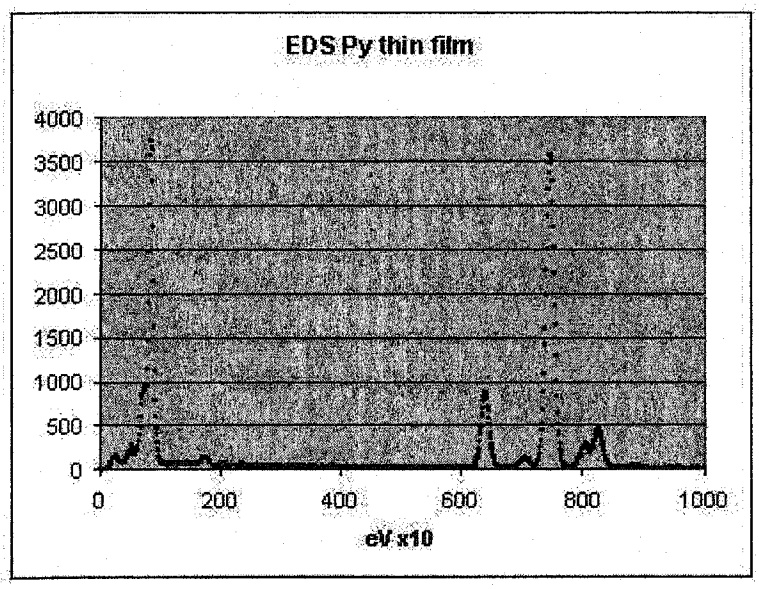

(b)

Fig. 2. EDS spectra (a) of the sample from a Permalloy target and (b) from 15nm thin Permalloy film. The EDS spectrum of thin Permalloy film was taken using following parameters: acceleration voltage 200kV, 200sec live time, 80k magnification, spot size 2, dead time ~20%, count rate ~1100cps. Two EDS spectra of Permalloy target sample were taken at 80k and 500k magnification.

The numerical fit of the experimental points with an analytical Gaussian function $f(x) = a_0\ Exp[-(x-x_0)^2/d_0^2]$ gives following results:

- Target sample background = 35, Ni K_α target peak area 59517.8, a_0=3650 (experimental max. value=3650), x_0=27.1, d_0=9.2.
- Fe K_α target peak area 16430.6, a_0=1030 (experimental max. value=1060), x_0=41, d_0=9.0,
- Thin film sample background = 20, Ni K_α thin film peak area: 60793.8, a_0=3500 (experimental max. value=3580), x_0=28.3, d_0=9.8.
- Fe K_α thin film peak area: 13559.3, a_0=850 (experimental max. value=879), x_0=40.2, d_0=9.0.
- Assuming Ni and Fe only for target $Ni_{80}Fe_{20}$ EDS data give k-factor=1.177 and for Permalloy thin film concentrations Ni 84% and Fe 16%.

Assuming cell dimension a_{Ni} =3.52Å and a_{Fe} =2.874 Å, the measurement of radii of diffraction rings gives these *d*-spacing for following *(h,k,l)* planes:

- R_1=1.2cm, d_{111}=2.092 Å,
- R_2=1.4cm, d_{200}=1.793 Å,
- R_3=1.988cm, d_{220}=1.263,
- R_4=2.33cm, d_{311}=1.077 Å,
- R5=3.125cm, d_{420}=0.803.

Both EDS spectra of the Permalloy target show common peaks not coming from the Permalloy sample: Cu from copper grid, Si escape peak of silicon detector, O_2 incorporated during sputtering process and C in second (thin film) from the rest of PMMA resist (after lift-off procedure).

EDS spectra of the Permalloy target show several additional peaks not coming from the Permalloy sample: very high intensity of C from carbon thin film on Cu grid, Al and O_2 from grinding in the Al_2O_3 dish (see Fig. 2). A difference in ratios of intensities Ni/Fe from Permalloy target and Permalloy film is present, 3.44 and 4.07 respectively, with ratio of both ~1.183). The second thin film sample was prepared by sputtering, and the ratio of sputter-yields for Ni and Fe at 600V of energy of Argon ions was calculated to have the value 1.5/1.3=1.153. This value is in reasonable agreement with our EDS maximal intensity ratio 1.183, because energy of Ar ions during this sputtering was 480-490V.

The numerical fit with a Gaussian function (for peaks of Ni and Fe) gives the concentrations of Ni and Fe 84% and 16% respectively. These values can be improved by taking into account the other peaks. The *k*-factor 1.177 was calculated from known concentrations of the Permalloy target sample. One must take into account that the Permalloy target sample was much thicker than the Permalloy film sample and, in addition, there are Al and O_2 impurities from grinding procedure.

Summary

The diffraction analysis shows the polycrystalline phase of the Permalloy thin film sample. Dark spots in Fig. 1b with a diameter in range from 5 to 20nm are small crystals of Permalloy that diffracted electron beam in the bright field image. The images of Permalloy surface show that a real surface of this magnetic material is far from the ideal crystalline film used in numerical simulations of micromagnetic dynamics. In addition, the resulting concentration of the sputtered film was changed respectively to

the one of the $Ni_{80}Fe_{20}$ target because of different atomic masses of Ni and Fe, the deposition rates and a migration in the end of the magnetron sputtering process. An important influence on the composition of a Ni/Fe alloy has a high temperature of the sputter target during the deposition and a gradual aging/degradation of the Permalloy target.

Appendix 4. ***Electron beam lithography procedures for SEM LEO440 and Nanometer Pattern Generator System.***

1. Substrate preparation.

Quick cleaning of substrates can be done in baths of Acetone, IPA (isopropylalcohol) and followed by a dry air. Dirty substrates can cause significant non-homogeneities in the resist layers. It is recommended to do cleaning of substrates in "piranha" before thin film resists deposition.

Piranha recipe: (H_2SO_4: $H2O_2$ 3:1) for 5-15min (ultrasonic) bath, rinse in water until all rests of acids are removed (check in optical microscope for colored circular patterns) and dry/blow in air.

Use the Acetone bath or spinning (at 500-1000rpm) to remove old PMMA and Copolymer resists. For hard baked resists, the Acryl Strip (the Microchem resist remover) is more appropriate (stronger).

For LOR resist removal use 2 baths in Remover PG at 20-80C (the flash point is 88C), one bath in IPA, rinse in water and apply dry air.

To improve the resist/substrate adhesion, a pre-bake of substrates before the resist spinning (5min/200C on a hotplate or in an oven) is recommended.

2. Resist deposition.

2.1 Resist spinning, baking and development.

Drop a resist (several drops on $1cm^2$ substrate using pipette applicator) to cover entire substrate and immediately start the spinning (e.g. using small blue spinner with a vacuum) for approx. 40seconds, with a lowest acceleration and deceleration.

Spinning on substrates with existing structures can result in non-uniform thickness of the resist. A spinning of thin layers on a substrate with existing e.g. 300nm thick and 20μm wide metallic wires with 20μm gap between them typically results in uniform resist layers. However, it could be hard to reach sufficient uniformity of a resist layers on gold wires 300nm thick and 1μm wide because of their higher thickness/width ratios. In this case, a use of a spin-on-glass (optionally an SiO_2 layer) is recommended to make the top surface planar.

When spinning on thin membranes (e.g. 5x5mm substrate with 0.5x0.5mm membrane 50nm thin) is required, the use of double-sticky tape instead of vacuum is recommended to keep the substrate stuck while spinning. Extreme care must be done when handling the fragile membranes.

For extreme requirements (e.g. a writing of sub-50nm features), a long baking before spinning (to remove rests of water) is recommended. Baking is very important for good resist/substrate adhesion and to avoid resist swelling and/or narrow line closure. When baking a resist on hotplate, the use of (non-contact) temperature sensor is recommended (the real temperature at the hotplate's surface can be significantly lower than the temperature shown on the hotplate's display). Each user should take an appropriate amount of resist and keep it in a private small bottle.

2.2 PMMA.

Spinning of single layer of PMMA (polymethylmethacrylate) 950k, 495k, A4, A2, C4, C2 (A-in anisole, C- chlorobenzene, 4%, 2% concentration). The use of PMMA in

Anisole (A2) is recommended. Anisole and chlorobenzene for user solutions are available. Typical spinning time is 40seconds. For example, apply PMMA 950k A2 at 3000rpm for 40sec to get ~70nm thick layer. Check the Microchem spinning tables (spinning curves give correct film thickness for PMMA in anisole and for copolymer).
Baking time: 2-30min on hotplate at 180°C and 30min - several hours in an oven at 170°C.

To develop an exposed resist at ambient (~20°C) temperature, use 1st bath in 1:3 mix of MIBK(methyl-isobutyl-ketone) / IPA (Microchem) for 40sec, 2nd bath in IPA for 20sec and 3rd bath in water for 20sec (with a mild agitation).
After the development, bake the substrate for 2min at 100°C on a hotplate.

2.3 Copolymer.

Spinning a single copolymer-EL6 (in ethyl lactate, 6%):
Use 7000rpm (max. ~7500) for 40sec resulting in ~110nm thick layer.
Ethyl lactate for user solutions is available.
Baking time: 2-30min on hotplate at 150°C or 30min - several hours in an oven at 140°C. Development is similar as for PMMA (2.2).

2.4 Double layer copolymer / PMMA.

Spin copolymer EL6 to get 110nm thick 1st layer and bake it for 20-30min at 150°C on a hotplate. Let cool down for a minute, then rev the spinner up 3000rpm and apply 8-10 drops of PMMA 950k A2 (on rotating substrate) to get 2nd ~70nm thick layer. Do spinning for 40sec and the start promptly the baking at 150°C for 20-30min. The use of PMMA in chlorobenzene is not recommended because the chlorobenzene is a strong solvent and mixing of both layers will destroy major part of the lower copolymer layer. Development is similar as for PMMA (2.2).

2.5 Double layer LOR / PMMA 950k A2.

LOR 0.5A is a lift-off resist and its development rate depends (similarly as at related PMGI resist) on temperature and length of baking (see Microchem tables for spinning curves and baking tables).

Spin LOR 0.5A at 5000rpm for 40sec, bake it at 180°C on hotplate for 5min, and then apply 2nd layer of PMMA 950k A2 (bake it for >5min).

A development after an e-beam exposure:

1st step: the standard development of the top PMMA layer,

2nd step: with the developer CD-26 for 10sec (the development time depends on a pre-bake time and temperature). At LOR undercut rate ~4nm/sec the undercut of the LOR should be approx. 40nm. If baked longer and at higher temperatures (close and above 190°C) a development or a removal could be difficult.

Bake the substrate for 2min at 100°C on hotplate to remove rests of liquids.

2.6 Resist thickness measurement.

Make a scratch with a knife and use the Alpha-step to measure the resist thickness (scanning length 80um, rate 25). Other means for thickness measurement, such as the AFM, the optical profilometer and the ellipsometer, are also available.

2.7 Anti-charging layer deposition.

Working with non-conducting substrates, like a sapphire, a conductive coating is required (typically ~5nm of gold, sputtered for 12sec at Ar pressure 2-3mTorr with NanoFab's Bob sputter system from the lower gun). Be careful about the use of other sputtering device for Au coating. The discharge above the sputter target could easily irradiate a sensitive e-beam resist. It is important to have sufficient conductive connection between top layers of the substrate and the SEM holder when using double-sticky tape to hold the specimen.

3. Electron beam lithography with SEM LEO 440.

Typical current/voltage setting (small spot size, high resolution) of SEM LEO440 for EBL:

- 10 micron aperture
- 40kV acceleration voltage
- I_{fil}=3000-3040mA filament current (working at second peak)
- I_{beam}=20μA beam current

- I_{probe}=10-20pA probe current
- I_{spec}=5-10pA.specimen current, measuring with Faraday cup (FC)

I_{beam} and I_{probe} (I_{spec}) can be changed depending on data, writing field, required resolution or a speed of writing.

3.1 Change of the specimen.

Set the *Standby mode*, close the *Column isolation valve*, the *Gun isolation valve* should already be closed, vent the chamber, change the specimen, pump the chamber down, wait until the chamber vacuum Ready state is achieved and the column isolation valve can be re-opened ($5x10^{-6}$Torr).

3.2 Preparation and alignment of SEM.

The proper training of a user to control SEM vacuum system safely is critical.

With LaB6 filament the column is always under vacuum ($2\text{-}3x10^{-7}$Torr). SEM needs 2-3 hours after the start to stabilize (when starting from the Shutdown mode) or about 30min after the e-beam was temporary off (when in the Standby mode overnight or while chamber has been vented). The stage should be in FC position (default).

Below are procedures for SEM alignment.

3.2.1 Gun alignment.

1. Beam On with standard current/voltage setting
2. Choose SEM *Control Panel* (*^G*), *Apertures* (*Optibeam always checked*, default setting)
3. *Conjugate mode* unchecked (default)
4. *Emission mod,* at low magnification, MAG ~100, the *Working Distance* WD (focus) very long (~50mm)
5. Move the stage so the FC does not affect the emission image
6. Set *Shift mode, Depth mode* checked, place the emission image (typically a bright elliptical spot) to the center of the screen
7. Set *Tilt mode, Depth mode* unchecked, place the emission image (typically a bright large spot area) to the center of the screen

8. Check that the filament current is set at second emission peak (this step will be repeated more accurately later in *Normal mode* while measuring I_{spec}), repeat step 5 and 6

9. *Set the Normal mode,* move into FC position, set proper WD, run Shift+F2 (hysteresis removal procedure, required each time if WD was significantly changed, >50m)

10. Set the hardware switch (stage limits signal/ I_{spec} current measurement) on the left side of the SEM table to its "measure" position, set *Spot mode* and point the beam spot into FC

11. Using steps of 10mA change the I_{fil} to reach saturation (2^{nd} emission peak), do not set I_{fil} too high, it will shorten the filament lifetime only

12. Repeat steps 2 - 10

13. Adjust *Tilt (mode)* to find the maximum of I_{spec}

3.2.2 Beam alignment.

1. Move stage to alignment sample position and find an appropriate round object (0.2-1m) big

2. Set the best WD (focus)

3. At various MAG e.g. 10k, 50k, 100k MAG use the *Focus Wooble (in SEM Control, Apertures)* and aperture's XY micrometers for fine adjustment of the final aperture position

4. Run Shift+F2, set the best WD (focus), run Shift+F2

5. Set MAG x100k - x200k, defocus the image a bit

6. Set *Stigmatism (in SEM Control, Apertures)* and use mouse control buttons to adjust the astigmatism correction (typically StigX=10%, StigY=20%)

7. Set the best WD (focus), run Shift+F2, set the best WD (focus) again, run Shift+F2

8. Repeat all steps (optional, recommended if working on fine sub-100nm structures)

If the specimen was changed, check the gun/beam alignment again.

3.5 Focus alignment on a substrate.

At low MAG, ~100, 1k, 5k find the substrate, using XY move and rotation of the SEM stage, align the top edge of the substrate parallel with bottom line of the screen (to expose the smallest resist area at low MAG ~100) or parallel with the grid line.

Define the reference point on the substrate (e.g. the right upper corner marked with a scratch).

Find proper WD by moving the stage in the Z direction (using a dirt particle or burn the hole into the resist using *Beam spot mode* at MAG ~200k, for several minutes depending on the current, a substrate and the resist sensitivity. The resulting hole will have ~50-200nm in diameter. If you change the WD to find the focus, be sure you return to the original WD value (at which the focus and the astigmatism alignment was done) and run *Shift+F2* (a hysteresis removal procedure). Adjust the Z position to reach the right Z level & focus (WD).

For a single exposure (if the substrate is not significantly tilted) it is enough to move directly to the place 50-100um far (depends how large is the field of view of the exposure).

Do the alignment of the focus (Z position) at this alignment point, and then move to the point of the exposure.

If a substrate is tilted or exposures are at far distance each other, it is recommended to find the focus alignment at least at 3points on the substrate and the calculate (MATLAB procedure) right Z position for an arbitrary XY point on the substrate.

3.6 Design of patterns and exposure data.

NPGS and DesignCad help files are excellent sources of the information and examples for correct data preparation and exposure.

DesignCad Windows or DOS versions provide .DC2 (an ASCII format designed for NPGS) data files as the data input for NPGS .RF6 run files.

DC2 file contains pattern data such as lines with arbitrary thickness (zero thickness represents single pass of the e-beam), a filled polygon (closed areas for the exposure), circular and elliptical structures, and a text. Each pattern can be placed into different layers (up to 18). Each layer has independent set of colors (that correspond to different

doses or different exposure time for a given writing current).

NPGS application reads RF6 run file, DC2 data file, recognizes different layers and different colors in each layer. Except various colors, each layer contains the information about the magnification at which the exposure will be done, a center-to-center distance and a line-to-line space (parameters defining how dense the writing is), a specimen current, the exposure time and the calculated dose (area, line or point).

To estimate a writing time, run the *Time Test Mode* from NPGS Menu */Commands /Process Run File*.

3.7 Exposure.

Before running the exposure, the following steps must be done:

1. Check the hardware External Control Switch is in NPGS position (default)
2. Set the proper magnification of the SEM, usually 1000x
3. Set the switch to measure the I_{spec} current during the exposure
4. Set the scanning rate of SEM to 15 (the slowest scanning rate)
5. Set the switch of the Beam Blanker to "ON"
6. Turn ON the external control of SEM (from *Main menu, Tools*)
7. Unfreeze the SEM image
8. Move the substrate to the position for the exposure, launch the exposure process from NPGS Menu, write down the information for the NPGS Log file and start the writing.

4. Resist development.

Remove thin protective Au layer (if deposited) using the Au enchant (3-4 sec) and rinse the substrate in a water. Do the development as described in Section 2.1.

5. Inspection of results.

The exposed patterns (after development) are very well visible (down to 100-200nm) in optical microscope. To see fine patterns in the SEM, sputter ~5nm Au layer. Start at MAG 1k-3k, with I_{probe}~1pA. If the contrast is low try lower acceleration voltage ~5-8kV (required typically for Permalloy structures on a sapphire and/or a gold film).

6. Critical doses for various substrates/ resists combinations.

The exposure doses below are designed for following SEM and exposure data parameters:

- acceleration voltage 40kV
- working distance ~7mm
- writing current 10pA
- center-to-center distance/line-to-line space 10/10nm
- development time in MIBK:IPA/IPA/H_2O : 60/20/20sec
- baking time 2-10min at 180° on hotplate

Silicon + PMMA950k (100nm): 270μC/cm^2

Silicon + PMMA495k (100nm): 240μC/cm^2

Silicon + copolymer-EL6 (120nm): 100μC/cm^2

Sapphire + PMMA950k (100nm): 280μC/cm^2

Sapphire + copolymer-EL6 (120nm): 110μC/cm^2

Sapphire + Ti/Au (300nm) + PMMA950k (100nm): 175μC/cm^2

Sapphire + Ti/Au (300nm) + copolymer-EL6 (120nm): 70μC/cm^2 (dev 40/20/20sec)

Sapphire + Py (15nm) + PMMA950k 255μC/cm^2

Appendix 5. ***Optical analysis of a surface of thin film structures.***

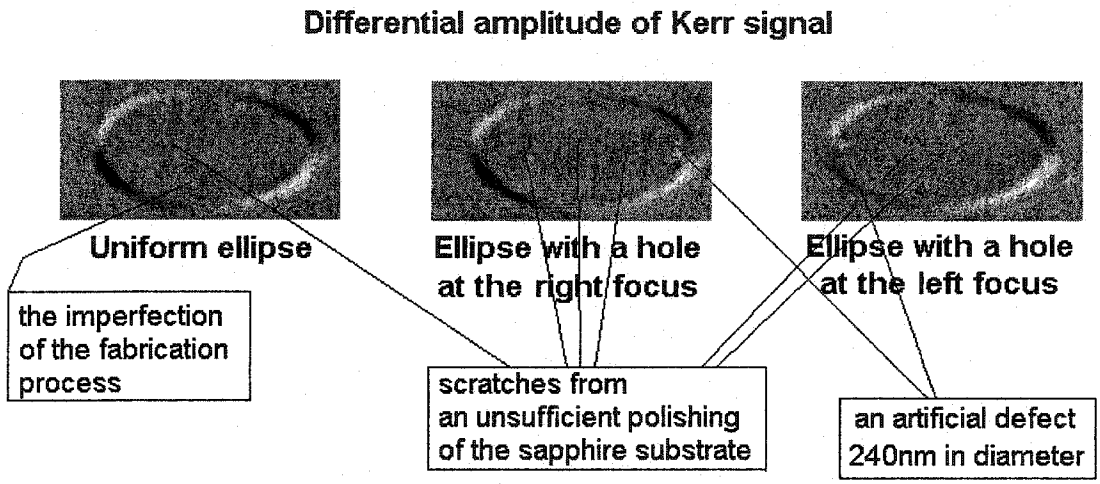

The images of three ellipses display the surface of the patterned Permalloy 15nm thin film. The probe beam was reflected from the substrate with the magnetic structure and split in two by the Wollaston prism of the MOKE microscope. Two photodiodes detected the optical signals and the final signal was created by the subtraction of signals of these two photodiodes.

The polishing of the sapphire substrate was insufficient and each magnetic structure is affected by the presence of scratches. A relatively shallow valley covered by a continuous sputtered Permalloy film represents each scratch. The ellipses in the middle and on the right have artificial defects in the right and left focus respectively. Except these designed defects, there are few imperfections caused by improper data for the e-beam-lithography writing process. The AFM scan of these structures was not done because of insufficient time.

Appendix 6. ***Analysis of temporal behavior of a magnetization of a Py square.***

The magnetic bias field lies in the plane of the magnetic film and its initial state has the central domain and two closure domains. The orientation of the closure domains depends on the magnitude of the DC bias, a "C" configuration can be formed, for example for the magnitude of the DC bias 4.6kA/m.

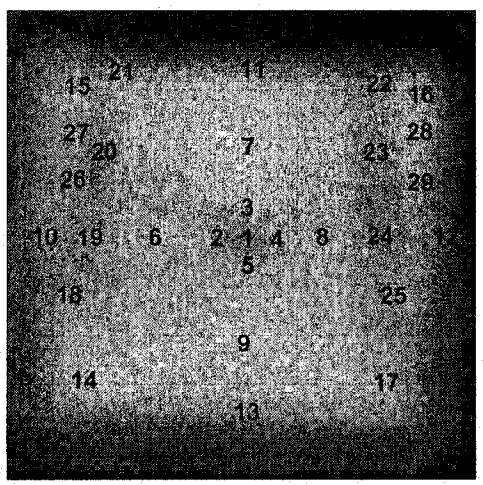

Fig. 1. The experimental Kerr image (at 225ps of time delay) of the 4μm square in DC magnetic bias 4.62kA/m (oriented horizontally) with closure domain structure, domain walls and a 240nm-diameter pinhole in the center. Numbers represent locations of probe focus where full time-domain curves were constructed (at each location, an average of 3 pixels was used). The magnitude of the pulse excitation was 640A/m and the rise time 200ps.

The magnetization oscillations strongly depend on the local magnitude value of the effective internal magnetic field. These local fields are determined by the domain wall structure. In time domain responses (see, for example, the line curve in the first graph in Fig. 2), the first peak of curve includes the parametric response to the excitation pulse. The height of this peak, relative to the amplitude of the subsequent oscillations, is very sensitive to the excitation pulse shape.

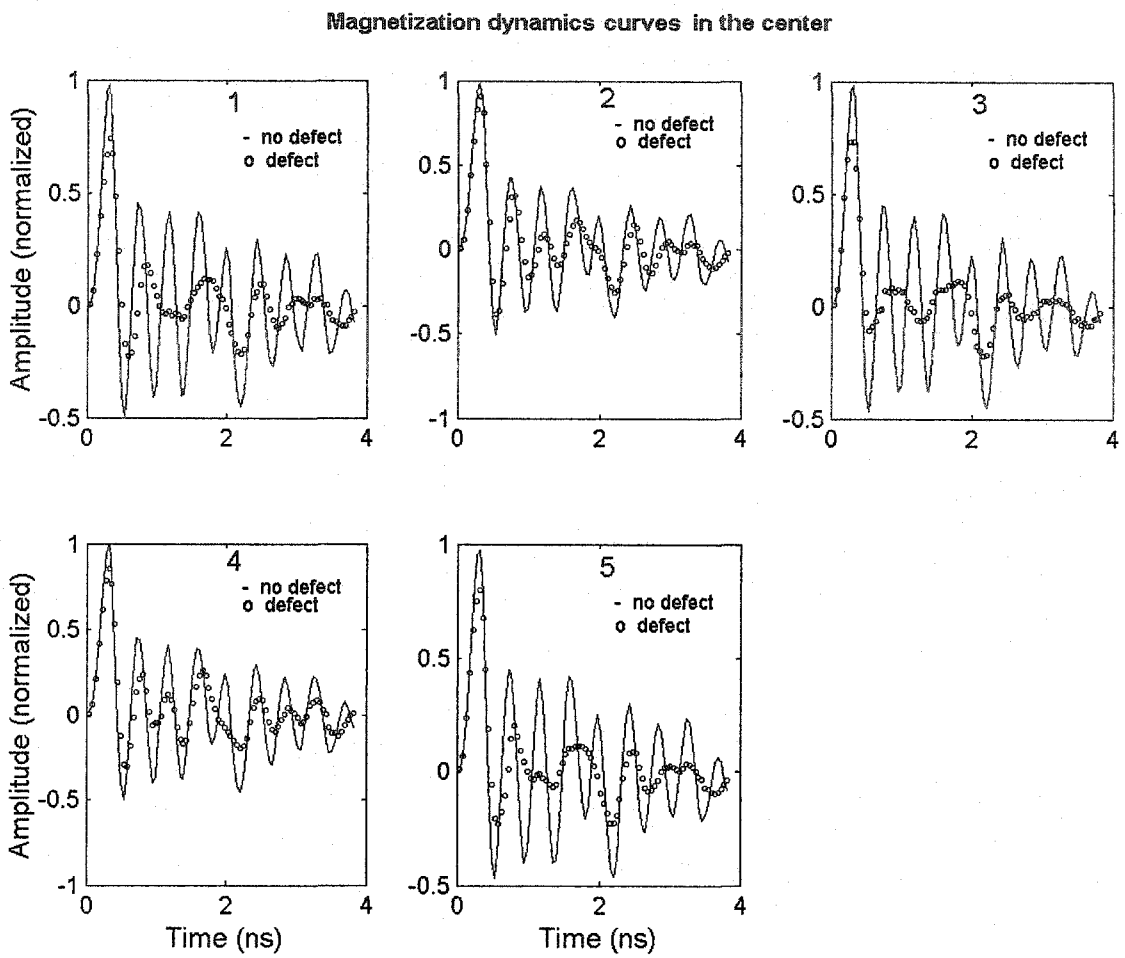

Fig. 2. Experimental broadband magnetization dynamics curves at the first five different points in and around the center of the magnetic platelets (with and without a pinhole, see the map in Fig. 1). The frequency of oscillations in the center of the uniform sample is 2.3GHz for all five points. The same frequency was found at points #2 and #4 of the sample with a pinhole, while the central #1, left #3, and right #5 points have complicated shape. At these points, no single frequency can be identified (possibly because of the probe spot is overlapping more than one mode, or this could be an evidence that in highly non-uniform internal fields around the defect the modes aren't spatially localized). The bias field magnitude was 4.6kA/m.

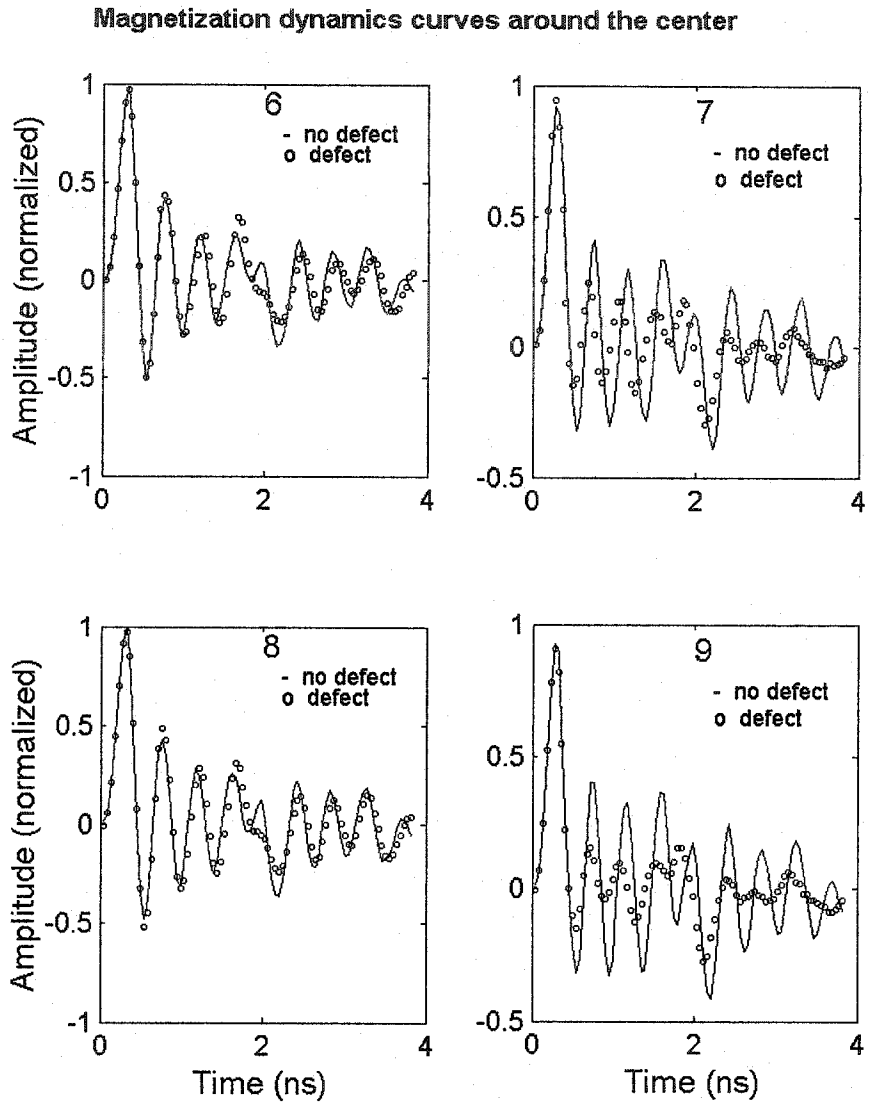

Fig. 3. Experimental broadband magnetization dynamics curves at four different points in the larger central area (around the area of the pinhole) of the magnetic platelets (see the map in Fig. 1). The frequency of oscillations at four points #6-#9 of the uniform sample is the same, 2.3GHz. The same frequency was found at the point #7 of the sample with pinhole, while the lower point #9 has frequency shifted up by 0.74GHz.

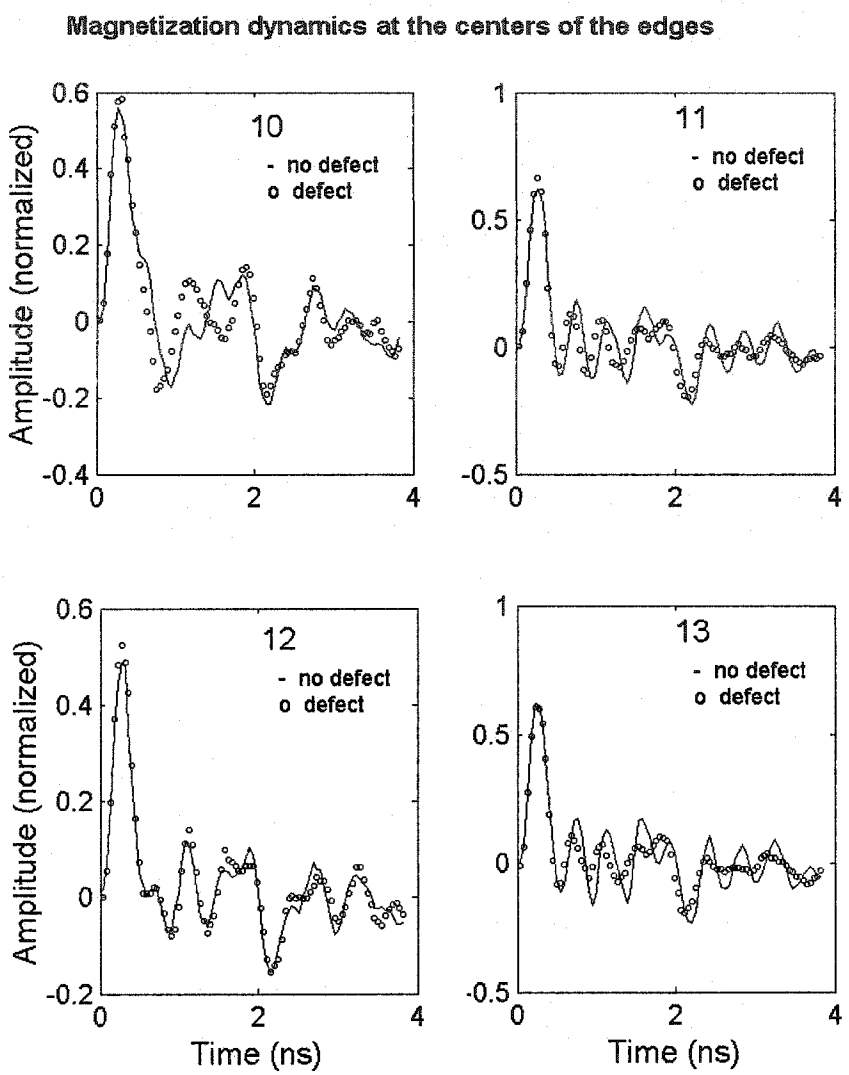

Fig. 4. Experimental broadband magnetization dynamics curves at four points in the center of the edges (see the map in Fig. 1). The frequency values at left-right points #10, #12 are 0.74GHz, 1.48GHz for the uniform sample and 1.48GHz for both points of the w/ pinhole sample. Higher values of the frequencies at #11, #13 (both samples) are 2.3GHz.

The oscillations of the polar component of magnetization measured at various points of the samples (see Figs. 2-8 with curves for both the uniform and with central pinhole platelets) are normalized to the height of the initial peak. Each curve was

extracted from the set of 92 spatial frames (scanning grid 96x96 points over the 6x6μm area) with the temporal step 45ps. The map of point locations is in Fig. 1. Each data point on the curves is an average over an area of seven neighboring scanning points.

This represents an effective area (that the magnetic signal was taken from) 800nm in diameter (assuming the effective diameter of the Gaussian beam at the focus ~500nm). The situation close to the pinhole (Fig. 2, dotted curves) is different. The "cusp" structures around the pinhole form a small domain wall structure with quadrupolar symmetry (with four domain walls pointing along the diagonals into the corners of the square. The resonance responses at the left-right (#2-#4) sides of the sample show similarities consistent with the "cusp" domain structures. The same conclusion comes from the comparison of data taken from up-down (#3-#5) boundaries at the pinhole. The number of oscillations is small, affected by the reflected pulses and there are not enough data points for reliable Fourier analysis. Comparing left-right and up-down data, the oscillations at the left-right side follow the frequency close to the uniform sample at 2.3GHz. The estimated frequency in "up" and "down" areas is shifted down by ~0.74GHz. The Fourier analysis was done on reduced sets of points (without initial pumping and reflected pulses that were excluded from the data set).

The data at #6-#9 have not changed the frequency (the uniform sample) except the influence of a pinhole at #7 and #9 (magnon launching from non-uniform fields).

The edge points reflect the proximity of non-magnetic areas and (#10 and #12) are affected by the presence of non-uniform fields of the closure domains. Curves at #10 and #12 reflect the presence of large uniform central domain having "nice" oscillations (not affected by a relatively distant pinhole).

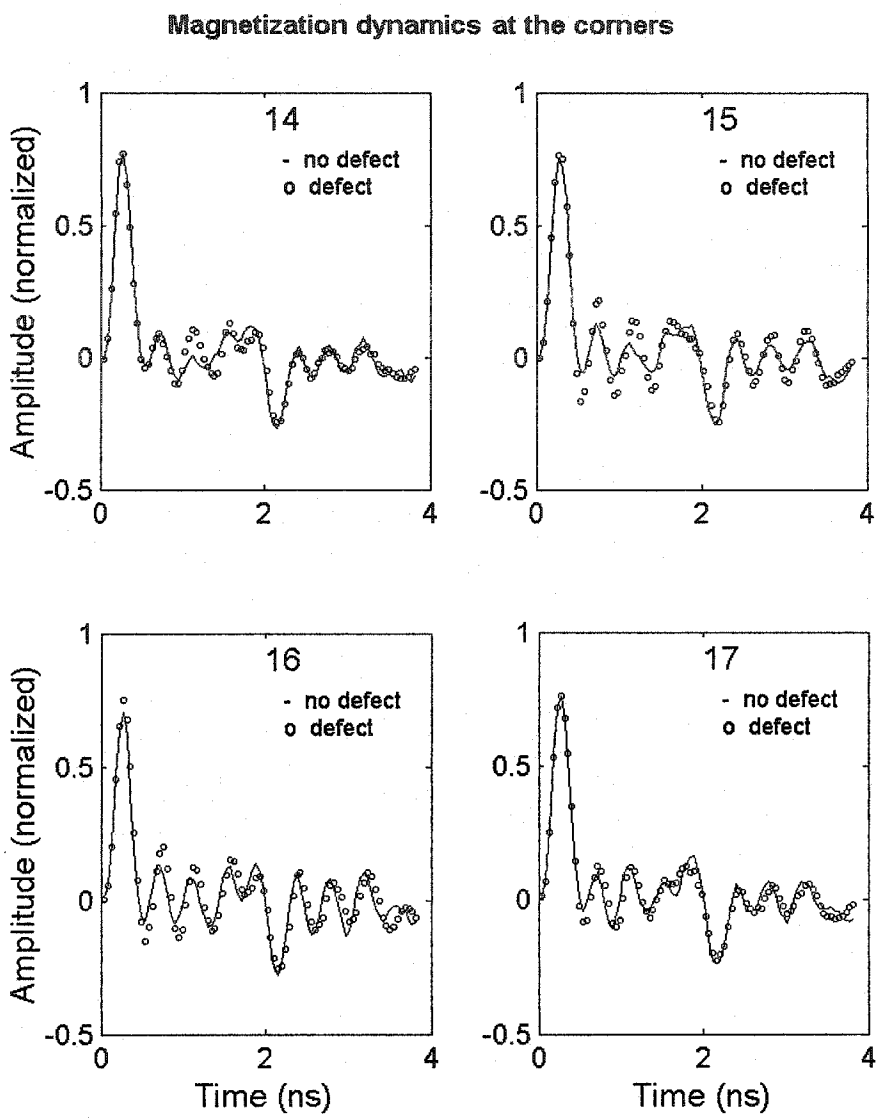

Fig. 5. Experimental broadband magnetization dynamics curves at four corner points of the magnetic square (see the map in Fig. 1). All four points (both samples) except #14 (the uniform one) show identical frequency values of 2.3GHz.

Similar comment can be said about corner points #14-#17. The oscillations of the uniform sample at #15 and #16 have surprisingly lower amplitudes of "ringing" peaks. A possible explanation still can lie in a relative drift (rotation) of the sample and, in addition, proximity of non-uniform (domain) fields.

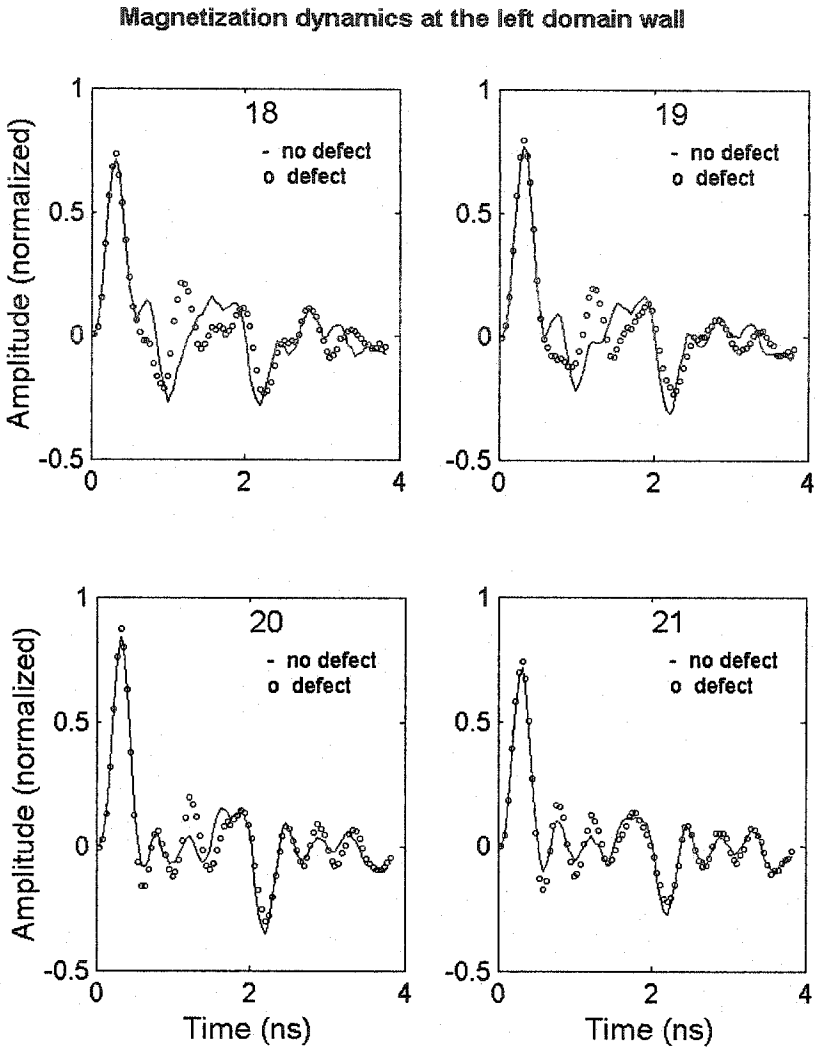

Fig. 6. Experimental broadband magnetization dynamics curves at four points at the left domain wall (see the map in Fig. 1). Each data point on the curves is an average over an area of three neighboring scanning points. The frequencies for the uniform and with-pinhole samples at points #18-#19 are low (approximately 0.74GHz) while at the end-point #21 approximately 2.3GHz.

Also the points at left and right domain walls (#18-#21 and #22-#25) don't display a single frequency of oscillations, however, an influence of a lower effective field (and

longer periods of oscillations) at the domain wall can still be recognized.

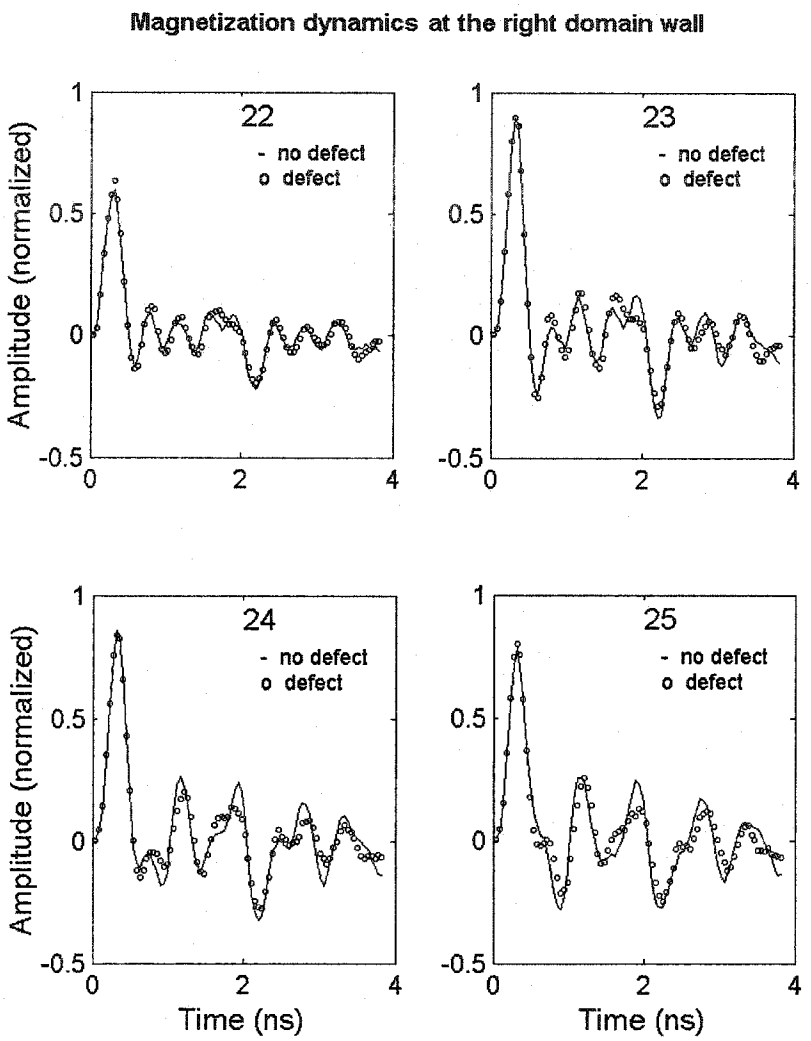

Fig. 7. Experimental broadband magnetization dynamics curves at four points at the right domain wall (see the map in Fig. 1). Each data point on the curves is an average over an area of three neighboring scanning points. The frequencies at points #22-#23 are higher (~2.3GHz) than at the points #24-#25 for both the uniform and internally patterned samples.

The analytical expression (2.66 Chapter 2) for the ferromagnetic resonance frequency of the infinite thin film (the Kittel formula) gives the value 2.13GHz (with the external in-plane DC bias 4.6kA/m, the saturation magnetization $M_0 = 57$kA/m and with the anisotropy field 477.6A/m). This value is close to the experimentally achieved frequency 2.3GHz.

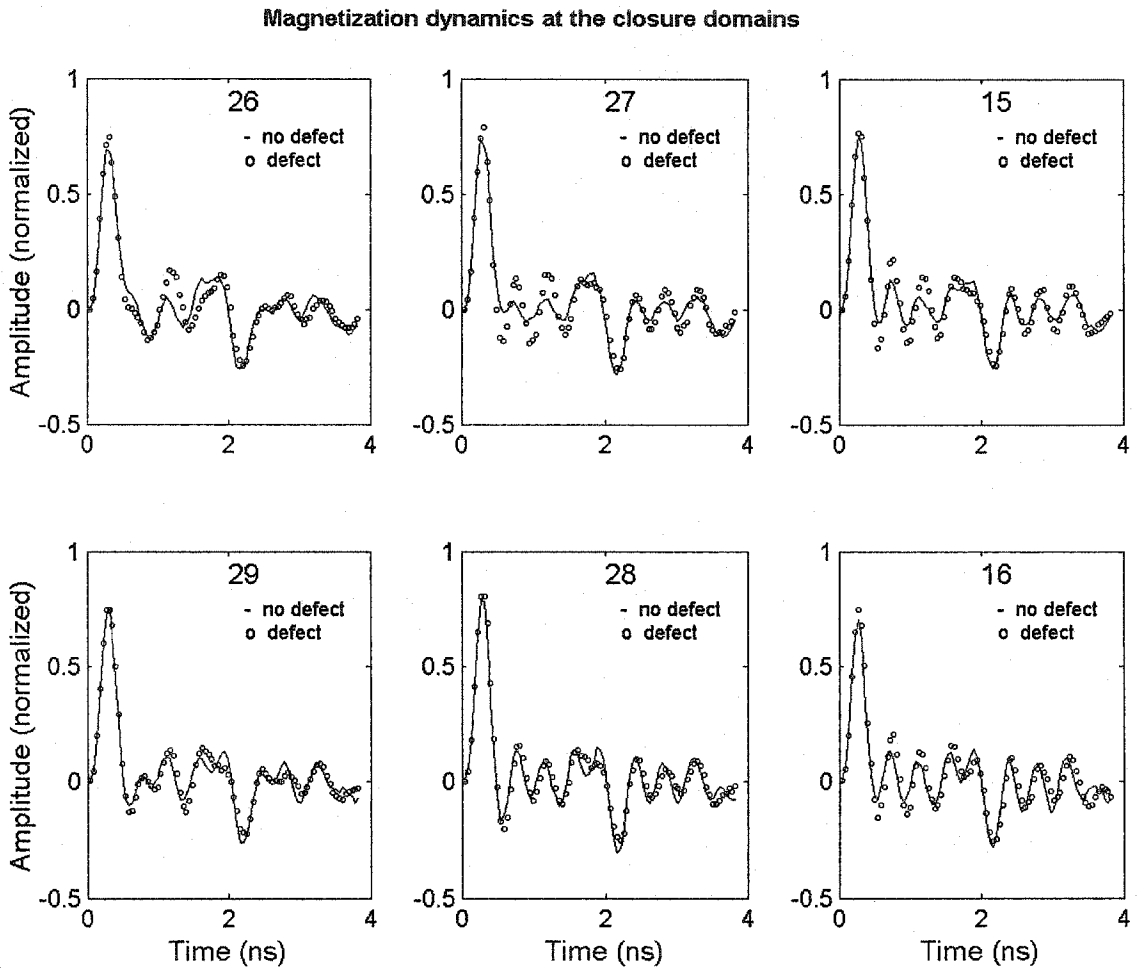

Fig. 8. Experimental broadband magnetization dynamics curves at three points in the area of the left (three graphs in the upper row) and right (the lower row) closure domains (see the map in Fig. 1). Similar patterns of the oscillations of the samples with and without the pinhole are clearly visible.

The resonance curves in the closure domains are very similar, albeit the Fourier analysis offers a larger spectrum of frequencies, relatively highest at the corners #15 and #16. The similarity of resonance curves (w/ and w/o a pinhole) documents that the domain walls produce sufficient "isolation" and that the influence of the pinhole (located in the sample's center) on the magnetization oscillations is minimal.

Appendix 7. *One-dimensional X-t scans at DC magnetic biases 3, 3.6, 4.6, 7.6, 18.3, and 60kA/m.*

Figs. 1-6 show the X-t scans of the magnetic squares w/o and w/ a pinhole. The effect of the pinhole is visible at lower magnetic bias fields (3 – 8kA/m). In addition, the lower experimental (optical) resolution does not allow for resolving of tiny details of magnetization oscillations around the pinhole and the domain walls. At very high DC magnetic bias fields >60kA/m (close to the saturation magnetization value) the non-uniform internal fields (at the domain walls and the edges of pinholes) are suppressed so much that the creation of magnons and the following magnon-magnon scattering is very weak. The indirect damping, which was important at lower bias fields, does not contribute to the relaxation and decay processes.

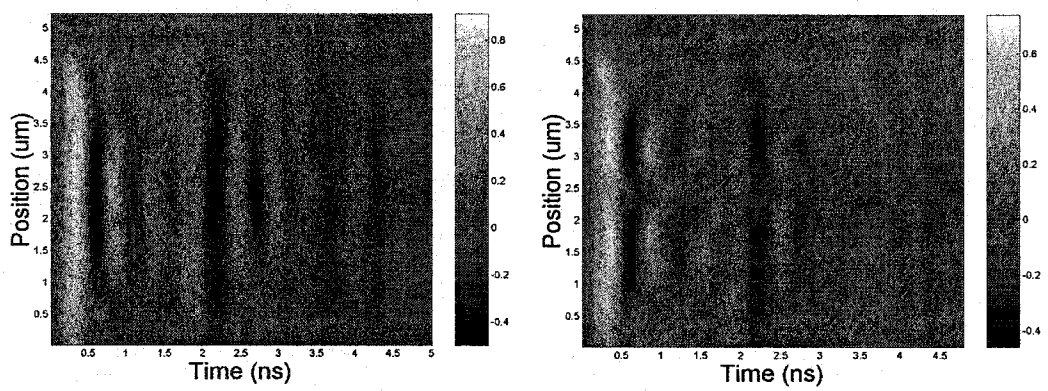

Fig. 1. One-dimensional X-t experimental scans of the magnetization dynamics. The scanning lines are drawn across the center of the platelet (parallel to the direction of the DC magnetic bias 2.95kA/m). The scans across the uniform and with pinhole samples are on the left and on the right respectively. The length of the time interval is 5ns.

As clearly seen in Fig. 6 the damping of the magnetization oscillation at 60kA/m bias is weaker than the one at lower bias fields, as, for example, is seen in Figs. 1.

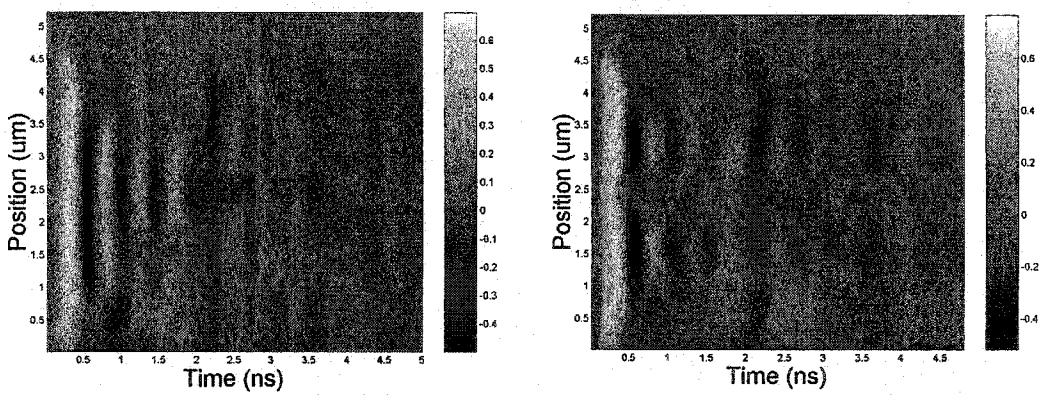

Fig. 2. One-dimensional X-t experimental scans of the magnetization dynamics. The scanning lines are drawn across the center of the platelet (parallel to the direction of the DC magnetic bias 3.58kA/m). The length of the time interval is 5ns.

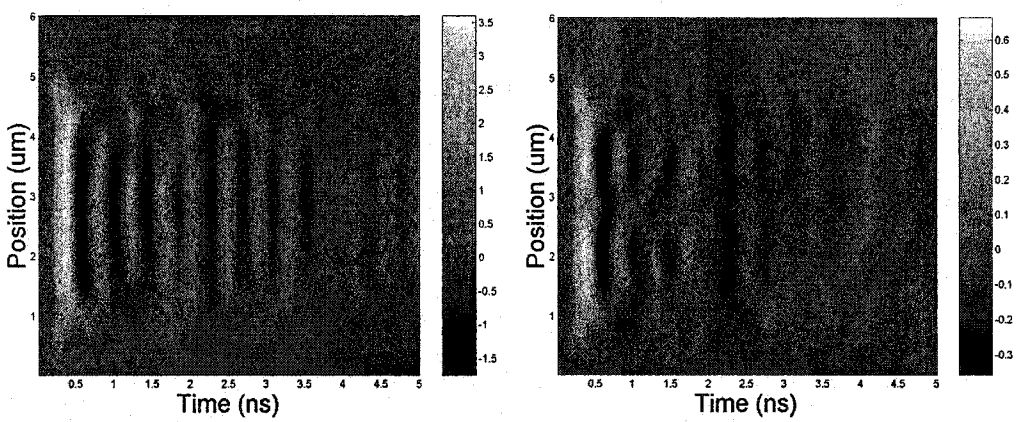

Fig. 3. One-dimensional X-t experimental scans of the magnetization dynamics. The scanning lines are drawn across the center of the platelet (parallel to the direction of the DC magnetic bias 4.62kA/m). The length of the time interval is 5ns.

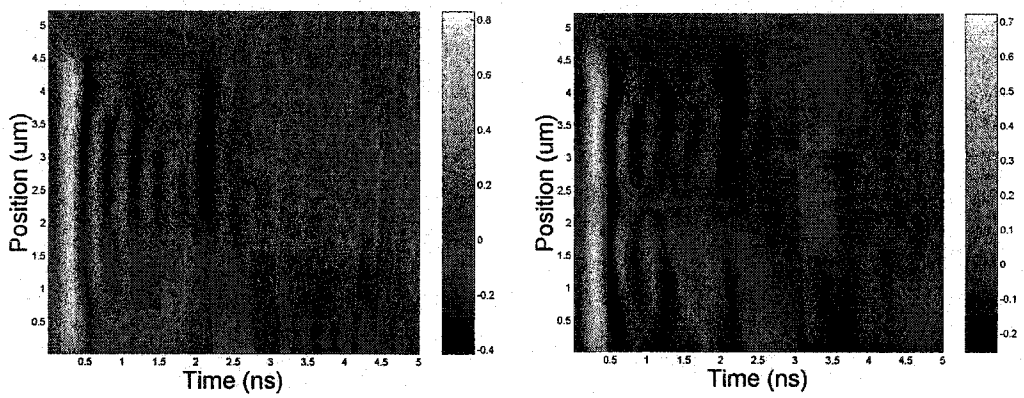

Fig. 4. One-dimensional X-t experimental scans of the magnetization dynamics. The scanning lines are drawn across the center of the platelet (parallel to the direction of the DC magnetic bias 7.64kA/m). The length of the time interval is 5ns.

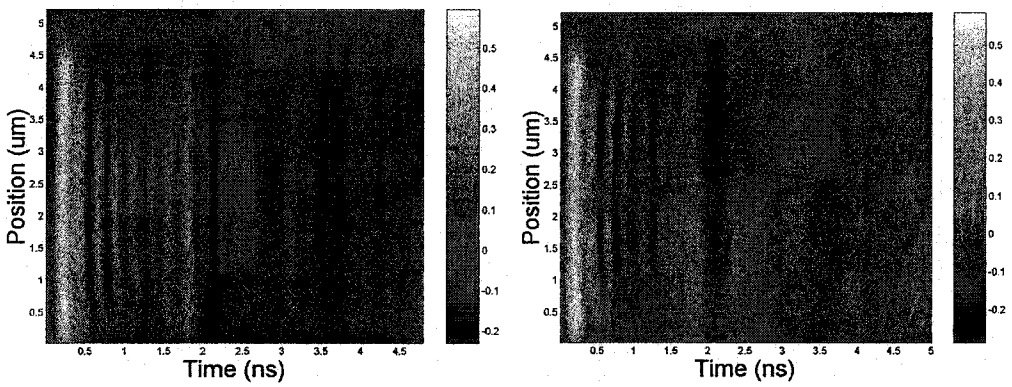

Fig. 5. One-dimensional X-t experimental scans of the magnetization dynamics at the DC magnetic bias 18.3kA/m. The length of the time interval is 5ns.

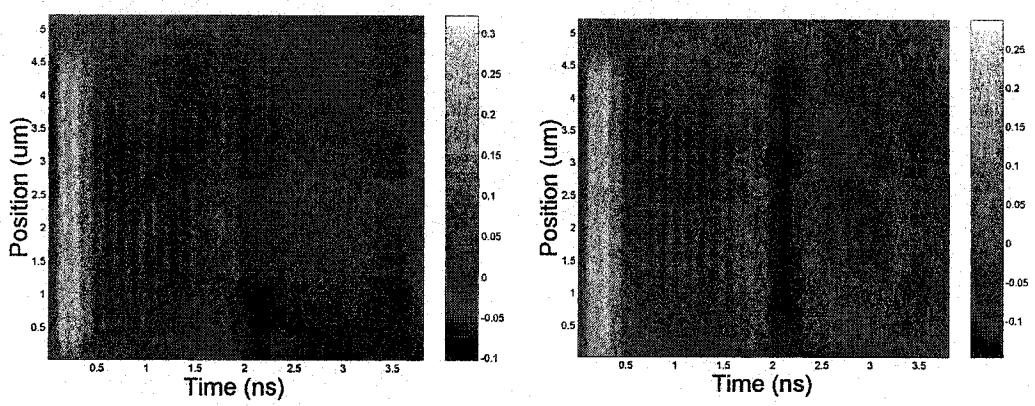

Fig. 6. One-dimensional X-t experimental scans of the magnetization dynamics at the DC magnetic bias 60kA/m. The length of the time interval is 5ns.

Appendix 8. ***Effects related to a high power of the probe beam.***

The power of the probe beam in front of the focusing objective was increased in a test trial with the magnetic ellipse with a pinhole at the left focus. Two values of probe power were used; a low power 5mW and a high one 15mW. The scanning was realized under regular scanning settings over an area 1.5x1.5μm at the right end of the ellipse. The scanning grid had 100x100 points (per frame). A time required for scanning one frame was about 20min or on average 120ms per point (based on 100ms waiting time and 20 ms time constants per point).

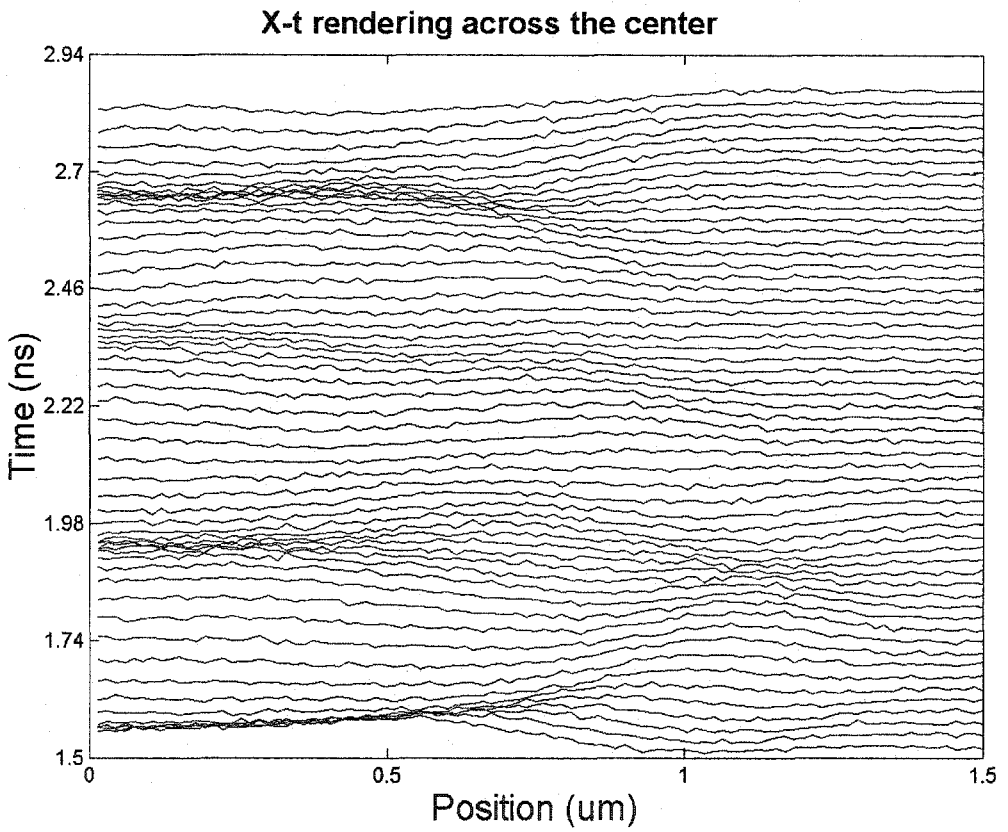

Fig. 1. 1-D rendering of a set of 2-D frames. Each curve represents a horizontal cut through the center of the magnetic element. Related spatial frames are in Fig. 2.The end of the ellipse has oscillating areas.

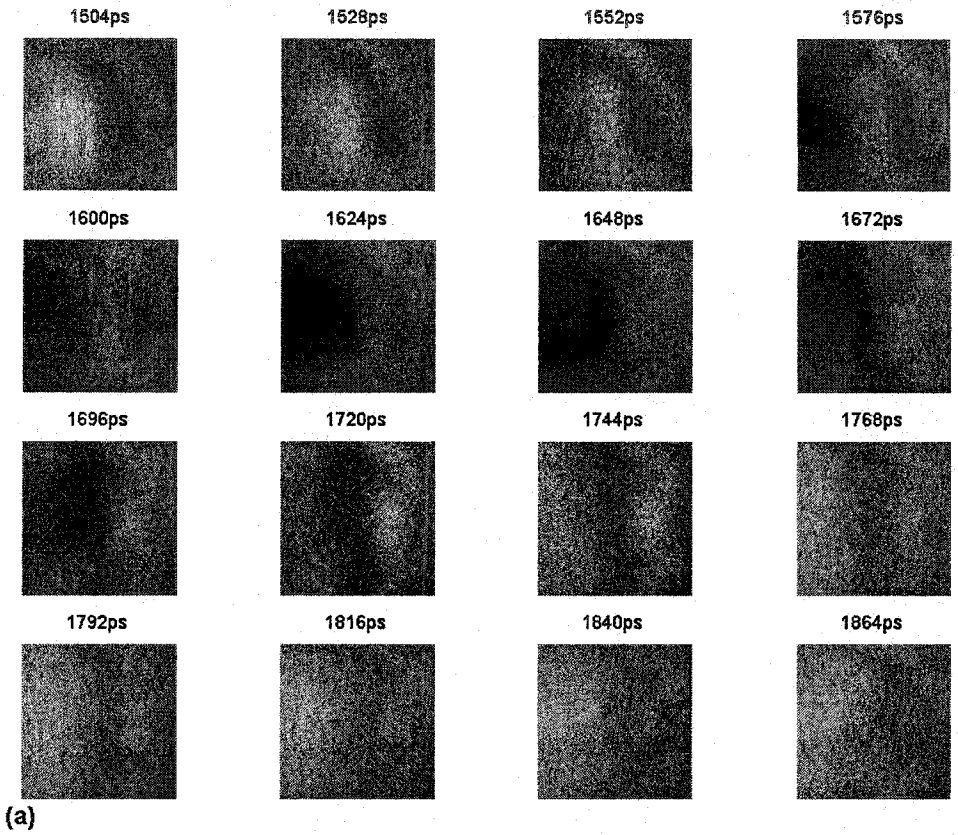

(a)

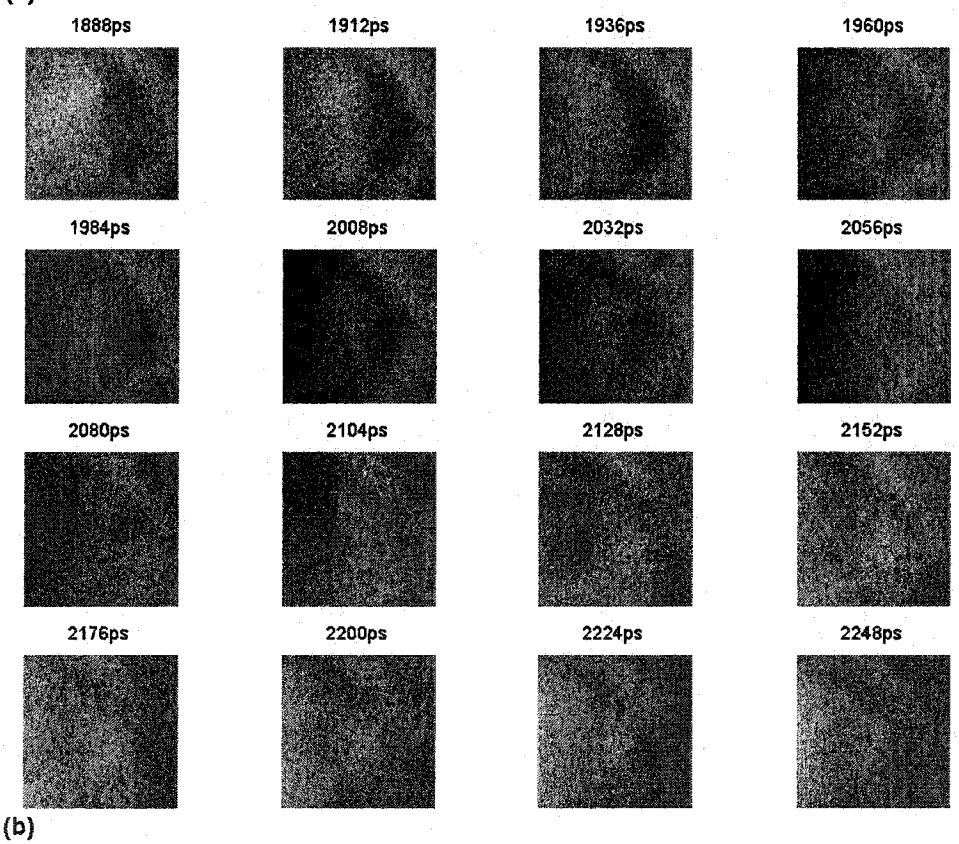

(b)

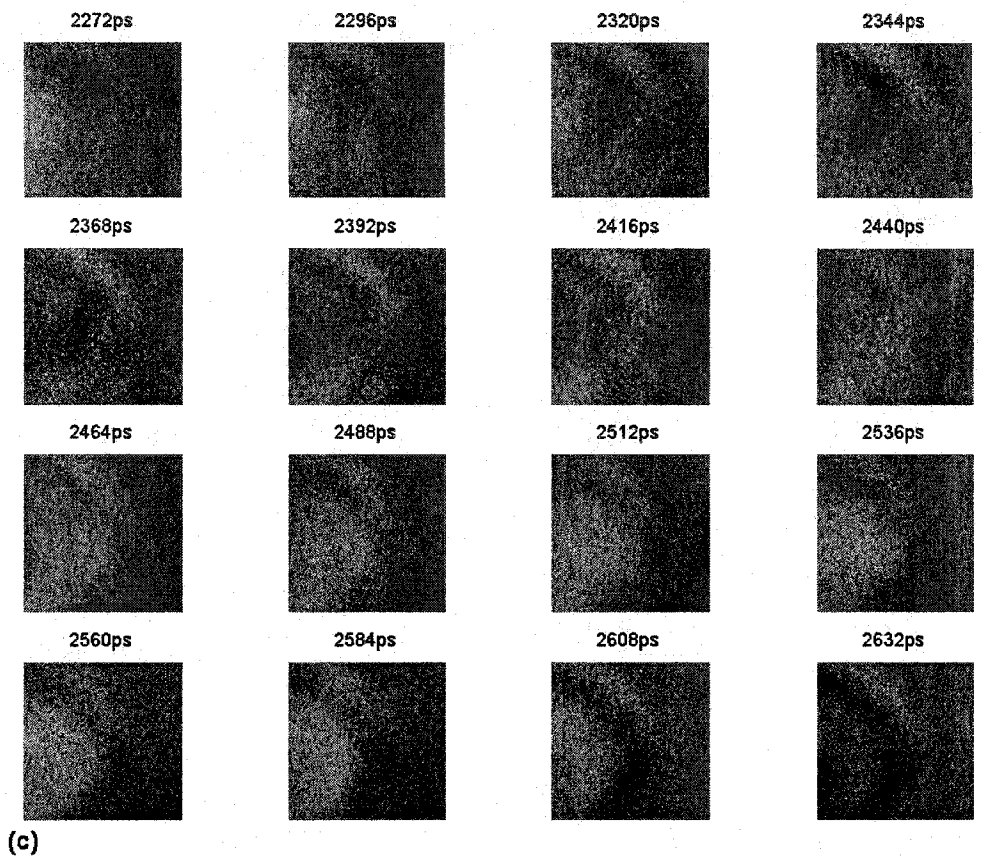

Fig. 2. Set of experimental 2-D frames a, b, c from the right end of the Permalloy ellipse scanned at probe power 5mW. The edges and small closure domain structures are clearly visible. The temporal step between frames is 24ps.The width of the scanned area is 1.5μm (100x100grid). The bright spots e.g. in frames 1696ps – 1768ps are clearly visible.

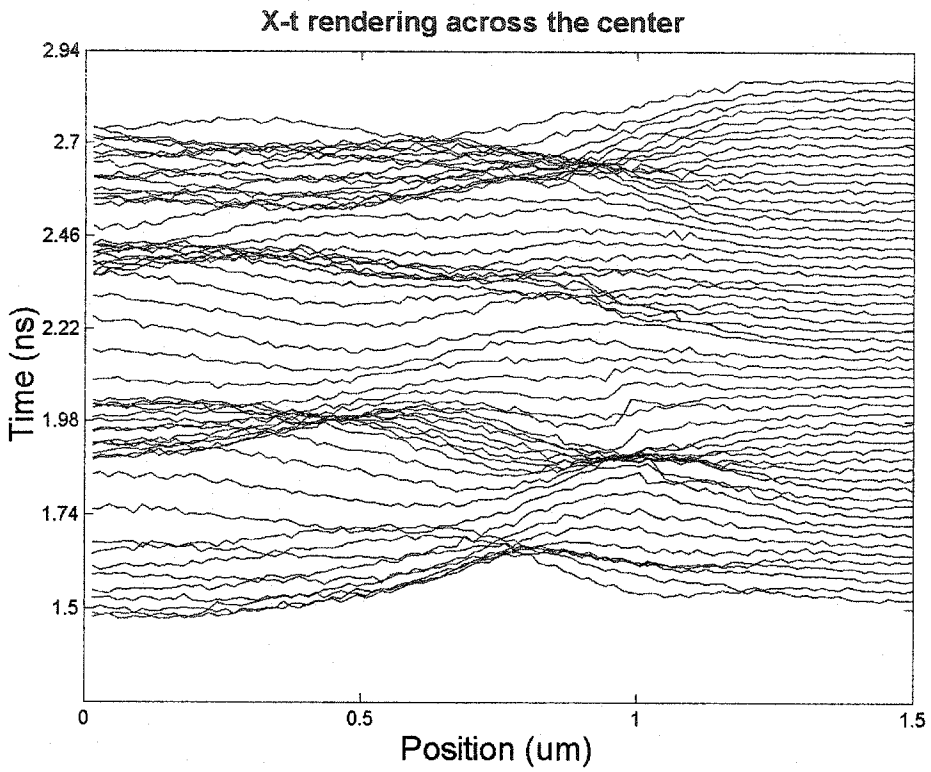

Fig. 3. 1-D rendering of a set of 2-D frames (higher 15mW probe power). Each curve represents a horizontal cut through the center of the magnetic element. Related spatial frames are in Fig. 4.The end of the ellipse has oscillating areas affected (dark/dense lines) by abrupt changes of the magnetization vector (caused by heating of the magnetic film by the probing spot).

The set of frames taken with a low probe power is shown on Figs. 2 (a, b, and c) with line rendering in Fig. 1. The images show the 2-D distribution of the polar component of the magnetization at the edges of the 15nm thick Permalloy ellipse and a closure domain structure. This magnetization distribution shows two bright spots that oscillate with the period approx. 400ps (equal to the period of magnetization oscillations measured at the center of the ellipse). These bright spots (see for example the time interval from 1696ps to 1768ps) represent higher angles of the out-of-plane component of the magnetization

vector. Three sets of frames in Fig. 2 a, b, c show the temporal evolution of the magnetization over 1.1ns long interval. The images in Fig. 4 a, b, c show the temporal evolution of the polar component of the magnetization but taken with a higher probe power. The sudden changes represented by the horizontal lines are consequences of a heating of the substrate & thin metallic film by the 15mW high probe power of a focused Gaussian beam.

An important role has the 120ms long time constant of the scanning procedure. The optical spot (effective width approx. 500nm) rests at each scanning point (of the 100x100 grid) for 100ms and is moved (~20ms needed) 15nm to the next point. After a row is finished, the spot is moved back on the other side of the scanning area (~20ms delay) to start a next row. Relatively large fraction of the magnetic structure is constantly illuminated and heated (in a time-dependent process). The higher temperature induces a local change of the magnetic properties of the magnetic film (also the domain structure) and relatively weak pumping pulse can locally increase the out-of-plane angle of the magnetization vector (e.g. at 2608ps Fig. 4c) or completely change the sign of the polar vector component (e.g. at 2632ps Fig. 4c).

To exactly simulate the whole contribution of heating (by 120ms long packets of 100fs long pulses with a period 12.5ns while the ~500nm large heat source is moving over the square area of 1.5μm) requires simultaneous solution of the equation of heat dissipation and the LLG equation of motion of magnetization (assuming a known temperature dependence of important material constants). The skin depth at these optical frequencies (~0.3×10^{15}Hz) is of the order of the magnetic film thickness and the film is heated almost instantly and uniformly over its thickness.

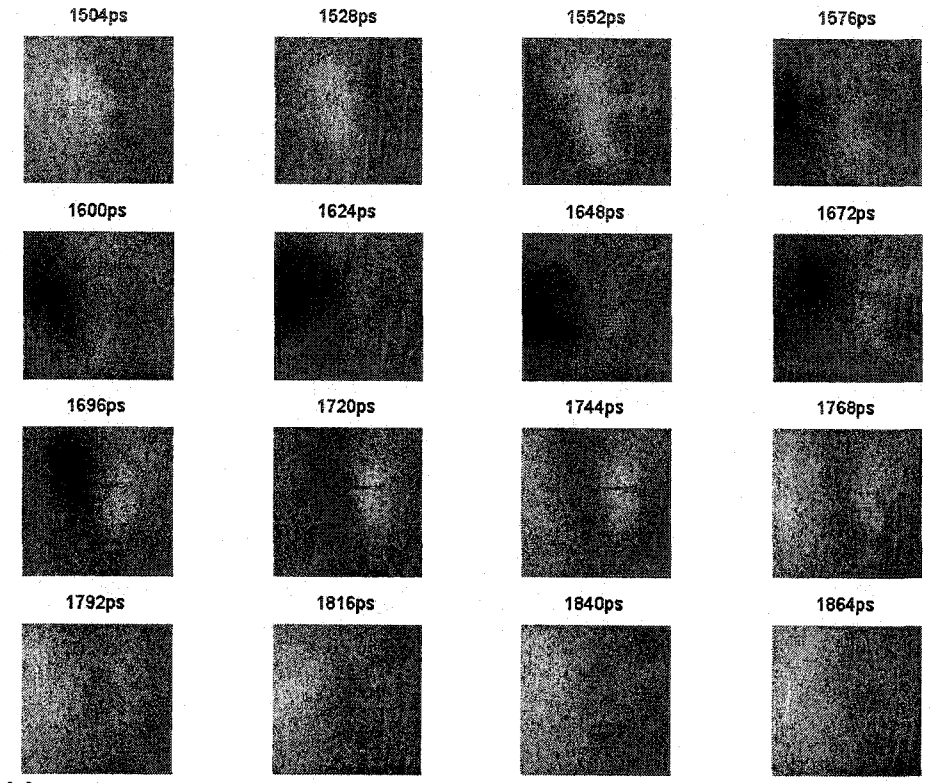

(a)

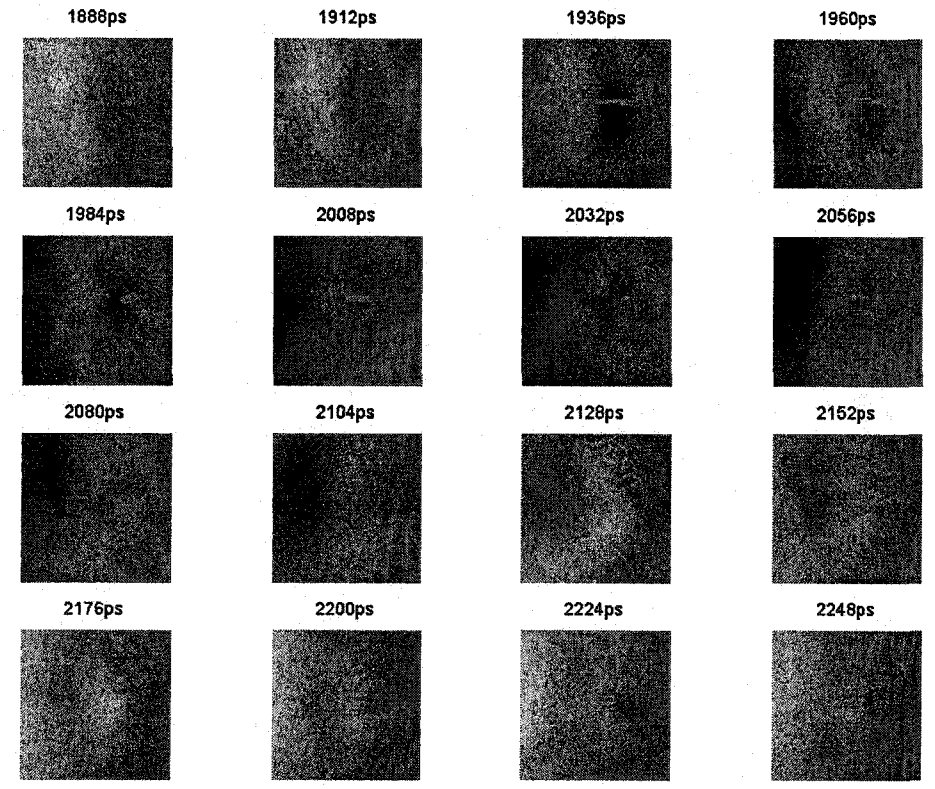

(b)

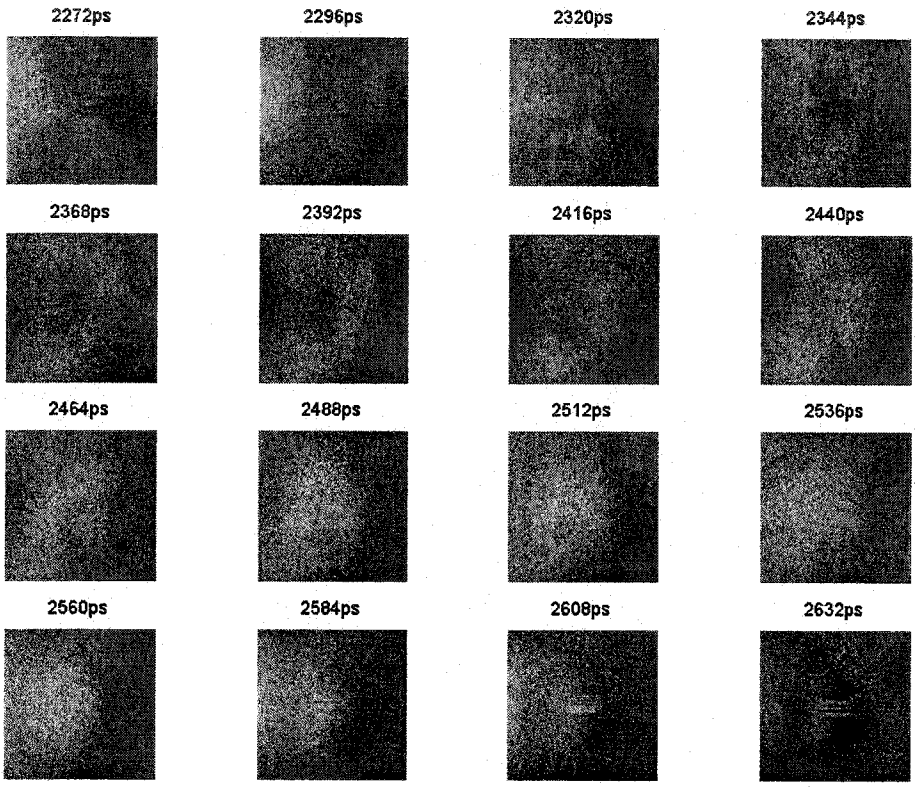

Fig.4. Set of experimental 2-D frames a (top), b, c (below) at high probe power 15mW from the right end of the Permalloy ellipse. The sudden changes of the out-of-plane component of the magnetization close bright spots and curved edges of the thin magnetic element (a high out-of-plane angle of the magnetization vector). The temporal step between frames is 24ps. The width of the scanned area is 1.5μm (100x100grid).

The processes of heat diffusion are very slow compared with the heating ultrafast probe pulse. From a point of view of changes of the magnetization oscillations one could conclude that the thermal equilibrium of the magnetic system is changed locally and the occupational number of thermal magnons (with wavelengths close the lattice constant) is temporarily increased. This could change the magnitude of the magnetization vector (by

increasing the number of non-uniform magnons). When heat source moves away, the magnetic system equilibrates back to the initial state.